STRUCTURE AND DYNAMICS OF MODEL SYSTEMS

STRUCTURE AND DYNAMICS OF MODEL SYSTEMS: FROM FERROFLUIDS TO BRAIN MEMBRANES

By

MATTHEW ALBERT BARRETT, B.Sc.

A Thesis
Submitted to the School of Graduate Studies
in Partial Fulfillment of the Requirements
for the Degree
Master of Science

McMaster University

MASTER OF SCIENCE (2012) McMaster University
(Physics) Hamilton, Ontario

TITLE: Structure and Dynamics of Model Systems: From Ferrofluids to Brain Membranes

AUTHOR: Matthew Albert Barrett, B.Sc.(University of Guelph)

SUPERVISOR: Dr. Maikel Christian Rheinstädter

NUMBER OF PAGES: xi, 153

Abstract

Soft condensed matter systems are a very diverse and challenging subject to study. To understand the complex macro-properties of such systems one approach is to characterize the microscopic structure and dynamics. A powerful technique for determining micro and nanoscale properties is scattering of radiation sources. Light, electron and neutron scattering techniques provide insight into the complicated molecular structures and the processes happening on these small scales.

We have used neutron and x-ray scattering techniques to determine structural and dynamical information from two different types of soft condensed matter systems. The microscopic nature of a cobalt magnetic fluid was studied using neutron scattering, and the structure and dynamics of molecules within lipid bilayers was studied with the use of both neutron and x-ray scattering.

Under strong magnetic fields, our cobalt fluid's small magnetic particles formed short chains, which we observed using neutron scattering.

In the lipid bilayer systems which were studied we determined the positional orientation of cholesterol, Aspirin, and ethanol molecules, observed the effect of temperature on some of these systems, characterized domains and dynamics, and recreated the molecular structures of Alzheimer's protein in a brain-like membrane.

Acknowledgements

First, my sincere thanks goes out to all of the collaborators who have helped make these projects possible. John Katsaras and Norbert Kučerka have shared their expertise of biophysical and membrane experiments and helped us through many of the snags encountered in the course of experiment and analysis. Andreas Deschner has been a great help with the programming and Monte Carlo simulations which were used in the magnetic fluid project, and have spilled over into other projects as well. An-Chang Shi's wide breadth of knowledge on phase transitions and soft condensed matter systems has been invaluable in thinking about the theoretical aspects of our projects.

The undergraduate students who have worked in our lab have also been absolutely vital to the success of our projects. Nick Jago and Mike Moore's perseverance is phenomenal, they toiled in the lab for the better part of their thesis projects determining the ideal protocol for preparing lipid bilayer samples. Rick Alsop's work creating samples and helping us interpret the data was outstanding. Randy Belanger, Golnaz Roshankar and Chris Huynh must be thanked for their hard work making a seemly endless amount of excellent samples and for jumping at the opportunity to fill in any gaps in our sample arrays. Songbo Zheng has been an excellent lab partner also, putting in countless hours figuring out preparation procedure and preparing excellent samples.

Martin Kaye's hard work and striving for perfection attitude has been inspiring for me, his fantastic M.Sc. thesis was an important resource and great jumping off point for my thesis. Laura Toppozini has done some amazing work in her short time in the group, and has been a great resource and discussion partner for my understanding of techniques and systems used in certain projets. Clare Armstrong's amazing artistic perspective has make it easy to visualize our systems and her wide knowledge of membrane physics has made her my go to person with any questions of analysis, conceptualization or artistic nature.

My parents and grandparents must also be thanked. Their enthusiasm and constant interest in my experiments has driven me to work hard and has also allowed me to practice unique ways of explaining concepts to non-physicists.

Most importantly Maikel Rheinstädter has been an unbelievable supervisor. His

flexibility, enthusiasm, patience and laboratory skills are unmatched by any other scientists I've worked with. Maikel has made it easy to get excited about my projects, and has helped me succeed, knowing the appropriate times to step in and help and when to allow me to figure things out for myself. He is the scientist I one day hope to be.

Contents

List of Figures

List of Tables

LIST OF TABLES

Chapter 1

Introduction

Neutron and x-ray scattering have been used extensively to discover the underlying microscopic structures found in a wide variety of samples: from superconductors, to polymer substances, to biological membranes. Although neutrons and x-rays are very different forms of radiation, the scattering theory which is used to explain how these types of radiation interact with matter, and the interpretation of the data extracted from neutron and x-ray scattering experiments has much overlap. The similarities and differences between x-ray and neutron scattering will be discussed in the following document using a magnetic fluid example, and plenty of biological examples.

Included in the following thesis are the results from three (and a half) neutron scattering experiments and four (and a half) x-ray scattering experiments.

The first of the neutron experiments describes the equilibrium behaviour of a cobalt magnetic fluid exposed to high magnetic fields. We find that cobalt particles form short chains (three or four particles in length), rather than the long (greater than 100 particle) chains predicted by theories.

Three x-ray scattering experiments are then discussed. In these experiments the bilayer structure of a saturated lipid, DMPC, with various amounts of Aspirin, cholesterol and combinations of both of these molecules. We see that Aspirin resides near the head groups of the DMPC lipid bilayer, cholesterol resides near the tails, and both molecules can simultaneously exist in a bilayer structure. We also observe empirically the saturation limit of ASA and cholesterol into a bilayer.

Two neutron scattering experiments involving domains will then be discussed.

One experiment uses the saturated lipid DPPC in single component bilayer format and by changing the coherence length of the neutron beam different phase domains become visible. The next experiment uses neutron scattering to observe cholesterol and DMPC bilayers and through the use of inelastic neutron scattering, dynamics corresponding to various phases are observed.

An experiment with ethanol molecules in a hydrated DMPC powder is observed with both x-ray and neutron scattering. (The half-experiments mentioned previously). The x-ray scans give structural data about the bilayers which form, and the neutron data allows us to see how ethanol changes the dynamics of the bilayer.

Finally, some initial results of an experiment involving brain-like membranes with Amyloid-β are discussed. By changing the cholesterol content of a mixed (saturated, unsaturated, charged) lipid bilayer Amyloid-β peptides were driven from a dispersed to aggregate state.

Chapter 2

Theoretical Background

2.1 Scattering

The static properties of the structure of matter have been probed with radiation since the discovery of x-rays by W.C. Röntgen in 1895. X-ray and neutron radiation are both non-destructive and non-invasive methods of determining microscopic details of fragile structures with great detail.[2]. Techniques used in scattering measure the momentum and energy of incoming and diffracted radiation and determine the composition and dynamical information of the sample of interest. Scattering provides insight into many different systems including super-conductors and other magnetic materials, metals, polymers, biological samples (particularly lipid bilayers) and many other systems. The range of some common scattering techniques as compared to size of biological samples can be seen in Figure 2.1.

To understand a scattering experiment, one must know specific details about the incident and diffracted radiation. By observing (or selecting) a specific angle and wavelength this knowledge can be achieved. The wavevectors of the incident and diffracted radiation are often denoted by $\overrightarrow{k_i}$ and $\overrightarrow{k_f}$, with $q = \frac{2\pi}{\lambda}$, where λ is the wavelength of the radiation. From these wavevectors, the scattering vector $\overrightarrow{q}$ is determined by taking the difference of the incident and final wavevectors, with the angle between the two denoted by 2θ. The scattering triangle shown in Figure 2.2 shows the geometry of these vectors.

One may also be interested in the energy of the incident and final wavevectors.

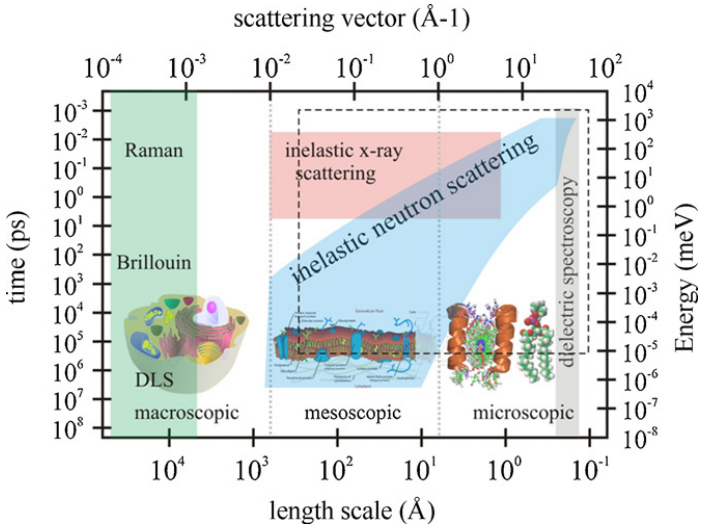

Figure 2.1: Length and time scales of selected spectroscopic techniques. Scattering techniques and their experimentally achievable ranges, in momentum and energy space. Scattering techniques cover dynamics from "macroscopic" (cells) to "microscopic" molecules. The dashed rectangle represents computer simulation range. Figure from [3].

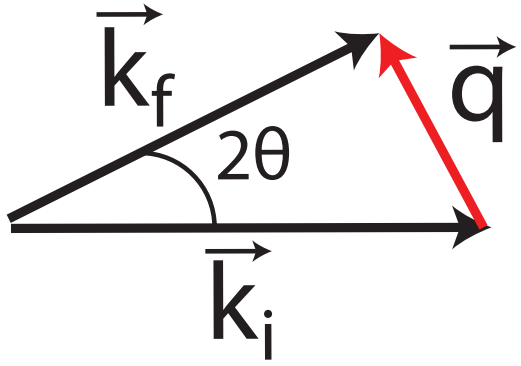

Figure 2.2: Scattering triangle - determination of scattering vector. By taking the difference of the final and incident wavevectors, the scattering vector $\vec{q}$ can be determined.

Energy calculations are needed for inelastic scattering, where a transfer of energy occurs and the sample gains or loses energy. First by multiplying by $\hbar$, we convert

to momentum (i.e. $\overrightarrow{p} = \hbar \overrightarrow{k}$). The equations below (equation 2.1, 2.2) show how to determine the energy of a wave (as in x-ray or light scattering) and of a particle (as in neutron or electron scattering).

$$E_{wave} = pc = \hbar kc = \frac{hc}{\lambda} \tag{2.1}$$

$$E_{particle} = \frac{p^2}{2m} = \frac{\hbar^2 k^2}{2m} \tag{2.2}$$

The difference between the initial and final energy of neutrons entering the leaving the sample is the energy transfer ($\hbar\omega$). If this value is zero, no energy is lost to the sample, and the scattering is elastic. If the energy transfer is non-zero, the loss or gain of energy represents an in-elastic scattering instance.

Elastic scattering provides details of structure of the system and information about equilibrium distances of scattering sites. Calculations using Bragg's law (equation 2.3) can be made to determine the spacing between scattering planes (d), if the angle between the incoming particle and that scattering plane (θ), and the wavelength (λ) are known. This is shown in Figure 2.3.

$$n\lambda = 2d \sin\theta \tag{2.3}$$

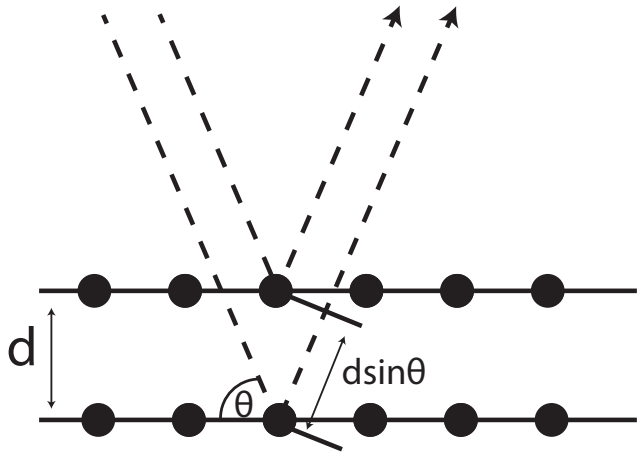

Figure 2.3: Visual representation of Bragg's Law.

A lattice with regular spaced scattering sites will possess a reciprocal space lattice,

which is defined by the set of all wavevectors which lead to constructive interference. This reciprocal lattice is unique to the wavelength of the radiation. We can now relate the reciprocal scattering vector to lattice spacings in real space d by a factor of 2π. (See equation 2.4).

$$|\overrightarrow{q}| = \frac{2\pi}{d} = \frac{4\pi \sin\theta}{\lambda} \tag{2.4}$$

Scattering radiation involves interference phenomena between the photons or neutrons scattered by the atoms or molecules. An experiment often involves counting the number of photons/neutrons scattered in a particular solid angle, and also determining the change in energy. The total scattering cross-section, which tells us the number of neutrons scattered per second, normalized to the flux helps is how the scattering at a particular position is defined. This is seen in equation 2.5.

$$\begin{aligned} \sigma_s &= \int (\frac{d\sigma}{d\Omega}) d\Omega, \\ with\ \frac{d\sigma}{d\Omega} &= (\frac{neutrons/s\ into\ d\Omega}{\Phi d\Omega}) \end{aligned} \tag{2.5}$$

Where $d\Omega$ is the solid angle which a detector subtends, Φ is the incident neutron flux, and the integral is over all directions. This cross-section has dimensions of area.[4]

Neutrons scatter from individual nuclei, where x-rays scatter from the electron cloud. Neutron radiation gives rise to incoherent and coherent scattering. For neutrons we can take advantages of the cross-sectional differences of hydrogen and deuterium to increase scattering contrast. From the spatial distribution of atoms in the sample, we can obtain the structure factor $S(\overrightarrow{q})$, essentially the amplitude of the scattered neutrons. The structure factor's magnitude squared is proportional to the intensity, as in equation 2.6.[4]

$$I(q)\alpha|S(\overrightarrow{q})|^2 \tag{2.6}$$

Both x-rays and neutrons can be used to determine the structure factor S($\overrightarrow{q}$). However there are reasons why one radiation source would be utilized over the other.

X-rays are chosen over neutrons in some cases due to the following reasons: it is possible to produce much higher intensity x-rays than neutron beams, the static

approximation holds to a high degree of accuracy - certain corrections which are made for neutrons are not necessary, and x-rays do not experience incoherent scattering. There are also some downsides to using x-ray scattering: x-rays scatter from electrons, rather than from the nuclei, and the scattering depends on an atomic form factor, the intensity of scattered x-rays becomes very small for $q \geq 5$ Å^{-1}. Due to the large absorption, reflection is the means of scattering, rather than transmission - which is a problem for reactive liquids prone to surface contamination.

Neutron scattering produces a form-factor which is independent of $\overrightarrow{q}$'s magnitude, and scattering is able to be observed through transmission due to the small absorption factor. The opportunity to take advantage of the incoherent scattering from hydrogen and deuterium also makes neutron scattering an attractive choice. Neutrons may have more than one interaction or scattering event in a sample, which makes it necessary to correct for the effects of multiple scattering in the sample.[5]

Properties of x-rays and neutrons are compared in Table 2.1.

X-ray and Neutron Properties		
Property	x-ray	Neutron
classification	wave	particle
mass	-	1.675x10^{-27} kg
charge	-	-
spin	-	s=-$\hbar/2$
velocity	c	$\leq$2200 m/s
momentum	$\hbar/c$	mv
energy	hc/λ	$\frac{1}{2}mv^2$
magnetic moment	-	-9.649x10^{-27} J/T
decay lifetime	-	885.9 $\pm$ 0.9 s
energy range	100 eV to 100 keV	$\sim$3x10^{-7} eV to $\sim$20 MeV

Table 2.1: Properties of x-rays from [2], properties of neutrons from [6]

2.1.1 Neutron Scattering

In 1920, Ernest Rutherford proposed the idea that the inconsistency between the atomic number of an atom and that atom's mass could be explained by the presence of some neutral particle within the nucleus. Experiments in the 1930s by Viktor Ambartsumian and Dmitri Ivanenko in the USSR, Walther Bothe and Herbert Becker

in Germany and James Chadwick in the UK verified this hypothesis and determined the mass of this chargeless particle.[7]

Due to the neutral charge of the neutron, the particle penetrate deeply into matter (much deeper than electrons or protons, which are stopped by electrostatic repulsion). Through elastic scattering, the details of microscopic structures are elucidated, and through inelastic scattering dynamical details can be determined.

The production of neutrons for scattering experiments occurs in two separate ways, through fission processes, or through spallation, each having some distinct advantages and disadvantages.

Fission for neutron production

Neutron beams with intensities suitable for scattering are produced in nuclear reactors. The fission of uranium nuclei results in neutrons with energies from 0.5 to 3 MeV. In reactors fast (MeV) neutrons are produced from the fission process of ^{235}U atoms. These neutrons are slowed by a room temperature heavy water moderator (in the case of National Research Universal reactor in Chalk River, for example) and emerge at $\sim$0.025 eV. Next these are monochromated using a monochromating crystal such as Pyrolytic graphite. The Institut Laue-Langevin (ILL) in Grenoble uses a 300 K heavy water moderator, and the emerging neutrons are centered at $\sim$1 Å. This peak can be shifted by allowing neutrons to equilibrate with a hot source or cold source (e.g. graphite at 2400 K at ILL or 40 K liquid hydrogen at National Institute of Standards and Technology at Gaithersburg). Figure 2.4 gives a schematic of a reactor and explains some necessary parts of the setup.

These type of sources produce neutron flux of greater than 10^{15} cm^{-2} s^{-1}. This flux is limited by the ability to remove heat from the core, it is unlikely to construct a reactor which would far surpass this range. To increase flux (and thus decrease time needed for scans) spallation sources have also been considered.

Experiments for papers I, V, VI and VII all use nuclear fission neutron sources, ILL (Grenoble), CNBC (Chalk River), ILL (Grenoble) and NIST (Gaithersberg), respectively.

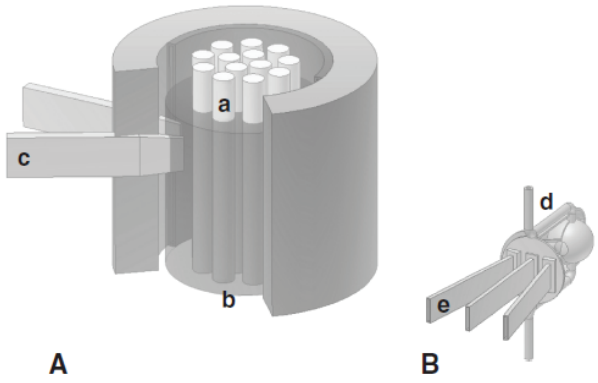

Figure 2.4: Nuclear reactor schematic
Schematic of nuclear reactor for production of thermal neutrons. Fuel rods (a) containing ^{235}U undergo fission when these atoms collide with moderated neutrons. The low probability that a fast neutron will encounter the Uranium atoms makes it necessary to use some moderator in the core to slow neutrons after they fission. water, heavy water, graphite or beryllium are commonly used. Thermal neutrons with a wavelength of $\sim$1.2 Å exit the reactor (b) via a beam tube or window (c). To lower the neutron speed (temperature) they interact with a colder moderator (d) and are transported to various spectrometers using total external reflection mirrors (e). From [4]

Spallation for neutron production

A spallation source is an accelerator driven neutron producer. High energy subatomic particles (typically protons) are produced in a linear accelerator and collide with a heavy metal target, releasing neutrons from the target's nuclei. Protons arrive in pulsed bunches (and thus the neutrons produced are also pulsed). The initial energy of the neutrons produced is quite high, and must be moderated from MeV to meV energy. There is much less heat per neutron than reactor sources, and thus flux can be much larger (10^{17} cm^{-2} s^{-1}). Certain techniques, such as time-of-flight are designed to allow for the pulsing, and thus compensate for the time-averaged flux disadvantage of pulsed neutron sources. ISIS (Oxford, UK), SNS (Oak Ridge National Lab, US) and soon the ESS (Lund, SE) are some examples of pulsed neutron sources, although none of these were used in our experiments.

Neutron temperatures

In Paper VII, neutron scans were done at ILL with two different instruments, the cold neutron triple-axis spectrometer, IN12 (also used for paper I) and the thermal neutron triple-axis spectrometer, IN8. Neutron "temperature" indicates the kinetic energy of a free neutron. Fast neutrons (just after fission) are slowed by passing through a moderating material (water, heavy-water, graphite or beryllium typically) which is at a regulated temperature. Kinetic energy relates to the speed and wavelength of the neutron, so one can change wavelength by moderation. Thermal neutrons have energies of $\sim$0.025 eV, and cold have energies of $\sim 10^{-5}$ eV up to the thermal value. For IN12 - the cold neutrons are produced using a Beryllium moderator and will be discussed in more detail in Section 5.2, IN8, on the other hand, has neutrons coming from the same source, but have much higher energies, due to the lack of Beryllium moderator in the beampath.

2.1.2 X-ray Scattering

X-rays were discovered by Röntgen in 1895 when he was examining radiation associated from electrodes which discharge in evacuated glass tubes. The tube which was under examination was covered with opaque paper and wood, so no visible light could escape, in spite of this opaque covering radiation was passing though the wood and paper coverings and appearing on a fluorescent screen in the distance. It seemed as if organic materials were invisible to this radiation, where metal would leave shadows on the fluorescent screen. Photographic paper was placed on the screen and these shadows were documented. By putting his hand in the beam path, he could see the bones inside.[8]

X-ray absorption depends strongly on the atomic number of the elements, and varies as Z^4 (where Z is the atomic number). Soon after the Braggs (father and son) determined through diffraction experiments that x-rays were simply electromagnetic radiation with short wavelengths.[2]

In 1912, Coolidge developed an x-ray generator tube in which the voltage and current could be controlled independently, with the limiting factor being the heat dissipation at the anode. The maximum power of such a device was $\sim$1 kW. This tube was the standard for close to 50 years, when it was discovered that by rotating

the anode would allow for heat to be dissipated over a much higher volume.

Anode X-ray sources

X-rays from tube or rotating anode sources are generated by accelerating electrons to a very high speed through a vacuum and directing them to a charged metal target, the anode. This will result in a continuous spectrum over a large range of wavelengths (bremsstrahlung radiation) with a few high intensity characteristic x-rays found in the top of the wavelength range. The bremsstrahlung radiation comes from electrons being decelerated and stopped in the metal (from *bremsen*, German for brake). The sharp charasteristic lines are generated from the vacancies created from an inner electron shell of the metal atom. When the outer shell electrons relax down to lower levels a photon with energy equal to the difference of these two levels is emitted. This is shown for Copper in Figure 2.5.

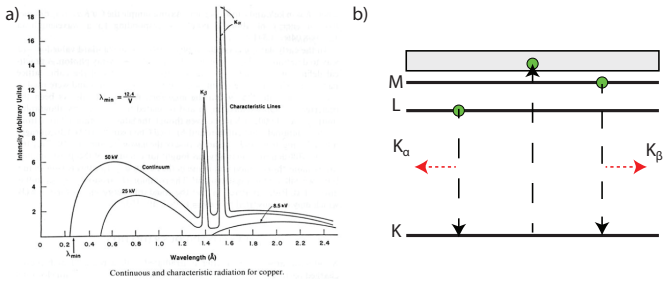

Figure 2.5: X-ray spectrum radiation from Copper target.
a) The Copper target produces continuous x-ray scattering intensity, with certain well defined characteristic K_{α_1}, K_{α_2} and K_β peaks at higher wavelengths. b) Schematic energy level diagram the K_α peak comes from electron dropping from L to K and K_β peak comes from electron dropping from M to K energy shell.[2]

The discrete K peaks which are obtained from x-ray scattering are most useful in scattering, it is far easier to obtain high resolution scans if the bandwidth of incoming x-rays is narrow. By the use of monocromating mirrors (constructed of a highly-oriented crystal, often graphite), a specific wavelength is chosen. This wavelength is different for different target metals. Table 2.2 displays this data.

Only a small fractions of the photons emitted are used, due to the small angular divergence of the beam, which must be less than a few squared milli-radian. The

Target		Wavelength (Å)		
Element	Atomic #	K_{α_2}	K_{α_1}	K_{β}
Cr	24	2.294	2.290	2.085
Fe	26	1.940	1.936	1.757
Co	27	1.793	1.789	1.621
Cu	29	1.544	1.541	1.392
Mo	42	0.7135	0.7093	0.6323
Ag	47	0.5638	0.5594	0.4970
W	74	0.2138	0.2090	0.1844

Table 2.2: Discrete x-ray peaks for characteristic scattering of common target metals. This scattering would be similar to the example of the Copper x-ray spectrum in Figure 2.5, with different characteristic peaks. Table adapted from [9]

source is not tunable, so the wavelength which is produced cannot be continuously changed, even if this is not the ideal wavelength.

Synchrotron X-ray sources

Although in our experiments, all the x-rays are generated through a rotating anode source, x-rays can also be produced via synchrotron radiation. This is a general term for radiation produced from charged particles which travel at relativistic speeds in magnetic fields, along a circular path. This radiation is produced in storage rings, where electrons or positrons circulate at a constant energy. This produces a large spectrum of radiation at high intensity, allowing the user to choose from a broad range of wavelengths. Sources such as the Canadian Light Source in Saskatoon, and many other synchrotron sources produce this sort of radiation.

2.2 Biological Membranes and Components

The neutron and x-ray scattering experiments were all (except for Paper I, a magnetic fluid) focused on biological samples, in particular cell membranes. Membranes are utilized by cells to separate the inside of the cell from the extracellular environment and for internal compartmentalization of the cell. A membrane is permeable to certain ions and molecules, and also relies on proteins to transport molecules in and out of the cell. These processes allow the cell to choose and maintain the concentration of

nutrients and ions in the cytoplasm.

In 1972, lipid bilayers were first characterized as being two-dimensional liquids. The fluid mosaic model [10] viewed the membrane as a liquid of freely flowing lipid and protein molecules. Since the fluid mosaic model was proposed, there have been improvements and additions to it. The membrane contains functional domains which are classified into three parts: 1)protein-protein complexes[11, 12]; 2)lipid rafts[13, 14]; and 3)cytoskeletal pickets and fences.[15, 16].

Although a biological cell is quite complex, containing lipids, proteins, macromolecules and sugars, model membranes with a reduced number of components are often used. These model membranes are possible to create artificially in the lab based on the property of the lipid membrane to self-assemble into the two-dimensional lipid bilayer. The lipid bilayer is the backbone of the cell membrane, and can host many of the other molecules important to the membrane. The lipid bilayer, due to the regular, repeating structures the lipids form, is an ideal candidate for x-ray and neutron scattering. Scattering relies on periodicity and repeated structure.

2.2.1 Lipids

Eukaryotic cells invest huge amounts of their resources into generating thousands of different types of lipids. In fact, ∼5% of the genetic information contained in a cell's genome is used for lipid construction and upkeep.[17] Broadly, lipids can be categorized as small hydrophobic or amphiphilic (possessing both hydrophobic and hydrophilic domains) molecules.

Eight categories of lipids exist, and of these eight, three are commonly found in cell membranes.[18, 19] Glycerolipids, sphyngolipids and glycerophospholipids are the three categories which are present in lipid bilayers.

- **Glycerolipids** Glycerolipids are composed of glycerols that are mono-, di- or tri- substituted, and function as energy storage in the fat molecules of animal tissues. These are found in membranes at up to 8mass%.[20]

- **Sphyngolipids**. Usually containing a amino alcohol called sphingosine which already has a hydrophobic chain. Only one tail must be attached to create these lipids. These lipids are found commonly in the liver and in red blood

cells at concentrations of up to 19mass%.[21] These are usually saturated or mono-unsaturated with chain lengths of 16-26 carbons.

- **Glycerophospholipids** These are the most abundant lipids in the membrane, making up more than 40mass% of the membrane in mammal cells.[22] The head of the lipid contains a phosphate (PO_4) group and these so-called phospholipids are the key molecules in bilayer formation. Phospholipids were first observed by Theodore Nicholas Gobey in 1847, when he studied phosphatidylcholine in egg-yolk, and which he described in detail some years later in 1874.[23] Phospholipids will be discussed in greater detail in the rest of this section.

Seen in Figure 2.6. The acyl "tails" of the phospholipid (hence forth referred to as lipid) molecule are composed of tightly packed CH_2 groups. The non-polarity of these CH_2 molecules prevent hydrogen bonding and ensure hydrophobicity. The "heads" of a lipid molecule contain the charged phosphate group and other polar groups as well, making it hydrophilic.

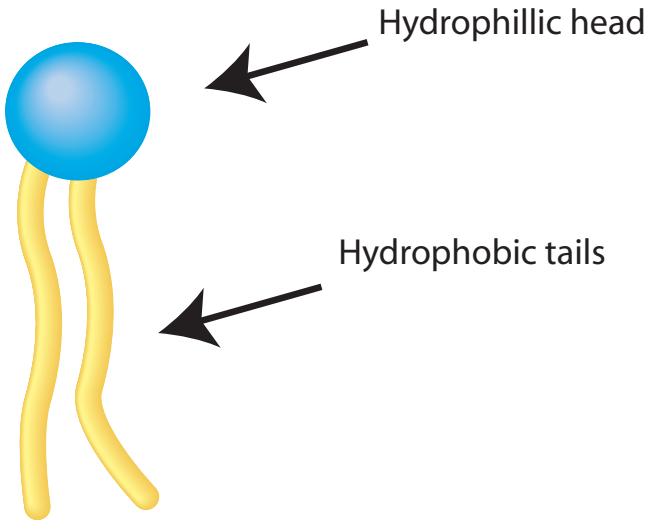

Figure 2.6: Cartoon of lipid molecule
Lipid molecule with hydrophilic head (coloured blue) and hydrophobic tails (yellow).

The other molecular groups in the head of the lipid, the electrical properties and the composition of the acyl tails allow further classification of lipid molecules. The common headgroups are phosphatidylcholine (PC), phosphatidylethanolamine

(PE) and phosphatidylserine (PS). PS contains one negative charge, while the other two contain counteracting charger (zwitterions). The tail chain length is typically from 12-24 carbons, and can contain from 0-6 carbon-carbon double bonds. A tail with no double bonds is called saturated, one double bond is monounsaturated and more than one is considered polyunsaturated. Tail characteristics are often expressed in the format (m:n), where m is the number of carbons from the backbone to the end of the tail and n the number of double bonds. A fourteen carbon saturated phosphatidylcholine lipid is shown in Figure 2.7.

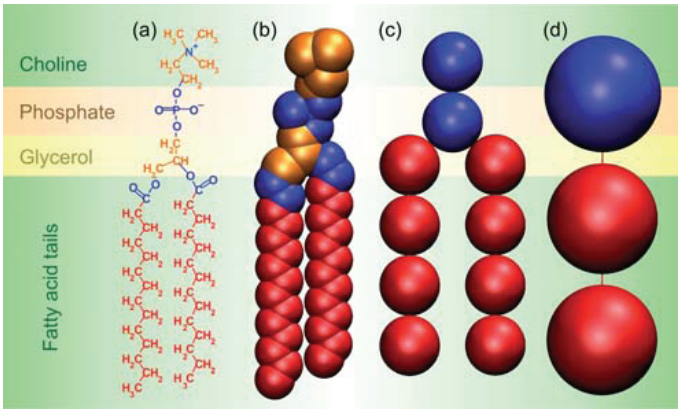

Figure 2.7: DMPC lipid and various simplifications
DMPC (14:0) lipid molecule. Blue regions are hydrophilic, orange hydrophobic in the headgroup and red regions are hydrophobic in the tail region.[24]

The abbreviation of a lipid tells much information about the molecule itself. Figure 2.8 provides the example for a DMPC molecule.

Some lipids commonly used in experimental biophysics are listed below. Most of the experiments (including papers II, III, IV, VI and VII) DMPC is used. In Paper V DPPC is lipid of choice. For Chapter 7 a mixture of lipids meant to replicate a mammalian brain was selected. This mixture contains DMPC, DOPC and DMPS.

2.2.2 Lipid Bilayers

Due to the amphiphilic nature of a lipid, when multiple lipid molecules are present in a polar (e.g. water) or non-polar (e.g. oil) solvent the lipid molecules will match their hydrophobic and hydrophilic domains and attempt to shelter the mismatched

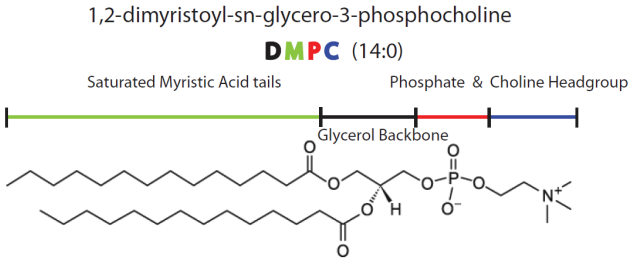

Figure 2.8: DMPC lipid structural information
The abbreviation of 1,2-Dimyristoyl-sn-Glycero-3-Phosphocholine gives information of the structural details of the lipid molecule. [25]

Properties of common experimental lipids				
Abbrev.	Formula	Chain Length	Molecular Weight (g/mol)	Gel-Fluid Transition (K)
DMPS	$C_{35}H_{65}NO_{10}PNa$	14:0	701.844	308
DPPC	$C_{40}H_{80}NO_8P$	16:0	734.039	314
DSPC	$C_{44}H_{88}NO_8P$	18:0	790.039	328
DOPE	$C_{41}H_{78}NO_8P$	18:1	744.034	283
DOPS	$C_{42}H_{77}NO_{10}PNa$	18:1	810.025	262
DMPC	$C_{36}H_{72}NO_8P$	14:0	677.933	297
DOPC	$C_{44}H_{84}NO_8P$	18:1	786.113	253

Table 2.3: Properties of experimental phospholipids. Chain length given in (m:n) format, where m is the number of carbon atoms in a single tail, and n the number of double bonds present. Fluid transition temperature is cited for a single component membrane composed solely of this lipid.[26] Bold entries were used in experiments discussed in the thesis.

region from the solvent. Assuming a polar solvent, depending on the type of lipid and its concentration structures such as micelles (a sphere of lipids with the hydrophobic tails in the centre) or bilayers (as would be seen in a cell membrane) are likely to form. This is shown in Figure 2.9

The bilayer structure forms when the headgroup and tails occupy roughly the same area. This will create an approximately flat structure. Depending on certain factors, including the temperature and hydration level, this bilayer configuration is able to experience three flat-lamellar phases: gel (L_β), ripple ($P_{\beta'}$) and fluid (L_α), although the ripple phase is not always present. These phases are shown in Figure 2.10.

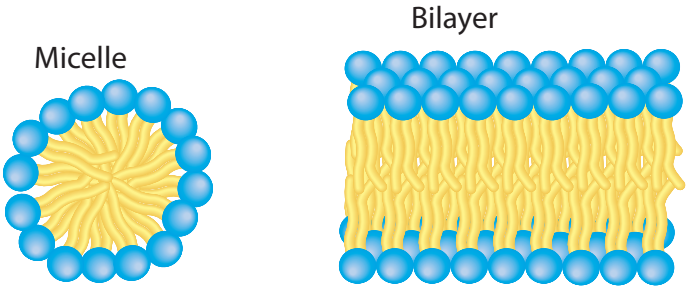

Figure 2.9: Lipid structures in polar solvent
Lipids form self-assemble in to structures such as micelles (left) and bilayers (right) when introduced to polar solvent (such as water).

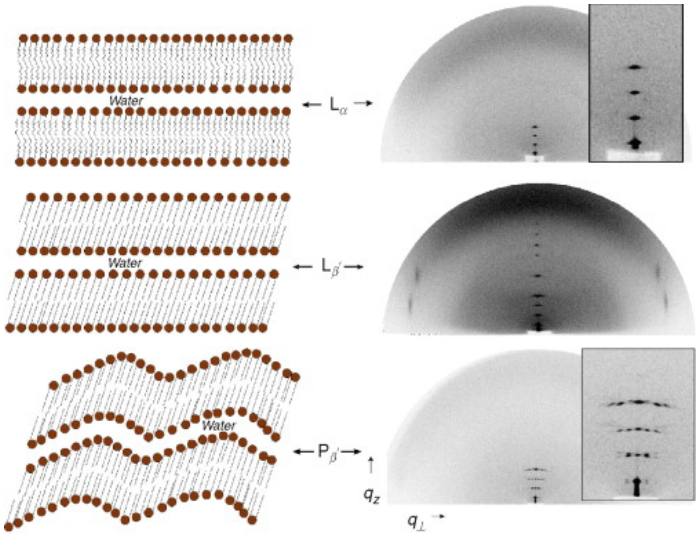

Figure 2.10: Phases of phospholipid bilayer cartoons and diffraction data.
Schematic of fluid (L_α), gel (L_β) and ripple ($P_{\beta'}$) phases of lipid systems in water is shown on the left. On the right diffraction patterns for these three phases are shown. Due to the rippling of the bilayer in the ripple phase bands of intensity rather than well defined points arise in the diffraction pattern.[27]

Papers V, VI and VII all discuss these phases and their transition temperatures.

Chapter 3

Cobalt Particle Magnetic Fluid: Chain Formation in High Magnetic Fields

Paper I

I. Barrett, M., Deschner, A., Embs, J., and Rheinstädter, M., (2011) *"Chain formation in a magnetic fluid under the influence of strong external magnetic fields studied by small angle neutron scattering."* Soft Matter. 7:6678-6683.

3.1 Understanding Magnetic Fluid Systems

One of the most commonly studied magnetic system is the condensed matter crystal lattice. Each point in the lattice is inhabited by an atom or molecule which exhibits magnetic properties. Particles interact via the direct exchange interaction. This is a generalization of the exchange interaction - a quantum mechanical effect which increases or decreases the expectation value of the energy or distance between two identical particles when their wave functions overlap.[28] For a ferromagnetic material with atoms confined to a lattice, the so called "direct exchange interaction" represents the Hamiltonian over all i and j pairs. This is described by equation 3.1.

$$U_i = -\sum_{i \neq j} J_{i,j} \overrightarrow{m_i} \cdot \overrightarrow{m_j} \tag{3.1}$$

Where U is the potential energy of particle i in our system, J is the exchange constant, and the m's are the magnetic moments of a particular particle. These interactions result in interesting effects such as superconductivity, quantum magnetism and heavy fermions.

A magnetic fluid system has properties which are quite different than a crystal magnetic system. Rather than all atoms being firmly fixed to a lattice, groups of atoms make up a lattice core which can be thought of as a single magnetic particle, with a giant spin (tens of thousands of μ_B). The particles found in the magnetic fluid are suspended in a carrier liquid, typically oil based. Particles are treated to prevent aggregation, either electrostatically or with a surfactant layer. The system behaves as a colloidal system until it experiences an external magnetic field. [29] Experiments have shown that various microstructures are formed in the fluid which result in interesting macroscopic properties.[30, 31] In Figure 3.1 a magnetic fluid is surrounding an electromagnet. The fluid becomes more viscous and resists gravity to form three dimensional patterns on the surface of this magnet.

The energy of a magnetic fluid system can be calculated from the interaction of each particle with an external magnetic field, as well as neighbouring particles. This is shown in equation 3.2:

$$U_i = -\overrightarrow{m_i} \cdot \overrightarrow{B} + \sum_j -\overrightarrow{m_i} \cdot \frac{\mu_o}{4\pi \hat{r_{ij}}} \{3(\overrightarrow{m_j} \cdot \hat{r_{ij}}) \hat{r_{ij}} - \overrightarrow{m_j}\} \tag{3.2}$$

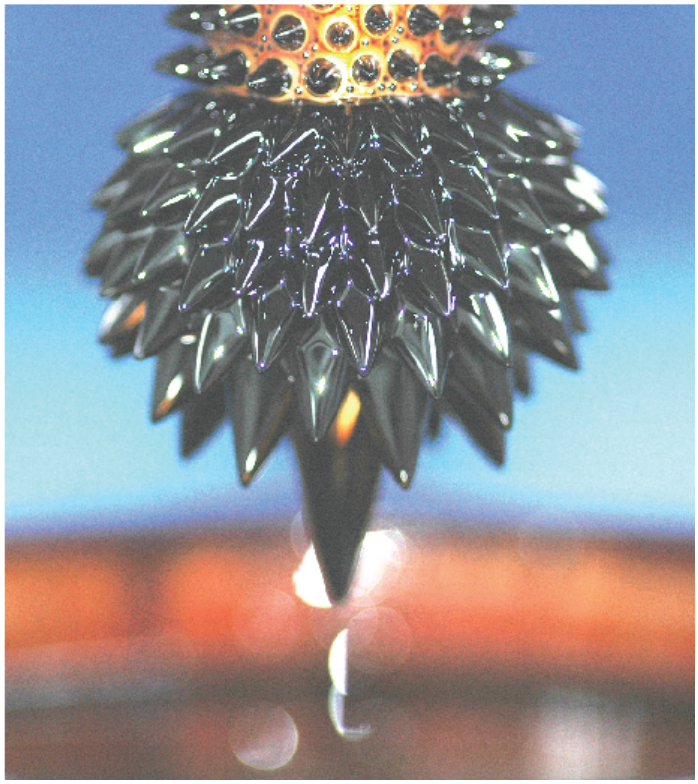

Figure 3.1: Photo of magnetic fluid on electromagnet
A magnetic fluid at the pole of an electromagnet. Three dimensional patterns form due to the microstructures present in the colloidal fluid. Photo from [32].

with $\overrightarrow{m_{i,j}}$ the magnetic moments of the particles, $\overrightarrow{B}$ the external magnetic field and $\mu_o = 4\pi \cdot 10^{-7} N/A^2$.

There are two types of relaxation responsible for the orientation of the magnetic moment of these particles. The Néel relaxation describes the direction of the magnetic moment relative to the orientation of the stationary magnetic core and was first theorized to explain "magnetic viscosity". Néel relaxation involves the lattice in the core of a magnetic particle reorienting (See the black region of the fluid in Figure 3.2). Brownian relaxation is described by the whole particle rotation in the fluid, where the magnetic moment is fixed to the particle itself, core included. As particles become sufficiently large, Néel relaxation becomes infinitely long, and Brownian relaxation prevails. [33] The core of the magnetic particles found in magnetic fluids are typically either magnetite, Fe_3O_4 or cobalt. Magnetite has a much lower magnetic moment

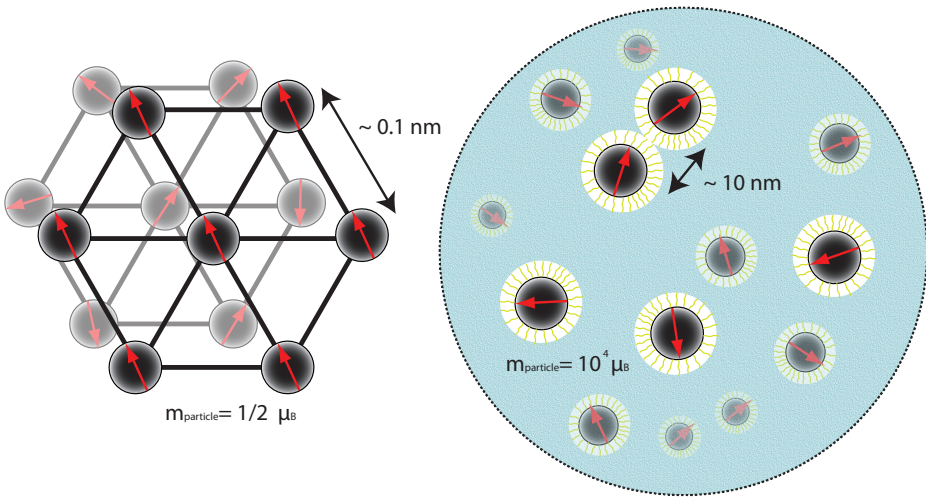

Figure 3.2: Magnetic systems: Lattice and fluid.
The crystal magnetic lattice on left with particles strongly bound to a hexagonal lattice. A magnetic fluid on the right with particles freely diffusing and rotating in a liquid suspension.

(two orders of magnitude smaller than cobalt cores, discussed in detail shortly), and has been studied extensively. In table 3.1 typical orders of magnitude of particles are compared between lattice and fluid systems. In Figure 3.2 the size of the particles, their respective magnetic moments, and an interpretation of their structural configuration is shown.

Comparison of model magnetic systems		
Property	Crystal Lattice	Fluid
particle spacing	∼0.1 nm	∼10 nm
magnetic moment	∼1/2 μ_B	∼10^4 μ_B
properties of interest	superconductivity [34] quantum magnetism	tunable macroscopic viscosity [29, 32] formation of microscopic chains

Table 3.1: A comparison of properties of crystalline and fluid magnetic systems. Due to the large particle size (and as a result the large particle spacing) Néel relaxation is almost infinitely longer than Brownian relaxation. Note that μ_B is the Bohr magneton, with $\mu_B = \frac{e\hbar}{2m_e} = 9.27 \cdot 10^{-24}$ J/T.[34]

The most important characteristics in defining a magnetic fluid are the volume fraction of the fluid (ϕ) and the dipolar coupling constant (λ). The fluid's volume

Cobalt Ferrofluid	MG	PCS	TP
$D_o(nm)$	11.0	19.0	-
$M_s(A/m)$	6512	-	-
σ (nm)	1.27	1.2	-
D_v (nm)	12.0	20	-
$D_{vol}(nm)$	13.5	22	16.2

Table 3.2: Values for the core-size D_o, and polydispersity parameter σ, saturation magnetization M_s, the volume averaged core-diameter D_v and volume weighted core-diameter D_{vol}, as taken from [1]. These were determined using the techniques magneto-granulometery (MG), photon correlation spectroscopy (PCS) and using a torsional pendulum (TP) technique. It is important to note that the particle diameter introduced before was also called σ, but in this paper it was referred to as D_o.

fraction represents the ratio between the volume of the magnetic particles contained to the total volume of the sample and can ranges from a very dilute solution ∼0.1% to ∼30%.[35] The dipolar coupling constant depends on the magnetic moment of the core (typically tens of thousands of μ_B for cobalt based fluids), as well as the diameter of the whole particle (σ, ∼10 nm), the temperature (T), Boltzmann factor (k_B) and permeability constant(μ_o and is shown in equation 3.3. The typical λ for a magnetite based magnetic fluid is close to 0.1, where for a cobalt particle magnetic fluid this unitless value is closer to 20, due in part to the much larger magnetic moment of cobalt. The large range in this value leads to particle dynamics which are more closely related to fluid dynamics for low λ, and much more dependent on magnetism for higher λ.

$$\lambda = \frac{m^2}{4\pi\mu_o kT\sigma^3} \tag{3.3}$$

Our sample's cobalt particles were measured in a variety of ways, including magneto-granulometry (MG), photon correlation spectroscopy (PCS) and torsional pendulum (TP) techniques. Figure 3.3 shows the distribution of particle sizes in the cobalt fluid. More detail on the fluids we used discussed in Table 3.2.

Magnetite based magnetic fluids have been well studied, and both macroscopic and microscopic structures have been determined. The large difference in magnetic moments of magnetite and cobalt warranted the question "Does a magnetic fluid with

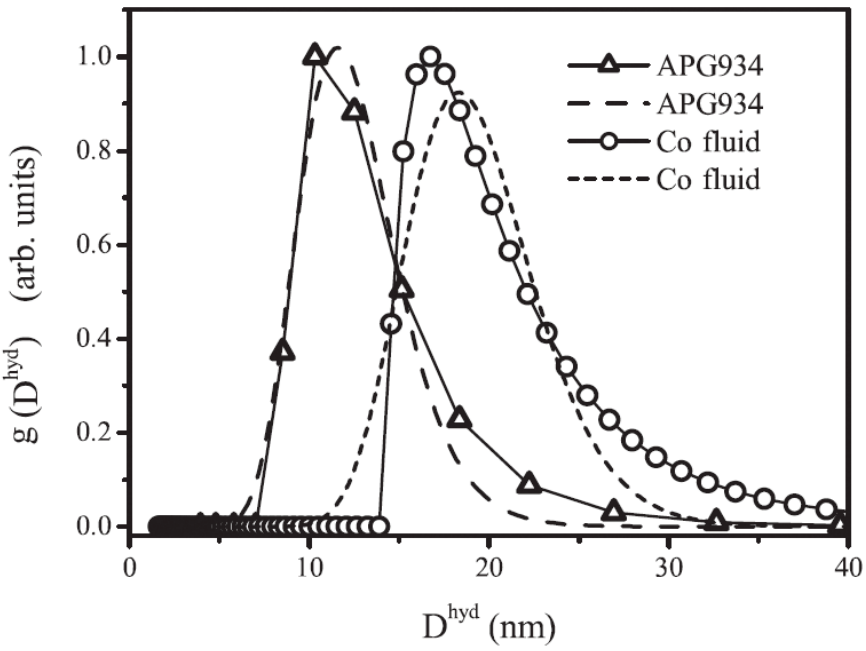

Figure 3.3: PCS measurement of hydration diameter of cobalt particles. Log-normal fits (dashed lines) of the number-weighted hydrodynamic-diameter distribution function g(D^{hyd}) for a magnetite fluid (APG934) and the cobalt fluid. From [1]

high dipolar coupling constant (cobalt based) behave the same as a lower coupling constant (magnetite based) fluid?". This study was done in two parts: first small angle neutron scattering was performed on the system with large external magnetic fields present (discussed in detail in Paper I), and second a computer simulation of particles in external magnetic fields was done to compare with experimental results.

3.2 Small-Angle Neutron Scattering

Small-angle neutron scattering (SANS) was used in this experiment. SANS takes advantages of elastic scattering at small angles (0.5^o to 10^o) to determine structural details of samples with a scale from ∼1-100 nm, and is quite effective at determining the shapes and sizes of particles in some homogenous medium.[36] The neutron beam is directed to the sample and elastically scattered on the nanometer scale, with atoms

inside the sample (as was discussed in Section 2.1). Nanometer sized scattering sites, of relatively uniform size allow the neutrons to interact strongly. Figure 3.4 shows a 30 m long SANS setup. This technique can also be achieved with a triple-axis spectrometer with precise angular control, which was used at the IN12 at ILL in Grenoble, France.

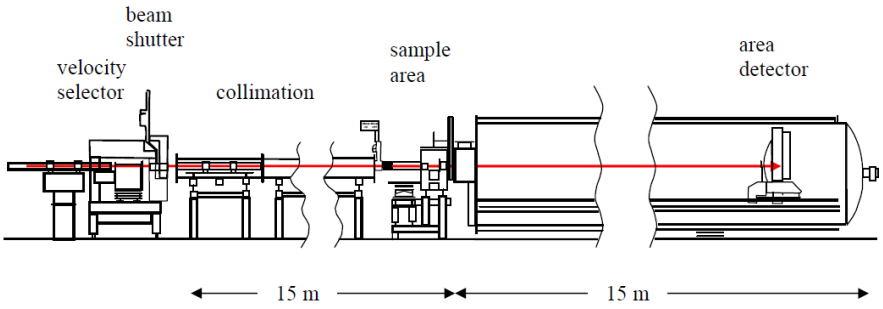

Figure 3.4: Schematic of SANS 30 m setup
A small angle neutron scattering setup based on the SANS instrument at National Institute of Standards and Technology (NIST), Gaithersberg, MD. [36]

Our experiment was quite unique due to the very strong magnetic field and the innovative scattering geometry. The superconducting split-coil horizontal field magnet which was used had a maximum field strength of 4 T (although for the experiment it was only necessary to use maximum of 2 T fields). The geometry of the split-coil ensured there was no coolant (liquid helium) in the beamline, and that we could change the scattering angle with respect to the magnetic field (up to 60^o). The angular freedom which was enabled by the triple-axis spectrometer and the magnetic environment allowed for scans along the axis of the magnetic field, and at 30^o and 60^o, as is seen in Figure 3.5 With these three scanning directions, a two dimensional overview of our sample can be obtained. With this 2D data we can determine the geometry of the aggregates forming in the system.

The simulation was a Monte-Carlo simulation programmed in Matlab and is discussed in Section 3.3 below. We expected that both of these investigations would result in similar findings, chain lengths scaling with external magnetic field length to long (hundreds of particle long) chains, which would be similar to the literature for magnetite fluids.

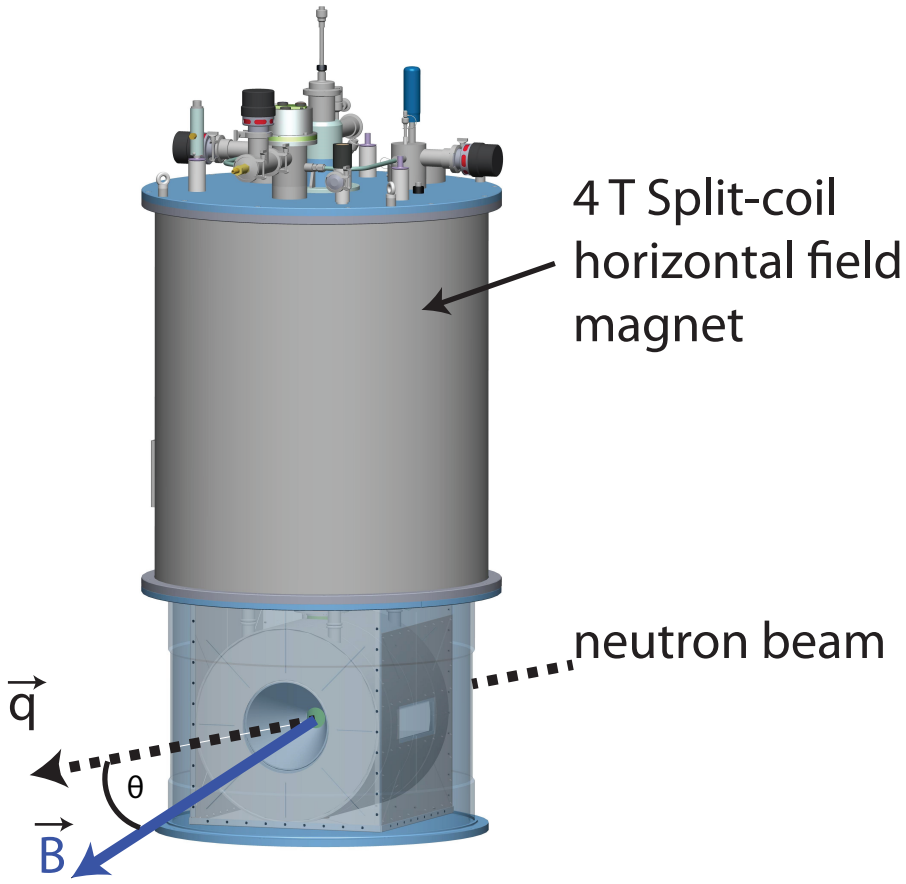

Figure 3.5: Superconducting split-coil horizontal field magnet
Schematic of scattering environment for high magnetic field with variable angle (θ). The angle between $\overrightarrow{q}$ and $\overrightarrow{B}$ was able to be varied through 0^o to 30^o to 60^o. Diagram adapted from [37]

3.3 Monte-Carlo Simulation of Cobalt Magnetic Fluid

To better understand the cobalt magnetic fluid system studied using small angle neutron scattering (Refer to Paper I) we developed a simple Monte-Carlo simulation. This simulation was vital to the interpretation of the experimental data and allowed us to speculate the behaviour of particles at a microscopic length-scale, which was compared to the experimental data.

3.3.1 Monte-Carlo technique

A detailed description of the Monte Carlo simulation technique is found in Figure 3.6. A flow diagram describing the program which we used.

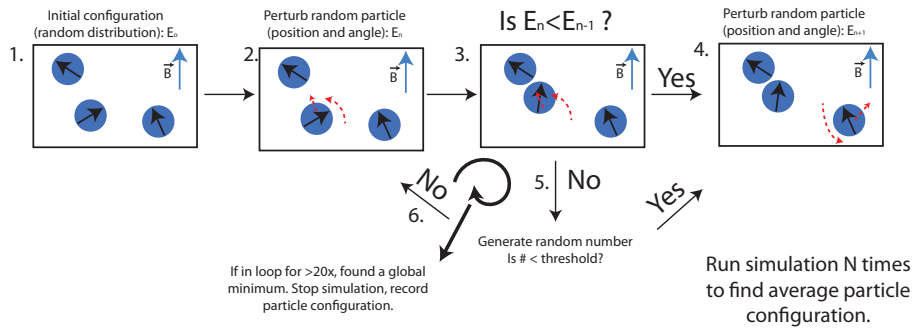

Figure 3.6: Flow diagram of Monte Carlo simulation
(1) Our Monte Carlo simulations involved taking a random initial configuration of particle position and angle of the magnetic moments and recording the system's total energy (Solving equation 3.4 for all particles). (2) One particle was chosen at random, and perturbed by a position and angle, the energy was again calculated, and (3) compared to the previous energy configuration. If the energy was minimized, (4) this configuration was accepted and a new particle was perturbed. If the energy was not minimized (5) a random number was generated, if this number is less than a threshold (0.2 for our simulation) we move to (4), otherwise we throw out the initial and go back to (2). If no lower energy state can be determined after 20 twenty tries, we accept this value as the equilibrium position.

$$U_i = -\overrightarrow{m_i} \cdot \overrightarrow{B} + \sum_j -\overrightarrow{m_i} \cdot \frac{\mu_o}{4\pi \hat{r_{ij}}} \{3(\overrightarrow{m_j} \cdot \hat{r_{ij}})\hat{r_{ij}} - \overrightarrow{m_j}\} \tag{3.4}$$

The Monte-Carlo simulation which we preformed was coded in Matlab, involved up to 200 particles (though a simulation of this size was extremely slow, <50 was more typical), and as many as 20 000 steps. The particles were placed in an external field, constant strength and direction for each. In all presented data our external field was oriented towards the top of the page, and the field strengths ranged from 0 T up to 2.0 T. This simulation environment is chosen specifically to best capture the sample environment of our experiment. Each step of the simulation involved a single particle moving in space on a 2D lattice, taking a step of length 1/2 σ (particle diameter) and undergoing a magnetic moment rotation of 5^o, corresponding to the

small Brownian relaxations which take place. After each step and reorientation the energy of the system was calculated using equation 3.2, for each particle interaction.

The simulation began with the particles distributed randomly with their magnetic moments also random in this 2D plane, and after each simulation step the calculated energy was compared to the previous step's energy. If the free energy was lower, the new step was considered valid. If the energy was larger a new random number from 0 to 1 was generated. If this number was larger than 0.2, the less favourable step was accepted. This procedure helps to avoid local energy minima. The equilibrium distribution of particles was observed for both low and high external magnetic fields. Typical distributions for low and high magnetic fields are visualized in Figure 3.7.

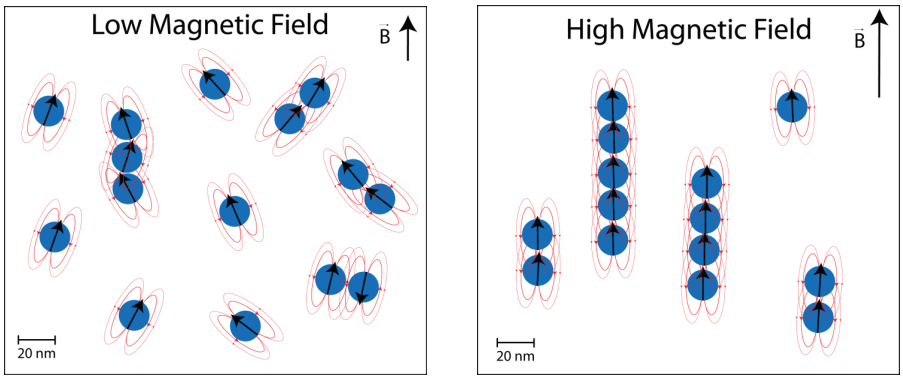

Figure 3.7: Monte-Carlo simulation.
Snapshots of the Monte-Carlo visualization, the figure on the left was done with a magnetic field of 0.1 T where on the right the high magnetic field is 2 T. Notice the average chain length of particles differing between the low and high external field cases.

From the simulations, we see average chain length is highly dependent on field strength, which is in qualitative agreement with our neutron scattering experiments. For small magnetic fields ($< 0.1\ T$) particles did not immediately orient in the direction of the external field. Particles did, however, form pairs with moments anti-parallel ($\uparrow\downarrow$) and occasionally formed pairs end to end ($\rightarrow\rightarrow$), but neither pair seemed stable. For magnetic fields larger than 0.1 T, magnetic moments were almost all

quickly oriented parallel with the external field. This prevented the vast majority of anti-parallel pairs for forming. In the range from 0.1 T to 0.5 T the average length of end to end chains which the particles formed was highly dependent on external field strength. The average chain length seemed to be proportional to the field magnitude. For particles in an external field greater than 0.5 T an average chain length of between 3 and 4 particles was typically observed. We call this the saturation correlation length of our cobalt particles.

At saturation it becomes less energetically favourable for new particles to add on to chains. Instead the particles or other chain segments are repelled from one another, which could be a microscopic cause of a viscosity increase.

The tunable viscosity that one sees in a magnetic fluid under the influence of a magnetic field may be explained by the orientation of these short particle chains.

3.4 Magnetic Field Visualizations

Our neutron scattering experiment (described in more detail in Paper I) took place in a high external magnetic field environment at Institut Laue-Langevin in Grenoble, France, on beamline IN12. The magnetic field was oriented in the plane of the neutron scattering. Our magnetic fluid sample sat in a vanadium sample can, between two thin concentric walls and thus a hollow centre. This allowed for a higher neutron flux than if it was a filled in can. The vanadium sample container would not provide extraneous Bragg peaks, as vanadium's coherent scattering cross section is more than 5x smaller than cobalt's - the major component of our magnetic particles [38]. The cylindrical sample allowed for us to make cylindrical symmetry simplifications and prevented anisotropic absorption and resolution effects.

It is also important that our sample container contained a material of very low relative magnetic permeability. Permeability is the ability of a material to support the formation of a magnetic field within itself, or the degree of magnetization a material obtains in response to an applied magnetic field. For simplicity, permeability is often quoted as relative permeability, scaled to the permeability in a vacuum ($\mu_o = 4\pi$ x 10^{-7} NA^{-2}. Concrete or air, for example, have a relative permeability of $\sim$1, the magnetic field is not distorted. With high permeability, the magnetic field would be

highly distorted, and might even be deflected away from the sample. We expect the particles in the experiment to align with the field lines. Since our small angle neutron scattering technique takes a statistical average over the whole sample, if chains were oriented in different directions through-out the sample it would be near impossible to parse the data. Figure 3.8 shows magnetic field lines for our cobalt magnetic fluid ($\mu_r = 1.01$) to another substance with higher permeability ($\mu_r \sim 50$). The higher permeability clearly results in an inhomogeneous magnetic field passing through the sample. Fortunately, this is not the case for our sample, the magnetic field lines are straight, we can confidently analyze the information from our neutron scattering experiment.

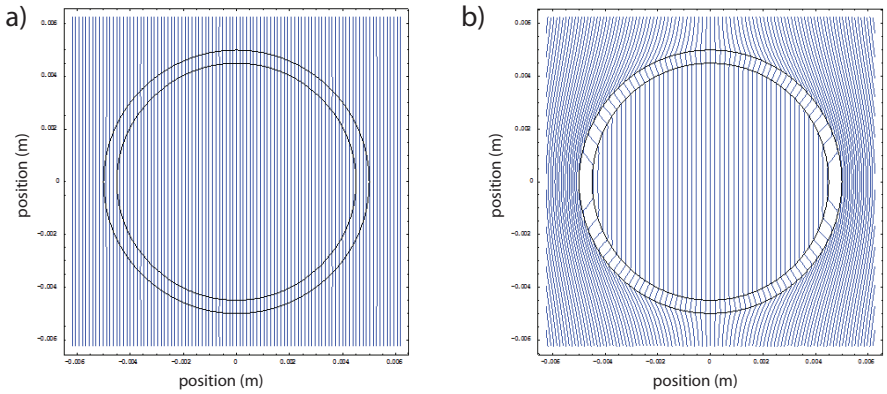

Figure 3.8: Magnetic permeability and field lines in sample.
a) Field lines from a 1 T magnet with sample permeability, μ_r =1.01. b) Field lines from a 1 T magnet with sample permeability, μ_r ∼50. In both cases the "sample" occupies the space between the two concentric circles. The low permeability case results in magnetic field lines which are parallel, not disturbed.

The vanadium walls, however, do lead to slight attenuation of the magnetic field inside of the sample container. This is estimated to be less than 5% of the original magnetic field, as the walls are quite thin (∼0.1 mm).

Preface to Paper I

In this experiment a cobalt particle magnetic fluid was placed into a 4 T horizontal field superconducting split-coil cryomagnet variable magnetic field, which ranged from 0 T to 2 T. This magnetic field was able to be oriented parallel with the scattering vector ($\overrightarrow{q}$), and at 30^o and 60^o. With this setup, we gained information about the microstructures in this fluid, and could observe at different angles, to get a 2D perspective. Instead of the long ($>$ 100 particle) chains found in magnetite based fluids, our cobalt based fluid had a saturation length of an average of $\sim$3.5 particles. We speculate the tunable viscosity that magnetic fluids are known for, in our case, was due to the interaction of these short particle groups rather than the bending of long chains.

The experiment was done by Jan Embs and Maikel Rheinstädter at the ILL in Grenoble. My role was the analysis of the neutron scattering data, determining the coherence length (size of scattering sites/particle chains) for different magnetic fields in the various orientation of the scattering vector, as well as development of Monte-Carlo simulations. Although the simulations weren't included directly in the paper, the visualization was helpful in thinking about how tunable viscosity could be explained crucial to interpret our data.

Since publication, two simulation papers from Dr. Faraudo's group in Barcelona have verified our finding of short chains in the cobalt based magnetic fluid. [39, 40]

View Online / Journal Homepage / Table of Contents for this issue
Dynamic Article Links

Soft Matter

Cite this: *Soft Matter*, 2011, **7**, 6678

www.rsc.org/softmatter

PAPER

Chain formation in a magnetic fluid under the influence of strong external magnetic fields studied by small angle neutron scattering

Matthew Barrett,[a] Andreas Deschner,[a] Jan P. Embs[b] and Maikel C. Rheinstädter*[ac]

Received 20th January 2011, Accepted 21st April 2011
DOI: 10.1039/c1sm05104k

We studied the aggregation of magnetic particles into chain-like structures in a cobalt-based magnetic fluid, exposed to external magnetic fields. The length of chain segments in very strong magnetic fields of up to 2 Tesla was measured *in situ* using small angle neutron scattering. Arrangement of the magnetic particles was studied with the scattering vector $\vec{Q}$ aligned parallel to the magnetic field lines, and at angles of 30° and 60° with respect to $\vec{B}$. Although chains several hundred particles in length were predicted, we observe a maximum correlation length of ~65 nm equivalent to 3–4 particles up to highest fields. We speculate that the interaction between chains, *i.e.*, the interplay between the entropy and energy of the system combined with the particular properties of the magnetic dipole–dipole interaction ultimately decide the length of the particle chains.

I. Introduction

Magnetic model systems are usually studied using ferromagnetic and antiferromagnetic Heisenberg, XY and Ising type interactions of different dimensionality.[1] In contrast to magnetic lattices, which are realized in magnetic crystals, magnetic fluids behave like highly permeable paramagnetic gases. Here, magnetic particles interact *via* long-range dipole–dipole interactions rather than short-range direct magnetic interactions. The magnetic fluid's macroscopic properties, such as a magnetic field dependent viscosity, are strongly determined by the magnetism of the embedded nanoparticles. These so-called "ferrofluids" are colloidal suspensions of nanodomain particles with a typical magnetic core diameter of $\sigma \sim 10$ nm in a liquid carrier,[2] see ref. 3 for a recent review. Magnetic relaxation is dominated by two distinct mechanisms. First, Néel relaxation, which describes the reorientation of the magnetic moment of a particle relative to its stationary magnetic core. Second, Brownian relaxation, in which the magnetic moment is tightly fixed to each particle, takes place *via* rotation of the whole particle relative to the fluid. For sufficiently large particles, the Brownian mechanism prevails as the Néel relaxation time becomes infinitely long.[4] The unique macroscopic properties of such a magnetic fluid are determined by the interactions between the giant magnetic moments of the particles (some ten thousand μ_B) and the presence of an external magnetic field, $\vec{B}$. In particular Small Angle Neutron Scattering (SANS) has proven to be a useful tool to investigate the microstructure of ferrofluids. Particle size distribution, interparticle interactions, phase diagrams and structure formation with and without an external magnetic field have been studied using this technique.[5–14]

In a magnetic fluid the magnetic cores are nanometre sized, single domain particles, usually made of magnetite, Fe_3O_4, or cobalt. To avoid agglomeration, these grains are coated by a polymeric layer, as is depicted in Fig. 1a. Ferrofluids are

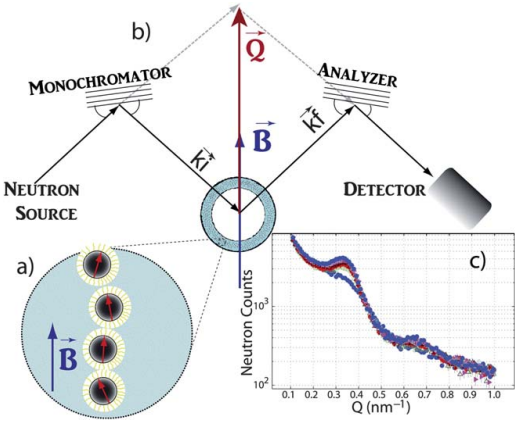

Fig. 1 (Colour online). a) Chain formation of magnetic particles. Cobalt cores (represented in black) each possess a thin polymer coating (represented in yellow). The magnetic moment is represented by an arrow. b) Schematic diagram of the experimental setup, with the magnetic field aligned parallel to the scattering vector, $\vec{Q}$. c) Small angle neutron scattering data for different magnetic field strengths.

[a]*Department of Physics and Astronomy, McMaster University, Hamilton, ON, Canada. E-mail: rheinstadter@mcmaster.ca*
[b]*Laboratory for Neutron Scattering, ETH Zürich & Paul Scherrer Institut, 5232 Villigen, PSI, Switzerland*
[c]*Canadian Neutron Beam Centre, National Research Council Canada, Chalk River, ON, Canada*

macroscopically superparamagnetic ($\mu \approx 1$), with a viscosity which can be tuned continuously using an applied magnetic field by the magnetoviscous effect.[3,15] In magnetite based ferrofluids, magnetic moments of about $10^4\ \mu_B$ were reported ($\mu_B = e\hbar/(2m_e) = 9.27 \times 10^{-24}$ J T^{-1}). They are well described by inclusion of magnetic terms in the Navier–Stokes equation[2] and their behavior is influenced by both hydrodynamics as well as magnetism (sometimes called magnetohydrodynamics). Alternatively, cobalt based magnetic fluids have larger magnetic moments of up to $8 \times 10^4\ \mu_B$, and their behavior is primarily determined by magnetic interactions, *i.e.* the interaction of a magnetic dipole with the external magnetic field and neighbouring magnetic particles. The potential energy, u, of a particle i can be written as:

$$u_i = -\vec{m}_i \cdot \vec{B} + \sum_j -\vec{m}_i \cdot \frac{\mu_o}{4\pi r_{ij}^3}\left\{3(\vec{m}_j \cdot \hat{r}_{ij})\hat{r}_{ij} - \vec{m}_j\right\}, \qquad (1)$$

with $m_{i,j}$ the magnetic moments of the particles, $\vec{B}$ the external magnetic field and $\mu_0 = 4\pi \times 10^{-7}$ N A^{-2}. The influence of particle interaction on the physical properties of the ferrofluid mainly depends on two parameters, the volume fraction of the particles, ϕ, and the dipolar coupling constant, λ. ϕ is given by $\phi = \frac{N}{V}\frac{\pi\sigma^3}{6}$, with σ the particle diameter. The dipolar coupling constant relates the dipole–dipole interaction energy of two contacting particles to the thermal energy k_BT, with k_B the Boltzmann constant (1.38×10^{-23} J K^{-1}) and T the absolute temperature. λ is defined as:

$$\lambda = \frac{m^2}{4\pi\mu_0 k_B T \sigma^3}. \qquad (2)$$

While λ in magnetite based ferrofluids is found to be $\lambda \sim 0.3$ at room temperature, the dipolar coupling in cobalt based ferrofluids is about two orders of magnitude stronger with λ values of up to $\lambda = 20$. For the magnetic fluid used in this study, we determined $\lambda = 18$. Because of the dominant magnetic dipole–dipole interaction cobalt based magnetic fluids are prime model systems to study fundamental properties in magnetic fluids, such as structure formation.

To explain certain magnetic properties, such as the large susceptibility, it was speculated that magnetic particles aggregate into larger structures, which show cooperative magnetic behaviour. Theoretical investigations started with de Gennes and Pincus,[16] later followed by Jordan.[17] In these works the ferrofluid is modeled as a monodisperse fluid of hard spheres of diameter σ, carrying central point dipoles of magnitude m. One-dimensional chains oriented along the field lines of an applied magnetic field, were predicted.[18,19] The length of these chains was speculated to be a monotonically increasing function of an external magnetic field. Long chains were also observed in Monte Carlo simulations of monodisperse ferrofluids.[20] Aggregation and structure formation have been studied and chain formation was observed with transmission electron microscopes (TEM) in freeze dried 2d films of magnetite based ferrofluids[21,22] and in both, polarized and non-polarized small angle neutron scattering with magnetic fields in the order of 0.01–0.2 T.[23–25] Small and moderate magnetic fields have been used to measure susceptibility and magnetization in standard laboratory experiments. For these field strengths the dipole–field interaction is comparable to thermal energies. In large external fields, however, the dipole–external field interaction should become the dominant term in eqn (1) and lead to the formation of long one-dimensional chains parallel to the magnetic field lines.[16,18,19] However, from *in situ* neutron diffraction experiments at room temperature, in the fluid state of the magnetic fluid, we find that the chain length saturates in large external magnetic fields of up to 2 T for chain segments of about 4 particles. This behavior can be speculated to be the result of the interaction between chain segments and stems from the competition between magnetic energy, the entropy of the nanoparticles and the peculiar properties of the dipole–dipole interaction of the giant magnetic moments, as will be discussed below.

II. Experiment

To study the aggregation of magnetic particles, we investigated a magnetic fluid composed of cobalt particles. The fluid was provided by Kardiotechnik, Berlin. The Co particles were coated by lauryol-sarcosine and dispersed in a diffusion pump oil (Edwards L9). A thickener agent consisting of either polyisobutylene-succinimide or Lubrizol 7761A was added to enhance the viscosity of the sample. Ferrofluids can be characterized by a number of techniques to determine the size of the magnetic core, thickness of the nonmagnetic layer as well as particle size distribution.[26–28] The investigated ferrofluid has been characterized using magneto-granulometry (MG), photon correlation spectroscopy (PCS) and torsional-pendulum (TP) measurements.[29–32] Values for the core-size D_o, polydispersity parameter σ, saturation magnetization M_s, the volume averaged core-diameter D_v and volume weighted core-diameter D_{vol} are listed in Table 1.

From measurements of the saturation magnetization, the volume fraction of cobalt in the undiluted samples was determined to be $\varphi = 1.5\%$. From this result, we determined the volume fraction of the whole particle (including both the cobalt core and polymer coating) to be $\varphi = 8.75\%$. The dynamic fluid viscosity was determined as $\eta = 0.5$ Pa s. From the values in Table 1 the thickness of the surfactant coating can be estimated to (2.5 ± 1.0) nm. This value takes into account the fact that different measurement techniques have access to different diameters; the TP as well as the PCS method are sensitive to the hydrodynamic diameter of the particles, whereas with MG the magnetic diameter is probed. In addition to this magnetic diameter, the particles show up with a so called magnetic dead layer close to the particle's surface.

Table 1 Values for the core-size D_o, polydispersity parameter σ, saturation magnetization M_s, the volume averaged core-diameter D_v and volume weighted core-diameter D_{vol}, as taken from ref. 31

Cobalt Ferrofluid	MG	PCS	TP
D_o (nm)	11.0	19.0	—
σ (nm)	1.27	1.2	—
M_s (A m^{-1})	6512	—	—
D_v (nm)	12.0	20	—
D_{vol} (nm)	13.5	22	16.2

Furthermore one has to keep in mind that the methods mentioned above are sensitive to different moments of the underlying particle size distribution; this point and its consequences are discussed in great detail in ref. 30–32.

The neutron diffraction experiments were conducted on the cold triple-axis spectrometer IN12 at the Institut Laue-Langevin in Grenoble, France. To avoid Bragg peaks from the sample container a double walled cylindrical vanadium sample can with an outside diameter of 10 mm, an inside diameter of 9 mm and a length of 60 mm was used. About 1.5 millilitres of ferrofluid was filled in the 1 mm space between inner and outer cylinder, as sketched in Fig. 1b. Note that the carrier fluid is a strong incoherent scatterer with correspondingly strong absorption. Geometry and volume of the can were designed to optimize scattering and minimize absorption of the ferrofluid. We calculated the magnetic field distribution for this set-up. As the ferrofluid used is superparamagnetic $\mu \approx 1$ the field inside the sample container does not distort with respect to the external field. We note that the vanadium walls of the cylinder lead to a slight attenuation of the magnetic field inside our sample container. We estimate this shielding effect to be less than 5%, as the thickness of the wall was less than 1/10th of a millimetre. This can was installed into a 4 T horizontal field cryomagnet. A neutron wavelength of 0.418 nm was used and the collimation was set to 35′-monochromator-10′-sample-10′-analyzer-30′-detector, resulting in an instrumental resolution of $\Delta Q = 0.06$ nm^{-1}. All experiments were conducted at room temperature, at $T = 293$ K. Small angle neutron scattering (SANS) was then measured in the presence of magnetic fields of up to 2 T. Due to the torque created by the large external magnetic field on our fluid, it was not possible to measure at higher fields. Preliminary tests have shown that the carrier fluid and polymer shells result in a high incoherent background, which makes it difficult to detect the small coherent correlation peaks. On a triple-axis spectrometer the analyzer cuts out only the elastically scattered neutrons. The quasi-elastic contributions of the protons to the background are omitted, reducing the background and improving the signal to noise ratio drastically. The combination of a low background, good Q-resolution, the use of an analyzer, and the option for a powerful horizontal magnet made IN12 highly suited for these measurements.

The static structure factor $S(Q)$ was determined in external magnetic fields of 0, 0.1, 0.25, 0.5, 1.0, 1.5, and 2 Tesla. We note, however, that at $B = 0$ T there was a remnant field due to hysteresis effects of the setup, which we estimate to be ~0.01 T. The scattering vector $\vec{Q}$ was placed parallel to the magnetic field lines, and at angles of 30° and 60°. Small angle scattering data are shown in Fig. 1c. To display only contributions from the coherent inter particle scattering, a q^{-4} background was subtracted from the data. The results are shown in Fig. 2 for $B = 0.1$ T and $B = 2$ T. The scans exhibit a pronounced correlation (Bragg) peak at ~ 0.34 nm^{-1}, corresponding to a particle–particle distance of ~18.5 nm. Assuming that the particles are in contact with each other, the particle size σ should be equivalent to the inter particle distance. This value is in good agreement with size determination by other techniques[29–32] and suggests that the polymer shells of the particles are in direct contact. A weak second order peak is visible in the data at higher magnetic fields,

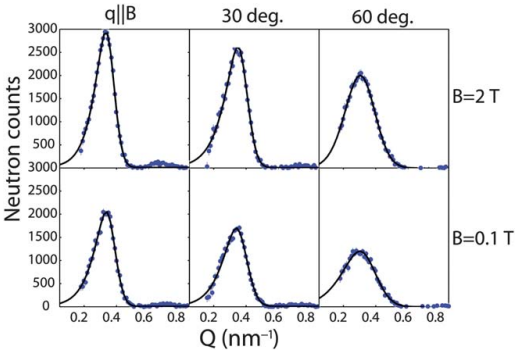

Fig. 2 (Colour online). Data at B-field strengths of 2 T (top row) and 0.1 T (bottom row) and at angles formed by the $\vec{Q}$-vector and $\vec{B}$-field, parallel, 30°, 60° (left to right). The solid lines are fits using an asymmetric Gaussian peak profile, as described in the text.

pointing to increased order, possibly due to the suppression of thermal fluctuations in the particles. The asymmetry of the peaks reflects the particle size distribution, which is well described by a log-normal distribution.[29–32] To fit the diffraction data we modified an Exponential-Gaussian hybrid function.[33] This asymmetric peak shape takes into account the asymmetry of the particle size distribution, convoluted with the Gaussian resolution of the spectrometer.

$$f_{\mathrm{egh}}(Q) = H(Q_0 - Q)\cdot A\exp\left(\frac{-(Q-Q_0)^2}{2\sigma_g^2 + \tau(Q-Q_0)}\right) + H(Q-Q_0)\cdot A\exp\left(\frac{-(Q-Q_0)^2}{2\sigma_g^2}\right) \quad (3)$$

with σ_g the Gaussian width, Q_0 the peak position, A as the amplitude, τ the asymmetry parameter and $H(x)$ the Heaviside step function.

The particle–particle distance, number and length of the corresponding chain segments could then be determined from position, amplitude and width of the correlation peak. Amplitude, peak width and position of the Bragg peaks for varying angles between $\vec{Q}$ and $\vec{B}$, as determined from the fits of the elastically scattered neutron data in Fig. 2, are depicted in Fig. 3. Some trends are visible: the intensity of the peaks increases with increasing field, and the peak widths are narrow in the direction of the magnetic field lines and become wider with increasing angle. As the peak intensity is proportional to the number of chain segments, this points to an increasing number of aggregates. The data in Fig. 3 strongly depend on the angle between scattering vector and applied magnetic field. The shape of the conglomerate is strongly anisotropic: it is elongated along the magnetic field lines as the peak width drastically increases with increasing angle. The width decreases as a function of the external field until about 0.25 T for all angles and stays constant for stronger fields. The position of the correlation peak shifts to larger Q values with increasing magnetic field, which points to a slightly decreasing inter particle distance at stronger fields, possibly due to the suppression of thermal fluctuations of the particles.

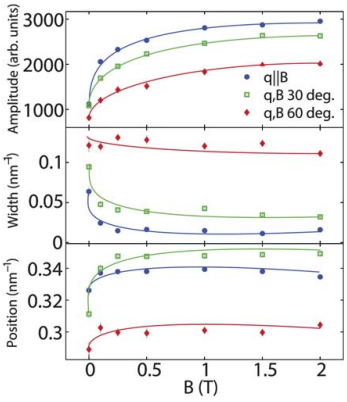

Fig. 3 (Colour online). Amplitude, peak width and position of the Bragg peak for angles of 0, 30 and 60° between $\vec{Q}$ and $\vec{B}$, as determined from the fits of the elastically scattered neutron data in Fig. 2. (Solid lines are guides to the eye.)

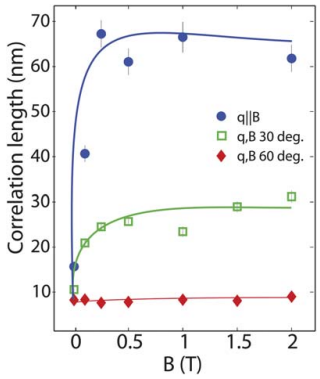

Fig. 4 (Colour online). Correlation length, ξ, at angles of 0, 30, and 60° between $\vec{Q}$ and $\vec{B}$. The correlation length for all angles shows a steep increase at small fields and saturates at high fields. (Solid lines are guides to the eye.)

Fig. 4 depicts the correlation length, calculated as $\xi = 1/\text{width}$, as a function of magnetic field. The correlation length parallel to the field lines, $\xi_{\|}$, shows a steep increase up to fields of about 0.25 T. The length of the chain segments then saturates for high fields at values of about 65 nm, which corresponds to chains between 3 and 4 particles (3.5 particles). The correlation length measured at 30° also increases at small fields to saturate at values of $\xi_{30} \sim 30$ nm. ξ_{60} appears to be constant at values of $\xi_{60} \sim 9$ nm, half a particle diameter.

III. Discussion

From the existence of pronounced Bragg peaks in the diffraction data in Fig. 2 we can conclude that the particles form aggregates. By varying the angle between the applied external magnetic field and momentum transfer vector we find evidence that these aggregates are strongly anisotropic and most likely resemble chain-like structures, oriented along the applied magnetic field lines. The value for σ is in good agreement with theoretical predictions and experimental observations reported by other techniques.[21–25] The amplitude, width and position of the observed Bragg peaks in Fig. 3, as a function of the external field, have a high rate of change for fields of about 0.25 T and saturate at higher magnetic fields. The area of the correlation peaks in Fig. 3a can be considered to be proportional to the number of chain segments in the system. With increasing magnetic field strength, we find that more chain segments form.

The correlation length parallel to the magnetic field lines, $\xi_{\|}$, as shown in Fig. 4, shows values of slightly less than ~18 nm at the smallest field, less than the distance between two particles. Note that our scattering experiment is not sensitive to the existence of monomers as single particles do not contribute to Bragg scattering. At low fields the fluid, therefore, most likely consists of a mixture of monomers and pairs of particles, so-called dimers. The axes of the dimers, however, are not well aligned along the external field as a result of the competition between dipole–dipole and dipole–field interaction. The projection along the field lines is then smaller than the particle distance. A possible structure of the magnetic fluid at small fields is sketched in Fig. 5a. $\xi_{\|}$ then saturates with higher fields, at values of ~65 nm,

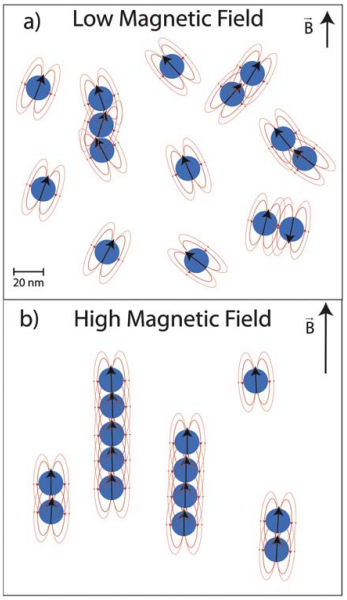

Fig. 5 (Colour online). Particle distribution, as suggested by the experimental data, at low and high field. In the small field case (a), the dipole–dipole interaction is comparable in magnitude to the dipole–field interaction, resulting in short, kinked chains. In the large field case (b), all magnetic moments are aligned parallel to the magnetic field lines resulting in well aligned chains. Depending on their relative position, chain segments can repel one another, making it difficult to form longer chains.

corresponding to an average chain length of 3.5 particles, as sketched in Fig. 5b. The dipole–field interaction term in eqn (1) is now dominant and all magnetic moments are perfectly aligned to the external field. As a result, the chains forming are well oriented along the field lines. Thermal fluctuations are suppressed as evidenced by the slightly decreasing inter-particle distance and the occurrence of higher order Bragg reflections as seen in Fig. 2. The chain length, however, seems to saturate at short chain segments. This experimental finding is in contrast to theoretical predictions of chain lengths increasing monotonically, with external magnetic fields.[16–20] While monodisperse systems were investigated in these studies, the effect of polydisperisity has also been studied.[34–36] It was found that a distribution of particle sizes may reduce the chain length. As smaller particles can be expected to have weaker interaction, the occurrence of large and small particles in a chain was speculated to induce stronger and weaker particle–particle bonds. Due to the variation in particle distribution, long chains may more easily break where two small particles are in contact with one another.

The lengths of the chain segments observed in this experiment are also shorter than the chain lengths reported from cryo-TEM experiments in vitrified 2d films of synthetic magnetite based ferrofluids. The occurrence of relatively short chain-segments in the cobalt based ferrofluid may be the result of strong external fields in combination with the large magnetic moments of the particles and the peculiar geometry of the dipole–dipole interaction. In strong external fields, all the spins should be aligned parallel to the external field. Pairs or short segments form first in low magnetic fields. To combine short chains into longer chains, segments must approach one another with appropriate directional orientation. If two chains approach head-to-tail there is an attractive interaction, which might lead to the formation of longer chains. Alternatively, segments which approach from the side experience a repulsive force because of the shape of the magnetic field lines; as pictured in Fig. 5. The magnetic field of a 1d chain is proportional to the number of particles in the chain. The magnetic dipole field lines, however, condense more closely around the chain as the chain length increases (compare Fig. 5 a and b). This can lead to the peculiar situation that long chain segments do not "feel" each other over large distances. They may, however, experience a strong repulsive interaction if they approach each other laterally. As has been speculated previously,[37] the strong inter-chain interaction therefore most likely prevents the formation of long chains. We note that our observation of relatively short chain segments agrees qualitatively with molecular dynamics simulations[38] and mean-field theories.[39] The formation of short chain segments was recently also reported from Langevin dynamics computer simulations,[40] in very good agreement to the values reported here.

The particular properties of magnetic fluids in a magnetic field, such as the tunable viscosity can at least partially be attributed to the repulsive interactions between relatively short chain segments. The situation is probably different in magnetite based ferrofluids with much weaker dipole–dipole interactions. Here longer chains may form because the repulsive force can possibly be overcome by thermal fluctuations more easily. Our experimental setup will be used in future experiments to study chain formation in magnetite based fluids. Longer chains are expected at strong magnetic fields as the inter-chain interaction is smaller when compared to the cobalt based fluid studied here.

IV. Conclusion

In summary, we have studied chain formation of magnetic particles in a cobalt based magnetic fluid in strong external magnetic fields of up to 2 T. In contrast to previous experiments and theoretical predictions, we observe relatively short chain segments of 3–4 particles. We speculate that the strong inter-chain interaction and the geometry of the magnetic dipole–dipole interaction prevent the formation of longer chains.

Acknowledgements

This research was partially funded by the Natural Sciences and Engineering Research Council of Canada (NSERC) and the National Research Council of Canada (NRC). We thank the Jülich Centre for Neutron Science (JCNS) and the Institut Laue Langevin for the allocation of beam time. We thank N. Buske (Kardiotechnik, Berlin) for providing the Cobalt-based ferrofluid.

References

1 L. de Jongh and A. Miedema, *Adv. Phys.*, 2001, **50**, 947.
2 R. Rosensweig, *Ferrohydrodynamics* (Cambridge University Press, England, 1985).
3 S. Odenbach, ed., *Colloidal Magnetic Fluids: Basics, Development and Application of Ferrofluids* (Springer, Heidelberg, 2009).
4 M. Shliomis, *Sov. Phys. Usp.*, 1974, **17**, 153.
5 D. Cebula, S. Charles and J. Popplewell, *J. Magn. Magn. Mater.*, 1983, **39**, 67.
6 R. Rosman, J. Janssen and M. Rekveldt, *J. Appl. Phys.*, 1990, **67**, 3072.
7 F. Boue, V. Cabuil, J. Bacri and R. Perzynski, *J. Magn. Magn. Mater.*, 1993, **122**, 78.
8 R. Mehta, P. Goyal, B. Dasannacharya, R. Upadhyay, V. Aswal and G. Sutariya, *J. Magn. Magn. Mater.*, 1995, **149**, 47.
9 E. Dubois, R. Perzynski, F. Boue and V. Cabuil, *Langmuir*, 2000, **16**, 5617.
10 G. Meriguet, E. Dubois, A. Bourdon, G. Demouchy, V. Dupuis and R. Perzynski, *J. Magn. Magn. Mater.*, 2005, **289**, 39.
11 C. Neto, M. Bonini and P. Baglioni, *Colloids Surf., A*, 2005, **269**, 96.
12 L. Pop and S. Odenbach, *J. Phys.: Condens. Matter*, 2006, **18**, S2785.
13 M. Klokkenburg, B. Erne, A. Wiedenmann, A. Petukhov and A. Philipse, *Phys. Rev. E: Stat., Nonlinear, Soft Matter Phys.*, 2007, **75**, 051408.
14 D. Bica, L. Vekas, M. Avdeev, O. Marinica, V. Socoliuc, M. Balasoiu and V. Garamus, *J. Magn. Magn. Mater.*, 2007, **311**, 17.
15 S. Odenbach, *J. Phys.: Condens. Matter*, 2004, **16**, R1135.
16 P. G. de Gennes and P. A. Pincus, *Eur. Phys. J. B*, 1970, **11**, 189.
17 P. Jordan, *Mol. Phys.*, 1973, **25**, 961.
18 K. Morozov and A. Lebedev, *J. Magn. Magn. Mater.*, 1990, **85**, 51.
19 V. S. Mendelev and A. O. Ivanov, *Phys. Rev. E: Stat., Nonlinear, Soft Matter Phys.*, 2004, **70**, 051502.
20 P. J. Camp and G. N. Patey, *Phys. Rev. E: Stat. Phys., Plasmas, Fluids, Relat. Interdiscip. Top.*, 2000, **62**, 5403.
21 M. Klokkenburg, R. P. A. Dullens, W. K. Kegel, B. H. Erné and A. P. Philipse, *Phys. Rev. Lett.*, 2006, **96**, 037203.
22 M. Klokkenburg, B. H. Erné, J. D. Meeldijk, A. W. A. V. Petukhov, R. P. A. Dullens and A. P. Philipse, *Phys. Rev. Lett.*, 2006, **97**, 185702.
23 A. Wiedenmann, U. Keiderling, M. Meissner, D. Wallacher, R. Gähler, R. May, S. Prévost, M. Klokkenburg, B. Erné and J. Kohlbrecher, *Phys. Rev. B: Condens. Matter Mater. Phys.*, 2008, **77**, 184417.
24 A. Wiedenmann and A. Heinemann, *J. Magn. Magn. Mater.*, 2005, **289**, 58.

25 A. Wiedenmann, A. Hoell and M. Kammel, *J. Magn. Magn. Mater.*, 2002, **252**, 83.
26 A. Ivanov and S. Kantorovich, *Phys. Rev. E*, 2004, **70**, 021401.
27 C. Holm, A. Ivanov, S. Kantorovich, E. Pyanzina and E. Reznikov, *J. Phys.: Condens. Matter*, 2006, **18**, S2737.
28 Z. Wang and C. Holm, *Phys. Rev. E*, 2003, **68**, 041401.
29 J. Embs, S. May, C. Wagner, A. Kityk, A. Leschhorn and M. Lücke, *Phys. Rev. E: Stat., Nonlinear, Soft Matter Phys.*, 2006, **73**, 036302.
30 J. P. Embs, B. Huke, A. Leschhorn and M. Lücke, *Z. Phys. Chem.*, 2008, **222**, 527586.
31 J. Embs, H. W. Müller, C. E. K. III, F. Meyer, H. Natter, B. Müller, S. Wiegand, M. Lücke, K. Knorr and R. Hempelmann, *Z. Phys. Chem.*, 2006, **220**, 153.
32 J. Embs, H. Müller, M. Lücke and K. Knorr, *Magnetohydrodynamics*, 2000, **36**, 320.
33 K. Lan, *J. Chromatogr., A*, 2001, **915**, 1.
34 E. Pyanzina, S. Kantorovich, J. Cerda, A. Ivanov and C. Holm, *Phys. Rev. E*, 2009, **107**, 571.
35 J. Cerda, E. Elfimova, V. Ballenegger, E. Krutikova, A. Ivanov and C. Holm, *Phys. Rev. E: Stat., Nonlinear, Soft Matter Phys.*, 2010, **81**, 011501.
36 J. Huang, Z. Wang and C. Holm, *Phys. Rev. E*, 2005, **71**, 061203.
37 L. Y. Iskakova and A. Y. Zubarev, *Phys. Rev. E: Stat. Phys., Plasmas, Fluids, Relat. Interdiscip. Top.*, 2002, **66**, 041405.
38 Z. Wang, C. Holm and H. W. Müller, *Phys. Rev. E: Stat. Phys., Plasmas, Fluids, Relat. Interdiscip. Top.*, 2002, **66**, 021405.
39 A. O. Ivanov, Z. Wang and C. Holm, *Phys. Rev. E: Stat., Nonlinear, Soft Matter Phys.*, 2004, **69**, 031206.
40 J. S. Andreu, J. Camachob and J. Faraudo, *Soft Matter*, 2011, **7**, 2336.

Chapter 4

X-ray diffraction of lipid membrane structure

Papers II, III, IV

II. Barrett, M., Zheng, S., Roshankar, G., Alsop, R. J., Belanger, R. K. R., Huynh, C., Kučerka, N., and Rheinstädter, M. C., (2012) *"Interaction of Aspirin (acetylsalicylic acid) with lipid membranes."* PLoS ONE 7(4): e34357.

III. Barrett, M., Zheng, S., Jago, N., Moore, M., Alsop, R. J., Shi, A. C., and Rheinstädter, M. C., *"The interaction of cholesterol with lipid membranes"*, (2012) - in preparation.

IV. Alsop, R. J., **Barrett, M.**, Zheng, S., and Rheinstädter, M. C., *"A molecular approach to the Low-Dose-Aspirin-Therapy"*, (2012) - in preparation.

4.1 X-ray scattering of ASA and Cholesterol in DMPC Bilayers

The samples discussed in this chapter were all prepared using lipids and certain other molecules, including ASA (acetylsalicylic acid), and cholesterol. The molecular nature of lipids, as well as the structures that they form are described in detail in Section 2.2. Their molecular structures are shown in Figure 4.1 and the properties are shown in table 4.1.

Properties of common experimental lipids			
Abbrev.	Formula	Molecular Weight (g/mol)	Melting Point (K)
ASA	$C_9H_8O_4$	180.157	408
Cholesterol	$C_{27}H_{46}O$	386.65	423

Table 4.1: Formula, molecular weight and melting points of ASA and Cholesterol molecules. These two molecules were of interest in Papers II, III and IV. Data from [41, 42]

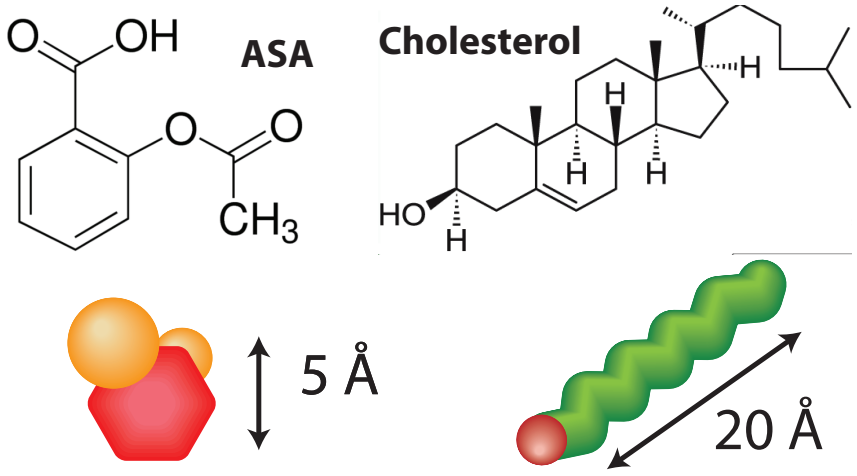

Figure 4.1: Structure of ASA and Cholesterol molecules.
Molecular structure of ASA and Cholesterol (Top) and cartoon structure of each molecule (bottom). [41, 42]

X-ray diffraction is a very powerful technique for understanding the structure of a highly ordered system. The system we observed were lipid bilayer structures, which

possess the necessary order to be a useful diffraction sample, and provides biologically relevant data. In the following experiments we observed the changes which occur in a saturated lipid bilayer (DMPC) with the addition of ASA, Cholesterol and both of these molecules.

4.2 Preparation of lamellar lipid bilayer samples

In particular, these samples were all created using a self-assembly process, resulting in highly-ordered multi-lamellar single solid supported bilayers discussed in section 2.2. Samples of this orientation are ideal for observation through x-ray scattering techniques. Because solid supported bilayers retain the thermodynamic and structural characteristics of a free bilayer, they are an ideal model system.[43, 44] The creation of solid supported bilayers is quite involved and took over a year of trials to perfect the sample creation protocol. The steps used to create these samples are listed below:

- **APTES (3-Aminopropyltriethoxysilane) treatment to ensure a medium-hydrophobic silicon surface**. Precut 1 cm x 1 cm (or 2 cm x 2 cm) silicon (100) wafers was the substrate used in supporting the bilayers we were producing. When the lipid-Chloroform/2,2,2-trifluoroethanol (TFE) solution was originally deposited on the silicon wafers not treated with APTES it was found than in less than 30 minutes dewetting occurred, due to the hydrophilic surface. Figure 4.2 shows the molecular makeup of the sample surface before and after being treated with APTES. To increase the hydrophobicity of the surface the APTES molecules bond to the surface with one to two siloxane bonds, and after being cured (3 h annealing process in vacuum) form a smooth ∼6 nm smooth surface on the wafers.[45] This process is well documented by Wang and Jin. [46]

- **Deposition of lipid solution.** Solutions of lipid (and other components) and solvent were prepared at a ratio of 15 mg/mL powdered components to chloroform/TFE (1:1 by volume) solution. The lipids have empirically been shown to dissolve such a solvent by Li *et. al.* [48]. The solution was vortexed prior to use to ensure even mixing of the solution and thus even distribution of

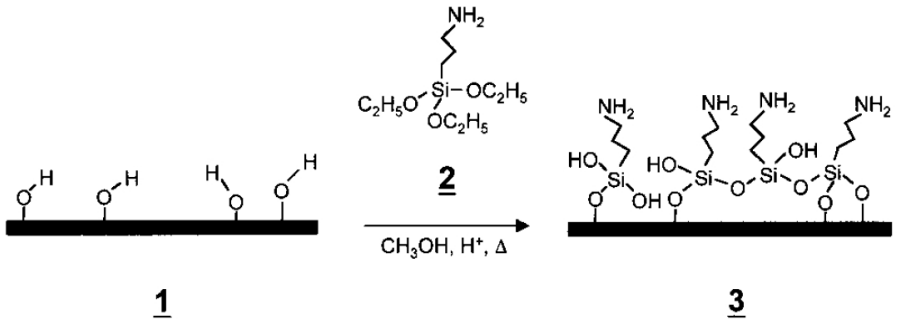

Figure 4.2: Si wafer APTES treatment
(1) Untreated silicon wafer contains polar (and thus hydrophilic) hydroxyl groups. (2) Treatment with alcohol, acid, heat and APTES molecules. (3) Thin APTES layer forms on the surface of the Si wafer ∼6 nm. From [47]

the bilayer components across the sample. Both the solution and wafers were placed on an undulating oscillator (Belly dancer) in its horizontal orientation, heated to 313 K prior to deposition. The sample stage moves with tilt 1, speed 15 to encourage the solution to explore the whole area of the silicon wafer. 50 μL of solution (containing 0.75 mg of Lipid) was deposited by high precision micropipettes onto each 1 cm^2 sample and 200 μL onto the 2 cm^2 samples, to conserve the sample thickness. (See Figure 4.3) Based on the area of the silicon wafer, the size of a typical bilayer and the amount of material added on, we expect ∼5000 bilayers to form on our surface.

- **Solvent evaporation in vacuum**. After a 30 minute drying time the wafers were carefully transferred to a vacuum oven preheated to 313 K. 24 h passed and the wafers were then removed. During this vacuum time, the chloroform/TFE solvent was allowed to evaporate and leave the sample. This process allowed the lipids to orient and form a rough lamellar bilayer structure.

- **Hydration of samples**. The samples were next placed into a sealed container alongside a beaker of K_2SO_4 saturated salt solution. This solution would create a relative humidity of somewhere between 97 % and 98 %. [49] This container was then moved into an incubator where the temperature was increased from 293 K to 303 K extremely slowly, ∼2 K/h. If hydration was pushed too fast,

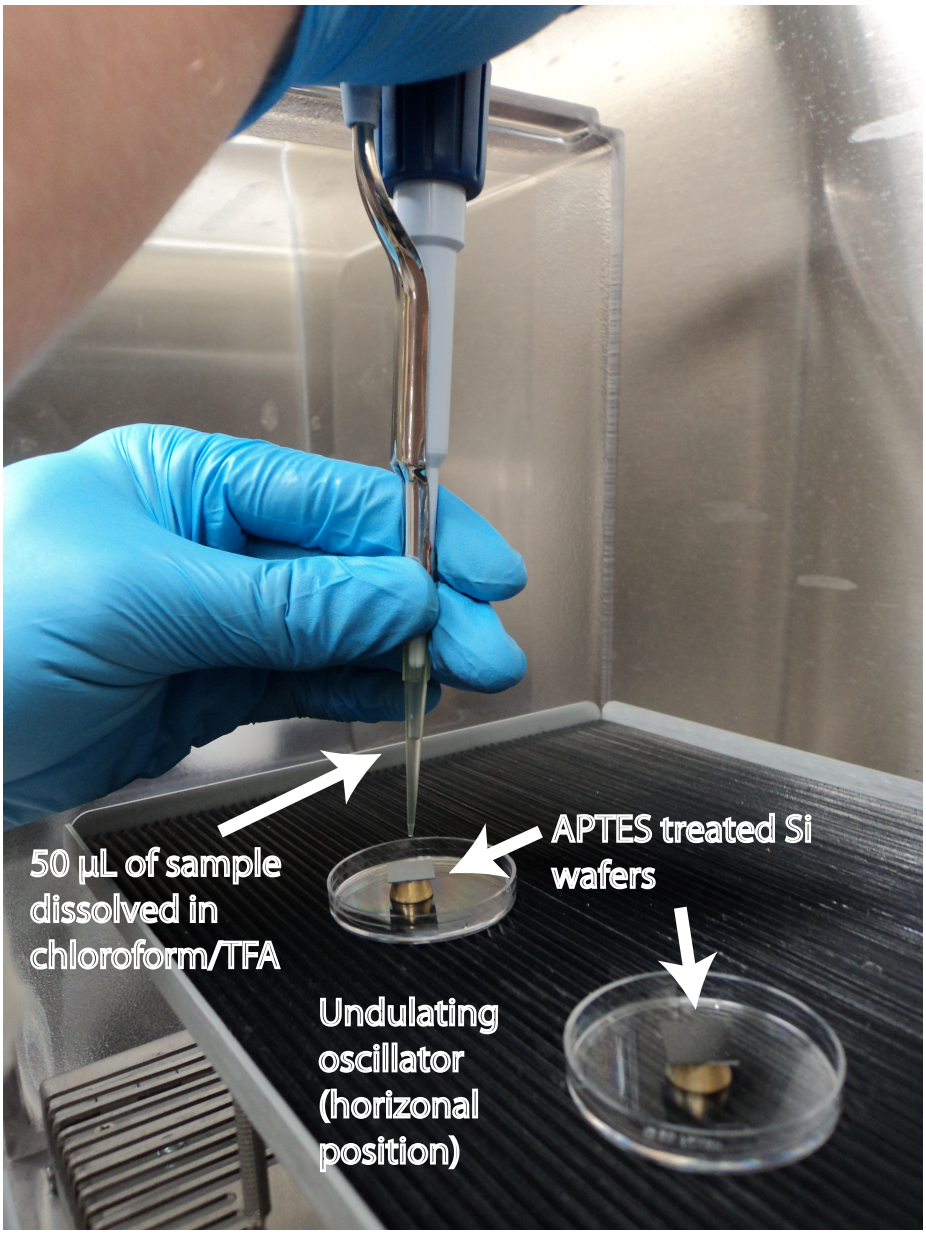

Figure 4.3: Sample deposition onto APTES treated silicon wafers
The sample solution and wafers were heated in the undulating oscillator at ∼313 K before deposition. Immediately after deposition, the sample stage was set in motion to distribute solution evenly across the surface of the substrate.

small spheres of presumably lipid were observed to form on the surface. This hydration fills the spaces between the head groups of layers in the bilayer, and

allows for more realistic bilayer behaviour.

- **Storage and pre-scan heating**. Series of samples with various percentage of lipid and ASA or cholesterol were created and used in each experimental study. The sample series for the ASA structural experiment was made with DMPC and ASA forming bilayers and is shown in detail in Paper II, Table I. The sample series for the Cholesterol structural experiment was also DMPC membranes, but with Cholesterol instead, and is listed in Paper III, Table I. For the Low-Dose Aspirin Therapy paper (Paper IV) samples were constructed with ASA and Cholesterol together in DMPC bilayers.The samples are stored in a fridge at 277 K. Prior to an x-ray scan, the samples are heated for 1 h in the incubator at 323 K. This erases any previous thermal history and ensures reproducible scans.

4.2.1 Scattering with BLADE

In section 2.1 scattering theory was discussed. The following x-ray scattering experiments were all done using the Biological Large Angle Diffraction Experiment (BLADE) in the Laboratory for Membrane and Protein Dynamics at McMaster University. BLADE is a Rigaku SmartLab Intelligent X-ray Diffraction System, capable of powder diffraction, thin film diffraction, SAXS and in-plane scattering. BLADE operates a 9 kW rotating Copper anode, 45 kV maximum voltage and 200 mA maximum current, this can produce x-ray intensity of up to 10^{10} photons mm^{-2} s^{-1}. The x-ray wavelength produced by this setup is λ=1.5418 Å. It has a very large 2 θ_χ (horizontal) and 2 θ (vertical) range. The sample can be viewed over a 95^o vertical range, and a 180^o horizontal range (with rotation of both the arms and the sample platform).[9] A unique feature of BLADE's setup is the sample can remain horizontal and stationary for the duration of a scan. The source and detector are on movable arms which are able to map out the surface of the Ewald sphere - allowing simple calculation of the incident ($\overrightarrow{k_i}$) and scattered ($\overrightarrow{k_f}$) wavevectors to be determined very simply. See Figure 4.4.

$$\overrightarrow{q} = \overrightarrow{k_f} - \overrightarrow{k_i} \tag{4.1}$$

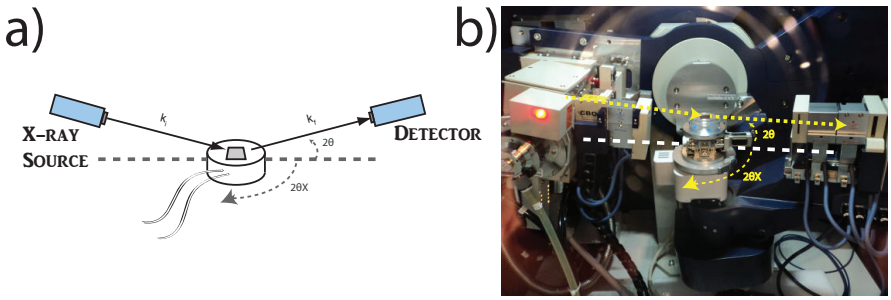

Figure 4.4: Schematic and photo of BLADE with scattering vectors.
a) Schematic diagram of BLADE scattering setup. b) Photograph of BLADE for comparison to schematic. Both a) and b) show the incident wavevector ($\overrightarrow{k_i}$) coming from the left and interacting with the sample (grey square), then the scattered wavevector ($\overrightarrow{k_f}$) going off to the right. To change the direction of the wavevectors the sample remains stationary, the source and detector move on the arms, essentially mapping out the Ewald sphere.

The Ewald sphere is a geometric construct where the radius of the sphere is $1/\lambda$. The origin is chosen on the surface of the sphere and the incident direction is along a radius. [50] Maxima are seen when the Bragg diffraction equation 4.1 is satisfied. Where $\overrightarrow{q}$ is inversely proportional to the length between two lattice planes. If there is a position on this radius where these conditions are satisfied, the detector will observe an increase in intensity. Since our setup moves along the Ewald sphere, it is not necessary to take a projection onto a planar detector.

Another useful design aspect of BLADE's setup is the horizontal sample. Keeping the sample horizontal mitigates the risk of the sample dripping and losing material if placed vertically, especially for the investigation of fluid films, and experiments involving high humidity. A photo overview of BLADE's components is found in Figure 4.5.

To use BLADE to obtain different scattering information there are a variety of Soller collimators (0.15, 0.5, 1.0, 2.5 and 5^o divergence) and height (2, 5, 10 mm) and width (0.5, 2, 5, 15 mm) limiting slits which can be used. Soller collimators are stacks of metal plates (with low transmissivity) spaced a few millimeters from one another. The angular divergence of the x-ray beam is narrowed by decreasing the spacing between plates, or by increasing the length of the plates. Changing these

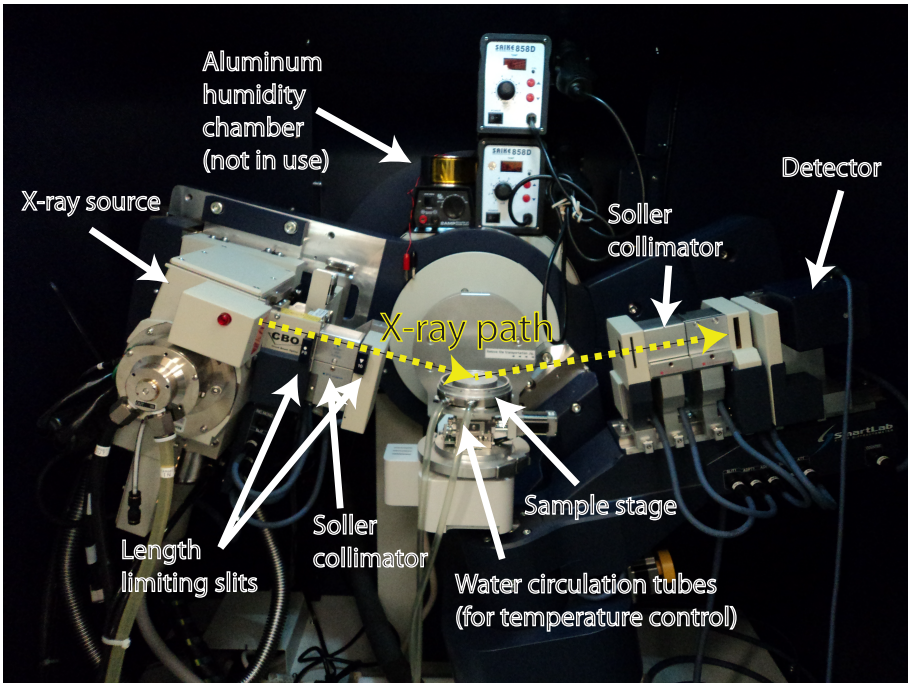

Figure 4.5: General overview photo of BLADE.
The x-ray path, optics, sample stage and hydration chamber inside the BLADE casing.

optics will allow for the precise selection of a particular $\overrightarrow{q}$ resolution. We used the in-plane and and reflectivity set-ups for our scans in the following experiments. [9] The path the x-ray beam follows through the optics is shown in Figure 4.6.

The sample environment in BLADE has a water bath cooling and heating system and thus is temperature controlled. With the addition of a humidity chamber we are able also to choose a relative humidity for our sample. The temperature is regulated in an external water bath, and water flows through a channel in the aluminum holder. This is shown in Figure 4.7. The humidity is set via saturated salt solutions (SSS). A salt, saturated with water, held at a constant temperature in a confined area will result in very precise relative humidity (R.H.) for that environment. For example at 20^o C, NaCl SSS results in ∼75% RH., KCl gives ∼85% RH and K_2SO_4 ∼97% RH. For other temperatures and a wide range of salt consult the table in [51].

The typical scan for most experiments was completed in 18 hours. This scan was a 2D reciprocal space map which covered the area from -0.3 $< q_{parallel} <$3.1 $Å^{-1}$ and

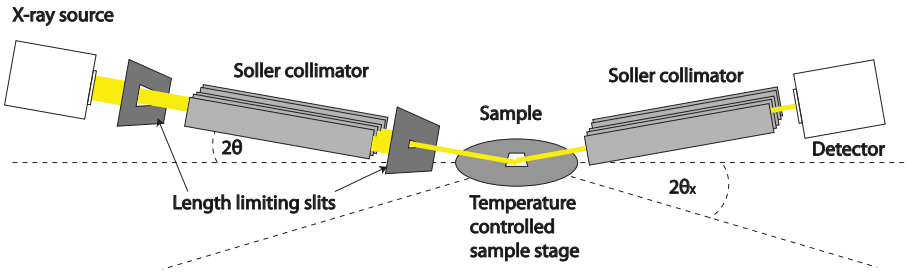

Figure 4.6: X-ray beam path and optics.
The X-ray beam (yellow) is generated in the x-ray source (left) and travels through collimators and length limiters before scattering with the sample. The scattered beam is also collimated then detected on the right side of the diagram.

$0 < q_z < 1.4$ Å^{-1}. This scan was done in sections, as is shown in Figure 4.8. Each in-plane scan consists of 288 points, and 80 of these scans are made (at various $\overrightarrow{q}_z$ values).

For each of the following experiments, data was acquired from our samples and compiled into a 2D reciprocal space map (typical data seen in figure 4.9). Our data ranged from -0.3 to 3.0 Å^{-1} in the horizontal or in-plane axis, and from 0 to 1.2 Å^{-1} vertical axis (-4.2^o < $2\theta_\chi$ < 43^o horizontal angular range, and $0^o < 2\theta < 17^o$ vertical angular range). This range of data provided us information about both the orientation of the molecules in our samples in and out of the plane of the bilayer. In real space this range allows us to see from large periodicity to ∼2 Å in-plane, and from large to ∼5 Å out-of-plane, although through Fourier transform we can obtain much higher resolution for the out-of-plane data. For each particular point in $\overrightarrow{q}_\parallel$ and $\overrightarrow{q}_z$ counts of scattered x-rays were recorded. The points with higher counts have a colour higher on the logarithmic scale on the right side. Each number on the log scale is 10^N, for example the maximum photon count would be in a red region and would correspond to 10^9 or 10^{10} photons/mm^2/s, see Figure 4.9. Since we have two dimensional scatterers sitting in planes, we see Bragg rods which extend

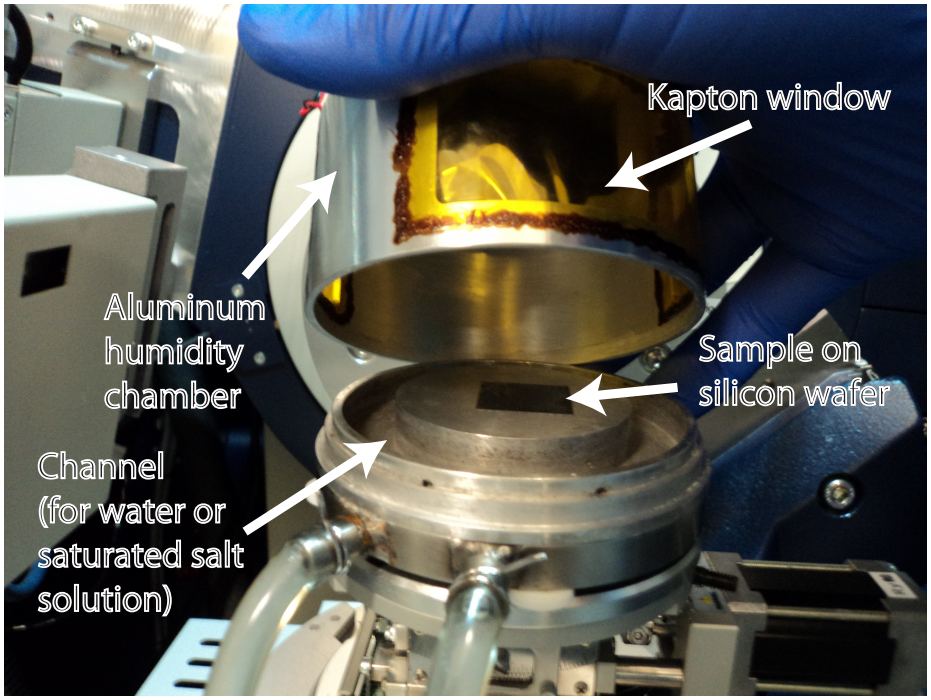

Figure 4.7: X-ray scattering humidity chamber on BLADE
Sample (seen in centre of platform) placed into humidity chamber with channel containing either pure water, or a saturated salt solution. Kapton windows allow high x-ray transmissivity and good thermal stability. Base of platform is temperature controlled (to ∼0.1 T).

upwards through a substantial amount of $\overrightarrow{q}_z$. If instead of rod shaped scatters we had just point scattering sites (for example atoms in crystals) the resulting diffraction pattern would instead be high intensity points with distance in reciprocal space being inversely related to nearest neighbour distance.

Most of our samples exhibit a low bilayer mosaicity (the degree of perfection of lattice translations throughout the sample), meaning the bilayer's lamella were very well aligned. (See Figure 4.10). A sample with all domains (or crystals) aligned would have a mosiacitiy of zero. In our samples we expect there were many small domains of continuous lipid bilayers present. These domains may be misaligned with respect to its neighbours, which leads to a higher mosiacity value. A low mosiacity is apparent in the vertical Bragg rods which are visible in most ordered samples. When these Bragg rods were not completely vertical, this was a sign of slight misalignment

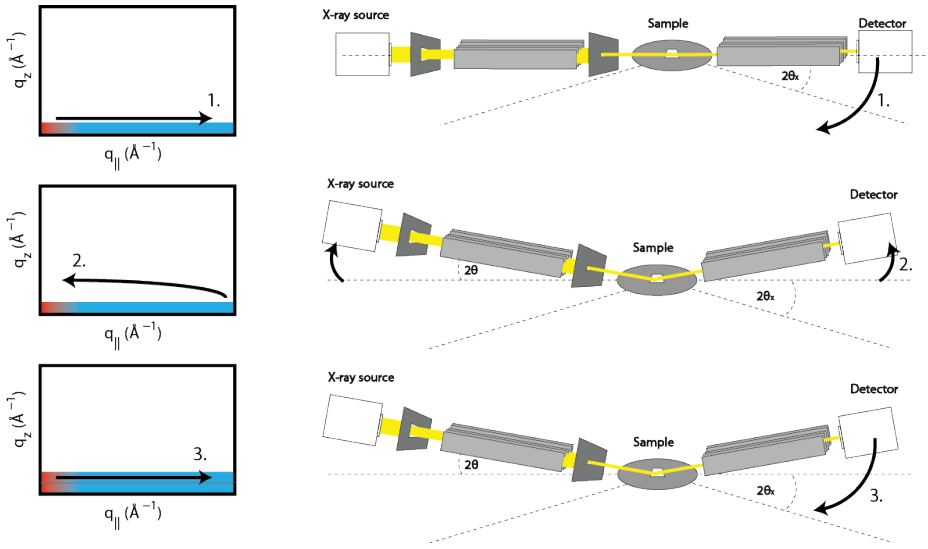

Figure 4.8: Typical scanning path of BLADE when obtaining a reciprocal space map (1) Starting at $\overrightarrow{q}_z$=0, a scan from -0.3 to 3.1 Å^{-1} in $\overrightarrow{q}_{parallel}$ was obtained . (2) The arms move back to $\overrightarrow{q}_{parallel}$=-0.3 Å^{-1} and move 0.0175 Å^{-1} higher in $\overrightarrow{q}_z$. (3) A scan in $\overrightarrow{q}_{parallel}$ happens at this new point. This process repeats for 80 scan lines, and takes a total of 18 h.

of lipid bilayer domains, and resembles a powder-like effect, as is present in Figure 4.11. These would appear circular if the ratio between the x-axis and y-axis were 1:1. The powder-like effect might be caused by the bilayers becoming less easy to pack as higher percentages of ASA or Cholesterol molecules are placed into the bilayer.

4.3 In-plane data analysis

Looking along the $\overrightarrow{q}_{\|}$ axis we see intensity peaks which relate to molecular order in the plane of the bilayer. The $\overrightarrow{q}_{\|}$ position is inversely related to the real-space separation d of the molecules, and can be determined using $q = 2\pi/d$.

In the case where a scan has only a single diffuse peak, we have a disordered system which has a distribution of nearest neighbour peaks, the with the center of the peak being the average distance. This is likely due to thermal fluctuations causing the scatterers in the sample to change their positions, rather than being fixed to a well defined average distance. If the diffuse peak is be symmetric, we can expect a Gaussian distribution around the center of the peak.

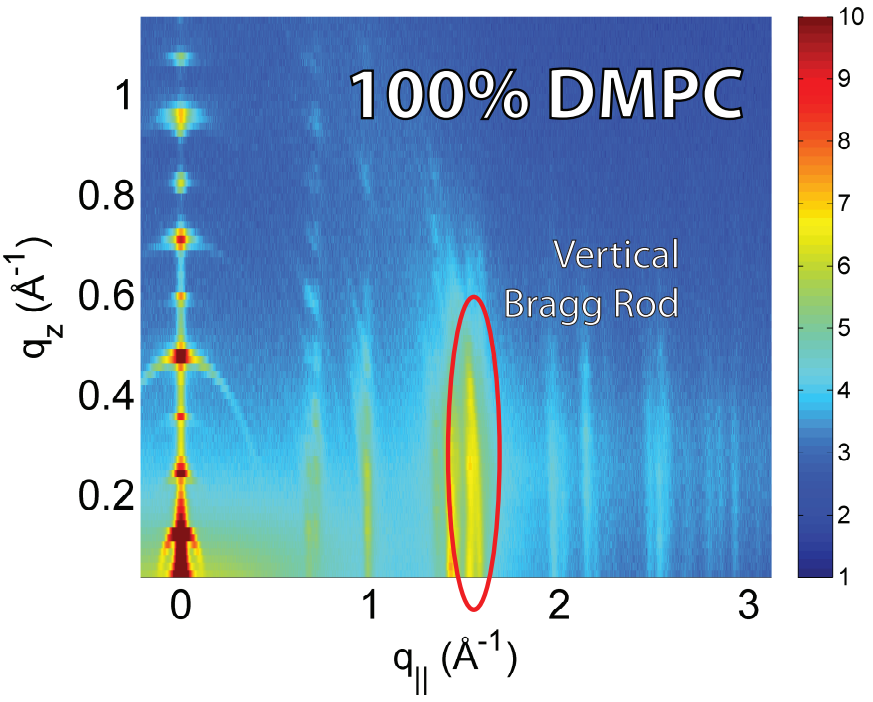

Figure 4.9: Pure DMPC sample, typical in-plane scattering data.
This 100% DMPC sample has been scanned using the in-plane capabilities of BLADE. Notice the large $\overrightarrow{q}$-range the scan encompasses and also the vertical Bragg peaks indicating low mosaicity (and thus well aligned domains). From this type of data we can obtain both in and out of plane structural information of the molecules present in the bilayer.

In the case where we see well defined narrow peaks, rather than a single diffuse peak, we can fit these peaks to simple unit cells and determine the in-plane structure of our molecules. For these fits we used PowderCell [52]. This program allows for fitting of atoms to unit cells. Since we had molecules instead we fit narrow peaks to our broad and often asymmetric peaks. This program allowed us to determine the structure factor to great precision, but left us with little information of the form factor of the scattering sites.

Figure 4.12 describes the process of interpreting the in-plane data we obtain from BLADE's scan. The periodic nature of the samples, with spacings of size d will result in Bragg peaks at locations of $q = \frac{2\pi}{d}$ on the $q_{||}$ axis. This is why a larger real space distance results in a smaller reciprocal space value.

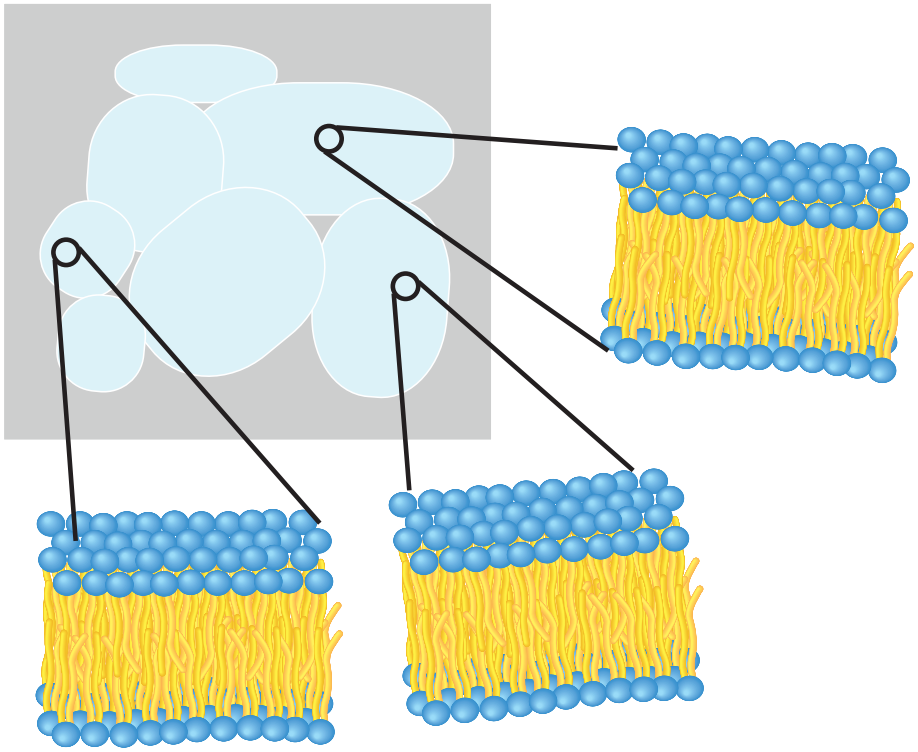

Figure 4.10: Cartoon depicting bilayer mosiacity.
Silicon wafer (grey) with many lipid bilayer domains. These domains are not visible by eye. Each domain contains one continuous and well aligned lipid bilayer. The amount of angular variation between bilayers in different domains will represent the mosiacity of our sample.

Starting from our reciprocal space map in Figure 4.13a) we sum the first 20 $\overrightarrow{q}_{\parallel}$ horizontal scan lines, from 0 to 0.3 Å^{-1} in $\overrightarrow{q}_{z}$. The result of this integration is a x-ray intensity vs $\overrightarrow{q}_{\parallel}$ plot. For analysis of this data using PowderCell the $\overrightarrow{q}_{\parallel}$ axis is converted to $2\theta_{\chi}$, using the relation shown in equation 4.2, with λ=1.5418 Å. This plot is shown in Figure 4.13b). With our Bragg peaks clearly visible after the integration we assign Miller indices to each of the peaks, and based on the peak position and ratios between peaks determine the real-space unit cell parameters of our molecules. This process gives us a feel for the separation of the molecules, and from this we check different real-space models for agreement with unit cell parameters, equal spacing of molecules and logical geometry. We use this to determine a particular molecular arrangement. In our example case, this is shown in Figure 4.13c).

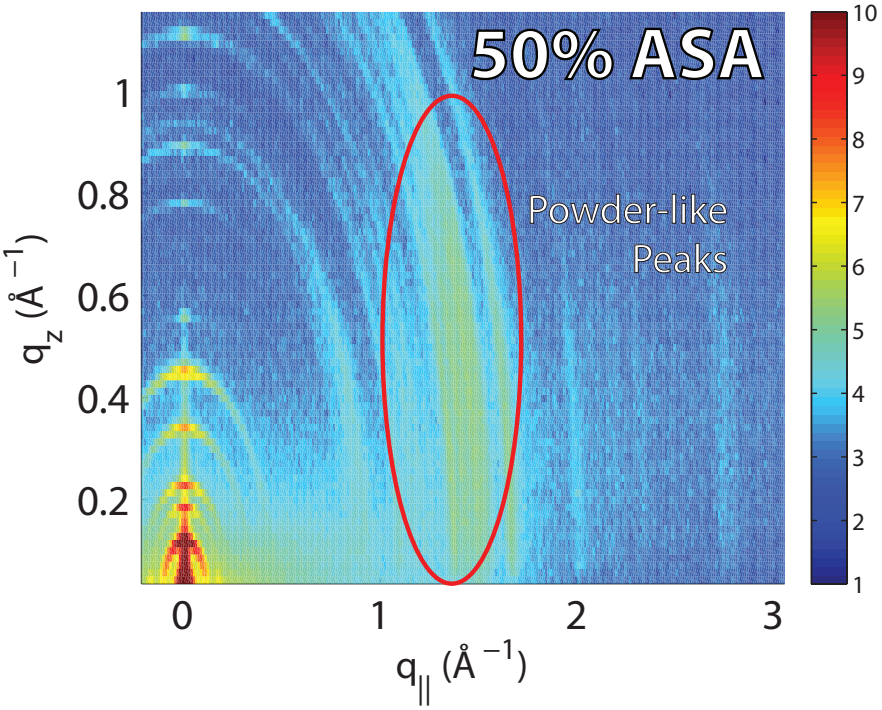

Figure 4.11: 50% ASA, 50% DMPC sample, typical in-plane scattering data. This 50% ASA sample has been scanned using the in-plane capabilities of BLADE. Due to the addition of large amounts of ASA (1:1 molar ratio) the bilayer's mosaicity increases.

$$|\overrightarrow{q}| = \frac{4\pi \sin\theta}{\lambda} \tag{4.2}$$

4.4 Reflectivity analysis

The other aspect of the reciprocal space maps that we used was the vertical scan of data, along $\overrightarrow{q}_{\parallel} = 0$. A sample of this is shown in Figure 4.14. This scan gets analyzed, and Fourier transformed. This process results in an electron density, which provides information about the vertical-bilayer components, based on which atoms possess more electrons. To gain higher resolution, in certain cases new reflectivity scans were performed, with different optics and stationary $2\theta_{\chi}$ arms, resulting in electron density profiles with Å resolution.

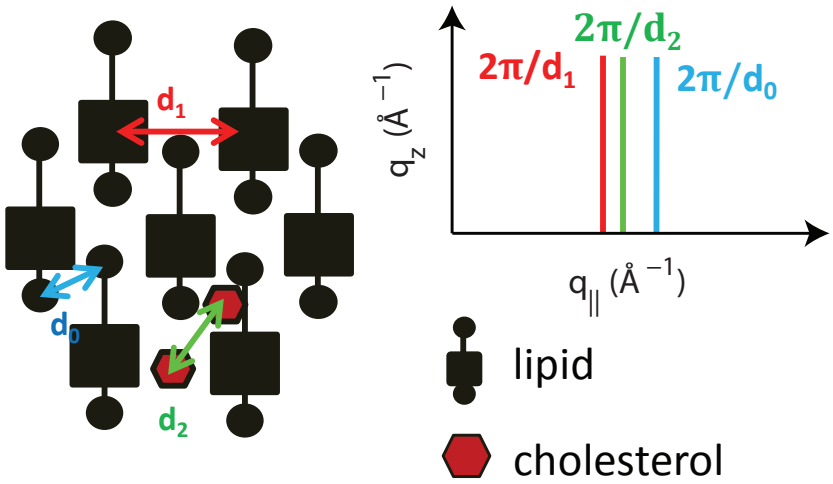

Figure 4.12: Cartoon of molecular arrangement and corresponding Bragg Rods The top view of lipid molecules in the plane of the bilayer. The characteristic separation distances of the molecular components (lipid tails, heads and ASA molecules) will appear as Bragg peaks in the reciprocal space map.

Once the q_z scan at $q_{\|} = 0$ is extracted, the position and area of each of the peaks is determined using a MatLab macro. The position and peak area are used to fit our data to the function $T(q_z)$ (Equation 4.3), which represents the discrete form factor of a single bilayer.[53] In this equation, n represents which peak, I_n is the area of the peak at position q_n, d_z is the bilayer d-spacing, determined by the relation $q = 2\pi/d$. This function is fit to our data, and the Fourier phase of each peak can be determined.

$$T(q_z) = \sum_n \sqrt{I_n q_n} \mathrm{sinc}(\pi d_z q_n - \pi n) \tag{4.3}$$

The determination of the Fourier phase of each peak was achieved through quick hydration scans. The sample was placed from a low humidity (~50% relative humidity) environment into our humidity chamber (Refer to Figure 4.7) with either pure water, or a saturated salt solution, depending what the final sample humidity should

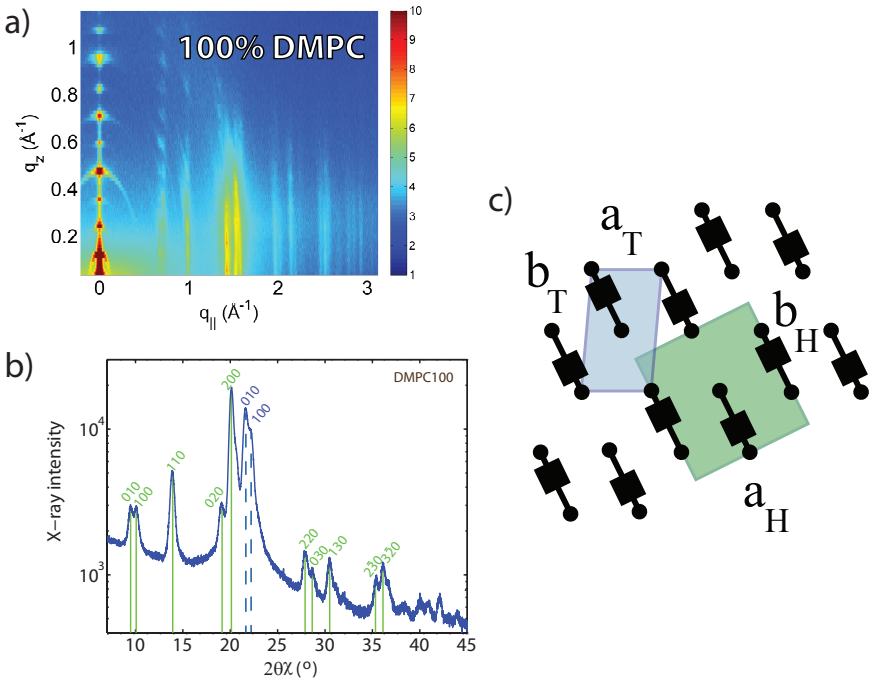

Figure 4.13: In-plane analysis process examples.
a)The raw 2D in-plane data (of a 100% DMPC sample. b)Integrated scans summing the $\overrightarrow{q}_{\parallel}$ data from 0 to 0.3 Å^{-1} in $\overrightarrow{q}_z$ Lipid head unit cell Bragg peaks given in green solid line, lipid tail in blue dotted line. c)The resulting real space unit cell, viewed from above the plane of the membrane, based on the Bragg peaks determined from the reciprocal space map. The lipid head unit cell is shown by the green rectangle, and tail by the blue rectangle.

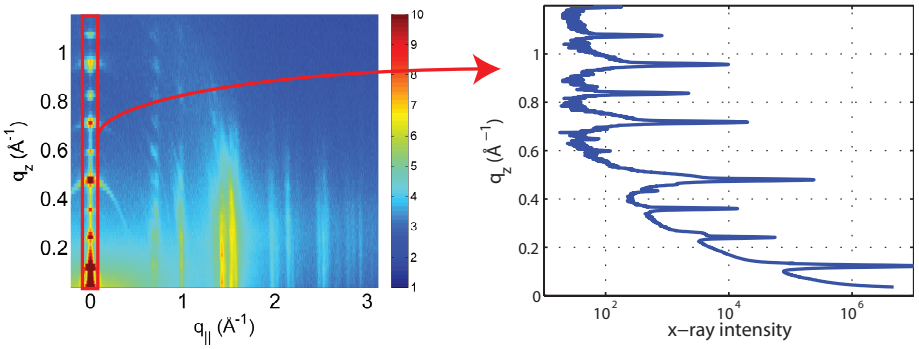

Figure 4.14: Reflectivity extraction from reciprocal space map.
The data along $\overrightarrow{q}_{\parallel} = 0$ is extracted and plotted. This data is a scan of a pure DMPC sample, and the peaks are spaced evenly. The periodicity of these high intensity peaks is representative of the inverse of the lamellar d-spacing.

be. Low resolution, quick reflectivity scans were performed, to create slightly different bilayer spacing, due to the hydration. This technique has been well documented in previous studies of other lipid bilayer systems. [53, 54] For our 100% DMPC sample our $T(q_z)$ function with hydration data points is shown in Figure 4.15.

Finally, with the phases determined, the high resolution reflectivity data is Fourier transformed into electron density in the bilayer, using equation 4.4.

$$\rho(z) = \rho_w + \frac{F(0)}{d_z} + \frac{2}{d_z}\sum_{n=1}^{N} F(q_n)\nu_n \cos(q_n z) \tag{4.4}$$

Here ρ_w is the electron density of bulk water, $F(q_n)$ is the bilayer form factor, which is multiplied by the phase ν_n either ± 1, as determined by the hydration procedure, and z the position in real space. This is shown graphically in Figure 4.16.

In the following experiments, the electron density of different concentrations of lipid and other membrane constituents were compared. An overlay of multiple concentrations allowed for the determination of position of molecules vertically in the bilayer.

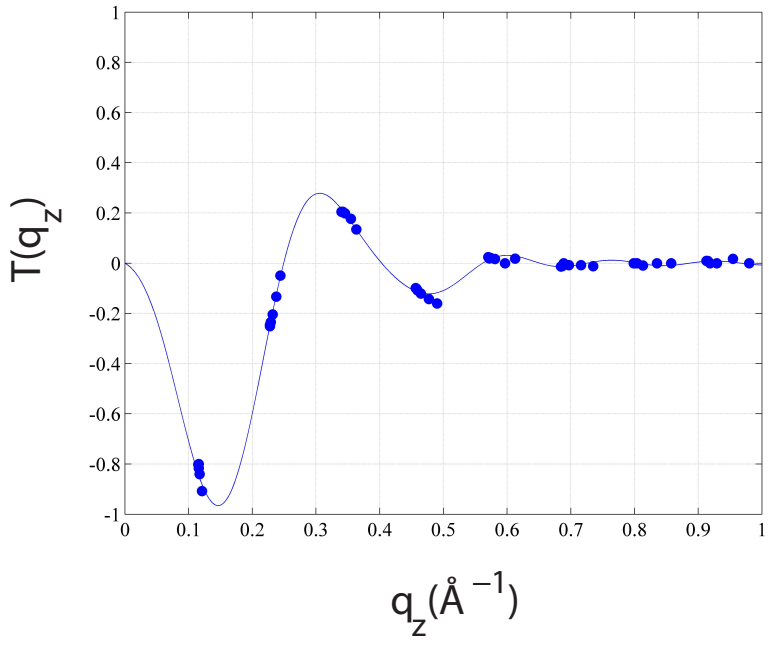

Figure 4.15: Form factor of 100% DMPC during hydration for phase determination. The phase problem for our DMPC bilayer sample is solved through reflectivity scans during hydration. The changing bilayer thickness with hydration causes the peak positions to shift, and the peak areas to change size. Many options for positive and negative phases for each peak were tested to determine the best fit.

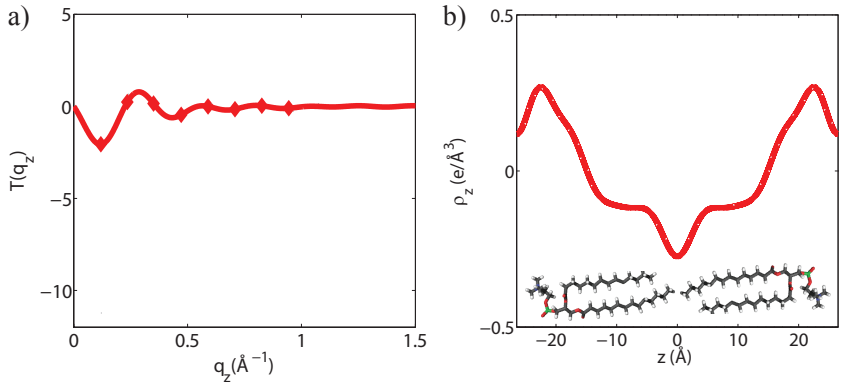

Figure 4.16: Form factor and electron density profile of 100 % DMPC
The form factor of our 100% DMPC sample a) is Fourier transformed into an electron density profile b) using equation 4.4. Overlaid on b) are two DMPC molecules, helpful in visualizing the bilayer. The presence of high atomic number atoms in the head group region of the lipid molecule (oxygen, phosphorus, nitrogen) causes a greater electron density in this part of the bilayer.

Preface to Paper II

In the following paper, we observed the structural order of lipid bilayers (DMPC) with acetylsalicyclic acid (ASA) at concentrations ranging from 0% ASA, (Pure DMPC bilayer) to 50 mol% ASA. This was the first time ASA molecules were observed in the lipid bilayer, and our observations were made with great precision, due to the excellent resolution provided by BLADE. We observed both the in-plane and out-of-plane structural orientation and position of ASA. The addition of a small amount of ASA causes the bilayer to leave the ordered pure DMPC state, and our samples remain disordered until the 40 mol% ASA sample. At 40 mol% ASA and higher, the lipid's head groups and tail groups, as well as the ASA molecules all form an ordered lattice. We also tested a sample with cholesterol and ASA, and determined both of these molecules can inhabit the same bilayer, which led to the experiments discussed in Paper IV.

The preparation of the bilayers was performed at the Labratory for Membrane and Protein Dynamics (LMPD) at McMaster University. I, along with the help of Songbo Zheng, Golnaz Roshankar, Richard Alsop, Randy Belanger and Chris Huynh created the samples. The samples were scanned using BLADE by Songbo and myself. I did the analysis of this data, in particular the development of the Matlab macro used for reflectivity analysis, with helpful discussions with Norbert Kučerka and Richard Alsop. Maikel Rheinstädter provided guidance and much advice throughout the whole process, conceived and designed the experiment. Maikel and I wrote the paper.

This paper was published in PloS One in April 2012.

OPEN ACCESS Freely available online

PLoS one

Interaction of Aspirin (Acetylsalicylic Acid) with Lipid Membranes

Matthew A. Barrett[1], Songbo Zheng[1], Golnaz Roshankar[1], Richard J. Alsop[1], Randy K. R. Belanger[1], Chris Huynh[1], Norbert Kučerka[2], Maikel C. Rheinstädter[1,2]*

1 Department of Physics and Astronomy, McMaster University, Hamilton, Ontario, Canada, **2** Canadian Neutron Beam Centre, National Research Council Canada, Chalk River, Ontario, Canada

Abstract

We studied the interaction of Aspirin (acetylsalicylic acid) with lipid membranes using x-ray diffraction for bilayers containing up to 50 mol% of aspirin. From 2D x-ray intensity maps that cover large areas of reciprocal space we determined the position of the ASA molecules in the phospholipid bilayers and the molecular arrangement of the molecules in the plane of the membranes. We present direct experimental evidence that ASA molecules participate in saturated lipid bilayers of DMPC (1,2-dimyristoyl-sn-glycero-3-phosphocholine) and preferably reside in the head group region of the membrane. Up to 50 mol% ASA molecules can be dissolved in this type of bilayer before the lateral membrane organization is disturbed and the membranes are found to form an ordered, 2D crystal-like structure. Furthermore, ASA and cholesterol were found to co-exist in saturated lipid bilayers, with the ASA molecules residing in the head group region and the cholesterol molecules participating in the hydrophobic membrane core.

Citation: Barrett MA, Zheng S, Roshankar G, Alsop RJ, Belanger RKR, et al. (2012) Interaction of Aspirin (Acetylsalicylic Acid) with Lipid Membranes. PLoS ONE 7(4): e34357. doi:10.1371/journal.pone.0034357

Editor: Peter Butko, Nagoya University, Japan

Received January 20, 2012; **Accepted** March 1, 2012; **Published** April 17, 2012

Funding: This research was funded by the Natural Sciences and Engineering Research Council of Canada (NSERC), the National Research Council Canada (NRC), the Canada Foundation for Innovation (CFI), and the Ontario Ministry of Economic Development and Innovation. Silicon substrates were partially provided by ComDev. The funders had no role in study design, data collection and analysis, decision to publish, or preparation of the manuscript.

Competing Interests: Silicon substrates for this project were partially provided by ComDev. This does not alter the authors' adherence to all the PLoS ONE policies on sharing data and materials.

* E-mail: rheinstadter@mcmaster.ca

Introduction

The molecular mechanism by which drugs interact with cell membranes has become a central issue in pharmacological science [1]. Aspirin (acetylsalicylic acid, ASA) is one of the most commonly used analgesic drugs. From infrared spectroscopy Casal, Martin and Mantsch speculated decades ago that aspirin is located in the lipid head group region of phospholipid bilayers [2]. We used x-ray diffraction to study the interaction between Acetylsalicylic Acid and saturated phospholipid bilayers made of dimyristoylphosphocholine (DMPC). Membranes containing up to 50mol% ASA were prepared.

In-plane and out-of-plane structure of the membranes in their gel (L_β) phase were determined from 2D x-ray intensity maps covering large areas of reciprocal space. We determine the location of the ASA molecules in the bilayer from electron density profiles perpendicular to the membranes and present the first direct experimental proof that ASA molecules participate in lipid bilayers and are located in the head group region of the bilayers. From wide angle x-ray diffraction experiments the arrangement of lipid and ASA molecules in the plane of the membrane was determined. While in pure DMPC bilayers, lipid head groups and tails show a high degree of positional order, small amounts of ASA lead to a disordered, fluid-like membrane. A 1:1 (lipid:ASA) ratio was found to be the solubility limit of ASA molecules in saturated phospholipid bilayers, with one ASA molecule attached to each lipid head group. We also investigated a membrane containing 5mol% ASA and 15mol% cholesterol and observed that ASA and cholesterol molecules coexist in saturated lipid membranes.

Materials and Methods

Sample preparation

Highly oriented multi lamellar membranes were prepared on single-side polished silicon wafers. 100 mm diameter, 300 μm thick silicon (100) wafers were pre-cut into 2×2 cm^2 chips. 1,2-dimyristoyl-sn-glycero-3-phosphocholine (DMPC), acetylsalicylic acid (ASA) and cholesterol (depicted in Figure 1 a)) were mixed in different ratios and dissolved in a 1:1 chloroform/2,2,2-trifluoroethanol (TFE) solution at a concentration of 15 mg/mL. The lipid solution did not spread well on ultrasonic-cleaned wafers and de-wetted during drying. The silicon substrates were, therefore, cleaned in a piranha acid solution made of 98% concentrated H_2SO_4 and 30% concentrated H_2O_2 at a ratio of 3:1 by volume. Wafers were placed in this solution, covered with parafilm and heated to 298 K for 30 minutes. This treatment removes all organic contamination and leaves the substrates in a hydrophilic state. We used silanization to cover the silicon surface through self-assembly with organo functional alkoxysilane molecules (APTES). The organic part of the APTES molecules was found to provide a perfect hydrophobic interface for the formation of the biological tissue. A 1% (by volume) solution of APTES and 99% ethanol was prepared. The wafers were immersed in the APTES solution and covered with parafilm, heated to 298 K and placed on a tilting incubator (20 speed, 3 tilt) for 12 hours. The tilting incubator

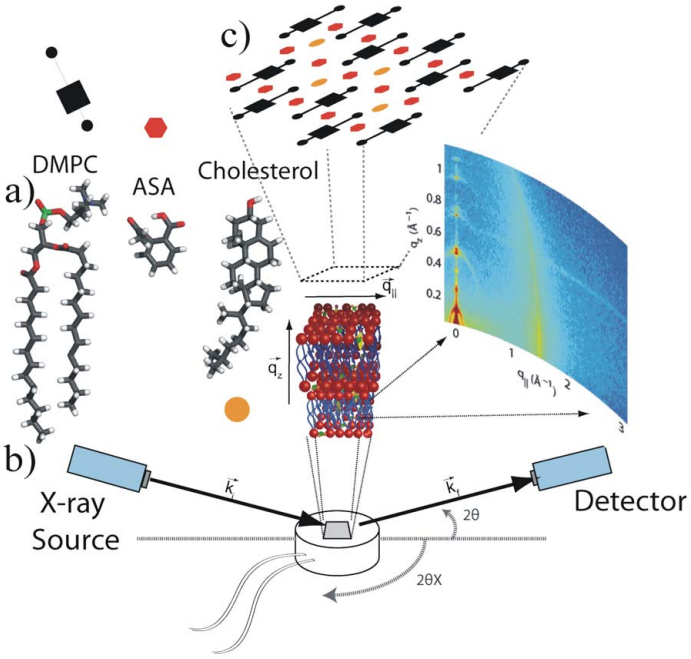

Figure 1. Experimental overview. a) Lipid, ASA and cholesterol molecule.b) Schematic diagram of the x-ray scattering experiment. The in-plane and out-of-plane structure of the membranes can be determined from the 2D intensity maps. Highly oriented multi lamellar membranes are used. 2θ and $2\theta\chi$ are the out-of-plane respective in-plane diffraction angles. c) Top view of the membrane to illustrate the molecular arrangement in the plane of the membrane. Lipids are depicted by a head group (■) and two tails (●). ASA and cholesterol molecules are represented by a hexagon and a circle, respectively.
doi:10.1371/journal.pone.0034357.g001

creates a circular flow in the beaker to ensure an even APTES distribution and prevent buildup on the surface of the wafers. The wafers were then placed in a clean pyrex dish and annealed in vacuum at 388 K for 3 hours to create a uniform coverage of the APTES molecules on the surface [3]. Each wafer was thoroughly rinsed three times by alternating with ~50 mL of ultrapure water and methanol. The methanol was cleaned using a 0.2 μm filter before use to avoid surface contamination. The tilting incubator was heated to 313 K and the lipid solution was placed inside to equilibrate. The wafers were rinsed in methanol, dried with nitrogen gas and placed in the incubator. 200 μL of lipid solution was applied on each wafer, and the wafers covered with a petri dish to let the solvent evaporate slowly to allow time for the membranes to form. Wafers were tilted during the drying process for 30 minutes (speed 15, tilt 1) such that the lipid solution spread evenly on the wafers. After drying, the samples were placed in vacuum at 313 K for 12 hours to remove all traces of the solvent. The bilayers were annealed and rehydrated before use in a saturated K_2SO_4 solution which provides ~98% relative humidity (RH). The hydration container was allowed to equilibrate at 293 K in an incubator. The temperature of the incubator was then increased gradually from 293 K to 303 K over a period of ~5 hours to slowly anneal the multi lamellar structure. This procedure results in highly oriented multi lamellar membrane stacks and a uniform coverage of the silicon substrates. About 3,000 highly oriented stacked membranes with a thickness of ~10 μm are produced using this protocol. The samples were stored in a refrigerator at 5°C and heated to 55°C for 1 h before scanning to erase a possible thermal history. This procedure in particular destroys possible crystalline L_C or sub-gel phases that may form during storage at low temperatures and low hydration, as has been reported in [4]. The high sample quality and high degree of order is necessary to determine in-plane and out-of-plane structure of the membranes and the position of the ASA molecules with high spatial resolution. Table 1 lists all samples prepared for this study.

X-ray scattering experiment

Out-of-plane and in-plane x-ray scattering data was obtained using the Biological Large Angle Diffraction Experiment (BLADE) in the Laboratory for Membrane and Protein Dynamics at McMaster University. BLADE uses a 9 kW (45 kV, 200 mA) CuKα rotating anode at a wavelength of 1.5418 Å. Both source and detector are mounted on movable arms such that the membranes stay horizontal during the measurements. Focussing multi-layer optics provides a high intensity parallel beam with monochromatic x-ray intensities up to 10^{10} counts/(mm^2 × s). This beam geometry provides optimal illumination of the solid supported membrane samples to maximize the scattering signal. All data were obtained in grazing incidence, small and wide angle scattering geometry. A sketch of the scattering geometry is shown in Figure 1 b). By using highly oriented membrane stacks, the in-plane ($q_{||}$) and out-of-plane (q_z) structure of the membranes can be determined. From the high resolution x-ray diffraction experiments we determine the molecular structure of the membranes in

Table 1. List of samples used.

Sample	DMPC (mol%)	ASA (mol%)	cholesterol (mol%)	Unit Cell	area per lipid (Å^2)	lipid tilt (deg)	d_z-spacing (Å)
1	100	0	0	head-groups: $a_H = 8.773$ Å, $b_H = 9.311$ Å, $\gamma_H = 90^\circ$, lipid tails: $a_T = 4.966$ Å, $b_T = 8.247$ Å, $\gamma_T = 94.18^\circ$	40.84 ± 0.1	6.5	55.3
2	99	1	0	lipid tails: $a_T = 4.23$ Å, $\gamma_T = 120^\circ$	41.4 ± 0.7	7.4	53.6
3	95	5	0	lipid tails: $a_T = 4.21$ Å, $\gamma_T = 120^\circ$	41.0 ± 0.7	8.0	55.3
4	90	10	0	lipid tails: $a_T = 4.22$ Å, $\gamma_T = 120^\circ$	41.1 ± 0.7	6.8	55.2
5	85	15	0	lipid tails: $a_T = 4.21$ Å, $\gamma_T = 120^\circ$	40.9 ± 0.7	5.0	49.1
6	80	20	0	head-groups: $a_H = 8.742$ Å, $b_H = 9.308$ Å, $\gamma_H = 90^\circ$, lipid tails: $a_T = 4.15$ Å, $\gamma_T = 120^\circ$	39.8 ± 0.1	6.7	46.7
7	75	25	0	lipid tails: $a_T = 4.22$ Å, $\gamma_T = 120^\circ$	41.2 ± 1.0	5.6	49.1
8	70	30	0	lipid tails: $a_T = 4.25$ Å, $\gamma_T = 120^\circ$	41.7 ± 1.2	6.3	49.1
9	60	40	0	lipid tails: $a_T = 4.19$ Å, $\gamma_T = 120^\circ$	40.5 ± 0.7	5.4	49.2
10	50	50	0	head-groups: $a_H = 8.729$ Å, $b_H = 9.337$ Å, $\gamma_H = 90^\circ$, lipid tails: $a_T = 4.950$ Å, $b_T = 8.252$ Å, $\gamma_T = 93.80^\circ$, ASA: $a_A = 5.74$ Å, $b_A = 3.30$ Å, $\gamma_A = 90^\circ$	40.75 ± 0.1	6.7	55.6
11	80	5	15	lipid tails: $a_T = 4.23$ Å, $\gamma_T = 120^\circ$	41.3 ± 0.9	3.5	49.1

List of all the samples prepared for this study, and their molecular composition. Unit cell dimensions, areas per lipid, lipid tilt angles, and d_z spacings are also given. See text for details.

doi:10.1371/journal.pone.0034357.t001

two different ways: (1) the out-of-plane membrane structure to determine the location of the different molecules in the membrane with sub-nanometer resolution and (2) the lateral organization of the different molecular components in the plane of the membrane, as sketched in Figure 1 c). The result of such an x-ray experiment is a 2D intensity map of a large area ($0.03\ \text{Å}^{-1} < q_z < 1.1\ \text{Å}^{-1}$ and $0\ \text{Å}^{-1} < q_\parallel < 3.1\ \text{Å}^{-1}$) of the reciprocal space, as sketched in Figure 1 b). All scans were measured at 20°C and 50% hydration, in the gel (L_{β}) phase of the bilayers [5,6]. Structural features are more pronounced in dry samples as fluctuations, which lead to attenuation and smearing of Bragg peaks, are strongly suppressed. The measurement of high-order Bragg peaks results in a high spatial resolution.

Specular reflectivity allows the determination of the structure and composition of membranes perpendicular to the plane of the membranes (see, e.g., [7,8]). The intensity of the reflected beam as a function of the perpendicular momentum transfer, q_z, is given by:

$$R(q_z) = \frac{16\pi^2}{q_z^2}|\hat{\rho}(q_z)|^2 \tag{1}$$

$\hat{\rho}(q_z)$ is the one-dimensional Fourier transform of the electron density $\rho(q_z)$, defined by:

$$\hat{\rho}(q_z) = \int_{-\infty}^{\infty} \exp(iq_z z)\rho(z)dz \tag{2}$$

Because of the stacking of the membranes, i.e., the convolution with the lamellar structure factor, the Fourier transform is not continuous but discrete. The different Fourier components are observed in the experiment as the integrated intensities of the out-of-plane Bragg peaks. $\rho(z)$ is approximated by a 1D Fourier analysis [9]:

$$\rho(z) = \rho_W + \frac{F(0)}{d_z} + \frac{2}{d_z}\sum_{n=1}^{N} F(q_n)v_n \cos(q_n z)$$

$$= \rho_W + \frac{F(0)}{d_z} + \frac{2}{d_z}\sum_{n=1}^{N} \sqrt{I_n q_n} v_n \cos\left(\frac{2\pi n z}{d_z}\right) \tag{3}$$

N is the highest order of the Bragg peaks observed in the experiment and ρ_W the electron density of bulk water. The integrated peak intensities, I_n, are multiplied by q_n to receive the form factors, $F(q_n)$ [10,11]. The bilayer form factor $F(q_z)$, which is in general a complex quantity, is real-valued in the case of centro-symmetry. The phase problem of crystallography, therefore, simplifies to the sign problem $F(q_z) = \pm|F(q_z)|$, and the phases, v_n, can only take the values ± 1. The phases v_n are needed to reconstruct the electron density profile from the scattering data following Equation (3). When the membrane form factor $F(q_z)$ is measured at several q_z values, a continuous function, $T(q_z)$, which is proportional to $F(q_z)$, can be fitted to the data [10–13]:

$$T(q_z) = \sum_n \sqrt{I_n q_n}\,\mathrm{sinc}(\pi d_z q_z - \pi n). \tag{4}$$

Once an analytical expression for $T(q_z)$ has been determined from fitting the experimental peak intensities, the phases v_n can be determined from $T(q_z)$ – this will be demonstrated below.

Results

In-plane structure

Figure 2 displays 2D x-ray intensity maps for Samples 1, 3, 6, 9, 10 and 11. The arrangement of the different molecular components in the plane of the membranes can be determined from the the in-plane scattering along $q_{\|}$. As introduced by Katsaras and Raghunathan [14,15], different molecular components, such as lipid tails, lipid head groups and also ASA and cholesterol molecules, can form molecular sub-lattices in the plane of the membrane leading to non-overlapping sets of Bragg peaks.

The 100% DMPC sample (Sample 1) in Figure 2 a) shows a number of well developed in-plane Bragg peaks along the $q_{\|}$-axis. The diffracted intensity has a distinct rod-like shape, typical for a 2D system. The out-of-plane scattering along q_z shows pronounced and equally spaced Bragg intensities due to the multi lamellar structure of the membrane sample. Analysis of the data and determination of the corresponding in-plane and out-of-plane structure will be discussed in detail below.

Some qualitative conclusions can already be drawn from the 2D data. The pattern changes by addition of 5mol% ASA (Figure 2 b)): the in-plane scattering shows one pronounced feature, only. Fewer Bragg peaks point to a short-ranged ordered, more fluid-like structure. Bragg peaks and molecular order are observed again at 20mol% ASA in Figure 2 c). Higher concentrated samples, such as 40mol% in Figure 2 d) appear to be disordered until an ordered pattern is observed at a concentration of 50mol% ASA (Figure 2 e)). The sample that contains ASA and cholesterol (Figure 2 f)) shows the fingerprint of a disordered membrane. The data in Figure 2 cover a large area of reciprocal space and are important to develop the molecular structure of the membrane systems. They are in particular important to detect or exclude structural features with mixed in-plane and out-of-plane properties, such as molecular tilts, which would in scattering with mixed, $q_{\|}$ and q_z components. The cartoons next to the data in Figure 2 display the corresponding molecular structures, as determined from the analysis below.

To determine the in-plane structure, data were cut along the $q_{\|}$-axis. Slices $0.03\ \text{Å}^{-1} < q_z < 0.3\ \text{Å}^{-1}$ were integrated to enhance the data quality. The results for Sample 1 are shown in Figure 3 a). As depicted in the cartoon in Figure 2 a), the Bragg peaks were assigned to two different molecular lattices, the lipid head groups and the lipid tails. An orthorhombic head group lattice (planar space group p2) with lattice parameters $a = 8.773$ Å and $b = 9.311$ Å ($\gamma = 90^\circ$) was found to best fit the data. The lattice of the lipid tails is commensurate with the head group lattice and the unit cell is determined by the relations [14,15]:

$$a_H^2 = \frac{1}{4}\left(9a_T^2 + b_T^2\right) - \frac{3}{2}a_T b_T \cos\gamma_T,$$

$$b_H^2 = a_T^2 + b_T^2 + 2a_T b_T \cos\gamma_T, \qquad (5)$$

$$\cos\gamma_H = \frac{3a_T^2 - b_T^2 + 2a_T b_T \cos\gamma}{2a_H b_H}.$$

The subscripts T and H denote parameters of the tail and head group lattices, respectively. Solving these equation gives a monoclinic unit cell with parameters $a_T = 4.966$ Å, $b_T = 8.247$ Å and $\gamma_S = 94.18^\circ$. The positions of the corresponding Bragg peaks are superimposed with the data in Figure 3 a) and show an excellent agreement. The molecular structure is shown in the cartoon to Figure 2 a) and the two units cells are drawn. The orthorhombic unit cell of the head group lattice contains two lipid molecules and has an area of $A_H = a_H b_H = 81.69$ Å^2. The area per lipid can also be determined from the unit cell of the tails, which contains one lipid molecule, to $A_T = a_T b_T \sin\gamma_T = 40.84$ Å^2.

The tilt of the lipid molecules in the gel phase can be determined from the scan in Figure 2 a). The diffracted intensity of the lipid tail peak at $q_{\|} = 1.48\ \text{Å}^{-1}$is not distributed homogenously along the rod, however peaks at a q_z value of $\sim 0.2\ \text{Å}^{-1}$, corresponding to a tilt angle of $\alpha = 6.5$ degs. Similar peak maxima are observed in the head group Bragg-rods, which leads to the conclusion that the whole lipid molecule is tilted by α.

Only one peak is observed at 5mol% ASA in Figure 2 b). Even at this relatively low concentration (ASA:lipids = 1:20) the presence of the ASA molecules inhibits long-range order of the lipid head groups or tails as evidenced by the absence of Bragg peaks belonging to head or tail unit cells. From the data in Figure 2 it can be concluded that the lattices belonging to head groups and ASA molecules have a high degree of positional disorder. In the case of ASA this is most likely the result of a stochastic distribution of the ASA molecules in the bilayer. The area per lipid can be determined when assuming that the lipid tails form a densely packed structure with hexagonal symmetry (planar group p6). The lipid area can then be determined from the distance between two head groups respective two lipids tails on a hexagonal lattice to $A_L = 4a_T^2/\sqrt{3}$. As the average distance between two tails is determined by the position, q_T, of the correlation peak to $a_T = 2\pi/q_T$, the area per lipid is determined to $A_L = 16\pi^2/\sqrt{3}q_T^2 = 41.0$ Å^2. The corresponding unit cell parameters and areas per lipid are given in Table 1; the hexagonal unit cell is also drawn in the cartoon to Figure 2 b), where the molecular structure is sketched.

A pattern of Bragg peaks related to ordering of the lipid head groups is observed at an ASA concentration of 20mol% ASA in Figure 2 c); however only one peak related to the lipid tails is observed pointing to a positional disorder of the tails. The presence of the ASA molecules at a ratio of 1:5 (ASA:lipid) induces a long-ranged ordered state between the lipid head groups, however, has little to no effect on the lipid tails. We find an orthorhombic unit cell for the head groups and a hexagonal symmetry for the lipid tails. The lattice parameters were determined from fitting the peak pattern in Figure 3 b) and are given in Table 1.

Higher concentrated samples (Samples 7–9) showed a disordered membrane structure with only the lipid correlation peak; 40mol% is shown as an example in Figure 3 d). The 20mol% sample therefore appeared to be special as this 1:5 ratio between ASA and lipids lead to an ordering between the lipid head groups.

Several Bragg peaks are observed at the high ASA concentration of 50mol% in Figure 2 e). The Bragg peaks can be assigned to the ordering of the lipid tails and the lipid head groups. We find additional peaks in the pattern in Figure 3 c) that we assign to ordering of the ASA molecules. Orthorhombic unit cells for head groups and ASA molecules, and a monoclinic cell for the lipid tails were determined. In this structure, each lipid molecule "hosts" one ASA molecule. While 40mol% ASA can still be dissolved in the DMPC bilayer, 50mol% ASA leads to a non-physiological, highly ordered state, which clearly marks the solubility limit of ASA in saturated phospholipid bilayers. The unit cell dimensions, lipid areas and lipid tilt for all samples are given in Table 1; the corresponding molecular structures and unit cells are sketched in the cartoons in Figure 2.

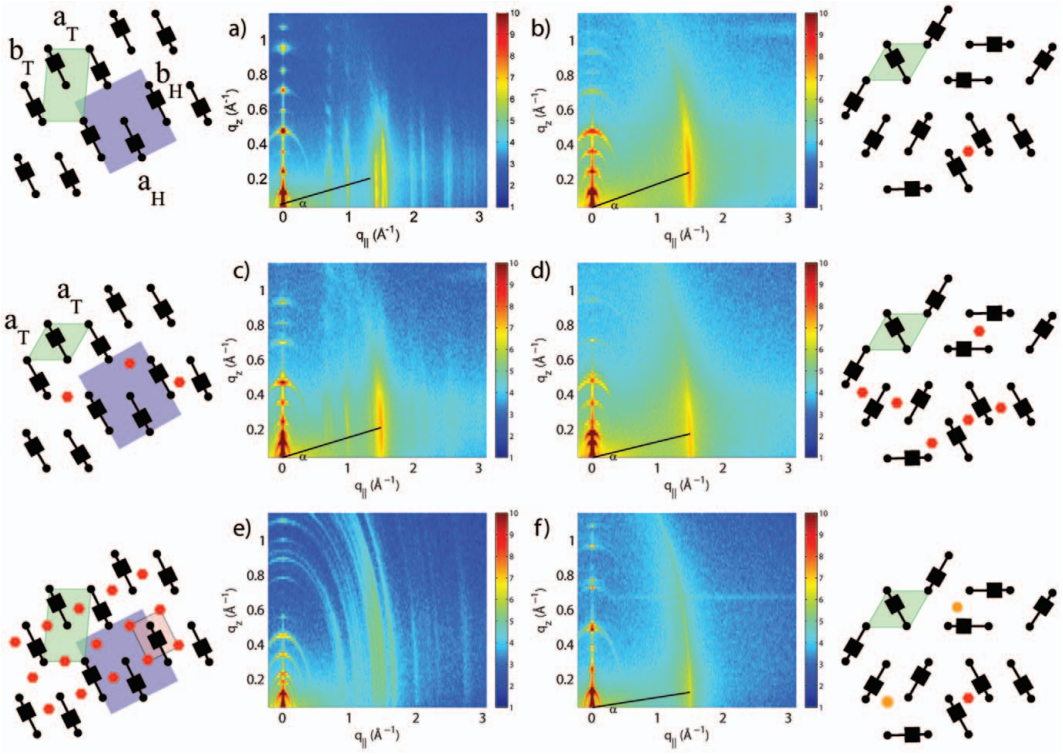

Figure 2. 2D x-ray intensity maps. 2D x-ray intensity maps of Samples 1, 3, 6, 9, 10 and 11 (100% DMPC, 5mol% ASA, 20mol% ASA, 40mol% ASA, 50mol% ASA in DMPC and 5mol% ASA and 15mol% cholesterol in DMPC. The cartoons depict a top view of the in-plane structure (see Figure 1 c)) as determined from an analysis of the Bragg peaks along the in-plane axis, $q_{||}$.
doi:10.1371/journal.pone.0034357.g002

Out-of-plane structure and electron densities

The d_z-spacing between two neighboring membranes in the stack can be determined from the distance between the well developed Bragg reflections ($d_z = 2\pi/\Delta q_z$) along the out-of-plane axis, q_z. The integrated intensity of these peaks is used to calculate the electron density profile perpendicular to the bilayers following Equation (3). Figure 4 b) shows typical out-of-plane data taking Sample 3 containing 5mol% ASA as an example. Seven pronounced Bragg peaks are observed. The d_z for this sample was determined to be 55.3 Å. Out-of-plane scans were measured for all samples in order to calculate the electron density profiles.

Figures 4 a) and c) display $T(q_z)$ and relative electron densities as determined using Equations (4) and (3) for Samples 1, 2, 3, and 11 (100 mol% DMPC, 1 mol% ASA, 5 mol% ASA, and 5 mol% ASA with 15 mol% cholesterol). Up to 10 Bragg orders were observed. $T(q_z)$ was fit to the experimentally determined peak intensities using Equation (4) to determine an array of phases v_n out of the corresponding 2^{10} combinations of ± 1. Figure 4 b) shows the best fits for all samples. All samples were well fit by the phase array $[\bar{1}11\bar{1}1\bar{1}1\bar{1}1]$. The corresponding relative electron densities in Figure 4b) show well developed features, which allow the determination of molecular positions in the membranes, as will be discussed below.

Discussion

The in-plane structure of the multi-component membranes was determined from the 2D measurements in Figure 2 and the analysis in Figure 3. Ordering of the molecular sub-lattices of lipid head groups, tails, and ASA molecules was observed by analyzing the corresponding sets of Bragg peaks. While the DMPC lipids showed ordered head group and tail structures in the pure lipid membranes, small amounts of ASA were found to lead to a suppression of long-range order and a more fluid-like structure of the bilayers. 50mol% ASA was determined to be the solubility limit of ASA in saturated lipid bilayers resulting in a non-physiological 2D crystal-like state. At this concentration, each lipid molecule "hosts" one ASA molecule. As a special case, addition of 20mol% ASA (a 1:5 ratio between ASA and lipid molecules) resulted in an ordered state of the head groups, as observed in the in-plane structure in Figure 2 c), while the tails still showed a fluid-like state with a high degree of positional disorder. This observation lead us to conclude that the ASA molecules preferably interact with lipid head groups and may, therefore, be located in the lipid head group region.

Lipid areas for all samples were determined from the in-plane scattering (see Table 1). The area that we determine for the pure DMPC sample can be compared to results published by Tristram-Nagle, Liu, Legleiter and Nagle [9], who provided a reference for

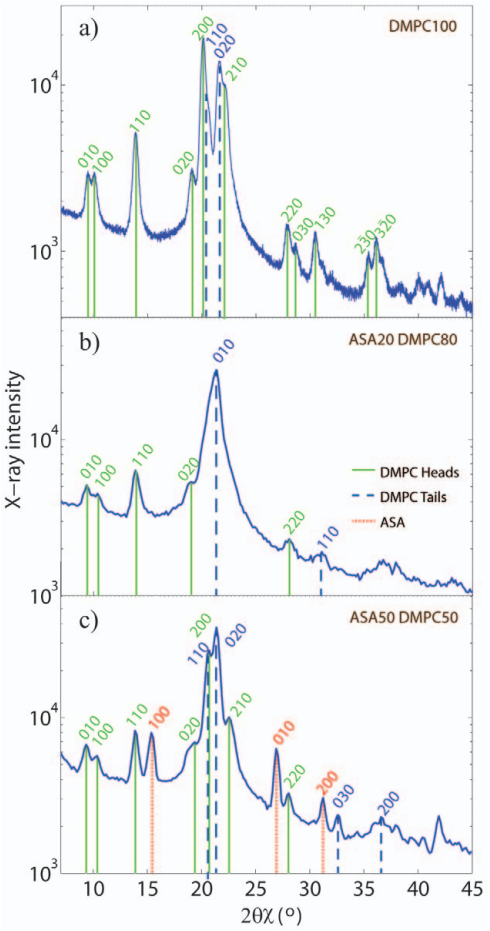

Figure 3. In-plane scattering integrations and fits. In-plane scattering of the Samples 1, 6 and 10. Slices 0.03 Å^{-1} < q_z < 0.3 Å^{-1} were integrated to increase the statistics and enhance the data quality. Bragg peaks assigned to lipid head groups are plotted in green, lipid tails in blue, and ASA in red. a) 100% DMPC: data are described by an orthorhombic unit cell for the head groups and a monoclinic tail unit cell. b) The 20mol% ASA sample shows an ordered head group lattice, and a disordered, hexagonal tail lattice. c) Ordered structures for head groups (orthorhombic), tails (monoclinic) and ASA molecules (orthorhombic) are found for 50mol% ASA.
doi:10.1371/journal.pone.0034357.g003

the structure of gel phase DMPC membranes. The authors find an area per lipid of ~47 Å^2 in fully hydrated bilayers at T = 10°C. The membranes in our study were measured at T = 20°C, however, significantly de-hydrated to 50% RH to enhance structural features. We note that the x-ray scans in Figure 2 show significantly more features as compared to the data observed by Tristram-Nagle *et al.* We determine lipid areas of ~41 Å^2. Dehydration obviously leads to a more closely packed lipid structure. An interesting observation is the fact that the area per lipid is almost constant for all ASA concentrations. It seems that the ASA molecules fill existing voids in the head group structure and do not increase the area per lipid (within the resolution of this experiment). This observation may be relevant to understand the physiological functioning of ASA. Changing the area per lipid changes important material properties of the membranes, such as permeability and elasticity. Future experiments will, therefore, determine structure of membranes containing ASA in fully hydrated gel and fluid phase membranes to elucidate this point in physiologically more relevant systems.

The position of the ASA molecule in the bilayer can be determined from electron density profiles. ρ_z of pure DMPC (Sample 1), 1mol% ASA (Sample 2), 5mol% ASA (Sample 3), and 5mol% ASA/15mol% cholesterol (Sample 11) are shown in Figure 4. In order to put ρ_z on an absolute scale, the electron densities were scaled to fulfil the condition $\rho(0) = 0.22$ e/Å^3 (the electron density of a CH_3 group) in the center of the bilayer, and $\rho(d_z/2) = 0.33$ e/Å^3 (the electron density of water, ρ_W) outside the bilayers. The electron density profile for DMPC (Sample 1) is depicted in Figure 5 a). The profile corresponds to a DMPC molecule in the well ordered gel state with both chains in all-trans configuration, as has been reported previously from [9]. The electron rich phosphorous group in the head group region can be identified by the peak in the electron density at ~22 Å. ρ_z monotonically decreases towards the bilayer center at $z = 0$; only CH_3 groups are found in the center.

To determine the position of ASA and cholesterol molecules in the bilayers, the electron densities of samples of different composition were compared. The electron densities for membranes containing 1mol% ASA and 5mol% ASA are depicted in Figure 5 b). Because both samples show a disordered scattering pattern, differences in the two electron densities should be directly related to the increased ASA content. The electron density in the 5mol% ASA was found to be increased in the head group region at z values of ~21 Å. As depicted in the Figure, an ASA molecule can be fitted at z values of 16 Å < z < 21 Å, with the hydrophilic, electron-richer oxygen groups at a z position of ~21 Å, pointing towards the hydration water. This orientation "protects" the hydrophobic part of the ASA molecule from the aqueous environment. The lower electron density towards the center of the bilayer most likely points to an increased disorder of the lipid tails in the 5mol% ASA sample, i.e., a higher number of gauche defects in the hydrocarbon chains. This conclusion is supported by the observation of a larger tilt angle of the lipid tails in the experiments, as listed in Table 1. The effect is qualitatively also visible in the 2D scans in Figure 2 a) and b), where the addition of 1mol% ASA suppresses long-range order of lipid head groups and tails and results in a disordered, more fluid state of the bilayers with a small d_z spacing.

A membrane containing ASA and cholesterol was included in the series (Sample 11) to study the possible interaction between the two molecules. The electron densities of Samples 3 (5mol% ASA) and 11 (5mol% ASA and 15mol% cholesterol) are shown in Figure 5 c). From the 2D scan in Figure 2 f) it can be concluded that this mixture still forms a homogenous multi lamellar structure and that cholesterol and ASA molecules co-exist in saturated lipid bilayers. By comparing the electron densities of Sample 3 and Sample 11 the position of the cholesterol molecule can be estimated. The electron density in the head group region is found to be lower when cholesterol is present as additional cholesterol acts as a spacer in chain region which dilutes the densities in head group region. The cholesterol ring structures lead to a slight increase in ρ_z at z values of ~12 Å, while the electron density in the cholesterol sample starts to be lower below 8 Å as it has only one tail, as compared to two DMPC tails. We conclude that cholesterol takes an upright position also in the presence of ASA

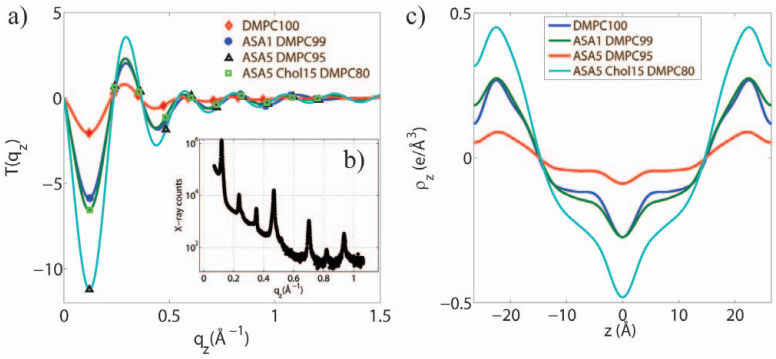

Figure 4. Electron density profile process. $T(q_z)$ (a) and calculated relative electron density profiles ρ_z (c) for 100% DMPC, 1mol% ASA, 5mol% ASA, and 5mol% ASA 15mol% cholesterol. The phases, v_n, are determined by the sign of $T(q_z)$ at the particular q_z-value. b) Out-of-plane scattering of the 5mol% ASA sample as an example. Seven pronounced Bragg peaks are visible.
doi:10.1371/journal.pone.0034357.g004

molecules, with the hydrophilic head pointing towards the aqueous environment. This upright position and orientation has been reported previously for cholesterol in saturated phospholipid bilayers made of DMPC and DPPC. The electron densities in Figure 5 c) definitely exclude that the cholesterol molecules take a flat position between the two leaflets, as it was reported recently for highly unsaturated lipid bilayers [16,17]. While the cholesterol takes an upright position in the hydrophobic membrane core parallel to the lipid tails, the ASA molecules preferably reside in the head group region. Due to their position in the lipid membrane, the two molecules can be expected to have a different impact on membrane properties: while cholesterol is known to reduce permeability and increase membrane rigidity, ASA may enhance permeability and make membranes more fluid and flexible.

In summary, we determined the in-plane and out-of-plane structure of highly oriented, solid supported membranes containing up to 50mol% of Aspirin (acetylsalicylic acid, ASA) using x-ray diffraction. All membranes were in a low-hydration (50% RH) gel phase to enhance structural features in the scattering experiment. We present direct experimental proof that the ASA molecules participate in saturated phospholipid membranes. The molecules were found to reside in the lipid head group region. The presence of the ASA molecule has a distinct effect on the in-plane structure of the membranes: while pure DMPC bilayers form highly ordered head group and tail lattices, addition of 1mol% ASA suppresses long-range order and results in a disordered, fluid-like state. The maximum solubility of ASA in saturated lipid membranes was found to be 50mol%, which results in a structure where each lipid molecule "hosts" one ASA molecule. At an ASA/lipid ratio of 1:5

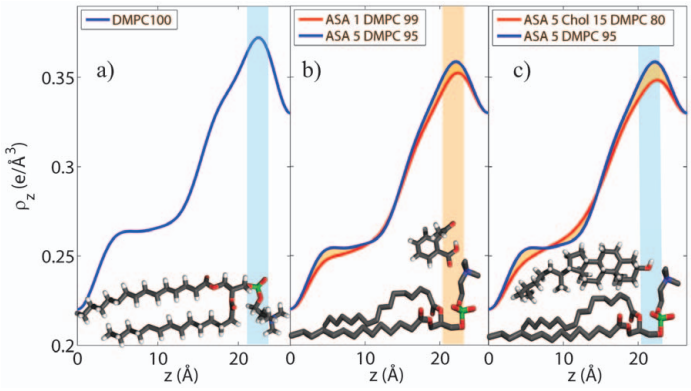

Figure 5. Normalized electron density profiles. a) Electron density profile of Sample 1 (100% DMPC) . b) The position of the ASA molecule can be determined from the electron densities of Sample 2 (1mol% ASA) and Sample 3 (5mol% ASA). The ASA molecule can be placed in the head group region of the bilayer, at z values of 16 Å$<z<$21 Å, with the hydrophilic oxygen groups at a z position of $\sim$21 Å, pointing towards the hydration water. c) By comparing electron densities of Sample 3 and Sample 11 the position of the cholesterol molecule can be determined. Cholesterol and ASA molecules co-exist in saturated lipid bilayers and cholesterol most likely takes an upright position with the hydrophilic head pointing towards the aqueous environment. DMPC, ASA and cholesterol molecules are drawn to visualize the most likely positions and orientations.
doi:10.1371/journal.pone.0034357.g005

(20mol% ASA) we observe positional order between the lipid head groups, while the lipid tails are still in a fluid-like state.

ASA and cholesterol molecules were found to co-exist in saturated lipid bilayers. As in saturated bilayers without ASA, cholesterol was determined to take an upright position. Our findings may be relevant to better understand the physiological function of Aspirin on a molecular level and for instance develop molecular models for the so-called "low-dose aspirin therapy". The technique presented in this paper can in the future also be used to study the interaction of highly topical drugs with artificial membranes mimicking certain types of tissue, such as brain or muscle tissue.

Author Contributions

Conceived and designed the experiments: MCR. Performed the experiments: MAB SZ GR RJA RKRB CH. Analyzed the data: MAB NK MCR. Contributed reagents/materials/analysis tools: MAB SZ GR RJA RKRB CH. Wrote the paper: MAB MCR.

References

1. Seddon AM, Casey D, Law RV, Gee A, Templer RH, et al. (2009) Drug interactions with lipid membranes. Chem Soc Rev 38: 2509–2519.
2. Casal H, Martin A, Mantsch H (1987) Infrared spectroscopic characterization of the interaction of lipid bilayers with phenol, salicylic acid and o-acetylsalicylic acid. Chemistry and Physics of Lipids 43: 47–53.
3. Vandenberg ET, Bertilsson L, Liedberg B, Uvdal K, Erlandsson R, et al. (1991) Structure of 3-aminopropyl triethoxy silane on silicon oxide. Journal of Colloid and Interface Science 147: 103–118.
4. Meyer HW, Semmler K, Rettig W, Pohle W, Ulrich AS, et al. (2000) Hydration of DMPC and DPPC at 4oc produces a novel subgel phase with convex-concave bilayer curvatures. Chem Phys Lip 105: 149–166.
5. Nomura K, Lintuluoto M, Morigaki K (2011) Hydration and temperature dependence of (13)C and (1)H nmr spectra of the dmpc phospholipid membrane and complete resonance assignment of its crystalline state. The Journal of Physical Chemistry B 115: 14991–5001.
6. de Meyer FJM, Benjamini A, Rodgers JM, Misteli Y, Smit B (2010) Molecular simulation of the dmpc-cholesterol phase diagram. The Journal of Physical Chemistry B 114: 10451–10461.
7. Pabst G, Kučerka N, Nieh MP, Rheinstädter M, Katsaras J (2010) Applications of neutron and x-ray scattering to the study of biologically relevant model membranes. Chemistry and Physics of Lipids 163: 460–479.
8. Fragneto G, Rheinstädter M (2007) Structural and dynamical studies from biomimetic systems: an overview. Comptes Rendus Physique 8: 865–883.
9. Tristram-Nagle S, Liu Y, Legleiter J, Nagle JF (2002) Structure of gel phase dmpc determined by x-ray diffraction. Biophysical Journal 83: 3324–3335.
10. Nagle JF, Wiener MC (1989) Relations for lipid bilayers. Biophys J 55: 309–313.
11. Nagle J, Zhang R, Tristram-Nagle S, Sun W, Petrache H, et al. (1996) X-ray structure determination of fully hydrated lα phase dipalmitoylphosphatidylcholine bilayers. Biophys J 70: 1419–1431.
12. King GI, Worthington CR (1971) Analytic continuation as a method of phase determination. Physics Letters 35A: 259–260.
13. Adachi T (2000) A new method for determining the phase in the x-ray diffraction structure analysis of phosphatidylcholine:alcohol. Chemistry and Physics of Lipids 107: 9397.
14. Katsaras J, Raghunathan VA, Dufourc EJ, Dufourcq J (1995) Evidence for a two-dimensional molecular lattice in subgel phase dppc bilayers. Biochemistry 34: 4684–4688.
15. Raghunathan VA, Katsaras J (1995) Structure of the L'_c phase in a hydrated lipid multilamellar system. Phys Rev Lett 74: 4456–4459.
16. Kučerka N, Marquardt D, Harroun T, Nieh MP, Wassall S, et al. (2009) The functional significance of lipid diversity: Orientation of cholesterol in bilayers is determined by lipid species. J Am Chem Soc 131: 16358.
17. Kučerka N, Marquardt D, Harroun T, Nieh MP, Wassall S, et al. (2010) Cholesterol in bilayers with pufa chains: Doping with dmpc or popc results in sterol reorientation and membrane-domain formation. Biochemistry 49: 7485.

Preface to Paper III

The following paper examines the interaction of cholesterol molecules with a DMPC lipid bilayer. Samples were prepared with 0% cholesterol (100 mol% DMPC) up to 60 mol% cholesterol. These samples were scanned using BLADE. We observed the in-plane and out-of-plane structural organization of the cholesterol and the lipids and have developed a model describing the saturation of cholesterol in a lipid membrane. It was shown that the DMPC bilayer can host up to 40 mol% cholesterol, and after this point it exhibits an ordered, crystal-like state. This observation sheds some light on the currently proposed lipid-cholesterol "umbrella model". This model would result in a saturation occurring at either 1:1 ratio of cholesterol to lipid, or 1:3, neither of these are seen.

The samples were made and scanned by Songbo Zheng, Nicholas Jago, Michael Moore, Richard Alsop and myself. I performed the data analysis, using much of the same code as was used for the ASA paper. Clare Armstrong developed visualizations for our paper. An-Chang Shi helped with the development of the theroetical interpretation of our system. The experiment was conceived and developed by Maikel Rheinstädter, who also wrote the paper. The paper is still in a draft state as of June 30, 2012 and will be submitted in the following weeks.

Solubility and lateral molecular order in membranes containing cholesterol

Matthew A. Barrett,[1] Songbo Zheng,[1] Richard J. Alsop,[1] Hannah Dies,[1] Aili Wang,[1] Nicholas Jago,[1] Michael Moore,[1] Clare L. Armstrong,[1] An-Chang Shi,[1] and Maikel C. Rheinstädter[1,2,*]

[1] *Department of Physics and Astronomy, McMaster University, Hamilton, ON, Canada*
[2] *Canadian Neutron Beam Centre, National Research Council Canada, Chalk River, ON, Canada*

(Dated: June 30, 2012)

Cholesterol molecules were introduced to multi-lamella DMPC lipid bilayer stacks in concentrations from 0mol% cholesterol to 60mol% cholesterol. Using in-plane and out-of-plane x-ray scattering the reciprocal space maps of each of these samples was obtained - providing insight into the structrual order of cholesterol and DMPC molecules in their gel (L_β) phase. From the analysis of these samples, it was shown that cholesterol exhibits a solubility limit of ∼38 %.

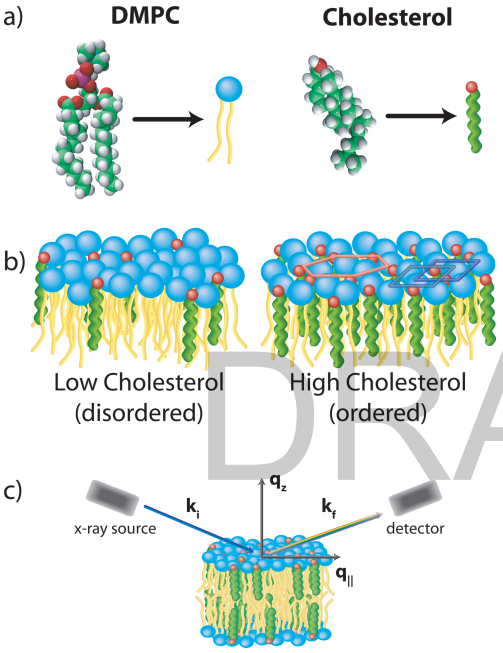

FIG. 1: a) Schematic representations of DMPC and cholesterol molecules. b) Possible model of the lipid arrangement in the presence of low and high cholesterol concentration phases present In DMPC systems with low cholesterol concentration, the lipids and cholesterol assume a disordered state. Once a critical level of cholesterol is present (∼ 40%), The cholesterol forms a sub-lattice, driving the lipids into a more well ordered arrangement. c) Schematic diagram of the x-ray scattering experiment.

Highly oriented multi lamellar membranes were prepared on single-side polished silicon wafers. 1,2-dimyristoyl-sn-glycero-3-phosphocholine (DMPC), and cholesterol (depicted in Figure 1 a)) were mixed in different ratios and dissolved in a 1:1 chloroform/2,2,2-trifluoroethanol (TFE) solution at a concentration of 15 mg/ml. The detailed sample preparation protocol is given in the Supplementary Material. Table I lists all samples prepared for this study.

Out-of-plane and in-plane x-ray scattering data was obtained using the Biological Large Angle Diffraction Experiment (BLADE) in the Laboratory for Membrane and Protein Dynamics at McMaster University. BLADE uses a 9 kW (45 kV, 200 mA) CuKα rotating anode at a wavelength of 1.5418 Å. Both source and detector are mounted on movable arms such that the membranes stay horizontal during the measurements. Focussing multi-layer optics provides a high intensity parallel beam with monochromatic x-ray intensities up to 10^{10} counts/(s×mm^2). This beam geometry provides optimal illumination of the solid supported membrane samples to maximize the scattering signal. All data were obtained in grazing incidence, small and wide angle scattering geometry. A sketch of the scattering geometry is shown in Figure 1 c). By using highly oriented membrane stacks, the in-plane ($q_{||}$) and out-of-plane (q_z) structure of the membranes can be determined. From the high resolution x-ray diffraction experiments we determine the molecular structure of the membranes in two different ways: (1) the out-of-plane membrane structure to determine the location of the different molecules in the membrane with sub-nanometer resolution and (2) the lateral organization of the different molecular components in the plane of the membrane. The result of such an x-ray experiment is a 2D intensity map of a large area (0.03 Å^{-1} < q_z <1.1 Å^{-1} and 0 Å^{-1} < $q_{||}$ <3.1 Å^{-1}) of the reciprocal space. This information is used to develop the molecular structure of the membrane samples. All scans were measured at 20°C and 50% hydration, in the gel (L_β) phase of the bilayers [1, 2]. Structural features are more pronounced in dry samples as fluctuations, which lead to attenuation and smearing of Bragg peaks, are strongly suppressed. The measurement of high-order Bragg peaks results in a high spatial resolution, as will be shown below.

Figure 2 displays 2D x-ray intensity maps for Samples 1, 2, 5, 8, 9 and 11. The arrangement of the different molecular components in the plane of the membranes

Sample	DMPC (mol%)	Cholesterol (mol%)	Unit Cell	area per lipid (Å^2)	d_H (Å)	d_z (Å)
1	100	0	head-groups: a_H=8.77 Å, b_H=9.31 Å, γ_H=90°, lipid tails: a_T=4.97 Å, b_T=8.25 Å, γ_T=94.18 °	40.84 ± 0.1	44.9	55.3
2	98	2	lipid tails: a_T=4.25 Å, γ_T=120°	41.8 ± 0.4	45.2	53.2
3	97	3	lipid tails: a_T=4.25 Å, γ_T=120°	41.8 ± 0.4	-	54.0
4	90	10	lipid tails: a_T=4.28 Å, γ_T=120°	42.3 ± 0.6	46.6	53.0
5	80	20	lipid tails: a_T=4.34 Å, γ_T=120°	43.5 ± 0.8	44.6	52.1
6	70	30	lipid tails: a_T=4.43 Å, γ_T=120°	45.4 ± 0.9	44.7	51.0
7	65	35	lipid tails: a_T=4.49 Å, γ_T=120°	46.5 ± 1.0	45.3	49.1
8	62.5	37.5	lipid tails: a_T=4.55 Å, γ_T=120°	47.8 ± 1.1	45.1	49.1
9	60	40	head-groups: a_H=8.6 Å, b_H=8.1 Å, γ_H=90°, lipid tails: a_T=7.1 Å, b_T=4.9 Å, γ_T=90°, Cholesterol: a_C=6.7 Å, b_A=4.55 Å, γ_A=120°	34.8 ± 0.1	44.0	50.5
10	55	45	head-groups: a_H=8.5 Å, b_H=8.2 Å, γ_H=90°, lipid tails: a_T=7.1 Å, b_T=4.9 Å, γ_T=90°, Cholesterol: a_C=6.8 Å, b_A=4.55 Å, γ_A=120°	34.8 ± 0.1	-	50.7
11	50	50	head-groups: a_H=8.4 Å, b_H=8.3 Å, γ_H=90°, lipid tails: a_T=8.0 Å, b_T=4.75 Å, γ_T=90°, Cholesterol: a_C=7.0 Å, b_A=4.55 Å, γ_A=120°	38.0 ± 0.1	-	50.7
12	45	55	head-groups: a_H=8.4 Å, b_H=8.3 Å, γ_H=90°, lipid tails: a_T=8.0 Å, b_T=4.9 Å, γ_T=90°, Cholesterol: a_C=7.0 Å, b_A=4.55 Å, γ_A=120°	39.2 ± 0.1	-	51.0
13	40	60	head-groups: a_H=8.4 Å, b_H=8.2 Å, γ_H=90°, lipid tails: a_T=8.1 Å, b_T=4.8 Å, γ_T=90°, Cholesterol: a_C=7.0 Å, b_A=4.55 Å, γ_A=120°	38.8 ± 0.1	-	52.0

TABLE I: List of all the samples prepared for this study, and their molecular composition. Unit cell dimensions, areas per lipid, lipid tilt angles, and d_z spacings are also given. Details are given in the text.

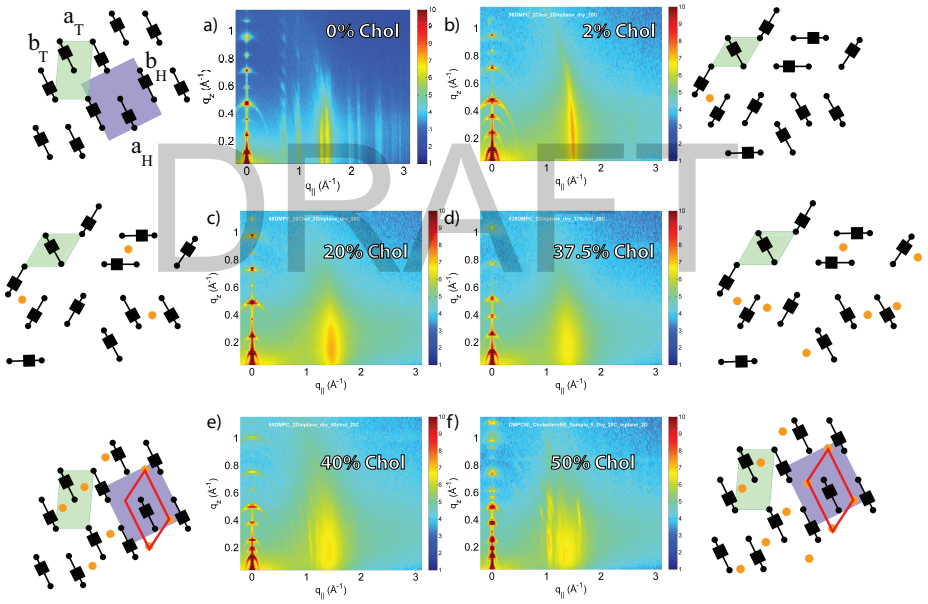

FIG. 2: 2D X-ray intensity maps of samples 1, 2, 5, 8, 9 and 11.(Pure DMPC, 2% cholesterol, 20% cholesterol, 37.5% cholesterol, 40% cholesterol, 50% cholesterol.) The cartoons next to each recpiroical space map depict the overhead (in-plane) view of the cholsetol and lipid molecules in the lattice. This data is determined from analysis of Bragg peaks along the $q_{||}$ axis.

can be determined from the the in-plane scattering along $q_{||}$. As introduced by Katsaras and Raghunathan [3, 4], different molecular components, such as lipid tails, lipid head groups and cholesterol molecules, can form molecular sub-lattices in the plane of the membrane leading to non-overlapping sets of Bragg peaks.

The 100% DMPC sample (Sample 1) in Figure 2 a) shows a number of well developed in-plane Bragg peaks along the $q_{||}$-axis. The diffracted intensity has a distinct rod-like shape, typical for a 2D system. The out-of-plane scattering along q_z shows pronounced and equally spaced Bragg intensities due to the multi lamellar structure of the membrane sample.

Some qualitative conclusions can be drawn from the 2D data. The pattern changes by addition of 2mol% cholesterol (Figure 2 b)): the in-plane scattering shows one pronounced feature, only. Fewer Bragg peaks point to a short-ranged ordered, more fluid-like structure. Higher concentrated samples, such as 37.5mol% in Figure 2 d) appear to be disordered until an ordered pattern is observed at a concentration of 40mol% cholesterol (Figure 2 e)). The data in Figure 2 cover a large area of reciprocal space and are important to develop the molecular structure of the membrane systems. They are in particular important to detect or exclude structural features with mixed in-plane and out-of-plane properties, such as molecular tilts, which would have $q_{||}$ and q_z components. The cartoons next to the data in Figure 2 display the corresponding molecular structure, as determined from the analysis below.

To determine the in-plane structure, data were cut along the $q_{||}$-axis. Slices 0.03 Å$^{-1} < q_z < 0.3$ Å^{-1} were integrated to enhance the data quality. The results for Sample 1 are shown in Figure 2 a). As depicted in the cartoon to Figure 2 a), the Bragg peaks were assigned to two different molecular lattices, the lipid head groups and the lipid tails. As discussed in detail in [3–5] the Bragg peaks in the pure lipid sample can be indexed by an orthorhombic head group lattice (planar space group p2) and a monoclinic unit cell for the lipid tails. The positions of the corresponding Bragg peaks are superimposed with the data in Figure 3 a) and show an excellent agreement. The molecular structure is shown in the cartoon to Figure 2 a) and the two units cells are drawn. The orthorhombic unit cell of the head group lattice contains two lipid molecules and has an area of $A_H = a_H b_H$=81.69 Å^2. The area per lipid can also be determined from the unit cell of the tails, which contains one lipid molecule, to $A_T = a_T b_T \sin\gamma_T$=40.84 Å^2.

Only one peak is observed at 2mol% cholesterol in Figure 2 b). Even at this relatively low concentration (ASA:lipids=1:50) the presence of the cholesterol molecules inhibits long-range order of the lipid head groups or tails as evidenced by the absence of Bragg peaks belonging to head or tail unit cells. From the data in Figure 2 it can be concluded that the lattices belonging to head groups and cholesterol molecules have a high degree of positional disorder. In the case of cholesterol this is most likely the result of a stochastic distribution of the cholesterol molecules in the bilayer. The area per lipid can be determined when assuming that the lipid tails form a densely packed structure with hexagonal symmetry (planar group p6). The lipid area can then be determined from the distance between two head groups respective two lipids tails on a hexagonal lattice to $A_L = 4a_T^2/\sqrt{3}$. As the average distance between two tails is determined by the position, q_T, of the correlation peak to $a_T = 2\pi/q_T$, the area per lipid is determined to $A_L = 16\pi^2/\sqrt{3}q_T^2$=?? Å^2. The corresponding unit cell parameters and areas per lipid are given in Table I; the hexagonal unit cell is also drawn in the cartoon to Figure 2 b), where the molecular structure is sketched.

Higher concentrated samples (Samples 9-13) showed a disordered membrane structure with only the lipid correlation peak; 37.5mol% is shown as an example in Figure 2 d). Several Bragg peaks are observed at a high cholesterol concentration of 40mol% in Figure 2 e). The Bragg peaks can be assigned to the ordering of the lipid tails and the lipid head groups. We find additional peaks in the patterns in Figure 3 that we assign to ordering of the cholesterol molecules. Orthorhombic unit cells for head groups and cholesterol molecules, and a monoclinic cell for the lipid tails were determined. In this structure, each lipid molecule "hosts" one cholesterol molecule. While 37.5mol% cholesterol can still be dissolved in the DMPC bilayer, 40mol% ASA leads to a non-physiological, highly ordered state, which clearly marks the solubility limit of cholesterol in saturated phospholipid bilayers. The unit cell dimensions, lipid areas and lipid tilt for all samples are given in Table I; the corresponding molecular structures and unit cells are sketched in the cartoons in Figure 2. The area per lipid, as determined from the unit cell parameters is shown in Figure 4.

The in-plane structure of the multi-component membranes was determined from the 2D measurements in Figure 2 and the analysis in Figure 3. Ordering of the molecular sub-lattices of lipid head groups, tails, and cholesterol molecules was observed by analyzing the corresponding sets of Bragg peaks. While the DMPC lipids showed ordered head group and tail structures in the pure lipid membranes, small amounts of cholesterol were found to lead to a suppression of long-range order and a more fluid-like structure of the bilayers. 40mol% ASA was determined to be the solubility limit of cholesterol in saturated lipid bilayers resulting in a non-physiological 2D crystal-like state. At this concentration, each lipid molecule "hosts" one cholesterol molecule.

Lipid areas for all samples were determined from the in-plane scattering (see Table I). The area that we determine for the pure DMPC sample can be compared to results published by Tristram-Nagle, Liu, Legleiter and Nagle [6], who provided a reference for the structure of the gel phase in DMPC membranes. The authors find an area per lipid of ∼47 Å^2 in fully hydrated bilayers at T=10°C. The membranes in our study were measured at T=20°C, however, significantly de-hydrated to 50% RH to enhance structural features. We note that the x-ray scans in Figure 2 show significantly more features

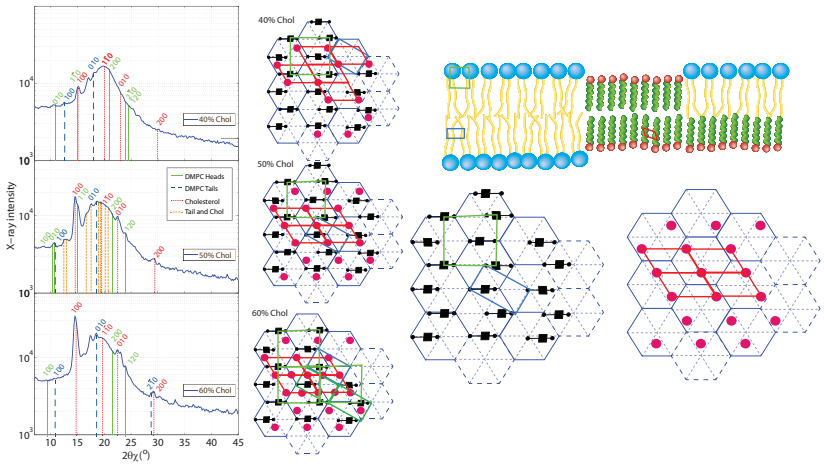

FIG. 3: In plane scattering of samples 9, 11, 13 (40%, 50% and 60% cholestrol in DMPC). Slices from the reciprocal space maps from 0.03 $\AA^{-1} < q_z < 0.3\ \AA^{-1}$ were integrated to increase statistics and enhance data quality. DMPC head group Bragg peaks are shown in green, DMPC tails in blue and cholesterol in red. The head groups in all cases are defined by orthorhombic unit cells, tails and cholesterol are monoclinic. These are fit to scale in the overhead lattice arrangements seen on the right. Notice as the percentage of cholesterol increases through samples the 100, 010 and 200 peaks become more pronounced. To account for peaks between 15 and 25^o in $2\theta_\chi$ which are not described by the unit cells coordination cells were fit between cholesterol and tail groups.

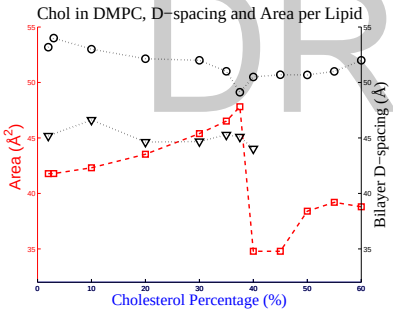

FIG. 4: Area of each lipid tail unit cell and d-spacing of our lipid bilayer with cholesterol. The data from table one was used to plot the area per lipid and d-spacing as cholesterol was introduced. The area increases as cholesterol is added until ∼38% cholesterol. At this percentage, it appears as if the lipid tails become ordered and leave the fluid phase. This is clear from Figure 2 as well, instead of one broad disordered Bragg peak at $q_{||}$ 1.5 $\AA^{-1}$ for 40% cholesterol many structural Bragg peaks are present. The d-spacing behaves in an opposite manner, as cholesterol is added, the bilayer decreases in height until ∼38%, where some sort of order causes the opposite effect.

as compared to the data observed by Tristram-Nagle *et al.* We determine lipid areas of ∼41 Å^2. De-hydration obviously leads to a more closely packed lipid structure. The area per lipid increases with increasing cholesterol content and shows an almost critical-like behavior.

We determined the in-plane and out-of-plane structure of highly oriented, solid supported membranes containing up to 60mol% of cholesterol using x-ray diffraction. All membranes were in a low-hydration (50% RH) gel phase to enhance structural features in the scattering experiment. We present direct experimental proof that the cholesterol molecules participate in saturated phospholipid membranes. The solubility limit of cholesterol in the saturated lipid bilayer was ∼38%, as above this limit, the lipid and cholesterol molecules formed highly ordered structures, indicating a crystalline state.

This research was funded by the Natural Sciences and Engineering Research Council of Canada (NSERC), the National Research Council Canada (NRC), the Canada Foundation for Innovation (CFI) and the Ontario Ministry of Economic Development and Innovation.

* rheinstadter@mcmaster.ca

[1] K. Nomura, M. Lintuluoto, and K. Morigaki, The Journal of Physical Chemistry B **115**, 14991 (2011).

[2] F. J.-M. de Meyer, A. Benjamini, J. M. Rodgers, Y. Misteli, and B. Smit, The Journal of Physical Chemistry B **114**, 10451 (2010).
[3] J. Katsaras, V. A. Raghunathan, E. J. Dufourc, and J. Dufourcq, Biochemistry **34**, 4684 (1995).
[4] V. A. Raghunathan and J. Katsaras, Phys. Rev. Lett. **74**, 4456 (1995).
[5] G. R. R. J. A. R. K. R. B. C. H. N. K. a. Matthew Barrett, Songbo Zheng, PLoS ONE **7**, 3457 (2012).
[6] S. Tristram-Nagle, Y. Liu, J. Legleiter, and J. F. Nagle, Biophysical Journal **83**, 3324 (2002).
[7] E. T. Vandenberg, L. Bertilsson, B. Liedberg, K. Uvdal, R. Erlandsson, H. Elwing, and I. Lundström, Journal of Colloid and Interface Science **147**, 103 (1991).
[8] H. W. Meyer, K. Semmler, W. Rettig, W. Pohle, A. S. Ulrich, S. Grage, C. Selle, and P. J. Quinn, Chem. Phys. Lip. **105**, 149 (2000).
[9] G. Pabst, N. Kučerka, M.-P. Nieh, M. Rheinstädter, and J. Katsaras, Chemistry and Physics of Lipids **163**, 460 (2010).
[10] G. Fragneto and M. Rheinstädter, Comptes Rendus Physique **8**, 865 (2007).
[11] J. F. Nagle and M. C. Wiener, Biophys. J. **55**, 309 (1989).
[12] J. Nagle, R. Zhang, S. Tristram-Nagle, W. Sun, H. Petrache, and R. Suter, Biophys. J. **70**, 1419 (1996).
[13] G. I. King and C. R. Worthington, Physics Letters **35A**, 259 (1971).
[14] T. Adachi, Chemistry and Physics of Lipids **107**, 9397 (2000).
[15] N. Kučerka, D. Marquardt, T. Harroun, M.-P. Nieh, S. Wassall, and J. Katsaras, J. Am. Chem. Soc. **131**, 16358 (2009).
[16] N. Kučerka, D. Marquardt, T. Harroun, M.-P. Nieh, S. Wassall, D. de Jong, L. Schäfer, S. Marrink, and J. Katsaras, Biochemistry **49**, 7485 (2010).

Supplementary Material

MATERIALS AND METHODS

Preparation of the Highly-Oriented Multi-Lamellar Membrane Samples

Highly oriented multi lamellar membranes were prepared on single-side polished silicon wafers. 100 mm diameter, 300 μm thick silicon (100) wafers were precut into 2×2 cm^2 chips. 1,2-dimyristoyl-sn-glycero-3-phosphocholine (DMPC), and cholesterol (depicted in Figure 1 a)) were mixed in different ratios and dissolved in a 1:1 chloroform/2,2,2-trifluoroethanol (TFE) solution at a concentration of 15 mg/ml. The lipid solution did not spread well on ultrasonic-cleaned wafers and de-wetted during drying. The silicon substrates were, therefore, cleaned in a piranha acid solution made of 98% concentrated H_2SO_4 and 30% concentrated H_2O_2 at a ratio of 3:1 by volume. Wafers were placed in this solution, covered with parafilm and heated to 298 K for 30 minutes. This treatment removes all organic contamination; however, it leaves the substrates in a hydrophilic state. We used silanization to cover the silicon surface through self-assembly with organo functional alkoxysilane molecules (APTES). The organic part of the APTES molecules was found to provide a perfect hydrophobic interface for the formation of the biological tissue. A 1% (by volume) solution of APTES and 99% ethanol was prepared. The wafers were immersed in the APTES solution and covered with parafilm, heated to 298 K and placed on a tilting incubator (20 speed, 3 tilt) for 12 hours. The tilting incubator creates a circular flow in the beaker to ensure an even APTES distribution and prevent buildup on the surface of the wafers. The wafers were then placed in a clean pyrex dish and annealed in vacuum at 388 K for 3 hours to create a uniform coverage of the APTES molecules on the surface [7]. Each wafer was thoroughly rinsed three times by alternating with ∼50 mL of ultrapure water and methanol. The tilting incubator was heated to 313 K and the lipid solution was placed inside to equilibrate. The wafers were rinsed in methanol, dried with nitrogen gas and placed in the incubator. 200 μL of lipid solution was applied on each wafer, and the wafers covered with a petri dish to let the solvent evaporate slowly to allow time for the membranes to form. Wafers were tilted during the drying process for 30 minutes (speed 15, tilt 1) such that the lipid solution spread evenly on the wafers. After drying, the samples were placed in vacuum at 313 K for 12 hours to remove all traces of the solvent. The bilayers were annealed and rehydrated before use in a saturated K_2SO_4 solution which provides ∼98% relative humidity (RH). The hydration container was allowed to equilibrate at 293 K in an incubator. The temperature of the incubator was then increased gradually from 293

K to 303 K over a period of ∼5 hours to slowly anneal the multi lamellar structure. This procedure results in highly oriented multi lamellar membrane stacks and a uniform coverage of the silicon substrates. About 3,000 highly oriented stacked membranes with a thickness of ∼10 μm are produced using this protocol. The samples were stored in a refrigerator at 5°C and heated to 55°C for 1 h before scanning to erase a possible thermal history. This procedure in particular destroys possible crystalline L_C or sub-gel phases that may form during storage at low temperatures and low hydration [8]. The high sample quality and high degree of order is necessary to determine in-plane and out-of-plane structure of the membranes and the position of the cholesterol molecules. Table I lists all samples prepared for this study.

X-ray Scattering Experiment

Out-Of-Plane Structure and Electron Densities

Specular reflectivity allows the determination of the structure and composition of membranes perpendicular to the plane of the membranes (see, e.g., [9, 10]). The intensity of the reflected beam as a function of the perpendicular momentum transfer, q_z, is given by:

$$R(q_z) = \frac{16\pi^2}{q_z^2} |\hat{\rho}(q_z)|^2 \qquad (1)$$

$\hat{\rho}(q_z)$ is the one-dimensional Fourier transform of the electron density $\rho(q_z)$, defined by:

$$\hat{\rho}(q_z) = \int_{-\infty}^{\infty} \exp(iq_z z)\rho(z)dz \qquad (2)$$

Because of the stacking of the membranes, i.e., the convolution with the lamellar structure factor, the Fourier transform is not continuous but discrete. The different Fourier components are observed in the experiment as the integrated intensities of the out-of-plane Bragg peaks. $\rho(z)$ is approximated by a 1D Fourier analysis [6]:

$$\begin{aligned} \rho(z) &= \rho_W + \frac{F(0)}{d_z} + \frac{2}{d_z}\sum_{n=1}^{N} F(q_n)\nu_n \cos(q_n z) \\ &= \rho_W + \frac{F(0)}{d_z} + \frac{2}{d_z}\sum_{n=1}^{N} \sqrt{I_n q_n}\nu_n \cos\left(\frac{2\pi n z}{d_z}\right) \end{aligned} \qquad (3)$$

N is the highest order of the Bragg peaks observed in the experiment and ρ_W the electron density of bulk water. The integrated peak intensities, I_n, are multiplied by q_n to receive the form factors, $F(q_n)$ [11, 12]. The bilayer form factor $F(q_z)$, which is in general a complex quantity, is real-valued in the case of centro-symmetry. The phase problem of crystallography, therefore, simplifies to the sign problem $F(q_z) = \pm|F(q_z)|$. and the phases, ν_n, can only take the values ±1. The phases ν_n are needed to reconstruct the electron density profile from the scattering data following Equation (3). When the membrane form factor $F(q_z)$ is measured at several q_z values, a continuous function, $T(q_z)$, which is proportional to $F(q_z)$, can be fitted to the data [11–14]:

$$T(q_z) = \sum_n \sqrt{I_n q_n}\mathrm{sinc}(\pi d_z q_z - \pi n). \qquad (4)$$

Once an analytical expression for $T(q_z)$ has been determined from fitting the experimental peak intensities, the phases ν_n can be determined from $T(q_z)$

Preface to Paper IV

This paper combines the experiments in Paper II and Paper III, essentially determining how a combination of ASA and cholesterol behave in a DMPC bilayer. By preparing samples from 0 to 40 mol% cholesterol and up to 12.5 mol% ASA we determine the area per lipid, membrane fluidity and the location of ASA and cholesterol molecules in the DMPC lipid bilayer. At high cholesterol and ASA concentration, ordered structures form, which is indicative of crystal-like membrane structure. ASA molecules tend to reside close to the hydrophilic head group of the membrane, closer to the center of the bilayer, and the cholesterol molecules nestle deeper in the bilayer, with the large tail groups occupying similar space as lipid's tail groups occupy. This information may be useful in developing a molecular model of low-dose Aspirin therapy, the daily introduction of a small amount of ASA to the body of patients at-risk of heart disease.

In this project, Richard Alsop was the primary investigator. My contribution included assisting in data analysis, using the Matlab reflectivity analysis macro, as well as discussions to determine the best PowderCell fits for in-plane analysis. This paper is still in draft form as of June 30th, 2012 and will be submitted in the following months.

A molecular approach to the Low-Dose-Aspirin-Therapy

Richard J. Alsop,[1] Matthew A. Barrett,[1] Songbo Zheng,[1] and Maikel C. Rheinstädter[1,2]

[1] *Department of Physics and Astronomy, McMaster University, Hamilton, ON, Canada*
[2] *Canadian Neutron Beam Centre, National Research Council Canada, Chalk River, ON, Canada*

(Dated: April 16, 2012)

We investigate the interaction between cholesterol and aspirin in lipid membranes. As shown recently [Barrett *et al.*, PLoS ONE, 2012] ASA and cholesterol molecules co-exist in saturated lipid bilayers. While the cholesterol molecules participate in the hydrophobic membrane core and align parallel to the lipid acyl tails, the ASA molecules were found to reside in the lipid head-group region. By using x-ray scattering we study the structure of lipid membranes containing between 0 and 40mol% cholesterol and up to 12.5mol% ASA. From these measurements we determine the area per lipid and the fluidity of the membranes. We find ordered, crystal-like structures at high cholesterol and ASA concentrations and determine molecular distances from the analysis of in-plane Bragg peaks. Our findings might be relevant to develop a molecular model for the Low-Dose-Aspirin-Therapy.

Introduction

The biological membrane is a complex structure, composed of various lipid species, sterols, proteins, and other small molecules. An important consequence arising from the complexity of the structure is fluidity [1]. By being fluid, the structure allows for vertical diffusion of small molecules and lateral diffusion of proteins [2]. Cholesterol, with its stiff hydrocarbon ring structure, is known to increase membrane rigidity and thus reduce fluidity. Cholesterol is therefore able to act as a physiological mediator of membrane fluidity. However, a high concentration of cholesterol often causes a disadvantageous decrease in fluidity, leading to reduced health of the individual. Possible effects of high cholesterol include high blood pressure, hypertension, and increased risk of myocardial events such as a heart attack.

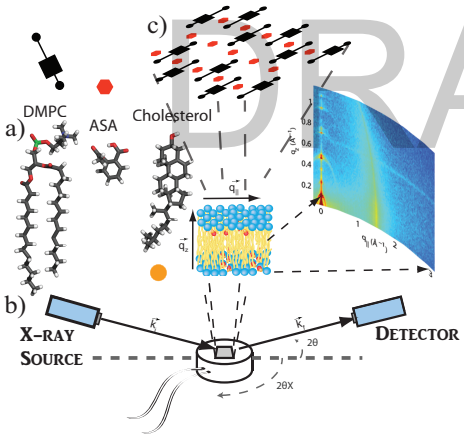

FIG. 1: **a) Lipid, ASA and cholesterol molecule.** b) Schematic diagram of the x-ray scattering experiment. The in-plane and out-of-plane structure of the membranes can be determined from the 2D intensity maps. Highly oriented multi lamellar membranes are used. 2θ and $2\theta\chi$ are the out-of-plane respective in-plane diffraction angles. c) Top view of the membrane to illustrate the molecular arrangement in the plane of the membrane. Lipids are depicted by a head-group (■) and two tails (•). ASA and cholesterol molecules are represented by a hexagon (●) and a circle (●), respectively.

Explaining and mitigating the adverse effects of cholesterol is a rich area. In particular, the field of membrane biophysics has proven effective in explaining and quantifying the effects of cholesterol in the context of model membrane systems. X-Ray and neutron scattering experiments have been able to probe the position of cholesterol within the membrane and quantify and understand the effects of cholesterol [3]. As well, biochemical and physiological studies have allowed for the discovery of many pharmaceuticals to specifically lower cholesterol levels, along with medications to reduce the symptoms and effects of high cholesterol. However, a common treatment for the primary and secondary prevention of myocardial events, in patients with high cholesterol, is the daily intake of the analgesic Aspirin (acetylsalicylic acid, ASA) as part of a regimen known as Low-Dose Aspirin Therapy [4–6].

The primary mechanism of the low-dose Aspirin therapy is believed to be through its anti-coagulant properties. The inhibition of COX-1 and COX-2 by higher dose Aspirin is understood to cause analgesic and anti-inflammatory effects, whereas lower doses, enough to inhibit COX-1 activity, are sufficient for anti-platelet activity [7, 8]. The anti platelet activity leads to reduced blood clot formation and hence reduced blockage of arteries and increased blood flow. However, a possible direct interplay between Aspirin and cholesterol within the membrane has not been studied. We recently demonstrated Aspirin, when introduced into model lipid membranes, resides within the phosphate head-groups due to its own hydrophilic chemistry, leading to an increase in fluidity of the membrane [9]. We present here an x-ray scattering study of the interplay between cholesterol and

ASA within model lipid membranes.

Lamellar stacks of bilayers containing ASA, cholesterol, and the saturated phospholipid dimyristoylphosphocholine (DMPC) were prepared. Samples contain up to 12.5mol% ASA and 40mol% cholesterol. We use 2D x-ray diffraction, covering large areas of reciprocal space, to probe the in-plane and out-of-plane structure of membranes in the gel (L_β) phase. From wide angle x-ray scattering experiments, the structures formed by lipid tails, lipid heads, cholesterol and ASA in-plane were determined for a range of membrane compositions.

Materials and Methods

Sample Preparation

Highly oriented multi lamellar membranes were prepared on single-side polished silicon wafers. 100 mm diameter, 300 μm thick silicon (100) wafers were precut into 2×2 cm^2 chips. 1,2-dimyristoyl-sn-glycero-3-phosphocholine (DMPC), acetylsalicylic acid (ASA) and cholesterol (as depicted in Figure 1) were mixed in different ratios and dissolved in a 1:1 chloroform/2,2,2-trifluoroethanol (TFE) solution at a concentration of 15 mg/ml. The lipid solution did not spread well on ultrasonic-cleaned wafers and de-wetted during drying. The silicon substrates were, therefore, cleaned in a piranha acid solution made of 98% concentrated H_2SO_4 and 30% concentrated H_2O_2 at a ratio of 3:1 by volume. Wafers were placed in this solution, covered with parafilm and heated to 298 K for 30 minutes. This treatment removes all organic contamination; however, it leaves the substrates in a hydrophilic state. We used silanization to cover the silicon surface through self-assembly with organo functional alkoxysilane molecules (APTES). The organic part of the APTES molecules was found to provide a perfect hydrophobic interface for the formation of the biological tissue. A 1% (by volume) solution of APTES and 99% ethanol was prepared. A 1 mL syringe was filled with 0.2 mL of dry nitrogen. This nitrogen was ejected into 99% APTES , and 0.2 mL of APTES is drawn into the syringe. This syringe is then submerged in 19.8 mL of ethanol before ejecting the APTES. This 20 mL APTES solution is sufficient to cover 10 wafers in an APTES monolayer. The wafers were immersed in the APTES solution and covered with parafilm, heated to 298 K and placed on a tilting incubator (20 speed, 3 tilt) for 12 hours. The tilting incubator creates a circular flow in the beaker to ensure an even APTES distribution and prevent buildup on the surface of the wafers. The wafers were then placed in a clean pyrex dish and annealed in vacuum at 388 K for 3 hours to create a uniform coverage of the APTES molecules on the surface [10]. Each wafer was thoroughly rinsed three times by alternating with ∼50 mL of ultrapure water and methanol. The methanol was cleaned using a 0.2 μm filter before use to avoid surface contamination. The tilting incubator was heated to 313 K and the lipid solution was placed inside to equilibrate. The wafers were rinsed in methanol, dried with nitrogen gas and placed in the incubator. 200 μL of lipid solution was applied on each wafer, and the wafers covered with a petri dish to let the solvent evaporate slowly to allow time for the membranes to form. Wafers were tilted during the drying process for 30 minutes (speed 15, tilt 1) such that the lipid solution spread evenly on the wafers. After drying, the samples were placed in vacuum at 313 K for 12 hours to remove all traces of the solvent. The bilayers were annealed and rehydrated before use in a saturated K_2SO_4 solution which provides ∼98% relative humidity (RH). The hydration container was allowed to equilibrate at 293 K in an incubator. The temperature of the incubator was then increased gradually from 293 K to 303 K over a period of ∼5 hours to slowly anneal the multi lamellar structure. This procedure results in highly oriented multi lamellar membrane stacks and a uniform coverage of the silicon substrates. About 3,000 highly oriented stacked membranes with a thickness of ∼10 μm are produced using this protocol. The samples were stored in a refrigerator at 5°C and heated to 55°C for 1 h before scanning to erase a possible thermal history. This procedure in particular destroys possible crystalline L_C or sub-gel phases that may form during storage at low temperatures and low hydration [11]. The high sample quality and high degree of order is a prerequisite to determine the in-plane structure of the membranes and the arrangement of cholesterol and ASA molecules.

Table I lists all samples prepared for this study.

X-ray scattering experiment

In-plane x-ray scattering data was obtained using the Biological Large Angle Diffraction Experiment (BLADE) in the Laboratory for Membrane and Protein Dynamics at McMaster University. BLADE uses a 9 kW (45 kV, 200 mA) CuKα rotating anode at a wavelength of 1.5418 Å. Both source and detector are mounted on movable arms such that the membranes stay horizontal during the measurements. Focussing multi-layer optics provides a high intensity parallel beam with monochromatic x-ray intensities up to 10^{10} counts/(s x mm^2). This beam geometry provides optimal illumination of the solid supported membrane samples to maximize the scattering signal. A sketch of the scattering geometry is shown in Figure 1. By using highly oriented membrane stacks, the in-plane ($q_{||}$) and out-of-plane (q_z) structure of the membranes can be determined. From the high resolution x-ray diffraction experiments we determine the lateral organization of the different molecular components in the plane of the membrane with sub-nanometer resolution, as sketched in Figure 1. The result of such an x-ray experiment is a 2D intensity map of a large area (0.03 $Å^{-1}$ < q_z <1.1 $Å^{-1}$ and 0 $Å^{-1}$ < $q_{||}$ <3.1 $Å^{-1}$) of the reciprocal space, as sketched in Figure 1. This information is used to develop the molecular structure

Sample	DMPC (mol%)	ASA (mol%)	cholesterol (mol%)	Unit Cell	area per lipid (Å^2)	lipid tilt (deg)	d_z-spacing (Å)
1	100	0	0	head-groups: a_H=8.773 Å, b_H=9.311 Å, γ_H=90°, lipid tails: a_T=4.966 Å, b_T=8.247 Å, γ_T=94.18 °	40.84 ± 0.1	6.5	55.3
2	80	0	20	a_T=4.36 Å,γ_H=120°	44 ± 1	6	50.1
3	70	0	30	a_T=4.42 Å,γ_H=120°	45.2 ± 2	6.5	49.36
4	60	0	40	head-groups: a_H=8.6 Å, b_H=8.1 Å, γ_H=90°, lipid tails: a_T=7.1 Å, b_T=4.9 Å, γ_T=90°, cholesterol: a_C=6.7 Å, b_C=4.55 Å, γ_C=120°	34.8 ± 1.5	6.7	45.92
5	95	5	0	a_T=4.21 Å,γ_H=120°	41 ± 1	8.0	55.3
6	80	5	15	a_T=4.24 Å,γ_H=120°	41.6 ± 1	3.5	49.1
7	65	5	30	a_T=4.42 Å,γ_H=120°	45.2 ± 1.5	6.03	48.89
8	55	5	40	head-groups: a_H=8.5 Å, b_H=8.5 Å, γ_H=90°, lipid tails: a_T=7.15 Å, b_T=5.02 Å, γ_T=90°, cholesterol: a_C=6.9 Å, b_C=4.55 Å, γ_C=120°	35.9 ± 1	6	44.77
9	90	10	0	a_T=4.21 Å,γ_H=120°	41 ± 1	6.8	53
10	75	10	15	a_T=4.26 Å,γ_H=120°	42 ± 1.5	7.7	51.55
11	60	10	30	a_T=4.39 Å,γ_H=120°	44.5 ± 2.5	6.9	44.5
12	50	10	40	head-groups: a_H=8.6 Å, b_H=8.1 Å, γ_H=90°, lipid tails: a_T=7.1 Å, b_T=4.95 Å, γ_T=90°, cholesterol: a_C=6.7 Å, b_C=4.55 Å, γ_C=120°	34.8 ± 3	6	47
13	62.5	7.5	30	a_T=4.46 Å,γ_H=120°	45.9 ± 1.5	6	50
14	57.5	12.5	30	a_T=4.49 Å,γ_H=120°	46.5 ± 1.5	5.3	50
15	52.5	7.5	40	head-groups: a_H=8.6 Å, b_H=8.1 Å, γ_H=90°, lipid tails: a_T=7.1 Å, b_T=4.9 Å, γ_T=90°, cholesterol: a_C=6.7 Å, b_C=4.55 Å, γ_C=120°	34.8 ± 1	5.8	44
16	47.5	12.5	40	head-groups: a_H=8.6 Å, b_H=8.1 Å, γ_H=90°, lipid tails: a_T=7.1 Å, b_T=4.9 Å, γ_T=90°, cholesterol: a_C=6.7 Å, b_C=4.55 Å, γ_C=120°	34.8 ± 1	5.8	44

TABLE I: List of all the samples prepared for this study, and their molecular composition. Unit cell dimensions, areas per lipid, lipid tilt angles, and d_z spacings are also given. Details are given in the text.

of the membrane samples. All scans were measured at 20°C and 50% RH, in the gel (L_β) phase of the bilayers [12, 13]. Structural features are more pronounced in dry samples as fluctuations, which lead to attenuation and smearing of Bragg peaks, are strongly suppressed. The measurement of high-order Bragg peaks results in a high spatial resolution, as will be shown below.

Results

To determine the orientation of the molecular components within the plane of the membrane, large areas of reciprocal space are sampled. 2D reciprocal space maps of selected samples are shown in Figure 2. The out-of-plane Bragg peaks along q_z are pronounced and equally spaced, indicating a lamellar structure. Bragg peaks observed along $q_{||}$ are indicative of order established in the plane of the membranes. As depicted in Figure 2 a) and in reference [9], a pure DMPC sample can find a free energy minimizing structure which displays large scale ordering. The in-plane peaks have a rod-like appearance, indicative of a 2D system. Through analysis of the peaks along $q_{||}$, we are able to determine unit cell parameters for lattices formed by the lipid head-groups and lipid tails by fitting the observed peak pattern to a theoretical model, as explained in more detail in [9]. The results are summarized in Table I.

Some quantitative conclusions can be drawn from the 2D intensity maps in Figure 2: While the pure DMPC membrane in Figure2 a) shows Bragg peaks due to the ordering of lipid head groups and tails, the introduction of small amounts of ASA or cholesterol proved enough to disturb the organization of the membrane, yielding a diffracted pattern with only one feature: a pronounced peak at $q_{||} \approx 1.5$ Å. The peak corresponds to short range order, described as a narrow range of nearest neighbour separations. The ASA or cholesterol are sparsely distributed within the plane of the membrane, and the tails take on a hexagonal structure. The 2D system can be described as more fluid, as the lipid tails and lipid head-groups are now permitted a greater number of configurations, compared to the ordered structure.

As we increase the concentration of cholesterol, this lipid peak begins to broaden. Cholesterol increases the area per lipid head-group for membranes in the gel phase, leading to skewing of the nearest neighbour peak towards lower $q_{||}$ values. Between 30mol% and 40mol% cholesterol, a phase transition is observed and distinct Bragg peaks associated with a higher order structure begin forming. The Bragg peaks correspond to an ordering of the lipid tails by the cholesterol molecules, and organization of cholesterol itself. The structure may be described by an orientation of the lipid heads by the cholesterol molecules. Details of this structure are described below.

Addition of ASA to a sample containing cholesterol at a concentration below the phase transition (15mol%, 30mol%) shows little change in the 2D fingerprint. The samples still appear disorganized, with lone broadening lipid peaks. At 40mol% cholesterol and 5mol% ASA, we observe the large scale structure associated with organi-

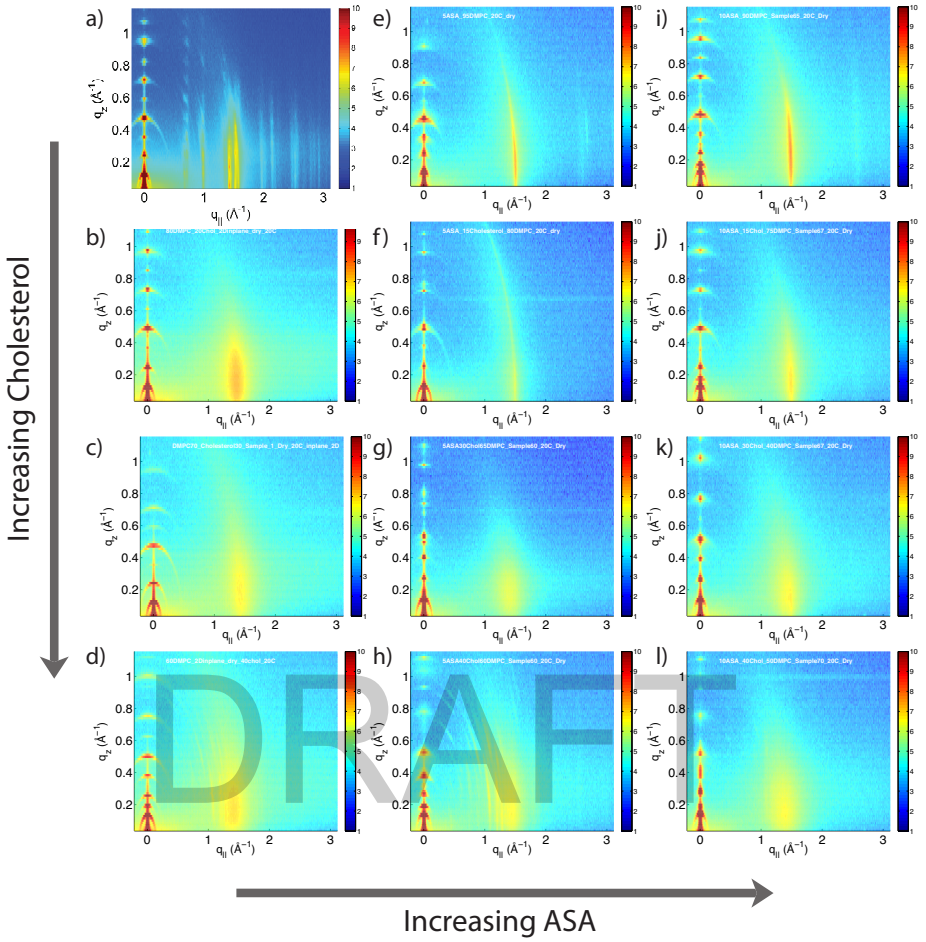

FIG. 2: 2D x-ray intensity maps of samples 1-12 a) 100mol% DMPC, b) 20mol% Cholesterol, c) 30mol% Cholesterol, d)40mol% Cholesterol, e) 5mol% ASA, f) 5mol% ASA + 15mol%Cholesterol, g) 5mol% ASA + 30mol% Cholesterol, h)5mol% ASA + 40mol% Cholesterol, i) 10mol% ASA, j) 10mol%ASA + 15mol%Cholesterol, k) 10mol% ASA + 30mol% Cholesterol, l) 10mol% ASA + 40mol% Cholesterol in DMPC.

zation by cholesterol. However, at 40mol% cholesterol and 10mol% ASA, this structure does not appear. Samples containing 40mol% cholesterol with 7.5mol% and 12.5mol% ASA were also prepared. The corresponding in-plane scans are shown in Figure 3. The 7.5mol% ASA sample shows some additional peaks, corresponding to cholesterol structure, but they are not as pronounced. The 12.5mol% sample still shows no long range ordering, similar to 10mol%.

Samples showing multiple Bragg peaks are fit with a superlattice model. In this model, the peaks observe correspond to large scale molecular ordering of the components of the sample. The Bragg peaks are fit with unit cells describing the structure of lipid heads, tails, cholesterol, or ASA. Samples 4,8,12,14 are fit with the superlattice model, as outlined in Figure 3. In these samples, peaks are fit with unit cells describing ordering of the lipid heads, the lipid tails, as well as a cholesterol molecular lattice. However, this did not fit all the peaks observed. In addition to a superlattice, we believe the lipid and cholesterol molecules are forming coordination shell structures. As outlined in [14], cholesterol introduced in

saturated lipid membranes may adopt the coordination shells as a way of minimizing cholesterol-cholesterol contacts. Our peak at $q_{||} = 1.2$ Å^{-1} suggests a coordination shell of radius 5.2 ÅÅ smaller peak at $q_{||} = 0.6$ Å^{-1} corresponds to the second order shell. Although increasing ASA tend to diminish the intensity of the peaks associated with this lattice, the position of these peaks does not change.

In addition to examining the structures formed by the components of the membrane, the x-ray scattering experiments allow us to measure other physical characteristics of the sample. The position of the lipid peak along $q_{||}$, assuming the tails form a densly packed structure with hexagonal symmetry, is a measure of the area per lipid. As outlined in Barrett *et al.* [9], the area per lipid can be determined from the parameters describing the lipid tail unit cell: $A_T = a_T b_T \sin\gamma_T$. For a sample with hexagonal organization, we may simplify this expression to $A_L = 4a_T^2/\sqrt{3}$. The position of the lipid correlation peak , q_T, is related to the unit cell of a hexagonal lattice by $q_T = 2\pi/a_T$. Therefore, we may express area per lipid with $A_L = 16\pi^2/(\sqrt{3}q_T^2)$. Area per lipid is 41.0 Å^2 for a 100mol% DMPC sample. As shown in Figure 5 a) area per lipid increases as a function of cholesterol concentration. As well, A_L increases as a function of ASA concentration (Figure 5 b). Figure 5b) shows only samples containing 30mol% cholesterol, with varying ASA. This subset of our data was chosen as it had the highest sample number of any fixed cholesterol concentration, with the exception of 40mol%. Determining A_L becomes complicated for the samples with high cholesterol and ASA concentration since, as outlined in the discussion, these may contain lipids in a lattice configuration as well as lipids in disordered state.

The diffracted intensity of the lipid peak is not distributed homogenously along the rod, and it is not peaked at $q_z = 0$, indicating the lipid molecules have a preferred tilt. The q_z value with maximum intensity along the lipid peak is a measure of the preferred tilt angle. For DMPC, this maximum is at q_z ∼0.2 Å^{-1}, corresponding to a tilt angle of α=6.5 degs. The bilayer thickness may be obtained by measuring the spacing of the reflective Bragg peaks along q_z. The spacing of the bilayers is related to the spacing of the peaks by $d_z = 2\pi/\Delta q_z$. For DMPC, $d_z = 55.3$ *Å*.

Discussion

X-ray scattering experiments were performed on DMPC membranes containing cholesterol and ASA. In-plane structures of the membranes are determined through analysis of x-rays scattered out-of-plane. We use these structures to infer and suggest a molecular model for the low dose Aspirin therapy. Scattering experiments were performed at 50mol% RH, and 20°C. This non-physiological state was selected as it allowed structural features to emerge. In the discussion that follows, we associate the degree of order within the 2D plane of the membrane as a qualitative measure of fluidity of the system. A membrane where the lipids are permitted many degrees of freedom will be more fluid, directly influencing characteristics such as permeability to small molecules, in analogy to the physiological version.

We previously solved the position of ASA and cholesterol along the bilayer normal [9]. Membranes containing cholesterol and or ASA were able to form multi-lamellar structures, indicating cholesterol and ASA are able to coexist within DMPC membranes. Using electron density profiles assembled from Fourier reconstruction of the reflective Bragg peaks along $q_{||} = 0$, ASA was found to reside among the head-groups of the lipid molecules. We suggest this is due to ASA's hydrophilic chemistry. As well, cholesterol was found to orient its long axis parallel with the bilayer normal, with the lone hydrophilic oxygen molecule among the head-groups of the lipid molecules. This position is predicted by theories of cholesterol in membranes such as the umbrella model; cholesterol requires the neighbouring lipid head-groups to shield its large hydrophobic ring structure from the aqueous environment. We suggest, since cholesterol and ASA both require committment from the neighbouring lipid head-groups, that the two molecules cannot occupy the same position in a 2D lattice.

With the position of the molecules out-of-plane determined, we turn the discussion to in-plane structures. Samples with low cholesterol or ASA show a high degree of disorder, and therefore high fluidity. The additional components are likely evenly dispersed among the lipid molecules. Reciprocal space maps show only a single peak with finite width, corresponding to a narrow range of nearest neighbour separations, achieved as an effort to minimize Van-der-Waal interactions. Addition of cholesterol, up to 30mol% acts to broaden the peak, as the cholesterol molecule now wedges itself among the tighly packed lipid gel structure. In the region of cholesterol, lipid distances increase, leading to skewing of the lipid peak to lower $q_{||}$ values.

The structure formed by cholesterol at 40mol% molecular ratio is an indicator of cholesterol's ordering and condensation ability appearing within our gel phase, saturated model lipid membranes. Cholesterol forces the lipid tails and lipid heads to adopt an ordered structure. Bragg peaks were also assigned to a repeated cholesterol lattice. In addition, the cholesterol and lipid molecules adopt a repeated coordination shell structure so that cholesterol-cholesterol contacts are minimized. Overall, the system is highly constrained and lipid molecules have a well defined position within the membrane to ensure the abundance of cholesterol is shielded from water.

Addition of ASA appears to disrupt this order. As ASA concentration increases in samples with 40mol% cholesterol, the Bragg peaks assigned to molecular lattices shrink compared to the broad nearest neighbour peak. At 10mol% ASA, almost no structure is observed. The samples are moving to more fluid structures with

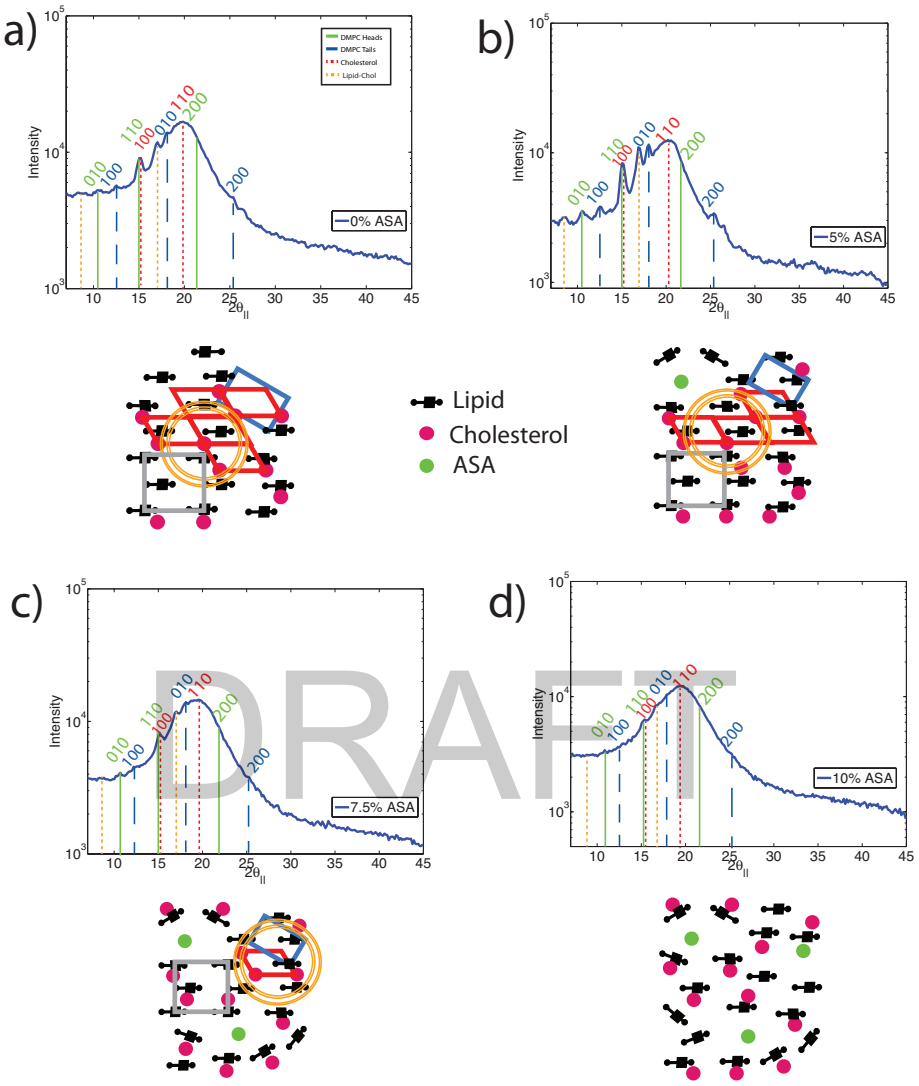

FIG. 3: Integrated intensities for samples 4,8,12,14 containing 40% cholesterol and 0%. 5%, 7.5%, and 10% ASA respectively. Lines on the plots indicate Miller indices of the unit cells assigned to the peaks. Cartoons on the right depict the solved structures represented by the intensity profile.

increasing ASA. As stated above, ASA and cholesterol cannot occupy the same location in a 2D lattice model. It is also not likely favorable for ASA and cholesterol to occupy neighbouring positions in the lattice, as ASA cannot provide the same barrier from water that a bulky lipid phosphate group can. Our model then suggests an ASA molecule in a DMPC + cholesterol membrane is surrounded by lipid molecules. These lipid molecules are not under the same pressure to order and shield a cholesterol molecule, so they are likely in a disordered state. There-

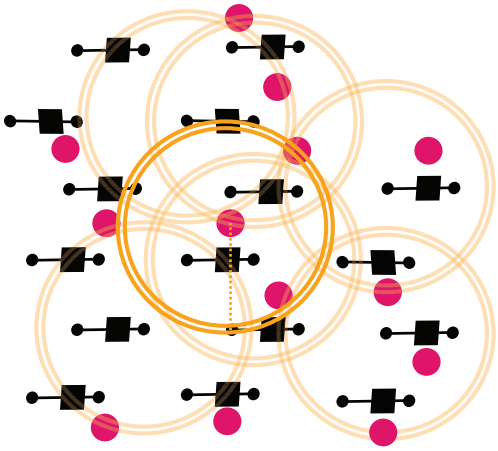

FIG. 4: Coordination shell model for cholesterol-lipid separation. The orange ring outlines the separation distance.

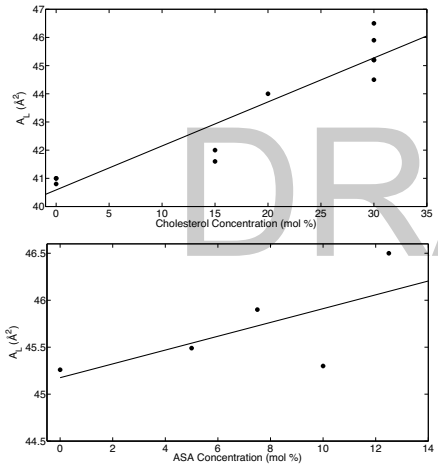

FIG. 5: Area per lipid as a function of a) Cholesterol concentration (samples 1-3, 5-7, 9-11,13,15) and b) ASA concentration (samples 3,7,11,13,15). Lines are placed to highlight the appropriate trend.

fore the absence of structure in membranes containing ASA and high cholesterol is caused by ASA's competition for lipid head-groups. Sample 12 bears resemblance to the fluid fingerprints of samples 2,3,5,6,7,9,10,11. The lipid correlation peak is very broad, likely due to the diversity of the sample.

This analysis is developed based on the observation that increasing ASA prohibits large scale organization of components in a the membrane. However, our model also suggests a single ASA molecule may produce disorder in its neighbouring lipids. Smaller ASA concentrations simply do not inhibit large scale structure. The effect of cholesterol is still strong enough to be detected by x-ray scattering experiments for 5mol% and 7.5mol% samples. This corollary of our argument, that ASA in higher concentrations disrupts large scale order but a single ASA locally disrupts order, is important when translating our model to physiological systems, and physiologically relevant ASA concentrations.

The study of the impact of pharmaceuticals and small molecules on membrane fluidity is not new [15]. For example, studies have been performed probing the changes in membrane fluidity caused by anti-inflammatory medication[16], anti-psychotics[17], anesthetics[18], and insecticides[19]. In particular, the anti-psychotic haloperidol and its pyridinium metabolite were shown to increase membrane fluidity and permeability as consequence of their interaction with the plasma membrane, in real tissue[17]. As well, increased platelet aggregation has been associated with decreased platelet membrane fludity[20–22]. In addition, β-carbolines were found to inhibit platelet activity by modifying platelet membrane fluidity[23]. We therefore suggest studies investigating ASA interacting with the membranes of real cells *in vivo* or otherwise be considered.

Conclusion

We determined the in-plane structures of highly oriented, solid supported membranes containing up to 12.5mol% ASA and 40mol% cholesterol using x-ray diffraction. All membranes were in a low-hydration (50% RH) gel phase to strengthen the signal from structural features. ASA and cholesterol were found to coexist within DMPC membranes. At 40mol% cholesterol, DMPC membranes were found to form highly organized structures, where the lipid heads, tails and cholesterol molecules formed molecular lattices. Addition of sufficient ASA eliminated this structure. We believe ASA prohibits the ordering effect of cholesterol in lipid membranes through competition for lipid headspace. The results presented here may be relevant for developing a complete molecular model for the low-dose Aspirin therapy.

Acknowledgments

This research was funded by the Natural Sciences and Engineering Research Council of Canada (NSERC), the National Research Council Canada (NRC), the Canada Foundation for Innovation (CFI) and the Ontario Ministry of Economic Development and Innovation.

[1] S. Singer and G. Nicolson, Science **175** (1972).
[2] G. Vereb, J. Szollosi, J. Matko, P. Nagy, L. Vigh, L. Matyus, and T. Waldmann, PNAS **100** (2003).
[3] G. Pabst, N. Kučerka, M.-P. Nieh, M. Rheinstädter, and J. Katsaras, Chemistry and Physics of Lipids **163**, 460 (2010).
[4] L. Hansson, A. Zanchetti, S. Carruthers, B. Dalhof, S. Julius, J. Menard, K. Rahn, H. Wedel, and S. Westerling, The Lancet **351** (1998).
[5] S. Weisman and D. Graham, Arch. Intern. Med **162** (2002).
[6] P. Ridker, J. Manson, J. Gaziano, J. Buring, and C. Hennekens, Annals of Internal Medicine **114** (1991).
[7] J. G. Roth, N. Stanford, and P. Majerus, Proc. Natl. Acad. Sci. U.S.A. **72** (1975).
[8] C. Patrono, L. Rodriquez, R. Landolfi, and B. C, The New England Journal of Medicine **83** (2005).
[9] M. Barrett, S. Zheng, G. Roshankar, R. Alsop, R. Belanger, C. Huynh, N. Kučerka, and M. Rheinstadter, PLoS ONE (2012).
[10] E. T. Vandenberg, L. Bertilsson, B. Liedberg, K. Uvdal, R. Erlandsson, H. Elwing, and I. Lundström, Journal of Colloid and Interface Science **147**, 103 (1991).
[11] H. W. Meyer, K. Semmler, W. Rettig, W. Pohle, A. S. Ulrich, S. Grage, C. Selle, and P. J. Quinn, Chem. Phys. Lip. **105**, 149 (2000).
[12] K. Nomura, M. Lintuluoto, and K. Morigaki, The Journal of Physical Chemistry B **0**, null (0).
[13] F. J.-M. de Meyer, A. Benjamini, J. M. Rodgers, Y. Misteli, and B. Smit, The Journal of Physical Chemistry B **114**, 10451 (2010).
[14] H. Martinez-Seara, T. Rog, M. Karttunen, I. Vattulainen, and R. Relgada, PLoS ONE **5** (2010).
[15] D. Goldstein, Ann. Rev. Pharmacol. Toxicol. **24** (1984).
[16] C. Sousa, C. Nunes, M. Lucio, H. Ferreira, J. Lima, J. Tavares, A. Corderio-Da-Silva, and S. Reis, J. Pharmacol. Sci. (2007).
[17] T. Murata, N. Maruoka, N. Omata, Y. Takashima, K. Igarashi, F. Kasuya, Y. Fujibayashi, and Y. Wada, Progress in Neuro-Pharmacology & Biological Psychiatry (2007).
[18] H. Tsuchiya, T. Ueno, and M. Mizogami, Bioinorganic & Medicinal Chemistry (2011).
[19] J. Blasiak, Comp. Biochem. Physiol. (1995).
[20] S. Shattil and R. Cooper, Biochemistry **15** (1975).
[21] K. Gousset, W. Wolkers, N. Tsvetkova, A. Oliver, C. Feild, N. Walker, J. Crowe, and F. Tablin, Journal of Cellular Physiology **190** (2002).
[22] P. Padmavathi, V. Reddy, P. Maturu, and N. Varadacharyulu, Journal of Atherosclerosis and Thrombosis **17** (2010).
[23] H. Tsuchiya and S. Ohmoto, Pharmacological Reports **62** (2010).

Chapter 5

Neutron scattering of model lipid membranes

Papers V, VI

V. Armstrong, C. L., **Barrett, M.**, Toppozini, L., Kučerka, N., Yamani, Z., Katsaras, J., Fragneto, G., and Rheinstädter, M. C., (2012) *"Co-existence of Gel and Fluid Lipid Domains in Single-component Phospholipid Membranes."* Soft Matter, 2012, 8, 4687-4694..

VI. Armstrong, C. L., **Barrett, M.**, Hiess, A., Shi, A. C., and Rheinstädter, M. C., *"Effect of Cholesterol on the Lateral Nano-Scale Dynamics of Fluid Membranes."*, European Biophysics Journal, 2012. (DOI 10.1007/s00249-012-0826-4)

5.1 Neutron and x-ray scattering differences

The two papers discussed in this section were based on experiments using neutron scattering. Neutron scattering and x-ray scattering both rely on the same physical principles, but are different in in certain ways. These differences were touched upon in section 2.1, but will be expanded upon in this section.

5.1.1 Coherent and incoherent scattering and scattering cross sections

Neutron scattering is a commonly chosen tool for studies of lipid bilayers because of the accessible time and length-scales. Neutrons scatter both coherently and incoherently.

Coherent scattering gives information of the relative position and motion of different particles in the sample. This information is used to develop the structure of the bilayer sample. At low momentum values, the coherent scattering shows excitation effects due to the presence of cooperative modes. [5]

Incoherent scattering depends on the motion of a single particle, rather than comparing position of different particles.

This structure factor, $S(\overrightarrow{q})$, can also be probed with x-ray scattering (as was seen in the previous chapter), but one must be aware of the differences. X-rays scatter from electrons, rather than nuclei, and the signal from higher atomic number atoms often drowns out smaller atoms. Neutrons interact with the nucleus of the atom, and the amount of surrounding electrons does not have the same effect on these particles. The scattering cross section is largest for hydrogen, and becomes smaller for other larger atoms. This is shown in Figure 5.1. Since hydrogen is such an abundant molecule in bio-physical samples, neutrons can be a valuable tool to observe these hydrogen rich molecules.

Neutron scattering data is obtained both elastically and inelastically. Elastic neutron scattering results in equilibrium structural data and the interpretation is quite similar to what was described for x-ray data in the previous chapter. Scans obtain information in both $\overrightarrow{q}_{\parallel}$ and $\overrightarrow{q}_{z}$, in and out of the plane of the membrane, respectively. It is possible to obtain the position of molecules in the bilayer using

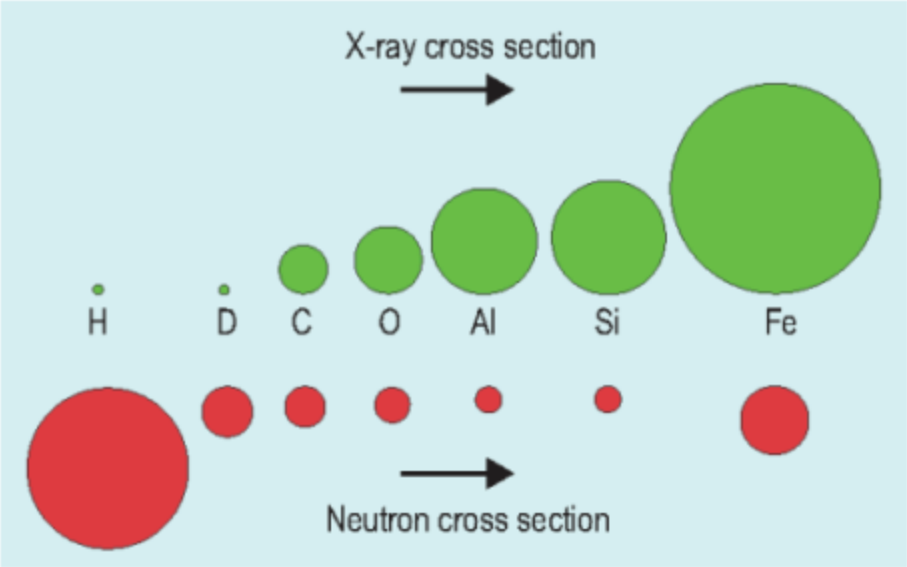

Figure 5.1: X-ray and neutron scattering cross-sections
Neutron and x-ray scattering cross-sections compared. Note the cross-sectional size of hydrogen for each scattering technique.[55]

the process outlined in Figure 4.16. Instead of determining an electron density, like was found in the x-ray scattering studies - one obtains the corresponding neutron scattering length density plot. This is shown in Figure 5.2. The high density peaks on the plot correspond to deuterium rich regions, such as the lipid tail and cholesterol ring structures at ±10 Å.

5.2 Neutron scattering facilities and instruments

Triple-Axis Spectrometers (TAS) were the neutron instruments used in both of the following papers in this section. The TAS instrumentation technique was developed in the 1950's by Dr. Bertram Brockhouse, a professor from McMaster University. The first results from one of Brockhouse's prototypes was published in 1955, and in 1956 the first true triple-axis spectrometer was built. Brockhouse was awarded the Nobel Prize in Physics in 1994 for his ground-breaking work. TAS allows for the selection of a particular point in energy and momentum space and the ability to measure the scattering function at this point. This is achieved through the precise control of the

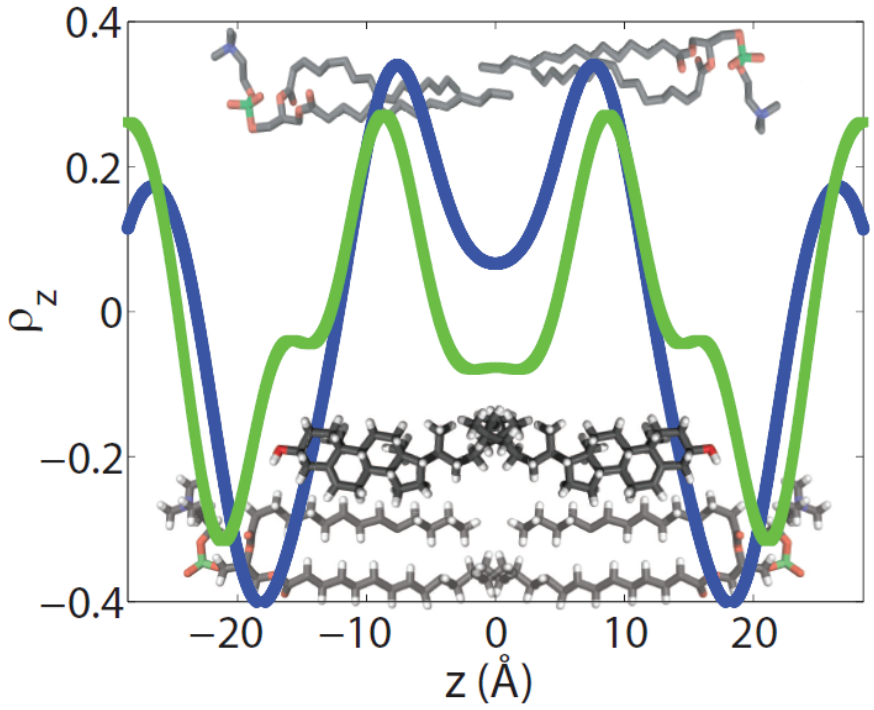

Figure 5.2: Neutron scattering length density of DMPC and cholesterol samples Neutron scattering length density of 5 mol% Cholesterol (Blue) in DMPC and 40 mol% Cholesterol (Green) in DMPC. Regions of high density correspond to hydrogen rich regions of our bilayer, as the neutron scattering cross-section of hydrogen is much higher than other atoms.[56]

axes of rotation of the monochromator, the sample and the analyzer.[57] As is shown schematically in Figure 5.3.

The three axes of rotation are indicated by the red arcs. The incident neutron energy is determined by a monochromator in a rotatable shielded drum (1). The energy is related to the incident wavevector $\overrightarrow{k_i}$, and can be changed by rotation of the monochromator, and the path in the drum where the neutrons exit. The sample sits on a platform which is also free to rotate (2), and the path to the analyzing monochromator is chosen. The analyzer crystal (3) may also rotate and the final wavevector $\overrightarrow{k_f}$ is determined by the angle of incidence the beam makes with the analyzing crystal. The beam's divergence in the horizontal direction is controlled by Soller collimators which are positioned after the monochromator, after the sample

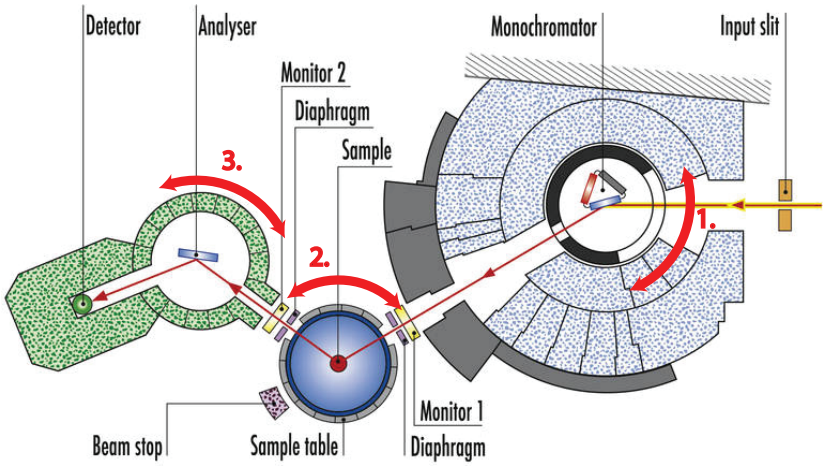

Figure 5.3: Triple-axis spectrometer schematic
Schematic of typical triple-axis spectrometer setup. The red arcs labeled 1, 2, and 3, represent the three axes of rotation which define a triple-axis instrument. Specifically 1. monochromator, 2. sample and 3. analyzer. Schematic adapted from ILL-IN8 Schematic diagram.[58]

and after the analyzer in the path of the neutron beam. Monochromating crystals (in our experiments Pyrolytic Graphite) are used to produce incident neutrons with a well defined energy, and to analyze the energy of the scattered neutrons. The axes are calibrated such that the $\overrightarrow{q}$ value can be fixed. [5] By rotating the monochromator and analyzer and keeping a constant scattering angle the energies of a specifically chosen $\overrightarrow{q}$ can be determined. A constant q scan can also be performed by holding either $\overrightarrow{k_i}$ or $\overrightarrow{k_f}$ constant and rotating through the scattering angle. To obtain a constant energy scan the magnitude of $\overrightarrow{k_i}$ and $\overrightarrow{k_f}$ are held constant and the scattering angle

is changed.[57] The ability to maintain these specific ratios in reciprocal space is a challenge, and was mechanically accomplished by Brockhouse through the use of gearboxes which he developed. This is now done electronically.

The experimental work for Paper V was carried out at the Canadian Neutron Beam Centre's N5 in Chalk River, an instrument attached to the National Research Universal (NRU) reactor. NRU has a variety of neutron scattering instruments, two of which are TAS. (E3 and N5 in Figure 5.4) The N5 instrument is most commonly used for biological samples. NRU has a maximum power level of 120 MW and at the N5 beamport a flux of (3.4±0.2)x10^9neutrons/cm^2/s.[59]

The instrumental components of N5 in this experiment were used in uncommon configurations, as the goal of the experiment was to achieve various neutron coherence lengths, to see the coexistence of different sized lipid fluid and gel domains. The technical specifications of N5, including what instrumental component options were available and used can be found in Table 5.1.

Technical Specifications of N5	
Instrumental Component	Choices available
Beam size	5 cm x 5 cm
Monochromating crystals	Be, Cu, Ge, pyrolitic graphite (PG), Si
Monochromator angle	Continuously variable from 15 - 120
Sample scattering angle	Continuously variable from 0 - 126
Analyzer take-off angle	Continuously variable from -120 - 120
Soller collimator slits	Blade spacing minimum 0.050", blades from 5.5" to 26" in length.

Table 5.1: Technical information of the capabilites of N5 Triple-Axis Spectrometer at Chalk River.

To explore many coherence lengths (from 30 to 242 Å) the collimators were held constant at with the collimation of 30'-monochromator-18'-sample-28'-analyzer-60'-detector (' indicates arcminutes, $1/60^{th}$ of a degree.) The monochromator and analyzer crystals were combinations of the 002 and 004 reflections of PG and incident wavelength was either 1.39 Åor 2.37 Å. Combinations of these component choices allowed the range of coherence lengths to be obtained.

The experimental work for Paper VI was carried out at the High-Flux reactor at Institut Laue-Langevin (ILL) in Grenoble, France. The ILL features a reactor with a very high neutron flux of 1.5x10^{15}/cm^2/s, at a thermal power of 58.3 MW. Two

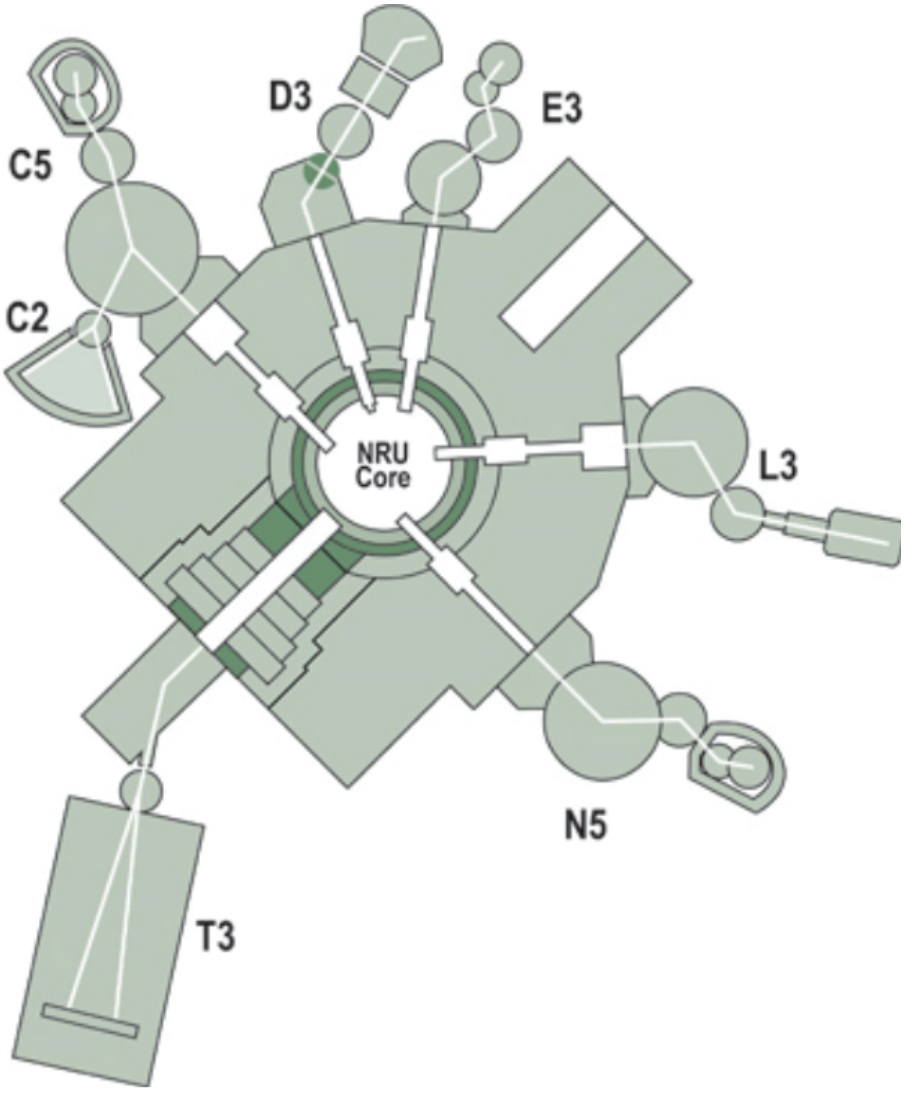

Figure 5.4: National Research Universal (NRU) reactor
Schematic diagram of NRU reactor at Chalk River, ON. A variety of neutron scattering instruments exist, N5 is commonly used for biological samples and was used for the experiments for Paper V.[60]

of ILL's instruments, the thermal neutron TAS IN8 and the cold neutron TAS IN12 were used to gather data for this experiment. From Figure 5.5 one can see how similar the two instruments are.

IN8 is an instrument which measures thermal neutrons, up to ∼20 meV and an

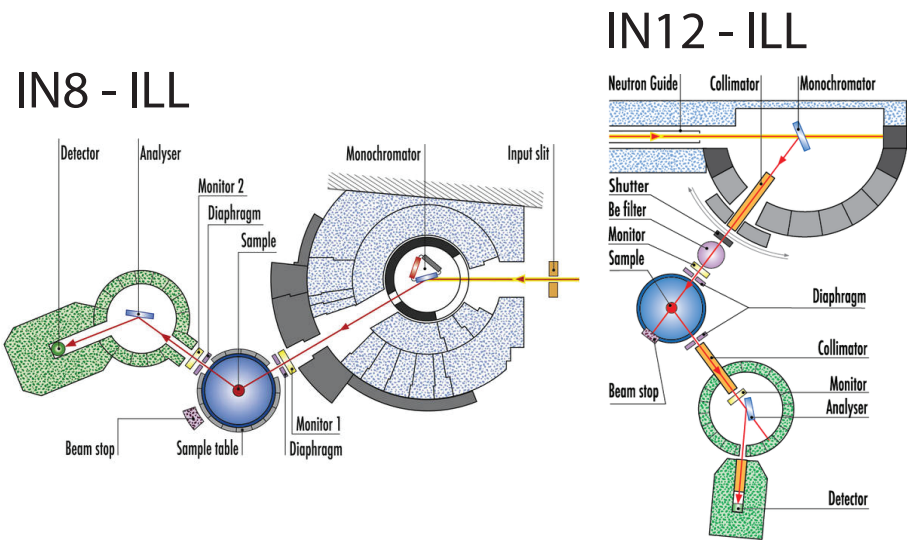

Figure 5.5: Schematic diagrams of IN8 and IN12 TASs at ILL
IN8 (left) and IN12 (right) instruments. Aside from the orientation of the neutron source (input slit and neutron guide) the general path of neutrons is quite similar for the two spectrometers. The main difference between the two is the energy of incident neutrons, which are moderated by the Beryllium filter in IN12. IN8 uses thermal neutrons, where IN12 uses cold neutrons. The energy range is lower for cold neutrons, but the resolution drastically enhansed. [58]

energy resolution of ∼1 meV. On the other hand, IN12 measures cold neutrons up to ∼4 meV with ∼0.1 meV resolution. Cold neutrons allow for low-energy excitations to be measured and give better resolution. Again, pyrolytic graphite monochromator and analyzer were used. The scans went from 0.4 Å^{-1} to 3 Å^{-1} in $q_{||}$ and energies of up to ∼20 meV. This energy range resulted in the ability to observe picosecond in-plane dynamics. We can observe these dynamics in terms of energy $E = \hbar\omega$, with ω the frequency (the reciprocal of the period). These dynamics were observed between 2 and ∼20 Å, from less than one lipid-lipid distance to almost 3 lipid-lipid distances.

Preface to Paper V

DPPC was used to create single-component phospholipid bilayer stacks for this experiment. Neutron scattering was performed on the DPPC sample while it was undergoing its main phase transition (from $P_{\beta'}$ to L_{α}), between 311 and 314 K and close to full hydration. The coherence length of the neutron beam defines the smallest observable structure size. By changing the optics of the neutron instrument the coherence length was set between 30 and 242 Å. Bragg peaks were observed from co-existing structures, all in the nanometer length scale. Rather than a continuous transition from gel to fluid a co-existence of these domains is observed.

The samples used in this experiment were prepared at McMaster University, and taken to N5 TAS in Chalk River for neutron scattering scans. The sample preparation and neutron scattering was done by Clare Armstrong, Laura Toppozini and Maikel Rheinstädter. The contacts from Chalk River also assisted with the experiment and interpretation of the results. I was a part of the experimental team for this experiment, and was involved in some hands-on instrumentation including modifying collimators and aligning monochromating crystals.

View Online / Journal Homepage / Table of Contents for this issue
Dynamic Article Links

Soft Matter

Cite this: *Soft Matter*, 2012, **8**, 4687

www.rsc.org/softmatter

PAPER

Co-existence of gel and fluid lipid domains in single-component phospholipid membranes

C. L. Armstrong,*[a] M. A. Barrett,[a] L. Toppozini,[a] N. Kučerka,[b] Z. Yamani,[b] J. Katsaras,[bc] G. Fragneto[d] and M. C. Rheinstädter*[ab]

Received 11th November 2011, Accepted 21st February 2012
DOI: 10.1039/c2sm07158d

Lateral nanostructures in membranes, so-called rafts, are believed to strongly influence membrane properties and functions. The experimental observation of rafts has proven difficult as they are thought to be dynamic structures that likely fluctuate on nano- to microsecond time scales. Using neutron diffraction we present direct experimental evidence for the co-existence of gel and fluid lipid domains in a single-component phospholipid membrane made of DPPC as it undergoes its main phase transition. The coherence length of the neutron beam sets a lower limit for the size of structures that can be observed. Neutron coherence lengths between 30 and 242 Å used in this study were obtained by varying the incident neutron energy and the resolution of the neutron spectrometer. We observe Bragg peaks corresponding to co-existing nanometer sized structures, both in out-of-plane and in-plane scans, by tuning the neutron coherence length. During the main phase transition, instead of a continuous transition that shows a pseudo-critical behavior, we observe the co-existence of gel and fluid domains.

1 Introduction

Clusters, rafts, nanodomains, and patches have become a central issue in cell membrane studies.[1–4] The heterogeneous organization of membrane constituents is not only believed to be essential for cellular functions such as signalling, trafficking and adhesion,[5–7] but also impacts material properties.[8] However, the experimental observation of these heterogeneities has proven to be challenging, as they are thought to be short-lived.[9–12] As such, in order for experimental techniques to unambiguously observe such structures, they must be capable of simultaneously accessing small length scales and fast (nano to microsecond) time regimes.

Lipid bilayers are established model systems for studying dynamics and functional aspects of complex biological membranes.[13,14] They also allow the investigation of heterogeneous structures, which mimic "rafts". Submicron sized domains in ternary mixtures of phospholipids and cholesterol have been observed using small angle neutron scattering (SANS).[15–19] Selective deuteration was used in these experiments to enhance the scattering of the heterogeneities, and domains in the range 20–200 nm radius were observed. Domains in these so-called raft forming lipid mixtures are thermodynamically stable and quasi-static, *i.e.*, changing on slow time scales of seconds or minutes. Heterogeneous structures have also been reported in single component lipid membranes: Rappolt *et al.* observed gel- liquid crystal phase co-existence in a DPPC membrane by driving the system far from equilibrium by an infrared temperature jump.[20] Pabst *et al.* observed co-existence of orthorhombic and hexagonal lamellar gel phases in single component DSPG membranes.[21] The experiments point, however, to a kinetically trapped, out-of-equilibrium state, which lead to an interdigitated, stable (on the time scale of the experiments) phase. The origin of the driving force behind phase separation in artificial and biological membranes is highly debated, as "rafts", thus far, have primarily been experimentally observed in either raft forming mixtures or far from equilibrium. Phase separation in biological membranes has very recently been related to non-equilibrium fluctuations of the cytoskeleton,[22] which are coupled to the local membrane curvature. Microdomains, on the order of 10–100 nm, have been theoretically predicted and small (75 nm), transient (250 msec) domains have indeed been observed in a biological membrane *in vivo* using particle tracking techniques.[23]

The aim of this work was to experimentally prove the existence of heterogeneities in a lipid membrane, which are (1) "small" (3–50 nm), (2) transient and (3) occur in thermal equilibrium under conditions that mimic physiological conditions, such as high hydration and high temperature. Those domains would be very difficult to "see" with standard techniques, however, they are speculated to occur in biological membranes and thought to be

[a]*Department of Physics and Astronomy, McMaster University, Hamilton, ON, L8S 4M1, Canada. E-mail: armstc5@mcmaster.ca; rheinstadter@mcmaster.ca; Fax: +(905)546-1252; Tel: +(905)525-9140 ext.23134*
[b]*Canadian Neutron Beam Centre, National Research Council, Chalk River, ON, K0J 1J0, Canada*
[c]*Neutron Scattering Science Division, Oak Ridge National Laboratory, Oak Ridge, TN, 37831-6100, USA*
[d]*Institut Laue-Langevin, 6 rue Jules Horowitz, B.P. 156, 38042 Grenoble Cedex 9, France*

physiologically relevant.[1–4] It has been speculated that small transient domains in phospholipid model membranes are responsible for the so-called pseudo-critical behaviour, without experimental proof so far.

Phospholipid bilayers are known to undergo an acyl-chain melting transition, the so-called main transition, from an ordered gel to a disordered fluid phase. Critical fluctuations and critical swelling—most likely due to co-existent gel and fluid domains—have been reported close to this phase transition.[24–38] These lipid bilayers are, therefore, ideal model systems for the study of domain formation. The system can be tuned through the gel-fluid phase co-existence region, simply by changing the temperature, as sketched in Fig. 1.

In this paper we use the coherence length of the neutron beam to clearly show direct experimental evidence for the co-existence of gel and fluid nanodomains in the temperature range of the main phase transition. While a continuous transition between the gel and fluid phase, and a pseudo-critical behaviour have been previously reported in the literature,[24–38] we observe co-existing gel and fluid domains indicative of a first order phase transition.

In most natural systems partially coherent waves are common. X-rays and neutrons have coherence lengths that are usually significantly longer than molecular lattice spacings, including protein-protein distances in biological membranes. The coherence of waves in periodic systems (lattices) is critical with regard to their dynamics, as interference effects, such as Bragg reflections, largely determine their propagation. Additionally, in less well ordered systems, the coherence length of the probe, ξ, may play an important role in the investigation of small structures, *i.e.*, when ξ is comparable to the size of the object in question.

A collimated beam of neutrons obtained by Bragg reflection from a single crystal, or a pair of phased Fermi choppers, is never 100% monochromatic. With regard to their wave properties, their longitudinal coherence length, ξ, is defined by eqn (1):[39]

$$\xi = \frac{\lambda^2}{\Delta\lambda}. \tag{1}$$

The energy of a neutron (in meV) with wavelength λ (in Å) is given by $E = 81.81/\lambda^2$,[40] such that

$$\frac{\Delta E}{E} = 2\,\frac{\Delta\lambda}{\lambda}, \tag{2}$$

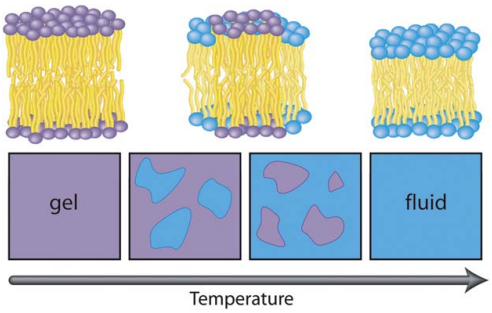

Fig. 1 Schematic of the gel-fluid transition in phospholipid membranes with co-existing gel and fluid domains.

where E is the incident neutron energy and ΔE is the instrumental energy resolution and will be discussed in more detail below. ξ can now be written as a function of E and ΔE, as follows:

$$\xi = \frac{2E}{\Delta E}\,\lambda = \frac{2E}{\Delta E}\sqrt{\frac{81.81}{E}} \sim \frac{18\sqrt{E}}{\Delta E}. \tag{3}$$

For cold neutrons with energies of ~4.5 meV and a typical monochromaticity by single crystal reflection of about 2%, the longitudinal coherence length is calculated to be approximately 450 Å (using eqn (3)). † Note, that the reason for the typically low monochromaticity of neutron beams is to avoid further compromising the already low flux "white" neutron beam, a situation that is very different for synchrotron X-rays. The longitudinal coherence length of X-rays reflected from a Si(111) monochromator with a wavelength resolution of $\Delta\lambda/\lambda \approx 1 \times 10^{-4}$ and $\lambda = 1$ Å is of the order of $\xi_{xray} = 10{,}000$ Å. The coherent properties of the scattering probe may play an important role for the investigation of small structures, such as nanoscale domains, comparable to or smaller than a given ξ – structures smaller than ξ may give spatially averaged values of, *e.g.*, peak positions and widths.

We investigated the packing and correlations of the lipid acyl chains in multi-lamellar phospholipid bilayers using neutron diffraction. DPPC, with two fully saturated acyl chains (di-16 : 0), was chosen for this study. Chain deuterated DPPC (DPPC-d62) was used to enhance out-of-plane and in-plane Bragg diffraction. By varying the coherence length of the incident neutron beam, we present direct experimental evidence for the co-existence of nanometer sized domains in single-component phospholipid membranes at temperatures close to the main phase transition. This technique can, in the future, be used to study rafts in membranes containing cholesterol and other lipid mixtures, and eventually in biological membranes.

2 Materials and methods

2.1 Sample preparation

Highly oriented multi-lamellar stacks of 1,2-dipalmitoyl-sn-*glycero*-3-phosphocholine (DPPC) were prepared on 2″ single-side polished Si wafers with a thickness of 300 μm. The coherent scattering of the lipid hydrocarbon chains was enhanced by using partially, tail deuterated lipids, *i.e.*, DPPC-d62. A solution of 20 mg mL^{-1} DPPC-d62 in 1 : 1 chloroform and 2,2,2-trifluoroethanol (TFE) was prepared. The Si wafers were cleaned by alternate 12 min sonications in ultra pure water and ethanol at 313 K. This process was repeated twice. 1 mL of the lipid solution was deposited on each Si wafer and allowed to dry. The wafers were kept in vacuum overnight to remove all traces of the solvent. The samples were then hydrated with heavy water, D_2O, and annealed in an incubator at 303 K for 24 h. Following this

† Note that the transverse coherence length ξ_t can be estimated to be $\xi_t \sim \lambda/\alpha$, where α is the divergence of the neutron beam. Long transverse coherence lengths of several micrometers are achieved in small angle neutron scattering (SANS) instruments by using small pinholes. The transverse coherence length in our setup is of the order of ~5 Å and small compared to the longitudinal coherence, as given in the Table to Fig. 2.

protocol, each wafer contained roughly 3 000 highly oriented stacked membranes with a total thickness of ~10 μm.

Twenty such Si wafers were stacked with 0.6 mm aluminium spacers placed in between each wafer to allow for the membranes to be hydrated. The "sandwich" sample was kept in a temperature and humidity controlled aluminium chamber. Hydration of the lipid membranes from the vapour phase was achieved by separately adjusting the temperature of the heavy water reservoir, the sample and the chamber cover. Temperature and humidity sensors were installed close to the sample. A water bath was used to control the temperature of the water reservoirs, and the temperature of the sample and its cover was controlled using Peltier elements. d_z-spacings of $d_z^{gel} = 70$ Å at 303 K and $d_z^{fluid} = 56$ Å at 315 K were achieved using this set-up. From values for d_z as function of relative humidity (RH) published for DMPC,[41] the hydration of the DPPC bilayers in this experiment can be estimated to better than 99.6%, close to full hydration. The main transition temperature, T_m, of deuterated DPPC is 310.5 K,[42] a value slightly lower than its protonated counterpart (T = 314.4 K).[24,42] The temperature of the pre-transition from the L_β to the $P_{\beta'}$ phase in deuterated DPPC-d62 was determined to be 302.9 K.[42] All measurements in this work were, therefore, done in the $P_{\beta'}$ and fluid L_α phase.

The samples were mounted vertically in the neutron beam such that the scattering vector (**Q**) could either be placed in the membrane plane ($\mathbf{q}_{\|}$), or perpendicular to the membrane ($\mathbf{q}_z$). Out-of-plane and in-plane structure could be measured by simply rotating the sample by 90 degrees.

2.2 Neutron experiment

Experiments were conducted using the N5 triple-axis spectrometer at the Canadian Neutron Beam Centre (Chalk River, ON, Canada). The three axis of the spectrometer refer to the axis of rotation of the monochromator, the sample and the analyzer. The incident and final neutron energies are defined by the Bragg reflections from pyrolytic graphite (PG) crystals. The divergence of the neutron beam is controlled by several neutron Soller collimators. A schematic of the instrument configuration is shown in Fig. 2. To achieve the different coherence lengths (eqn (3)) the energy of the incident neutrons and the energy resolution of the spectrometer must be varied. The incident energy is determined by the angle of reflection of the monochromator. To avoid higher order contributions, which also fulfil the Bragg condition, *i.e.*, $\lambda/2$, $\lambda/3$, a PG filter was used after the monochromator. Two incident energies were available using this setup, 14.5 meV and 42.3 meV, corresponding to neutron wavelengths of 2.37 Å and 1.39 Å respectively.

The energy resolution of a neutron triple-axis spectrometer is determined by: (1) the incident energy of the neutron beam; (2) the divergence of the neutron beam; and (3) the wavelength resolution of the monochromator and analyzer. The collimation was defined in four different regions of the beam path (c1, c2, c3, c4), as shown in Fig. 2. The tighter the collimation the better the energy resolution, however, this is achieved at the cost of a reduced neutron flux. In addition, the choice of a Bragg reflection plays a role in the energy resolution. In the case of PG

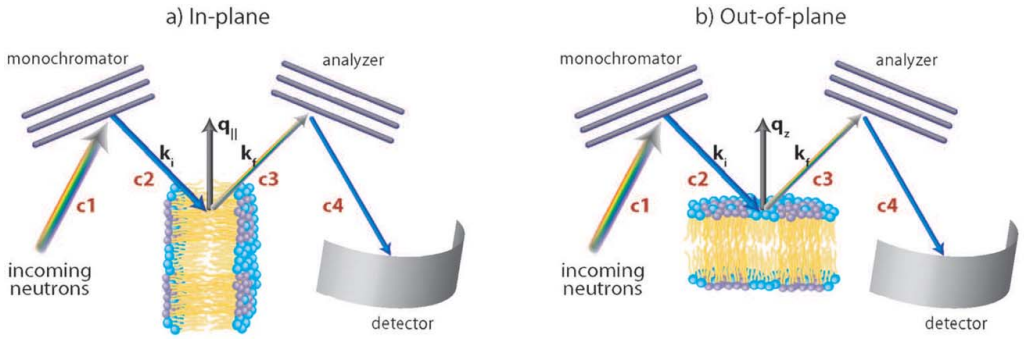

ξ (Å)	Monochromator	Analyzer	Collimation (minutes) (c1-c2-c3-c4)	Wavelength (Å)	Incident Energy (meV)	Energy Resolution ΔE (meV)	Q Resolution ΔQ ($Å^{-1}$)
30	PG(002)	PG(002)	30-18-28-60	1.39	42.3	3.915	0.032
33	PG(004)	PG(002)	30-18-28-60	1.39	42.3	3.504	0.032
46	PG(002)	PG(004)	30-18-28-60	1.39	42.3	2.524	0.032
64	PG(004)	PG(004)	30-18-28-60	1.39	42.3	1.821	0.033
103	PG(004)	PG(002)	30-18-28-60	2.37	14.5	0.6643	0.018
152	PG(002)	PG(004)	30-18-28-60	2.37	14.5	0.451	0.019
242	PG(004)	PG(004)	30-18-28-60	2.37	14.5	0.2836	0.019

Fig. 2 Geometry of the triple axis spectrometer. a) Orientation of the sample for in-plane scans, such that **Q** is in the plane of the membrane ($\mathbf{q}_{\|}$). b) Orientation of the sample for out-of-plane scans, such that **Q** is perpendicular to the plane of the membrane ($\mathbf{q}_z$). The table displays the instrumental settings used to achieve the different coherence lengths, ξ, using eqn (3). k_i and k_f are the incident and final neutron wave vectors ($k = 2\pi/\lambda$).

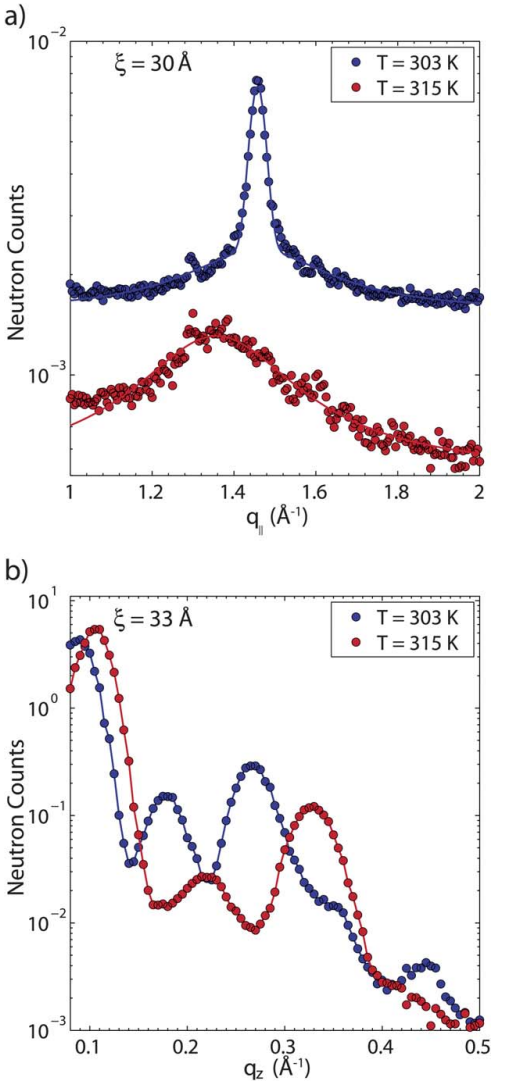

Fig. 3 Scans of gel and fluid DPPC bilayers at $T = 303$ K and $T = 315$ K, respectively. a) In-plane ($q_{||}$) scan showing the lipid acyl chain correlation peak. b) Out-of-plane (q_z) curves displaying the change in d_z-spacing between gel and fluid phase bilayers.

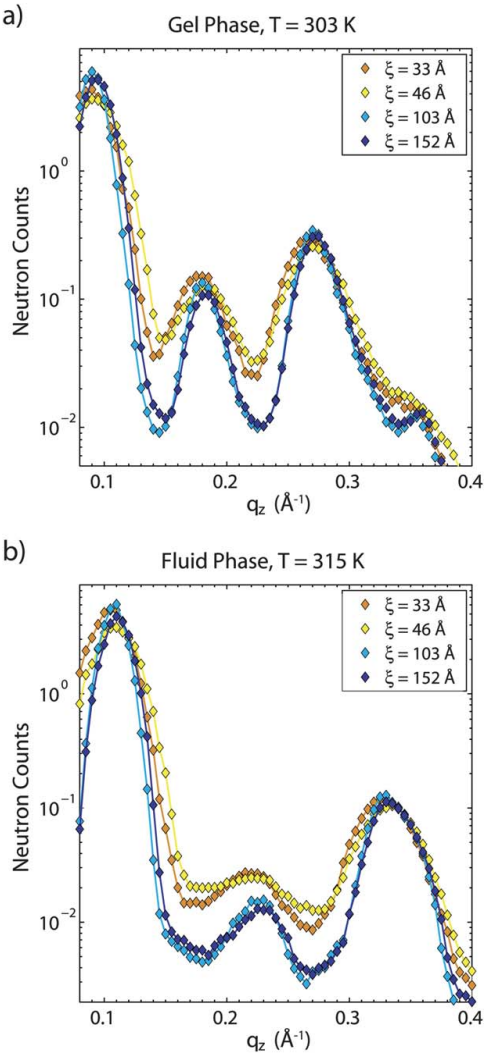

Fig. 4 Out-of-plane scattering curves of stacked DPPC-d62 membranes probed with different coherence length neutrons (33 Å< ξ < 152 Å). a) Gel phase and b) fluid phase bilayers. Curve shapes change as a function of q_z resolution, as listed in the Table to Fig. 2.

crystals, both the PG(002) and PG(004) reflections can be used for monochromatization. According to Bragg's law, the energy resolution is improved with higher angles of reflection (*i.e.* PG(004)), which also happens to reduce neutron flux. The table in Fig. 2 lists the different configurations used and their corresponding coherence lengths.

Collimation was kept constant during the course of the experiment. Coherence lengths between 30 and 242 Å were achieved by using different incident energies and two different PG reflections. The momentum resolution, ΔQ, is also given in the Table to Fig. 2. A good Q resolution usually implies the use of fine collimation and a corresponding large coherence length. In order to enable small nanometer sized structures to become visible, poor energy and Q resolution are needed, which at first sounds counter intuitive – to be discussed later.

3 Results

Fig. 3 shows the in-plane (a) and out-of-plane (b) measurements of gel phase ($T = 303$ K) and fluid phase ($T = 315$ K) DPPC

membranes. The in-plane scan depicts the lipid acyl chain correlation peak, which is the result of the close packed lipid tails making up the hydrophobic membrane core. The correlation peak occurs at 1.46 Å^{-1} in the gel phase, and at 1.37 Å^{-1} in the fluid phase, corresponding to nearest neighbour distances of 4.3 Å and 4.6 Å. The narrow width of the gel peak indicates a well-ordered structure; the peak broadens significantly and loses intensity in the fluid phase of the bilayers due to increased fluctuations.[38] The d_z-spacing between two neighbouring membranes in the stack can be determined from the spacing between the well developed Bragg reflections ($d_z = 2\pi/\Delta q_z$) in the out-of-plane curves in Fig. 3 (b). d_z-spacings of 70 Å and 56 Å are observed for gel and fluid DPPC bilayers, respectively, and the data were obtained with a neutron coherence length of 33 Å.

Fig. 4 depicts out-of-plane curves in the gel and fluid phase measured at different coherence lengths. The peaks are well described by Gaussian peak profiles. The broadening of the peaks changes slightly due to the difference in q_z resolution, as listed in the Table in Fig. 2. However, the position of the Bragg peaks in the different out-of-plane curves does not change as a function of ξ. The resolution (and coherence properties) of the neutron spectrometer are, therefore, not crucial in determining membrane structure deep in the gel or the fluid phase.

The in-plane structure of bilayers in the vicinity of the main phase transition temperature, T_m, was investigated in more detail (Fig. 5). Only one correlation peak at $q_{\|} = 1.46$ Å^{-1}, corresponding to the gel phase is observed at $T = 303$ K. When increasing the temperature, a second correlation peak appears at

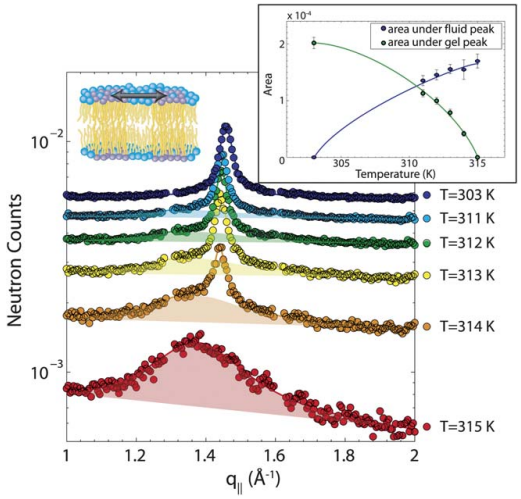

Fig. 5 In-plane scans of DPPC-d62 bilayers at 303 K<T<315 K. (Aluminium Bragg peaks from the humidity chamber were cut out at around $q_{\|} = 1.3$ and 1.6 Å^{-1} for clarity.) Correlation peaks corresponding to co-existing gel and fluid phases are observed close to the main transition temperature, T_m ($\xi = 30$ Å). The inset to the figure displays the area under the fluid and gel peaks, determined from fits of Lorentzian profiles, as a function of temperature. Note that the in-plane scans are plotted on a logarithmic scale to make the broad lipid peak more visible. The corresponding areas are displayed using a linear y-axis.

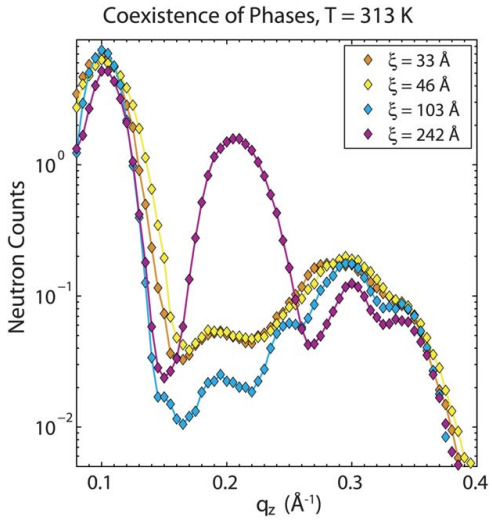

Fig. 6 Out-of-plane scattering curves resulting from stacked DPPC membranes near the main transition temperature ($T_m = 313$ K), probed with different neutron coherence lengths, ξ. The three well-developed, out-of-plane Bragg peaks observed with $\xi = 242$ Å split when the coherence length is reduced to $\xi \leq 103$ Å.

the nominal fluid position ($q_{\|} = 1.37$ Å^{-1}). The intensity of the gel peak is reduced with increasing temperature, while the fluid peak increases. Only the fluid peak is observed at $T = 315$ K. The data in Fig. 5, measured using a small coherence length, show the co-existence of the gel and the fluid peaks with increasing temperature. The area under the correlation peaks, which was determined from fits of Lorentzian peak profiles, is proportional to the volume of their respective phases, and are graphically depicted in the inset to Fig. 5. The fluid phase grows when heating through the transition at the cost of gel phase domains. Based on this data, the co-existence region extends from ~311–314 K.

Out-of-plane curves at $T = 313$ K are shown in Fig. 6. The data measured at high energy and q_z resolution, with a ξ of 242 Å, show three well-defined Bragg peaks with a d_z spacing of 63 Å. We note that this d_z-spacing is the average between d_z^{gel} and d_z^{fluid} ((70 Å + 56 Å)/2 = 63 Å) as determined from gel and fluid phase data (in Fig. 3 (b)). At smaller coherence lengths ξ, however, a peak splitting is observed. Each of the out-of-plane Bragg peaks splits into several separate reflections. The splitting occurs between 103 Å< ξ < 242 Å. Although the width of the Bragg reflections is resolution limited, the Bragg width of the ξ = 242 Å reflection is considerably broader than the instrumental resolution (given in the Table of Fig. 2). Significant peak broadening with improving q_z resolution is consistent with the averaging of individual Bragg peaks.

4 Discussion

The transition from gel ($P_{\beta'}$) to fluid (L_α) phospholipid bilayers has previously been reported to show critical behavior ("critical

swelling").[24–38] The lamellar spacing d_z, but also the nearest neighbour distance of lipid molecules in-the-plane of the membrane, mimic the critical behaviour observed in second order magnetic order-disorder transitions.[38] Critical behaviour is expected in second order phase transitions, with no co-existence of low and high temperature phases. However, a latent heat has been found in the main transition of phospholipid bilayers, which clearly identifies this transition as being of first order.[24–26] The observation of a pseudo-critical behaviour has, therefore, been puzzling and has resulted in a lively and ongoing debate in the literature.

Experimental evidence for co-existing gel and fluid domains has been reported. Inelastic neutron experiments on DMPC previously reported evidence for the co-existence of small nanometer gel and fluid domains in the temperature range of the main phase transition[38] – based on the co-existence of the corresponding excitations in the spectra. The long wavelength dispersion relation, as measured with a neutron spin-echo spectrometer, showed a pronounced soft mode at a length scale of about 420 Å.[8] It was speculated that domains may be responsible for the extreme softness, *i.e.*, the very low value for the bending modulus of phospholipid bilayers in the range of the phase transition, known as "critical softening".[34] Bending of the membrane most likely occurs at the interface between two nanodomains, which costs less energy than bending a pure gel or fluid domain. The diameter of these domains can be estimated to be 420 Å from this experiment. The relaxation rate of domain pattern fluctuations of aqueous solutions of vesicles near the fluid-gel phase transition temperature was found to show a pronounced slowing near the main phase transition in ultrasonic spectra.[10] Finally, co-existing gel and fluid domains in single-component lipid membranes were also reported from computer simulations.[12,43]

The two in-plane Bragg peaks shown in Fig. 5 present direct experimental evidence for co-existing gel and fluid domains in single-component phospholipid bilayers in the range of the main phase transition. Based on the lengths scales accessible in this experiment, limits for the domain size can be determined. The longest coherence length available in this experiment indicates that the lower limit for the size of those domains is ~242 Å in diameter, which is in good agreement with estimated values determined by the neutron spin-echo measurements.[8] However, because the smallest available neutron coherence length was 30 Å, our experiment can not rule out the existence of even smaller structures that include only a few lipid molecules. Instead of a critical behaviour with a continuously shifting peak, as was reported by Rheinstädter *et al.*,[38] we observe the co-existence of gel and fluid like domains, with their ratio changing as a function of temperature. The main transition in phospholipid membranes was, therefore, found to show the characteristics of a first order phase transition, in agreement with calorimetric experiments[24–26]

In out-of-plane scattering experiments, with good momentum resolution and corresponding high neutron coherence length, a continuous change of the lamellar d_z spacing is observed, as depicted in Fig. 6 for a coherence length of $\xi = 242$ Å, while a splitting of the Bragg peaks is observed at smaller coherence lengths. In the pure gel or fluid phase, all neighbouring membranes are in the same state, although different scenarios may develop in the transition region. The two neighbouring

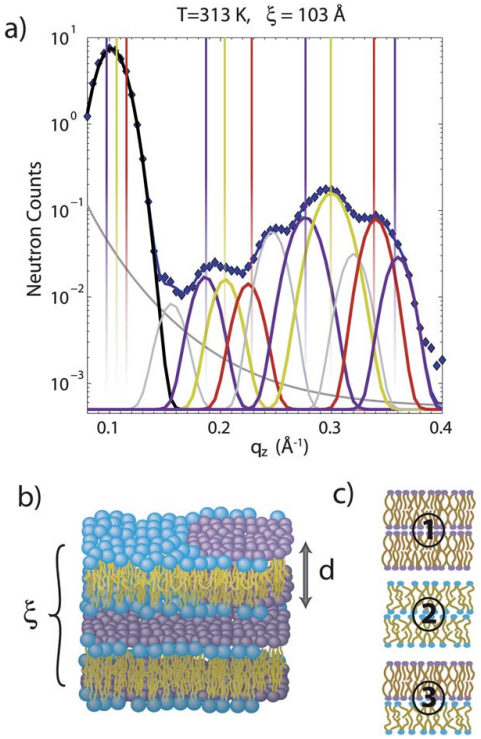

Fig. 7 a) Out-of-plane scattering curves of stacked DPPC membranes near the transition temperature ($T = 313$ K), probed with a coherence length of $\xi = 103$ Å. Fitting of the data reveals Bragg peaks from the different phases: fluid, gel, and intermediate phases. No fine structure of the first Bragg peak at around $q_{\|} = 0.10$ Å^{-1} could be resolved; it is, therefore, fit by a single peak (black line). Bragg peaks corresponding to the gel phase bilayers are shown in purple, those corresponding to fluid phase bilayers are shown in red, and those corresponding to mixed phase bilayers are shown in yellow. Additional peaks are shown in grey. b) Sketch of the multi-lamellar membrane patch with co-existing gel and fluid domains. c) Illustration of the three possible stacking scenario. Scenario 3 results in a d_z space which is the average of the fluid and gel spacing.

membranes may be: (1) both in the gel phase; (2) both in the fluid phase; or (3) one in the gel phase and the other in the fluid phase. The three scenarios are depicted in Fig. 7 c). When a gel region of the bilayer happens to be next to a fluid region, a long neutron coherence length (greater than $d_z^{gel} + d_z^{fluid}$) will average over the two d_z-spacings and result in an average d_z value between d_z^{gel} and d_z^{fluid}. The d_z spacing of 63 Å at $T = 313$ K, therefore, points to a multi-lamellar membrane structure with neighbouring gel and fluid domains. Based on this assumption, the critical coherence length ξ can be estimated to equal 126 Å. For ξ less than 126 Å, the neutron coherence only covers a single membrane, as shown in Fig. 7 b).

Fig. 7 shows a fit of the out-of-plane scattering curve measured at $\xi = 103$ Å (Fig. 6). Eleven Bragg peaks can be identified and could be fit to the data and assigned to different d_z spacings and

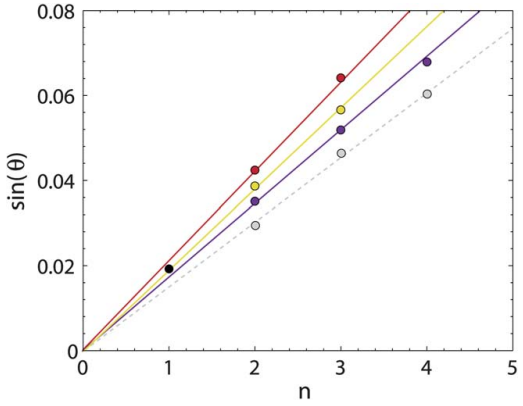

Fig. 8 Plot of $s\,i\,n\,(\theta) = \lambda n/2\,d$. Peaks belonging to the same d_z-spacing fall on a straight line through the origin. The 11 Bragg peaks fit in Fig. 7 a) can be assigned to 4 different d-spacings, namely, 56 Å, 63 Å, 70 Å, and 77 Å.

phases. To assign the peaks to different phases, Bragg's law can be re-written as $s\,i\,n\,(\theta) = \lambda n/2\,d$. Therefore, by plotting $sin(\theta)$ *vs.* the (estimated) order of the different Bragg reflections (n), peaks which belong to the same d_z-spacing will fall on a straight line through the origin. This plot is shown in Fig. 8. The 11 Bragg peaks can be assigned to 4 different d_z-spacings, namely, 56 Å, 63 Å, 70 Å, and 77 Å. The d_z spacings of 70 Å and 56 Å agree perfectly with the d_z spacings found in gel and fluid phase. The intermediate phase, with a d_z spacing of 63 Å, can be assigned to scenario (3), with neighbouring gel and fluid domains in the membrane stack. There is an additional series of reflections in Fig. 8. These peaks fall on a line through the origin with a slope corresponding to a d_z spacing of 77 Å. This d_z spacing does not correspond to one of the three proposed scenarios, gel, fluid and gel–fluid. However, it is well known that unexpected or quasi-forbidden Bragg peaks can appear in soft materials[44] to adapt to macroscopic constraints. The melting of a membrane patch from the gel to the fluid state inside a stack of membranes is sketched in Fig. 7 b). The size difference between d_z^{gel} and d_z^{fluid} would create a distortion of the multi-lamellar structure. Because the membrane stack is an elastic medium, this is associated with an energy cost. One way for the system to comply with the macroscopic constraints is to try to keep the overall thickness constant, by creating membranes with a larger d_z spacing to compensate for the difference $d_z^{gel} - d_z^{fluid}$. The observed spacing of $d_z = 77$ Å may correspond to the thickness of a DPPC bilayer where all the lipids are in all-*trans* configuration (*i.e.*, fully stretched out). This type of structure is not energetically favourable at high temperatures and just a consequence of the macroscopic constraints given by the membrane stack.

A comment is in order. Following the Gibbs' Phase Rule in condensed systems (without a co-existing gas phase) the number of independent intensive properties (F), such as temperature and pressure, depends on the number of components (C), and the number of co-existing phases in thermal equilibrium (P): F = C − P + 1. The observation of co-existing domains over a given temperature interval in a single lipid system implies F = 0, *i.e.*, a single point in temperature-pressure phase space (critical point). This observation of co-existing gel and fluid domains over a certain temperature range, therefore, seems to contradict the phase rule. Gibbs' rule, however, does not apply to *transient*, short lived domains, as discussed by Ehrig *et al.*[11] The fluctuation period of these transient domains was determined to be ~10 ns from experiment[10] (DMPC bilayers) and MD simulations[12] (DPPC bilayers). By tuning the energy resolution ΔE in the Table in Fig. 2, the neutron diffraction experiments can also become temporally sensitive. Time resolution is defined by $\tau = \hbar/\Delta E$. As the energy resolution is ~1 meV, only structures which fluctuate at times slower than 1 picosecond will lead to correlation peaks. The lower limit for the lifetime of the fluctuating structures observed in our experiment is, therefore, determined to be ~1 picosecond, in agreement to the MD simulations.

While this experiment proves the co-existence of domains in single-component phospholipid bilayers, future experiments will be conducted in multi-component lipid membranes and membranes containing cholesterol to detect possible raft structures. By scanning the neutron coherence length ξ, the size of those structures will be determined using the technique developed in this work.

5 Conclusions

The coherent properties of photons and neutrons are used to study structure and dynamics in elastic and inelastic X-ray and neutron scattering experiments. Matching the coherent properties of the scattering probe with those of the sample becomes important in soft-matter and biology because of: (1) the missing long ranged order; and (2) the large length scales involved. Good monochromaticity is a prerequisite for atomic resolution in crystal and protein structure determinations. Such radiation is also highly coherent with large coherence lengths, of the order of several thousands of Angstroems. A large coherence length may, however, average over small structures, such as nanoscale domains. By controlling ξ in a neutron diffraction experiment, we present direct experimental evidence for co-existing gel and fluid domains in a phospholipid bilayer. Instead of a continuous phase transition from the well ordered gel into the fluid phase, which adheres to a well-known critical behaviour, we observe a first order transition with a co-existence of gel and fluid domains.

Nanodomains are not only important to understand fundamental properties of model membranes, but also to better understand complex biological membranes and the formation and function of lipid rafts.[4,45,46] Additional examples are the recently emerging nanoferroelectrics[47] and nanoscale magnetic domains in thin magnetic films.[48] The development of neutron instrumentation which enables the control of the neutron coherence length can be envisioned for the future. Such an instrument would not only be important for the investigation of biological materials, but in all systems where fluctuating nanodomains determine material properties.

Acknowledgements

We thank the Canadian Neutron Beam Centre for the allocation of beam time and the staff at CNBC for their support. This

research was partially funded by the Natural Sciences and Engineering Research Council of Canada (NSERC), the Canada Foundation for Innovation (CFI), the Ontario Ministry of Economic Development and Innovation, and the National Research Council Canada (NRC). John Katsaras is supported through ORNL's Laboratory Directed Research and Development (LDRD), and Program Development programs.

References

1 D. M. Engelman, *Nature*, 2005, **438**, 578–580.
2 D. Lingwood and K. Simons, *Science*, 2009, **327**, 46–50.
3 K. Simons and E. Ikonen, *Nature*, 1997, **387**, 569–572.
4 C. Eggeling, C. Ringemann, R. Medda, G. Schwarzmann, K. Sandhoff, S. Polyakova, V. N. Belov, B. Hein, C. von Middendorf, A. Schönle and S. W. Hell, *Nature*, 2009, **457**, 1159–1162.
5 P.-F. Lenne and A. Nicolas, *Soft Matter*, 2009, **5**, 2841–2848.
6 T. Apajalahti, P. Niemelä, P. N. Govindan, M. S. Miettinen, E. Salonen, S.-J. Marrink and I. Vattulainen, *Faraday Discuss.*, 2010, **144**, 411–430.
7 E. Watkins, C. Millerb, J. Majewski and T. Kuhl, *Proc. Natl. Acad. Sci. U. S. A.*, 2011, **108**, 6975–6980.
8 M. C. Rheinstädter, W. Häussler and T. Salditt, *Phys. Rev. Lett.*, 2006, **97**, 048103.
9 P. S. Niemel, S. Ollila, M. T. Hyvnen, M. Karttunen and I. Vattulainen, *PLoS Comput. Biol.*, 2007, **3**, e34.
10 B. Bruning, E. Wald, W. Schrader, R. Behrends and U. Kaatze, *Soft Matter*, 2009, **5**, 3340–3346.
11 J. Ehrig, E. P. Petrov and P. Schwille, *New J. Phys.*, 2011, **13**, 045019.
12 T. Murtola, T. Róg, E. Falck, M. Karttunen and I. Vattulainen, *Phys. Rev. Lett.*, 2006, **97**, 238102.
13 G. Pabst, N. Kučerka, M.-P. Nieh, M. C. Rheinstädter and J. Katsaras, *Chem. Phys. Lipids*, 2010, **163**, 460–679.
14 G. Fragneto and M. Rheinstädter, *C. R. Phys.*, 2007, **8**, 865–883.
15 J. Pencer, T. Mills, V. Anghel, S. Kruegar, R. Epand and J. Katsaras, *Eur. Phys. J. E*, 2005, **18**, 447–458.
16 J. Pencer, V. Anghel, N. Kucerka and J. Katsaras, *J. Appl. Crystallogr.*, 2006, **39**, 791–796.
17 V. Anghel, N. Kucerka, J. Pencer and J. Katsaras, *J. Appl. Crystallogr.*, 2007, **40**, 513–525.
18 J. Pencer, V. Anghel, N. Kucerka and J. Katsaras, *J. Appl. Crystallogr.*, 2006, **39**, 791–796.
19 C. Nicolini, P. Thyagarajan and R. Winter, *Phys. Chem. Chem. Phys.*, 2004, **6**, 5531–5534.
20 M. Rappolt, G. Pabst, G. Rapp, M. Kriechbaum, H. Amenitsch, C. Krenn, S. Bernstroff and P. Laggner, *Eur. Biophys. J.*, 2000, **29**, 125–133.
21 G. Pabst, S. Danner, G. Deutsch and A. Raghunathan, *Biophys. J.*, 2007, **93**, 513–525.
22 P. Sens and M. Turner, *Phys. Rev. Lett.*, 2011, **106**, 238101.
23 A. Sergé, N. Bertaux, H. Rigneault and D. Maruet, *Nat. Methods*, 2008, **5**, 687–694.
24 S. Mabrey and J. Sturtevant, *Proc. Natl. Acad. Sci. U. S. A.*, 1976, **73**, 3862–3866.
25 S. Andersen, A. Jackson and T. Heimburg, *Prog. Neurobiol.*, 2009, **88**, 104–113.
26 T. Heimburg and D. Jackson, *Proc. Natl. Acad. Sci. U. S. A.*, 2005, **102**, 28.
27 P. Mason, J. Nagle, R. Epand and J. Katsaras, *Phys. Rev. E: Stat. Phys., Plasmas, Fluids, Relat. Interdiscip. Top.*, 2001, **63**, 030902.
28 G. Pabst, J. Katsaras, V. A. Raghunathan and M. Rappolt, *Langmuir*, 2003, **19**, 1716–1722.
29 R. Zhang, W. Sun, S. Tristram-Nagle, R. L. Headrick, R. M. Suter and J. F. Nagle, *Phys. Rev. Lett.*, 1995, **74**, 2832–2835.
30 J. Lemmich, K. Mortensen, J. Ipsen, T. Hø nger, R. Bauer and O. Mouritsen, *Phys. Rev. Lett.*, 1995, **75**, 3958.
31 F. Chen, W. Hung and H. Huang, *Phys. Rev. Lett.*, 1997, **79**, 4026–4029.
32 J. Nagle, H. Petrache, N. Gouliaev, S. Tristram-Nagle, Y. Liu, R. Suter and K. Gawrisch, *Phys. Rev. E: Stat. Phys., Plasmas, Fluids, Relat. Interdiscip. Top.*, 1998, **58**, 7769–7776.
33 G. Fragneto, T. Charitat, E. Bellet-Amalric, R. Cubitt and F. Graner, *Langmuir*, 2003, **19**, 7695–7702.
34 N. Chu, N. Kučerka, Y. Liu, S. Tristram-Nagle and J. F. Nagle, *Phys. Rev. E: Stat., Nonlinear, Soft Matter Phys.*, 2005, **71**, 041904.
35 T. Salditt, *J. Phys.: Condens. Matter*, 2005, **17**, R287–R314.
36 T. Salditt, *Curr. Opin. Colloid Interface Sci.*, 2000, **5**, 19–26.
37 M. Vogel, C. Münster, W. Fenzl and T. Salditt, *Phys. Rev. Lett.*, 2000, **84**, 390–393.
38 M. Rheinstädter, C. Ollinger, G. Fragneto, F. Demmel and T. Salditt, *Phys. Rev. Lett.*, 2004, **93**, 108107.
39 H. Rauch, *Found. Phys.*, 1993, **23**, 7–36.
40 G. Squires, *Introduction to the theory of thermal neutron scattering*, Dover Publications, Inc., Mineola, New York, 1978.
41 N. Kučerka, Y. Liu, N. Chu, H. I. Petrache, S. Tristram-Nagle and J. F. Nagle, *Biophys. J.*, 2005, **88**, 2626–2637.
42 J. Katsaras, R. F. Epand and R. M. Epand, *Phys. Rev. E: Stat. Phys., Plasmas, Fluids, Relat. Interdiscip. Top.*, 1997, **55**, 3751–3753.
43 S. Leekumjorn and A. Sum, *Biochim. Biophys. Acta, Biomembr.*, 2007, **1768**, 354–365.
44 S. Förster, A. Timmann, C. Schellbach, A. Frömsdorf, A. Kornowski, H. Weller, S. Roth and P. Lindner, *Nat. Mater.*, 2007, **6**, 888–893.
45 J. Oelke, A. Pasc, A. Wixforth, O. Konovalov and M. Tanaka, *Appl. Phys. Lett.*, 2008, **93**, 213901.
46 H. J. Risselada and S. J. Marrink, *Proc. Natl. Acad. Sci. U. S. A.*, 2008, **105**, 17367–17372.
47 J. Scott, *Science*, 2007, **315**, 954–959.
48 O. Shpyrko, E. Isaacs, J. Logan, Y. Feng, G. Aeppli, R. Jaramillo, H. Kim, T. Rosenbaum, P. Zschack, M. Sprung, S. Narayanan and A. Sandy, *Nature*, 2007, **447**, 68–71.

Preface to Paper VI

In this study, inelastic neutron scattering experiments on 5 mol and 40 mol% cholesterol in DMPC bilayer was performed at the High-Flux reactor at Institut Laue-Langevin (ILL) in Grenoble, France. The excitation spectrum of the samples was measured to high lateral values ($\overrightarrow{q}_{\parallel}$=3 Å^{-1}). By comparing the low cholesterol and high cholesterol samples it was apparent that the inclusion of cholesterol was responsible for a pronounced stiffening of the hydrocarbon tails of the membrane for gel and fluid bilayers, even though the bilayer was more disordered in this state. The nano-scale dynamics of the high-cholesterol liquid ordered phase was also elucidated, appearing softer than fluid bilayers, but more ordered than gel bilayers.

These experiments were done on the IN8 thermal triple-axis spectrometer and the IN12 cold triple-axis spectrometer at ILL. The data was analyzed at McMaster by Clare Armstrong. My role was to determine neutron scattering length distributions to determine the position of the cholesterol molecules in the DMPC bilayers. To do so I used Matlab code that I developed for the x-ray experiments. The macro was modified to give neutron scattering length density, rather than electron density plots. Figure 4 b,c,d show the process of the Fourier transform to determine the neutron scattering length density. From this plot we can say with confidence that the cholesterol molecules are participating in the DMPC bilayer, and can pinpoint the position of the cholesterol and lipid molecules.

Eur Biophys J
DOI 10.1007/s00249-012-0826-4

ORIGINAL PAPER

EBSA
Biophysics in Europe

Effect of cholesterol on the lateral nanoscale dynamics of fluid membranes

Clare L. Armstrong · Matthew A. Barrett · Arno Hiess · Tim Salditt · John Katsaras · An-Chang Shi · Maikel C. Rheinstädter

Received: 2 March 2012 / Revised: 3 May 2012 / Accepted: 7 May 2012

Abstract Inelastic neutron scattering was used to study the effect of 5 and 40 mol% cholesterol on the lateral nanoscale dynamics of phospholipid membranes. By measuring the excitation spectrum at several lateral $q_{\parallel}$ values (up to $q_{\parallel} = 3$ Å^{-1}), complete dispersion curves were determined of gel, fluid and liquid-ordered phase bilayers. The inclusion of cholesterol had a distinct effect on the collective dynamics of the bilayer's hydrocarbon chains; specifically, we observed a pronounced stiffening of the membranes on the nanometer length scale in both gel and fluid bilayers, even though they were experiencing a higher degree of molecular disorder. Also, for the first time we determined the nanoscale dynamics in the high-cholesterol liquid-ordered phase of bilayers containing cholesterol. Namely, this phase appears to be "softer" than fluid bilayers, but better ordered than bilayers in the gel phase.

Keywords Lipid membrane · Cholesterol · Lateral membrane dynamics · Nanoscale dynamics · Liquid-ordered phase · Inelastic neutron scattering · Dispersion relation

Special Issue: Scattering techniques in biology: marking the contributions to the field from Peter Laggner on the occasion of his 68th birthday.

C. L. Armstrong (✉) · M. A. Barrett · A.-C. Shi · M. C. Rheinstädter
Department of Physics and Astronomy, McMaster University, ABB-241, 1280 Main Street West, Hamilton, ON L8S 4M1, Canada
e-mail: armstc5@mcmaster.ca

A. Hiess
European Spallation Source ESS AB, P.O. Box 176, 22100 Lund, Sweden

T. Salditt
Institute for X-Ray Physics, Georg-August-University Göttingen, Friedrich-Hund-Platz 1, 37077 Göttingen, Germany

J. Katsaras
Neutron Sciences Directorate, Oak Ridge National Laboratory, Oak Ridge, TN 37831-6100, USA

J. Katsaras · M. C. Rheinstädter (✉)
Canadian Neutron Beam Centre, National Research Council, Chalk River, ON K0J 1J0, Canada
e-mail: rheinstadter@mcmaster.ca

Introduction

Cholesterol is an essential structural component of eukaryotic cell membranes capable of modulating their permeability and molecular organization. It is either obtained from foods of animal origin or synthesized in the endoplasmic reticulum, a multifold membranous structure that is also capable of producing phospholipids, including different types of membranes (Ridsdale et al. 2006). In association with lipid rafts (i.e., functional domains), cholesterol has also been implicated in cell signaling processes (Simons 1997; Brown 2000; Petrie et al. 2000; Papanikolaou et al. 2005; Pike 2006).

Cholesterol and saturated lipid species preferentially partition into liquid-ordered domains, away from unsaturated, liquid-disordered lipid species. In particular, cholesterol, because of its rigid planar structure, preferentially interacts with sphingolipids (e.g., sphingomyelin) and their highly ordered saturated hydrocarbon chains, but not exclusively (Pike 2009). Moreover, cholesterol has been shown to interact strongly with phosphatidylcholine (PC) lipids that have saturated hydrocarbon chains (Vist 1990).

Published online: 23 June 2012

In pure lipid bilayers, cholesterol modulates the molecular organization of lipids, namely by disrupting the regular packing of gel phase di-saturated PC membranes and restricting the reorientation of these same membranes when in the liquid-disordered phase (Vist 1990). However, at sufficiently high concentrations of cholesterol (i.e., >25 mol%), the so-called liquid-ordered state, which is characterized by rapid hydrocarbon chain reorientation but high conformational order, is formed over a wide range of temperatures smearing out the traditional gel and liquid crystalline phases (Fig. 1) (Mouritse 2010).

Although cholesterol is known to modulate the behavior of membranes, in the recent past it has been shown that lipid bilayers made of polyunsaturated fatty acids (PUFAs, namely, di-20:4 PC) can cause cholesterol to sequester to the bilayer center (i.e., laying flat with its hydroxyl group in the middle of the bilayer) (Harroun et al. 2006, 2008), a location that is significantly different from cholesterol's nominal upright orientation, where its hydroxyl group is located near the lipid/water interface (Léonard et al. 2001). However, the addition of just 5 mol% of dimyristoyl phosphatidylcholine (DMPC, di-14:0 PC) to those same PUFA bilayers causes cholesterol to revert to its nominal upright orientation (Kučerka 2009). This has been explained in terms of the "umbrella" model (Petrie et al. 2000; Papanikolaou et al. 2005), which suggests that cholesterol molecules associate strongly with ordered hydrocarbon chains (usually ones that are fully saturated) in such a manner that they are shielded from contact with the aqueous environment by the lipid head group. It seems obvious then that, although cholesterol can modulate the structural (e.g., chain packing) and mechanical (e.g., bending modulus) properties of bilayers, the bilayers themselves can, on the other hand, also modulate cholesterol's behavior.

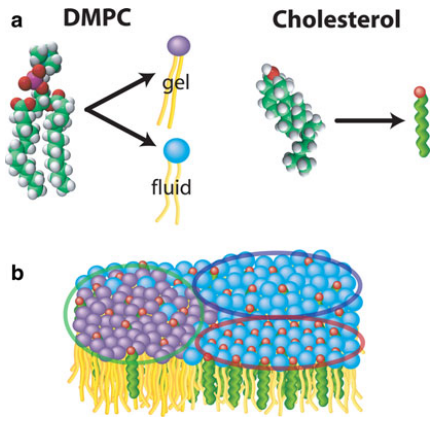

Fig. 1 **a** Schematic representations of DMPC and cholesterol molecules. In the gel phase, the lipids tails are in the all-trans configuration. At the main transition temperature lipid hydrocarbon tails "melt", resulting in fluid phase bilayers. **b** Schematic model of the possible phases present in DMPC/cholesterol systems. The gel, fluid and liquid-ordered phases are highlighted by the *green*, *blue* and *red circles*, respectively

We have studied the short wavelength fluctuations in DMPC membranes containing 5 and 40 mol% cholesterol using inelastic neutron scattering. Complete dispersion relations of gel, fluid and liquid-ordered membranes were obtained by measuring the excitation at different lateral momentum transfers. From experimentally obtained spectra, we were able to extract the "softness" of the hydrocarbon membrane core on the nanometer length scale, a length scale comparable to molecular distances within the membrane. We found that the bilayer's hydrocarbon core became significantly less fluid in the presence of cholesterol. In the liquid-ordered state, however, the system not only assumed a high degree of molecular order (associated with the high cholesterol content), but there was a concomitant softening of the nanoscale elastic properties, a feature more akin to fluid bilayers.

Materials and methods

Sample preparation

Highly oriented multi-lamellar stacks of 1,2-dimyristoyl-sn-glycero-3-phosphocholine (DMPC) and cholesterol were prepared on 2-inch-diameter, 300-μm-thick, single-side polished Si wafers. The coherent scattering of the lipid hydrocarbon chains was enhanced by using tail deuterated lipids, i.e., DMPC-d54. The use of protonated cholesterol enabled the experiment to detect changes in hydrocarbon chain structure and dynamics. A 20 mg/ml suspension of DMPC-d54 and cholesterol dissolved in 1:1 chloroform and 2,2,2-trifluoroethanol (TFE) was prepared. Two different samples were fabricated for this study; specifically, a sample containing 5 mol% cholesterol and another with 40 mol% cholesterol, a concentration found in biological membranes. The Si wafers were cleaned by alternate 12-min sonications in ultra-pure water and ethanol at 313 K. This process was repeated twice. Then 1 ml of the lipid solution was deposited on each Si wafer and allowed to dry. The wafers were kept in a vacuum overnight to remove all traces of the solvent. The samples were then hydrated with heavy water (D_2O) and annealed at 303 K for 24 h. Following this protocol, each wafer contained roughly 3,000 highly oriented membranes, totaling $\sim$10 μm in thickness.

Twenty sample-containing Si wafers were stacked with 0.6-mm aluminium spacers placed in between each wafer to enable proper hydration of the membranes. The stack of

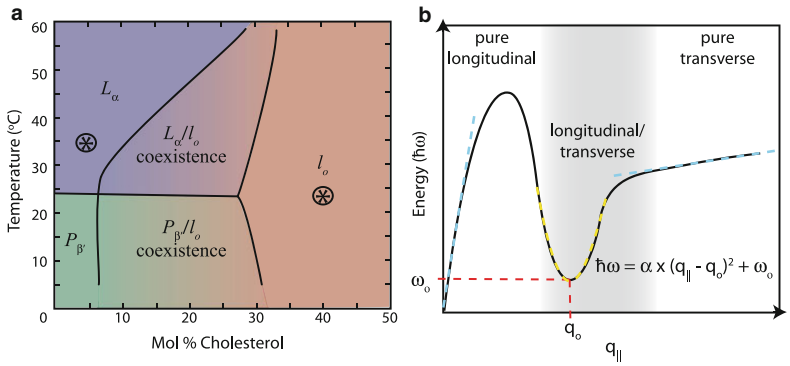

Fig. 2 **a** Schematic phase diagram of a DMPC cholesterol system as reported by, e.g., Vist 1990; Almeida et al. 1992; Thewalt and Bloom 1992; de Meyer 2009; de Meyer et al. 2010. Besides the well-known gel and fluid phase, the so-called liquid-order phase, is observed at high cholesterol concentrations. The 5 mol% cholesterol sample is in the L_α phase, while the 40 mol% sample is clearly in the l_o phase, as depicted by the ⊛. **b** A typical lateral dispersion curve observed in lipid systems (see, e.g., Chen et al. 2001; Weiss et al. 2003; Chen et al. 2003; Rheinstädter et al. 2004a; Tarek et al. 2001; Hub et al. 2007; Kaye et al. 2011). The $q_{\|}$ range around the minimum is well described by a parabolic fit. The dispersion is linear at small $q_{\|}$ values due to high-frequency sound propagation with longitudinal polarization. The high-$q_{\|}$ regime is also linear; however, a transverse polarization has been previously observed

Si wafers were kept in a temperature- and humidity-controlled aluminium chamber, a so-called humidity chamber, during the course of the experiment. Hydration of the lipid membranes from the vapor phase was achieved by separately adjusting the temperature of the heavy water reservoir, the "sandwich" stack of Si wafers and the sample chamber's cover. Temperature and humidity sensors were installed close to the sample, and a water bath was used to control the temperature of the water reservoirs. Using this setup, a lamellar repeat spacing (d_z-spacing) of 53.1 Å was achieved for the fluid phase low cholesterol sample, which is comparable to the fluid phase of pure DMPC. For example, from the published values for d_z as a function of relative humidity (RH) published for pure DMPC (Kučerka 2005), the hydration of the DMPC bilayers in this experiment is estimated to be $\sim$99.5% (100% RH corresponds to fully hydrated bilayers) (Katsaras 1998).

The samples were mounted vertically in the neutron beam such that the scattering vector (**Q**) could either be placed in the plane of the membrane ($\mathbf{q}_{\|}$) or perpendicular to the membrane ($\mathbf{q}_z$). Out-of-plane and in-plane structure could be measured by simply rotating the sample by 90°.

The phase diagram of phospholipid membranes containing different amounts of cholesterol remains an active field of research (Vist 1990, Almeida et al. 1992; Thewalt and Bloom 1992; de Meyer 2009; de Meyer et al. 2010). A schematic phase diagram of DMPC/cholesterol membranes is shown in Fig. 2a. It has been speculated that the relatively stiff cholesterol molecules align parallel to the hydrocarbon lipid tails and suppress lipid tail fluctuations (Róg et al. 2009), thereby affecting the membrane's dynamical properties. Most studies agree that three phases are observed, depending on temperature and cholesterol concentration: the rigid gel (ripple) $P_{\beta'}$ phase, the fluid L_α phase and the liquid-ordered l_o phase. The gel and fluid phases are well known from single component phospholipid bilayers. However, the l_o phase is solely observed at high concentrations of cholesterol. This bilayer phase is somewhat peculiar as it appears to be well ordered (similar to the gel phase); however, the lipids exhibit a diffusion coefficient that is comparable to that of fluid bilayers.

At low cholesterol content the bilayers undergo a phase transition from the gel to the fluid phase, as in pure lipid bilayers. The temperature of this so-called main transition T_m is slightly shifted towards higher temperatures. However, at high cholesterol concentrations ($\gtrsim$40 mol%), the main transition of liquid-ordered membranes was found to be suppressed, while at intermediate cholesterol concentrations (i.e., between about 10–30 mol%) most studies report a coexistence between gel and l_o, or L_α and l_o phases. The 5 mol% cholesterol sample was measured at $T = 308$ K (35 °C), while all scans for the 40 mol% sample were conducted at $T = 297$ K (24 °C). These temperatures were selected based on the schematic phase diagram in Fig. 2a. In an attempt to measure the system in one phase, temperatures were chosen far from the speculated phase boundaries. The phases at which these samples were studied are shown in Fig. 2a. The 5 mol% sample is, therefore, made up of fluid phase DMPC bilayers. As the phase transition was found to be suppressed in the l_o phase, the temperature is not a critical parameter for the high cholesterol sample.

Neutron-scattering experiment

Experiments were conducted using two different triple-axis spectrometers (TAS) co-located at the Institut Laue-Langevin high flux neutron reactor (Grenoble, France). The three axis of the spectrometers refer to the axes of rotation of the monochromator, the sample and the analyzer. The incident and final neutron energies are defined by the Bragg reflections from pyrolytic graphite (PG) crystals. Divergence of the neutron beam is controlled by several neutron Soller collimators. A schematic of the instrument configuration is shown in Fig. 3. In-plane and out-of-plane structure and dynamics can be measured simultaneously on a TAS by simply rotating the sample by 90°.

Neutrons with energies up to 20 meV were measured on the thermal TAS IN8 instrument with an energy resolution of $\sim$1 meV. Cold neutron spectrometers are inherently higher energy resolution instruments and enable the measurement of low-energy excitations (up to $\sim$5 meV). These measurements were conducted on the cold TAS IN12, which has an energy resolution of $\sim$0.2 meV.

The energy and $q_{\|}$ resolution of a neutron triple-axis spectrometer are determined by the incident neutron energy, the divergence of the neutron beam and the wavelength resolution of the monochromator and analyzer. The incident energies, energy range, $q_{\|}$ range and resolution of the two spectrometers used for this study are listed in Table 1. By combining a cold and thermal TAS, a $(\hbar\omega, q_{||})$ range of 0.4 $\text{Å}^{-1} < q_{\|} < 3$ Å^{-1} and energies of up to $\sim$20 meV were accessible. As a result, our experiments were sensitive to picosecond dynamics in the plane of the membrane, covering length scales from between 2 and $\sim$20 Å. These distances range from less than a lipid-lipid interaction to one encompassing almost three lipid molecules.

Results

Neutron diffraction

Our setup permitted for the determination of the out-of-plane and in-plane structure of 2 mol% cholesterol/membrane samples. By rotating the sandwich sample by 90°, the scattering geometry can be switched (with respect to the Si substrates) from transmission to grazing incidence. To study in-plane structure ($\mathbf{q}_{||}$), the scattering vector $\mathbf{Q}$ is located in the plane of the membrane (i.e., transmission geometry). In grazing incidence, $\mathbf{Q}$ is normal to the Si and membrane plane ($\mathbf{q}_z$), enabling us to study out-of-plane structure.

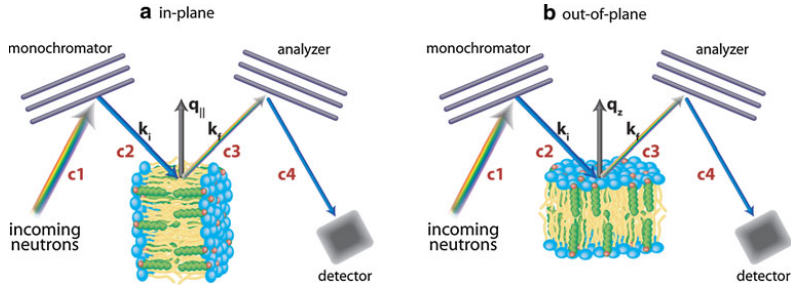

Fig. 3 Schematic representation of a triple axis spectrometer geometry. **a** Orientation of the sample for in-plane scans such that $\mathbf{Q}$ is in the plane of the membrane ($\mathbf{q}_{||}$). **b** Orientation of the sample for out-of-plane scans such that $\mathbf{Q}$ is perpendicular to the plane of the membrane ($\mathbf{q}_z$). $\mathbf{k_i}$ and $\mathbf{k_f}$ are the incident and final wave vectors, respectively; $c1$–$c4$ indicate the positions of the neutron collimators that were used to control the $\mathbf{Q}$ and energy resolutions

Table 1 $q_{\|}$ and q_z and energy resolutions of the two spectrometers used in this study

Instrument	Incident neutron energy (meV)	Accessible energy range (meV)	Energy resolution (meV)	Accessible $q_{\|}$ range (Å^{-1})	$q_{\|}$ resolution (Å^{-1})
IN12	4.7	0–5	0.165	0–3	0.01
IN8	14.7	0–25	1.01	0–3	0.02

Instrumental setup, including collimation, was 30′–monochromator–30′–sample–30′–analyzer–60′–detector on IN12 and ø–monochromator–30′–PG filter–sample–30′–analyzer–ø–detector on IN8

In-plane structure

The lipid acyl chain positional correlation peak is the result of closely packed acyl chains making up the hydrophobic core of the membrane, as shown in Fig. 4a. The Bragg peaks from the two samples are well fit by Lorentzians. The peak in the 40 mol% sample is more pronounced and slightly shifted toward smaller $q_{||}$-values. This implies an enhanced order of the lipid tails at 40 mol% cholesterol. The distance between two lipid chains increases from 4.53 Å ($q_{||} = 1.39$ Å^{-1}) to 4.59 Å ($q_{||} = 1.37$ Å^{-1}), as determined from the fits to the Bragg peaks ($d = 2\pi/q_{||}$). The widths of the Bragg peaks also increase, albeit slightly, from $\Delta q_{||} = 0.13$ Å^{-1} to $\Delta q_{||} = 0.14$ Å^{-1}, which indicates a larger distribution of nearest-neighbor distances. The presence of cholesterol molecules seems to have little effect on hydrocarbon chain packing. The packing of lipid acyl chains is the result of a balance between attractive and repulsive forces resulting from tail fluctuations, i.e., between the free energy and entropy of the hydrocarbon tails. Incorporation of cholesterol molecules should, in theory, drastically increase the area per lipid. However, the area per lipid in the presence of cholesterol is comparable to lipid areas found in pure lipid bilayers, as cholesterol is believed to suppress hydrocarbon chain fluctuations.

It should be noted that the curves in Fig. 4a have not been shifted with respect to each other. The background in the 40 mol% sample is drastically increased because of the presence of protonated cholesterol, which contributes to the strong incoherent background.

Out-of-plane structure

Specular reflectivity allows for the determination of bilayer structure perpendicular to the plane of the membrane [see, e.g., Pabst 2010; Fragneto 2007]. The intensity of the

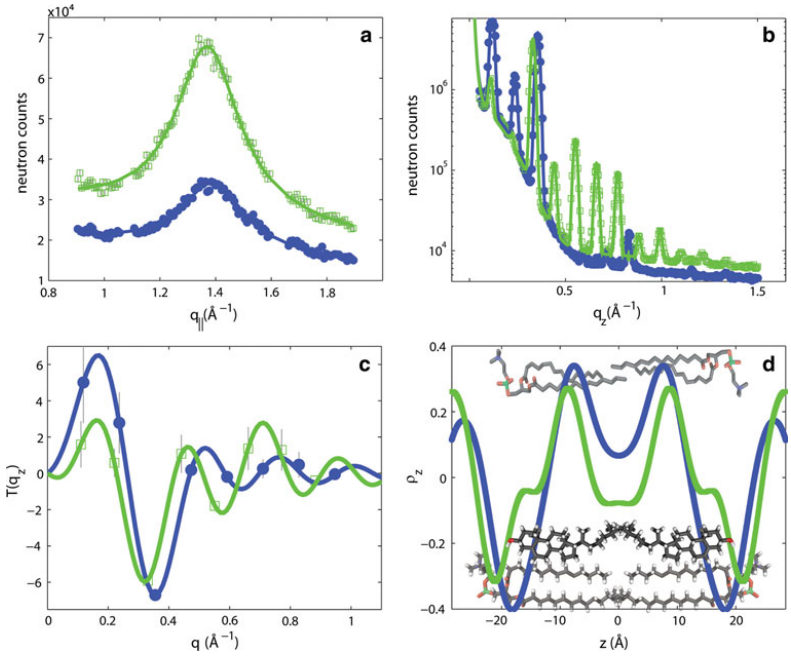

Fig. 4 Overview of the diffraction data: the *blue solid lines* and data points correspond to the 5 mol% cholesterol sample, while the *green solid lines* and data points refer to the 40 mol% cholesterol sample. **a** In-plane scattering ($q_{||}$) used to measure the acyl chain-chain positional correlation peak. Two spurious Bragg peaks from the humidity chamber at $\sim$1.1 Å^{-1} and $\sim$1.65 Å^{-1} were omitted from the scans. The *solid lines* are the Lorentzian fits to the experimental data. **b** Out-of-plane scattering (q_z) and the observation of several Bragg peaks. The position and area of each Bragg peak was determined through the fitting of a Gaussian, including the q^{-4} background. **c** $T(q_z)$, as determined by Eq. (4). Data points correspond to the integrated intensities of the different out-of-plane Bragg peaks from (**b**). The phases v_n are determined by the sign of $T(q_z)$ at the q_z position of the corresponding Bragg reflection. **d** Scattering density profile, ρ_z, calculated using Eq. (3). The location of the cholesterol molecules within the lipid bilayer can be deduced by the ρ_z of the two different mol% cholesterol membranes (5 mol%, blue; 40 mol%, *green*). Lipid and cholesterol molecules are shown schematically. The data shown were collected using the IN8 thermal TAS

reflected beam as a function of the perpendicular momentum transfer, q_z, is given by:

$$R(q_z) = \frac{16\pi^2}{q_z^2}|\hat{\rho}(q_z)|^2, \quad (1)$$

where $\hat{\rho}(q_z)$ is the one-dimensional Fourier transform of the neutron scattering length density and is defined by:

$$\hat{\rho}(q_z) = \int_{-\infty}^{\infty} \exp(iq_z z)\rho(z)dz. \quad (2)$$

Because the membranes are stacked (i.e., there is a convolution with the lamellar structure factor), the Fourier transform is not continuous, but discrete. The different Fourier components are observed in the experiment as the integrated intensities of the out-of-plane Bragg peaks. $\rho(z)$ is approximated by a 1D Fourier analysis (Tristram-Nagle et al. 2002) as follows:

$$\begin{aligned}\rho(z) &= \rho_W + \frac{F(0)}{d_z} + \frac{2}{d_z}\sum_{n=1}^{N} F(q_n)v_n \cos(q_n z) \\ &= \rho_W + \frac{F(0)}{d_z} + \frac{2}{d_z}\sum_{n=1}^{N} \sqrt{I_n q_n} v_n \cos\left(\frac{2\pi n z}{d_z}\right), \end{aligned} \quad (3)$$

where N is the highest order Bragg peak observed experimentally, and ρ_W is the scattering length density of bulk water. The integrated peak intensities, I_n, are multiplied by q_n to retrieve the form factors, $F(q_n)$ (Nagle 1989, Nagle et al. 1996). We note that Eq. (3) is used to calculate absolute scattering length densities if the curves are normalized by using $F(0)$ and ρ_W. As the setup used in this study is not optimized for quantitative reflectivity measurements, we present relative rather than absolute scattering length densities. By comparing the two samples, these measurements can be used to determine the position of molecules within the bilayers, as will be shown below.

The bilayer form factor $F(q_z)$, which is in general a complex quantity, is real in the case of centro-symmetry. The ubiquitous crystallographic phase problem, therefore, simplifies to $F(q_z) = \pm|F(q_z)|$, where the phases, v_n, can only take on values of ± 1. Assigned values for v_n are needed to reconstruct the scattering length density profile from the data following Eq. (3). When the membrane form factor $F(q_z)$ is measured at several q_z values, a continuous function, $T(q_z)$, which is proportional to $F(q_z)$, can be fit to the data (Nagle 1989; Nagle et al. 1996; King 1971; Adachi 2000):

$$T(q_z) = \sum_n \sqrt{I_n q_n}\ \mathrm{sinc}(\pi d_z q_z - \pi n). \quad (4)$$

Once an analytical expression for $T(q_z)$ has been determined from fitting the various Bragg peaks, the v_n values can be determined from $T(q_z)$. The d_z-spacing between two neighboring membranes in the stack can be determined from the positions of the Bragg reflections ($d_z = 2\pi/\Delta q_z$) along the out-of-plane axis, q_z.

Figure 4b shows out-of-plane scans for the 5 and 40 mol% cholesterol samples. Up to ten distinct Bragg peaks are observed and are used to reconstruct the scattering length density. Figure 4c, d displays $T(q_z)$ and relative scattering length densities as determined using Eqs. (4) and (3). $T(q_z)$ was fitted to the experimentally determined peak intensities using Eq. (4) to calculate an array of v_n values out of the corresponding 2^{10} combinations, assuming a phase of $+1$ or -1. Figure 4c shows the best fits to the data. Both samples were well fitted using the following combination of phases: $11\bar{1}1\bar{1}1\bar{1}1\bar{1}$. The resulting scattering length densities are plotted in Fig. 4d. This type of sample preparation (chain deuterated lipids hydrated by heavy water) accentuates the water contribution, i.e., the layer between the membranes at $\sim$24 Å. The minima at about 20 Å correspond to the protonated lipid head groups. The scattering length density then increases toward the bilayer centre, i.e., $z = 0$. The sharp dip at the centre of the 5 mol% cholesterol sample is the tell-tale sign of a fluid membrane, i.e., the increasing number of kink-defects lower the density of the lipid tails in the bilayer centre.

At 40 mol% cholesterol, a peak at $\sim$18 Å appears, and the density at the membrane centre experiences a further decrease, showing a plateau, however, instead of a dip. Lipid and cholesterol molecules can tentatively be fit to this structure, and are schematically illustrated in Fig. 4d. The peak at $\sim$18 Å is most likely related to the presence of the hydrophilic head of the cholesterol molecule (Léonard et al. 2001). Since cholesterol makes up 40 mol% of the membrane, the density of carbon atoms in the centre of the membrane is further reduced, as cholesterol has a single chain compared to the two acyl chains of a lipid molecule. It seems, however, that the presence of cholesterol suppresses lipid tail fluctuations, as the scattering length density in the membrane centre remains constant. Our data (Fig. 4) support the notion that cholesterol molecules assume an upright orientation (Léonard et al. 2001) with their hydrophilic head residing in the lipid head group region. The data in Fig. 4 are in excellent agreement with neutron diffraction results in cholesterol-containing polyunsaturated lipid membranes (18:0-22:6n3-PC) (Mihailescu et al. 2011), where the cholesterol molecule was also found in an upright position. This observation is also consistent with the commonly accepted umbrella model of cholesterol interaction with lipid bilayers (Huang 1999).

Membrane dynamics

Motions in lipid membranes range from long wavelength undulation and bending modes, with typical relaxation

times on the order of nanoseconds and lateral length scales of several hundred lipid molecules (i.e., tens of nanometers), to short wavelength density fluctuations in the picosecond range and nearest-neighbor length scales (Rheinstädter et al. 2004a, Pfeiffer et al. 1989; König et al. 1992; Pfeiffer et al. 1993; König et al. 1994, 1995; Lipowsky and Sackmann 1995; Lindahl and Edholm 2000; Bayerl 2000; Salditt 2000; Rheinstädter et al. 2005, 2006, 2007) Different techniques have been used to study the different types of motions. For example, local dynamics in lipid bilayers (i.e., individual lipid molecules), such as vibration, rotation, libration (hindered rotation) and diffusion, have been investigated by incoherent neutron scattering (König et al. 1992, 1994, 1995; Pfeiffer et al. 1993; Meinhold et al. 2007) and nuclear magnetic resonance (NMR) (Bloom and Bayerl 1995; Nevzorov and Brown 1997) in order to determine the short wavelength translational and rotational diffusion constants. On the other hand, collective bilayer undulations have been examined by coherent scattering experiments using neutron spin-echo spectrometers (Pfeiffer et al. 1993, Rheinstädter et al. 2005, Meinhold et al. 2007, Takeda et al. 1999) and Dynamic Light Scattering (DLS) (Hirn et al. 1999; Hirn and Bayerl 1999; Hildenbrand and Bayerl 2005). TAS has been shown to be a well suited technique for the study of collective membrane dynamics (Rheinstädter et al. 2004a; Kaye et al. 2011; Rheinstädter et al. 2006b; Rheinstädter et al. 2009; Armstrong et al. 2011; Rheinstädter et al. 2004; Rheinstädter 2008). The dynamics that we are interested in are the propagation of short-wavelength density waves in the plane of the membrane, which can be thought of in terms of phonon-like excitations. These collective molecular motions determine, for instance, the elasticity of membranes (Rheinstädter et al. 2006a) and are speculated to be relevant for interactions between membrane embedded proteins (Rheinstädter et al. 2009) and membrane transport properties (Rheinstädter et al. 2004a; Kaye et al. 2011; Paula et al. 1996). Propagating modes lead to peaks in the neutron spectra at well-defined excitation energies. By measuring the excitation energies at different $q_{\|}$ values, i.e, different length scales, complete dispersion relations can be determined. However, we would like to point out that these types of dynamics are different from relaxational dynamics. A well-known example of a relaxation process in lipid membranes is the diffusion of lipids and other molecules in the plane of the membrane. The eigenfrequency of a relaxation dynamic is $\hbar\omega = 0$, which leads to a quasi-elastic broadening of the central line of the neutron spectra. Relaxational dynamics are usually slow (on the order of nano- to microseconds), while the propagating modes take place on the picosecond time scale. The two types of dynamics can be well distinguished in inelastic neutron scattering experiments. For example, diffusion is determined by measuring the broadening of the quasi-elastic peak, while in the case of propagating wave-like excitations (which are of particular interest to us), they are observed as inelastic peaks at excitation energies $\hbar\omega \neq 0$ meV.

A typical lipid dispersion relation in lipid membranes is shown in Fig. 2b. This in-plane dispersion relation was determined using several techniques in DMPC and DLPC—i.e., inelastic X-ray scattering (Chen et al. 2001, 2003; Weiss et al. 2003), inelastic neutron scattering (Rheinstädter et al. 2004a, Rheinstädter et al. 2004) and molecular dynamics (MD) simulations (Tarek et al. 2001; Hub et al. 2007; Kaye et al. 2011). The lipid dispersion curve has a generic shape, namely at small $q_{\|}$ values (long length scales) there is a linear region $\hbar\omega \propto q_{||}$ as the excitation propagates in the form of long-wavelength sound waves. The dispersion then goes through a maximum before a minimum is observed close to the nearest-neighbor distance (~ 1.5 Å^{-1}) of two lipid acyl tails. Beyond this minimum, a second linear regime is observed at high $q_{\|}$. Recently Kaye et al. 2011. studied the polarization of these excitations by combining neutron scattering and MD simulations. In a longitudinal wave, the C-atoms of the hydrocarbon tails are displaced along the direction of the propagating wave—in a transverse wave, particles are displaced perpendicular to the propagation direction. According to Kaye et al. (2011), the long-wavelength modes are purely longitudinal in nature. At high in-plane momentum transfers $q_{\|}$ (i.e., beyond the dispersion minimum), pronounced transverse properties were observed. However, in the vicinity of the dispersion minimum, the excitations have a mixed, longitudinal and transverse character. Because these excitations have been associated with the transport of small molecules in bilayers (Paula et al. 1996), the longitudinal and transverse fluctuations have been speculated to be relevant for the in-plane and trans-membrane transport of small molecules, such as water (Kaye et al. 2011, Paula et al. 1996).

Two types of inelastic scans were conducted. Specifically, constant-$q_{\|}$ scans, in which a $q_{\|}$ value is selected and held constant while the energy transfer $\hbar\omega$ is scanned, and constant-energy scans, for which the spectrometer is tuned to a certain energy transfer, $\hbar\omega$, and the momentum transfer $q_{\|}$ is varied. Both types are usually employed to measure dispersion relations. As a general rule, energy scans are usually used when the dispersion relation is flat. On the other hand, constant-$q_{\|}$ scans are usually better suited to measure steep parts of the dispersion. Examples of constant-energy and constant-$q_{\|}$ scans are shown in Fig. 5. The position of the excitations as function of $\hbar\omega$ and $q_{\|}$ is then determined from the positions of peaks in these scans. The constant-energy scans at $q_{\|} = 1.2$ Å^{-1} in Fig. 5a show two well-defined peaks at ~ 1.3 and ~ 2.1 meV in the

5 mol% cholesterol sample. Four peaks can be fit to the spectrum at a higher cholesterol concentration (as shown in Fig. 5b) at energies between 1 and 4 meV. The corresponding fitting functions consist of narrow Gaussian components centered at an energy transfer $\hbar\omega = 0$, which are used to describe the instrumental energy resolution (see Table 1), a broader Lorentzian component as a result of relaxational dynamics (also present in the systems studied) and damped harmonic oscillators (dho) for the excitations.

Figure 5c depicts constant-$q_{\|}$ scans in the two samples. Both scans show a broad component centered at $\sim q_{\|} = 1.38$ Å^{-1} and two narrow satellite peaks. As will be shown below, the broad peak is related to a minimum in the dispersion relation, i.e, a flat, horizontal region, while the narrow peaks are associated with the steeper branches. The solid lines in Fig. 5c are fits using Gaussian peak profiles—two narrow and a broad Gaussian peak were fitted to the two scans.

The use of a thermal TAS increases the available energy range. Figure 5d shows energy scans at $q_{\|} = 3$ Å^{-1} and an energy transfer of up to 20 meV. An excitation at $\sim$16 meV is visible as a pronounced peak in the spectra. This excitation was predicted by Tarek et al. (2001) and refers to an optical phonon associated with the dynamics of the terminal methyl end groups. The observed energy values are in excellent agreement with the theoretical values.

Several constant-$q_{\|}$ and constant-energy scans were performed on the two spectrometers to carefully scan the accessible energy and $q_{\|}$ range for excitations. These excitations could be assigned to dynamics in the gel, fluid and liquid-ordered states of the membrane.

Dispersion relations

Figure 6 shows all of the measured excitations (as function of energy transfer $\hbar\omega$ and momentum transfer $q_{\|}$) in the 5 and 40 mol% cholesterol samples as determined from the inelastic scans shown in Fig. 5. Excitation data measured using the cold and thermal TAS are depicted by circular

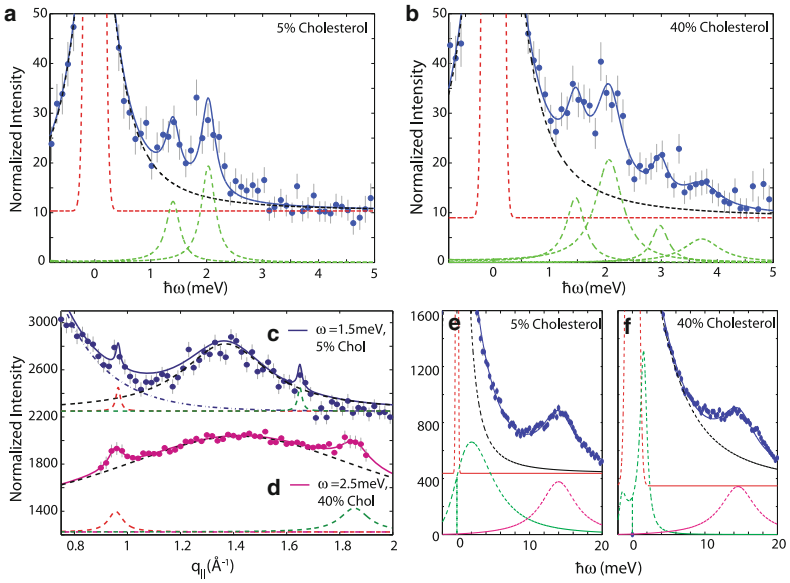

Fig. 5 Overview of the inelastic data: constant-$q_{\|}$ scan at $q_{\|} = 1.2$ Å^{-1}. The instrumental resolution is fit with a Gaussian (*red*), and the relaxation dynamics by a Lorentzian (*black*) function. The satellite excitations peaks are fit with damped harmonic oscillators (*green*), with the total fit shown in *blue*. **a** Data of 5 mol% and **b** 40 mol% cholesterol concentration samples. Constant-energy scan showing peaks fitted with Lorentzian curves: **c** 5 mol% cholesterol at $\hbar\omega$ = 1.5 meV. The Lorentzian fits are depicted by *dashed black*, *red* and *green curves*, with an exponential used to fit the background (*dashed blue*). The total fit is shown as a *solid blue line*. **d** 40 mol% cholesterol at $\hbar\omega$ = 2.5 meV. The Lorentzian fits are indicated by *dashed black*, *red* and *green curves*, with the constant background and the total fit depicted by *dashed magenta* and *solid magenta lines*, respectively. High-energy constant-$q_{\|}$ scans at $q_{\|} = 3$ Å^{-1}—the instrumental resolution is fit using a Gaussian (*red*), while a Lorentzian (*black*) function is used to describe the relaxation dynamics. The satellite excitation peaks are fit with damped harmonic oscillators (*green and magenta*), with the total fit shown in *blue*. **e** 5 mol% and **f** 40 mol% cholesterol concentrations. The green curves correspond to the low energy excitations from *a*, *b* and *c*, which cannot be resolved using the high-energy setup

and diamond-shaped symbols, respectively. The excitations were grouped into three different dispersion relations as follows: Pronounced and narrow excitations were assigned to the gel phase as the more ordered state of the lipid tails is expected to lead to well-defined excitations. Broad inelastic peaks are more likely the result of fluctuations in the fluid phase. The corresponding dispersion relations are similar to those shown in Fig. 2b. There was, however, a set of excitations (Fig. 6) that did not follow the gel or fluid dispersion curves, and was clearly outside of the error bars for those excitations. We tentatively assigned those excitations to the liquid-ordered state.

The data for the 5 mol% cholesterol sample (Fig. 4a) can be compared to the dispersion relations for gel and fluid DMPC and DPPC bilayers, as previously reported from inelastic X-rays (Chen et al. 2001, 2003; Weiss et al. 2003), neutron scattering (Rheinstädter et al. 2004a; Kaye et al. 2011) and MD simulations (Tarek et al. 2001; Hub et al. 2007). The shape of the gel dispersion curve agrees very well with ones in the literature. The energy value in the dispersion minimum is slightly increased (from 1 meV to $\sim$1.5 meV) in the presence of cholesterol. Only one excitation could clearly be identified at $q_{||}$ values of $\lesssim$0.9 Å^{-1}, and we assigned this excitation to the gel phase as we expect it to be the most pronounced. Therefore, the fluid and liquid-ordered dispersion relations do not have data points below $q_{||} \sim 1$ Å^{-1}. As reported previously (Rheinstädter et al. 2004a), compared to the gel dispersion curve, the fluid dispersion curve appears to be less pronounced, with a higher energy value in the dispersion minimum, and lower (softer) energies at high $q_{||}$ values. This new dispersion curve, which we assigned to the liquid-ordered state shows, not only a very low minimum energy, but also very low energy values at high $q_{||}$.

All energy values for the 40 mol% cholesterol sample appear to be shifted to higher energies (Fig. 6b), the trademark of more rigid interactions, which lead to higher eigenfrequencies. In both the high and low cholesterol samples, three dispersion curves could be identified and assigned to the gel, fluid and tentatively to the liquid-ordered phases. In order to analyze the differences between the different states in the low and high cholesterol samples, the energy values around the dispersion minimum were fitted using a parabola:

$$\hbar\omega = \alpha \times (q_{||} - q_0)^2 + \omega_0. \quad (5)$$

The region around the minimum of the dispersions shown in Fig. 6 was fitted using Eq. (5). The fitted values for α and ω_o are listed in Table 2.

Because the bilayers were hydrated by heavy water, the experiment is potentially also sensitive to collective hydration water dynamics. We note, however, that we expect the corresponding signals to be small. The range of hydration water excitations, as reported from inelastic neutron scattering (Paciaroni et al. 2008), is shown in Fig. 6a, b. Two of the data points in Fig. 6b can most likely be assigned to hydration water dynamics.

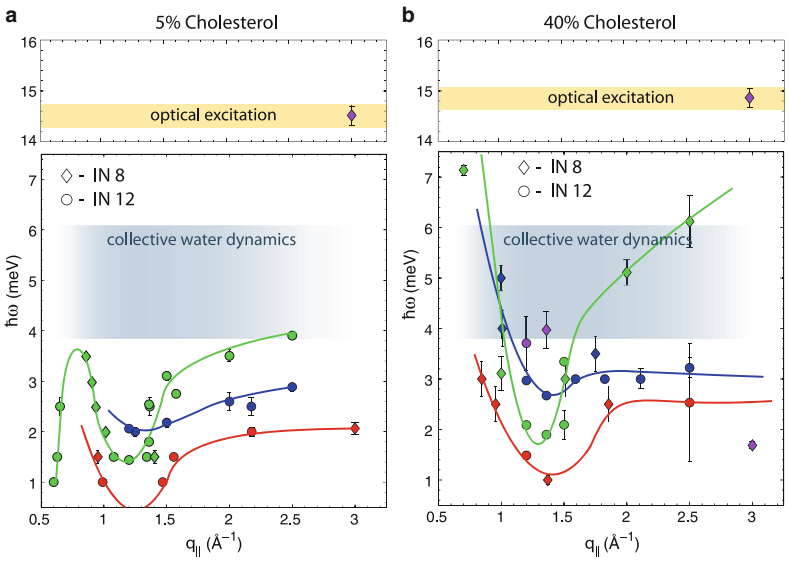

Fig. 6 Energy dispersion curves for DMPC bilayers with **a** 5 mol% cholesterol and **b** 40 mol% cholesterol. The dispersion curve corresponding to the gel phase is shown in *green* and the fluid phase in *blue*. The liquid-ordered phase, arising from the high concentration of cholesterol in the sample, is depicted by the *red curve*. The *blue band* at $\sim$4–6 meV represents the region where excitations due to hydrating water are observed (Paciaroni et al. 2008). The *yellow band* represents an optical excitation at 14–15 meV, which was predicted by MD simulations (Tarek et al. 2001)

Table 2 Results of parabolic fits using Eq. (5) to the dispersion minima in Fig. 6

	α	(meV × Å^2)	ω_0 (meV)	
	5 mol% chol	40 mol% chol	5 mol% chol	40 mol% chol
Gel	16.3	30.3	1.38	1.80
Fluid	4.9	10.7	1.99	2.63
Liquid-ordered l_o	9.8	6.6	0.44	1.09

α is the slope of the parabola, and ω_0 is the energy offset. α can be thought of as a nanoscale bilayer "stiffness" on length scales corresponding to lipid tail-tail distances

Discussion

The lateral short-wavelength dynamics of the lipid tails in the hydrophobic membrane core have previously been studied in DMPC (Weiss et al. 2003; Chen et al. 2003; Rheinstädter et al. 2004a; Hub et al. 2007; Brüning et al. 2010; Kaye et al. 2011) and DLPC (Chen et al. 2001; Tarek et al. 2001) membranes, and the corresponding dispersion relations have been determined by inelastic X-ray scattering (IXS), inelastic neutron scattering and computer simulations. In this article we have determined complete energy dispersion curves for a DMPC membrane containing different amounts of cholesterol, a system previously studied by IXS (Weiss et al. 2003; Chen et al. 2003). The shape of the dispersion curves observed from the neutron and X-ray experiments is similar to that of a pure bilayer system (Fig. 2b). The same type of excitation curve has also been reported recently in bilayers with ethanol (Kaye et al. 2011). It can therefore be concluded that this type of dispersion relation is generic to lipid membranes, even in the presence of molecules, such as ethanol and cholesterol. Ethanol and cholesterol represent two different classes of molecules, i.e., ethanol molecules predominantly reside in the lipid-head group region, while cholesterol molecules interact extensively with the membrane's hydrophobic core. Although the dynamics of the lipid chains are altered by the presence of cholesterol, nevertheless, the membrane's basic characteristics seem to be preserved.

The lateral dynamics dispersion curve exhibits three characteristic regimes: a linear regime at small $q_{||}$, a minimum at a wavelength corresponding to the nearest-neighbor lipid tail distance, and finally, a second linear regime at large $q_{||}$. The linear regime at small $q_{||}$-values is related to a long wavelength sound-like propagation in the plane of the membrane. The corresponding excitations are thus longitudinal. The speed of sound is determined from the initial linear slope of the dispersion curve at small $q_{||}$-values up to the first maximum (see Fig. 2). Dynamics at small $q_{||}$ values are usually difficult to access in inelastic neutron scattering experiments because of the so-called kinematic restriction. It is related to the fact that energy and momentum of the neutrons are conserved during the scattering process and the parabolic shape of the energy as a function of $q_{||}$, $\hbar\omega = \hbar^2/(2m_n) \times q_{||}^2$, as for instance discussed in (Rheinstädter et al. 2004). While the absolute energies of the 5 mol% cholesterol dispersion relation in Fig. 6a fall into the accessible range, the energies significantly increase in the presence of 40 mol% cholesterol, such that the corresponding excitations were no longer accessible. The determination of the speed of sound is, therefore, beyond the scope of this study. Dynamics at higher $q_{||}$ values around the dispersion minimum and beyond are the domain of inelastic neutron scattering. The final linear regime of the dispersion relation corresponds to a propagating mode with predominantly transverse properties. In the case of pure lipid membranes, the slope or propagation velocity in this region is small. The maxima and minimum in the dispersion curve correspond to a crossover behavior, connecting these two propagating modes at small and large $q_{||}$. In particular, the flat region at the dispersion minimum may be related to a non-propagating standing-wave resulting from lipid tail dynamics with mixed longitudinal and transverse properties. The characteristics of these modes in pure lipid membranes have been previously reported (Kaye et al. 2011).

The introduction of cholesterol to the lipid membrane leads to additional propagating modes, as shown in Fig. 5. Because the inclusion of additional components increases the system's degrees of freedom, it is natural to expect that the addition of cholesterol will result in more dynamic modes, as shown in Fig. 6. One interesting observation is that the dispersion curves all exhibit the same features, i.e., two linear regimes at small and large $q_{||}$ connected by a crossover regime with two maxima and a minimum. This strongly suggests that these features are generic to such systems. We therefore speculate that they are related to the fact that lipid membranes are self-assembled layered structures whose properties are closely related to that of smectic liquid crystals.

It is interesting to note that the dispersion curve, shown in Fig. 6, resembles the energy of a quasiparticle in superfluid helium, where the parabolic minimum part of the spectrum is termed the roton [see, e.g., (Annet 2004)]. The different behavior of the dispersion curves indicates different modes of molecular motions. Comparing to superfluid helium, we can speculate that the linear phonon-like dispersion curve implies that the motion of the molecules are rigidly coupled, leading to a propagating sound-like wave. On the other hand, the parabolic dispersion curve near the minimum may indicate a different type of collective mode in which a moving molecule couples strongly

to its neighbors. As one molecule moves, the neighboring molecules must move out of its way, leading to a different collective mode of motion, as depicted in Fig. 7. Phenomenologically, the minimum of the dispersion curves is well described by a parabola [Eq. (5)]. The coefficient α of the parabola can thus be viewed as a parameter characterizing the generalized rigidity of the system on the nanometer-length scale. It is interesting to note that increasing the cholesterol content in the system leads to larger α in the gel and fluid branches of the dispersion curve, and a smaller α in the liquid-ordered branch. The energy offset ω_0 in the dispersion minimum, corresponding to the roton energy gap, can be related to the excitation energy of a "soft-mode." The occurrence of a soft mode often indicates a structural phase transition if the energy cost of this mode goes to zero, i.e., $\omega_0 = 0$. A smaller value of ω_0 might then be related to a structure with a higher degree of order; a full analysis of this feature will be presented in a future paper.

Some qualitative conclusions can be drawn from the data and the phenomenological analysis: From the values for α and ω_0 shown in Table 2, one can speculate that the gel phase has, not surprisingly, a higher degree of order and is considerably stiffer than the fluid phase. The addition of cholesterol has two distinct effects: it makes the chain dynamics in both phases stiffer (α increases by a factor of ~ 2 between 5 and 40 mol% cholesterol), while at the same time, ω_0 also increases significantly, pointing to a more disordered molecular structure. The high cholesterol content liquid-ordered phase combines low values for α, corresponding to soft nanoscale dynamics, and at the same time, low values of ω_o, indicating a high level of order in the system. As has been previously speculated, the liquid-ordered phase seems to combine properties of rigid gel and soft fluid bilayers. In IXS experiments (Weiss et al. 2003; Chen et al. 2003), the addition of cholesterol leads to a significant increase in the high-frequency sound speed, pointing to a more rigid state at large length scales (small $q_{||}$-values).

In Fig. 6 we observe the coexistence of excitations of gel, fluid and liquid-ordered phases. The separation of saturated and unsaturated phosphatidylcholine/cholesterol mixtures into nanometer-sized liquid-ordered and liquid-disordered phases was reported recently from MD simulations (de Meyer et al. 2010; Risselada 2008; Herrera 2012). Cholesterol was also found to collectively self-organize in phospholipid membranes (Martinez-Seara et al. 2010), which can also lead to a dynamic phase separation on the nanometer scale. These small (3–50 nm) and transient (nano- microsecond) heterogeneities in membranes are very difficult to resolve with standard experimental techniques. Inelastic neutron-scattering experiments on DMPC reported evidence for the co-existence of small nanometer gel and fluid domains in the temperature range of the main phase transition (Rheinstädter et al. 2004a)—based on the co-existence of the corresponding excitations in the spectra. Such domains were also found in MD simulations (Murtola et al. 2006; Ehrig et al. 2011). Recently, Armstrong et al. (2012) have used the coherence length of neutrons to observe co-existing gel and fluid domains in a phospholipid bilayer over a range of temperatures. The authors speculated that these small transient domains could be responsible for the so-called pseudo-critical behavior in phospholipid bilayers. The results in Fig. 6 now represent experimental evidence for the coexistence of gel, fluid and liquid-ordered phases in DMPC membranes containing different amounts of cholesterol. The corresponding domains can be speculated to be nanometer sized and short-lived.

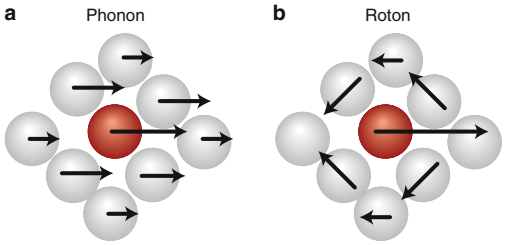

Fig. 7 **a** Molecular dynamics of particles participating in the propagating sound-like wave, i.e., the longitudinal phonon at small $q_{||}$-values (*long length scales*) and **b** in the "roton" at $q_{||}$-values in the dispersion minimum. These dynamics are expected to show a mixed, longitudinal and transverse character as neighboring particles couple strongly. Figure adapted from Annett (2004)

Conclusion

In summary, we present a neutron-scattering study of the lateral nanoscale dynamics in phospholipid membranes containing 5 and 40 mol% cholesterol. By measuring the excitation spectrum at several lateral $q_{||}$ values (up to $q_{||} = 3$ Å^{-1}), complete dispersion relations corresponding to gel, fluid and liquid-ordered bilayers were determined. The dispersion relations have a generic shape in single component lipid bilayers, i.e., there is an initial linear regime because of high-speed sound propagation and a second linear regime at high $q_{||}$. The two linear regimes are connected by a maximum before a minimum is observed around nearest-neighbor distances between to lipid tails. The generic shape of these dispersion curves is preserved in the presence of cholesterol. A coexistence of excitations corresponding to gel, fluid and liquid-ordered phases was also observed. We therefore speculate the coexistence of

nanometer-sized, and possibly transient, gel, fluid and l_o domains in membranes containing cholesterol. Such nanodomains have long been previously suggested, with evidence coming from computer simulations and more recently from experiment (Simons 1997; Murtola et al. 2006; Ehrig et al. 2011; Armstrong et al. 2012; Engelma 2005; Eggeling et al. 2009; Lingwood 2010).

The region around the dispersion minimum was fitted using a phenomenological parabolic fitting method. The two parameters, i.e., the slope and the energy offset, were related to the bilayer's elastic properties on distances corresponding to hydrocarbon tail distances and molecular order. The inclusion of cholesterol has a distinct effect on the collective dynamics of the lipid hydrocarbon chains. Namely, we observe a pronounced stiffening of the membrane on nanometer length scales in both the gel and fluid phases, and also greater molecular disorder. For the first time, we have determined the nanoscale dynamics in the high-cholesterol liquid-ordered phase of DMPC bilayers. This phase seems to combine the properties of the gel and fluid phases, appearing softer than the fluid phase, but better ordered than the gel phase. Future experiments will offer a more complete description of these features, and a quantitative model will be put forth regarding the molecular properties of multi-component lipid bilayers.

Acknowledgments This research was funded by the Natural Sciences and Engineering Research Council of Canada (NSERC), the National Research Council Canada (NRC), the Canada Foundation for Innovation (CFI) and the Ontario Ministry of Economic Development and Innovation. John Katsaras is supported by Oak Ridge National Laboratory's (ORNL) Program Development (PD) and Laboratory Directed Research and Development (LDRD) programs.

References

Adachi T (2000) A new method for determining the phase in the X-ray diffraction structure analysis of phosphatidylcholine:alcohol. Chem Phys Lipids 107:93–97

Almeida P, Vaz W, Thompson T (1992) Lateral diffusion in the liquid phases of dimyristoylphosphatidylcholine/cholesterol lipid bilayers: a free volume analysis. Biochemistry 31:6739–6747

Annett JF (2004) Superconductivity, superfluids and condensates. Oxford University Press, Oxford

Armstrong CL, Sandqvist E, Rheinstadter MC (2011) Protein-protein interactions in membranes. Protein Pept Lett 18:344–353

Armstrong C, Barrett M, Toppozini L, Kucerka N, Yamani Z, Katsaras J, Fragneto G, Rheinstädter MC (2012) Co-existence of gel and fluid lipid domains in single-component phospholipid membranes. Soft Matter 8:4687–4694

Bayerl T (2000) Collective membrane motions. Curr Opin Colloid Interface Sci 5:232–236

Bloom M, Bayerl T (1995) Membranes studied using neutron scattering and NMR. Can J Phys 73:687–696

Brown DA, London E (2000) Structure and function of sphingolipid- and cholesterol-rich membrane rafts. J Biol Chem 275:17221–17224

Brüning B, Rheinstädter MC, Hiess A, Weinhausen B, Reusch T, Aeffner S, Salditt T (2010) Influence of cholesterol on the collective dynamics of the phospholipid acyl chains in model membranes. Eur Phys J E 31:419–428

Chen S, Liao C, Huang H, Weiss T, Bellisent-Funel M, Sette F (2001) Collective dynamics in fully hydrated phospholipid bilayers studied by inelastic X-ray scattering. Phys Rev Lett 86:740–743

Chen PJ, Liu Y, Weiss TM, Huang HW, Sinn H, Alp EE, Alatas A, Said A, Chen SH (2003) Studies of short-wavelength collective molecular motions in lipid bilayers using high resolution inelastic X-ray scattering. Biophys Chem 105:721–741

de Meyer F, Smit B (2009) Effect of cholesterol on the structure of a phospholipid bilayer. Proc Natl Acad Sci USA 106:3654–3658

de Meyer FJM, Benjamini A, Rodgers JM, Misteli Y, Smit B (2010) Molecular simulation of the dmpc-cholesterol phase diagram. J Phys Chem B 106:10451–10461

Eggeling C, Ringemann C, Medda R, Schwarzmann G, Sandhoff K, Polyakova S, Belov VN, Hein B, von Middendorf C, Schönle A, Hell SW (2009) Direc observation of the nanoscale dynamics of membrane lipids in a living cell. Nature 457:1159–1162

Ehrig J, Petrov EP, Schwille P (2011) Phase separation and near-critical fluctuations in two-component lipid membranes: Monte Carlo simulations on experimentally relevant scales. New J Phys 13:045019

Engelman DM (2005) Membranes are more mosaic than fluid. Nature 438:578–580

Fragneto G, Rheinstädter M (2007) Structural and dynamical studies from bio-mimetic systems: an overview. CR Phys 8:865–883

Harroun T, Katsaras J, Wassall S (2006) Cholesterol hydroxyl group is found to reside in the center of a polyunsaturated lipid membrane. Biochemistry 45:1227–1233

Harroun T, Katsaras J, Wassall S (2008) Cholesterol is found to reside in the center of a polyunsaturated lipid membrane. Biochemistry 47:7090–7096

Herrera FE, Pantano S (2012) Structure and dynamics of nano-sized raft-like domains on the plasma membrane. J Chem Phys 136:1–33

Hildenbrand MF, Bayerl TM (2005) Differences in the modulation of collective membrane motions by ergosterol, lanosterol, and cholesterol: a dynamic light scattering study. Biophys J 88:3360–3367

Hirn RB, Bayerl TM (1999) Collective membrane motions in the mesoscopic range and their modulation by the binding of a monomolecular protein layer of streptavidin studied by dynamic light scattering. Phys Rev E 59:5987–5994

Hirn R, Bayerl T, Rädler J, Sackmann E (1999) Collective membrane motions of high and low amplitude, studied by dynamic light scattering and micro-interferometry. Faraday Discuss 111:17–30

Huang J, Feigenson GW (1999) A microscopic interaction model of maximum solubility of cholesterol in lipid bilayers. Biophys J 76:2142–2157

Hub JS, Salditt T, Rheinstädter MC, de Groot BL (2007) Short range order and collective dynamics of DMPC bilayers. acomparison between molecular dynamics simulations, X-ray, and neutron scattering experiments. Biophysical J 93:3156–3168

Katsaras J (1998) Adsorbed to a rigid substrate, dimyristoylphosphatidylcholine multibilayers attain full hydration in all mesophases. Biophys J 75:2157–2162

Kaye MD, Schmalzl K, Nibali VC, Tarek M, Rheinstädter MC (2011) Ethanol enhances collective dynamics of lipid membranes. Phys Rev E 83:050,907

King GI, Worthington CR (1971) Analytic continuation as a method of phase determination. Phys Lett 35A:259–260

König S, Pfeiffer W, Bayerl T, Richter D, Sackmann E (1992) Molecular dynamics of lipid bilayers studied by incoherent quasi-elastic neutron scattering. J Phys II France 2:1589–1615

König S, Sackmann E, Richter D, Zorn R, Carlile C, Bayerl T (1994) Molecular dynamics of water in oriented dppc multilayers studied by quasielastic neutron scattering and deuterium-nuclear magnetic resonance relaxation. J Chem Phys 100:3307–3316

König S, Bayerl T, Coddens G, Richter D, Sackmann E (1995) Hydration dependence of chain dynamics and local diffusion in l-alpha-dipalmitoylphosphtidylcholine multilayers studied by incoherent quasi-elastic neutron scattering. Biophys J 68:1871–1880

Kučerka N, Marquardt D, Harroun T, Nieh MP, Wassall S, Katsaras J (2009) The functional significance of lipid diversity: orientation of cholesterol in bilayers is determined by lipid species. J Am Chem Soc 131:16358–16359

Kučerka N, Liu Y, Chu N, Petrache HI, Tristram-Nagle S, Nagle JF (2005) Structure of fully hydrated fluid phase DMPC and DLPC lipid bilayers using X-ray scattering from oriented multilamellar arrays and from unilamellar vesicles. Biophys J 88:2626–2637

Léonard A, Escrive C, Laguerre M, Pebay-Peyroula E, Néri W, Pott T, Katsaras J, Dufourc EJ (2001) Location of cholesterol in dmpc membranes. a comparative study by neutron diffraction and molecular mechanics simulation. Langmuir 17:2019–2030

Lindahl E, Edholm O (2000) Mesoscopic undulations and thickness fluctuations in lipid bilayers from molecular dynamics simulations. Biophys J 79:426–433

Lingwood D, Simons K (2010) Lipid rafts as a membrane-organizing principle. Science 327:46–50

Lipowsky, R, Sackmann, E (eds) (1995) Structure and dynamics of membranes, handbook of biological physics. vol 1, Elsevier, Amsterdam

Martinez-Seara H, Róg T, Karttunen M, Vattulainen I, Reigada R (2010) Cholesterol induces specific spatial and orientational order in cholesterol/phospholipid membranes. PLoS ONE 5:e11162

Meinhold L, Smith JC, Kitao A, Zewail AH (2007) Picosecond fluctuating protein energy landscape mapped by pressure-temperature molecular dynamics simulation. Proc Natl Acad Sci USA 104:17261–17265

Mihailescu M, Soubias O, Worcester D, White S, Gawrisch K (2011) Structure and dynamics of cholesterol-containing polyunsaturated lipid membranes studied by neutron diffraction and nmr. J Membr Biol 239:63–71

Mouritsen O (2010) The liquid-ordered state comes of age. Biochim Biophys Acta 1798:1286–1288

Murtola T, Róg T, Falck E, Karttunen M, Vattulainen I (2006) Transient ordered domains in single-component phospholipid bilayers. Phys Rev Lett 97:238102

Nagle JF, Wiener MC (1989) Relations for lipid bilayers. Biophys J 55(55):309–313

Nagle J, Zhang R, Tristram-Nagle S, Sun W, Petrache H, Suter R (1996) X-ray structure determination of fully hydrated lα phase dipalmitoylphosphatidylcholine bilayers. Biophys J 70:1419–1431

Nevzorov A, Brown M (1997) Bilayers from comparative analysis of 2H and 13C NMR relaxation data as a function of frequency and temperature. J Chem Phys 107:10288–10310

Pabst G, Kučerka N, Nieh MP, Rheinstädter M, Katsaras J (2010) Applications of neutron and X-ray scattering to the study of biologically relevant model membranes. Chem Phys Lipids 163(6):460–479

Paciaroni A, Orecchini A, Cornicchi E, Marconi M, Petrillo C, Haertlein M, Moulin M, Schober H, Tarek M, Sacchetti F (2008) Fingerprints of amorphous ice-like behavior in the vibrational density of states of protein hydration water. Phys Rev Lett 101:148104

Papanikolaou B, Papafotika A, Murphy C, Papamarcaki T, Tsolas O, Drab M, Kurzchalia TV, Kasper M, Christoforidis S (2005) Cholesterol-dependent lipid assemblies regulate the activity of the ecto-nucleotidase cd39. J Biol Chem 28:26406–26414

Paula S, Volkov A, Van Hoek A, Haines T, Deamer D (1996) Permeation of protons, potassium ions, and small polar molecules through phospholipid bilayers as a function of membrane thickness. Biophys J 70:339–348

Petrie R, Schnetkamp P, Patel K, Awasthi-Kalia M, Deans J (2000) Transient translocation of the b cell receptor and src homology 2 domain-containing inositol phosphatase to lipid rafts: evidence toward a role in calcium regulation. J Immunol 165:1220–1227

Pfeiffer W, Henkel T, Sackmann E, Knorr W (1989) Local dynamics of lipid bilayers studied by incoherent quasi-elastic neutron scattering. Europhys Lett 8:201–206

Pfeiffer W, König S, Legrand J, Bayerl T, Richter D, Sackmann E (1993) Neutron spin echo study of membrane undulations in lipid multibilayers. Europhys Lett 23:457–462

Pike L (2006) Rafts defined: a report on the keystone symposium on lipid rafts and cell function. J Lipid Res 47:1597–1598

Pike L (2009) The challenge of lipid rafts. J Lipid Res 50:S323–S328

Rheinstädter MC (2008) Collective molecular dynamics in proteins and membranes. Biointerfaces 3:FB83–FB90

Rheinstädter MC, Ollinger C, Fragneto G, Demmel F, Salditt T (2004a) Collective dynamics of lipid membranes studied by inelastic neutron scattering. Phys Rev Lett 93:108107

Rheinstädter MC, Ollinger C, Fragneto G, Salditt T (2004) Collective dynamics in phospholipid bilayers investigated by inelastic neutron scattering: exploring the dynamics of biological membranes with neutrons. Phys B 350:136–139

Rheinstädter MC, Seydel T, Demmel F, Salditt T (2005) Molecular motions in lipid bilayers studied by the neutron backscattering technique. Phys Rev E 71:061,908

Rheinstädter MC, Häussler W, Salditt T (2006a) Dispersion relation of lipid membrane shape fluctuations by neutron spin-echo spectrometry. Phys Rev Lett 97:048103

Rheinstädter MC, Seydel T, Häußler W, Salditt T (2006b) Exploring the collective dynamics of lipid membranes with inelastic neutron scattering. J Vac Sci Technol A 24:1191–1196

Rheinstädter MC, Seydel T, Salditt T (2007) Nanosecond molecular relaxations in lipid bilayers studied by high energy resolution neutron scattering and in-situ diffraction. Phys Rev E 75:011907

Rheinstädter MC, Schmalzl K, Wood K, Strauch D (2009) Protein-protein interaction in purple membrane. Phys Rev Lett 103:128104

Ridsdale A, Denis M, Gougeon PY, Ngsee JK, Presley JF, Zha X (2006) Cholesterol is required for efficient endoplasmic reticulum-to-golgi transport of secretory membrane proteins. Mol Biol Cell 17:1593–1605

Risselada HJ, Marrink SJ (2008) The molecular face of lipid rafts in model membranes. Proc Natl Acad Sci USA 105:17367–17372

Róg T, Pasenkiewicz-Gierula M, Vattulainen I, Karttunen M (2009) Ordering effects of cholesterol and its analogues. Biochim Biophys Acta 1788:97–121

Salditt T (2000) Structure and fluctuations of highly oriented phospholipid membranes. Curr Opin Colloid Interface Sci 5:19–26

Simons K, Ikonen E (1997) Functional rafts in cell membranes. Nature 387:569–572

Takeda T, Kawabata Y, Seto H, Komura S, Gosh S, Nagao M, Okuhara D (1999) Neutron spin echo investigations of membrane undulations in complex fluids involving amphilphiles. J Phys Chem Solids 60:1375–1377

Tarek M, Tobias D, Chen SH, Klein M (2001) Short wavelength collective dynamics in phospholipid bilayers: a molecular dynamics study. Phys Rev Lett 87:238101

Thewalt JL, Bloom M (1992) Phosphatidylcholine: cholesterol phase diagrams. Biophys J 63:1176–1181

Tristram-Nagle S, Liu Y, Legleiter J, Nagle JF (2002) Structure of gel phase dmpc determined by X-ray diffraction. Biophys J 83:3324–3335

Vist R, Davis JH (1990) Phase equilibria of cholesterol/dipalmitoylphosphatidylcholine mixtures: 2 h nuclear magnetic resonance and differential scanning calorimetry. Biochemistry 29:451–464

Weiss T, Chen PJ, Sinn H, Alp E, Chen S, Huang H (2003) Collective chain dynamics in lipid bilayers by inelastic X-ray scattering. Biophys J 84:3767–3776

Chapter 6

Ethanol in DMPC powder membranes

Paper VII

VII. Toppozini, L., Armstrong, C. L., **Barrett, M.**, Zheng, S., Luo, L., Nanda, H., Sakai, V. G., and Rheinstädter, M. C., (2012) *"The interaction of Ethanol with Lipid Membranes seen by X-ray and Neutron Scattering."* - in preparation.

6.1 Powder vs aligned samples

The samples in the lipid bilayer experiments discussed previously were all aligned lamellar bilayer samples. In Paper VII, rather than samples composed of self-assembled oriented bilayers the lipid samples take a powder orientation. These particular powder samples were constructed by mixing dry lipid powder with water (deuterium dioxide in the neutron case) and ethanol (deuterated ethanol for the neutron sample), in a 2mol% ethanol ratio. Because of the volatility of the ethanol molecule, a constant ethanol concentration in the bilayers can only be achieved when the membranes are immersed in a water/ethanol solution. The damp solution of lipid and solvent is spread in a thin layer (∼1 mm thick) over a glass slide for the x-ray experiment (see Figure 6.1), and applied as a thin film to the inner wall of a hollow aluminum cylinder. The x-ray sample is placed on the temperature controlled sample stage, where water from a water bath circulates below the aluminum platform. The temperature is stable to 0.1 ^{o}C. The neutron sample was mounted inside of a cryostat, with temperature control from $7^oC < T < 62^oC$, to access the entire range from gel (L_β) to ripple ($P_{\beta'}$) to fluid phase (L_α), with stability of better than 0.1 ^{o}C.

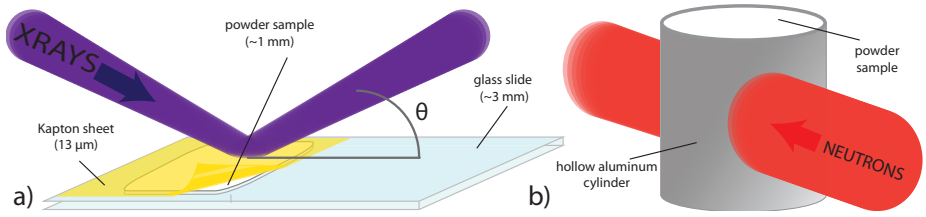

Figure 6.1: Sketch of sample environment used in x-ray powder experiment. a) A 1 mm deep square with side length 25 mm containing the DMPC and solvent (either pure water or water ethanol) is indented into a glass slide. To prevent evaporation of the solvent, the area is enclosed using a sheet of Kapton, sealed with vacuum grease. b) The hollow aluminum cylinder with inside wall prepared with a thin film layer of powder sample.[61]

Since the sample is an isotropic powder, instead of taking a 2D reciprocal space map, all of the structural information (in-plane and out-of-plane) can be collected in one scan. A cartoon showing the typical arrangement of the small domains is found in Figure 6.2.

From Figure 6.3 a typical reflectivity scan is shown. This scan covers q values

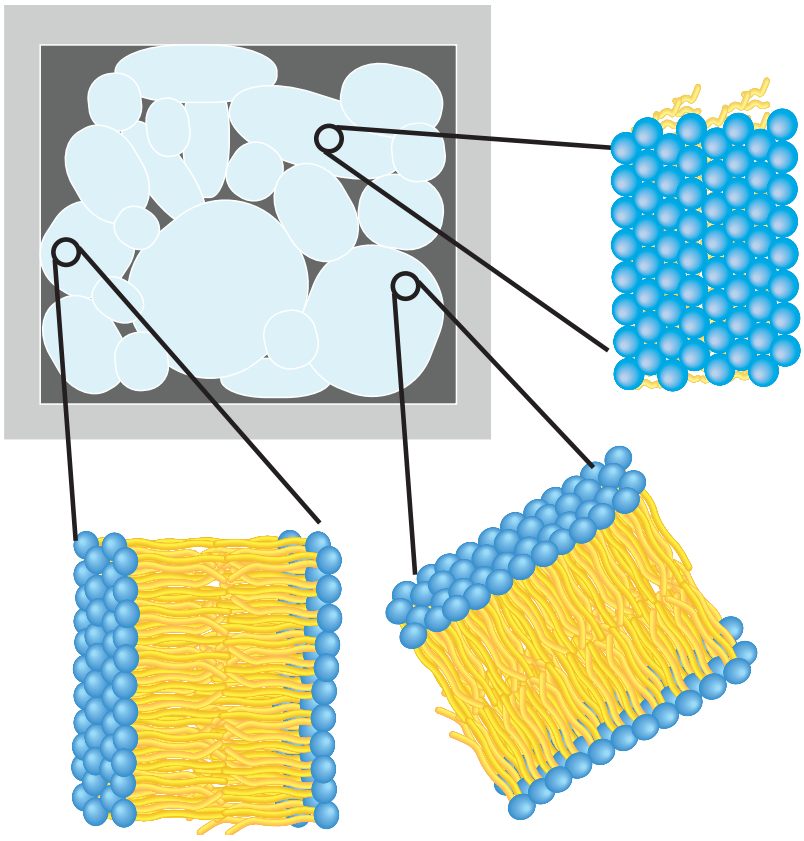

Figure 6.2: DMPC domains in powder sample arrangement
Many small domains are present in the sample. Each domain has bilayer structures. Rather than the high similarity between domains like the low mosiacity sample shown previously 4.10, the domains in a powder sample are much smaller, and are not biased to sit in a certain orientation. Domains are randomly oriented such that bilayers are sitting with their planar axis parallel and perpendicular with the substrate, and every angle in between. Only a single scan is necessary to obtain all structural information.

from q=0 to q=2.5 $Å^{-1}$, and contains both in-plane and out-of-plane data. The first few Bragg peaks observed from q=0 to q 0.5 $Å^{-1}$ have regular spacing and are the fingerprint of the lamellar spacing of the bilayers. The spacing of the peaks (Δq) is inversely related to the bilayer d-spacing (with $\Delta q=2\pi/d$). At q-values larger than 0.5 $Å^{-1}$ we see one peak, fit to a red curve, which is the fingerprint of a tail-tail hexagonal distribution similar to the Bragg rods observed in Figure 4.9. The two data sets acquired from this reflectivity scan (in and out of plane) are then treated

separately using analysis similar to the previously discussed x-ray procedure. The out-of-plane peaks in the low-q regime are fit to a $T(q_z)$ function as shown in equation 4.3 and Fourier transformed to determine the electron density. The in-plane peak which appears at $\sim$1.5 $Å^{-1}$ is converted to real-space and gives information on the average lipid tail-tail spacing.

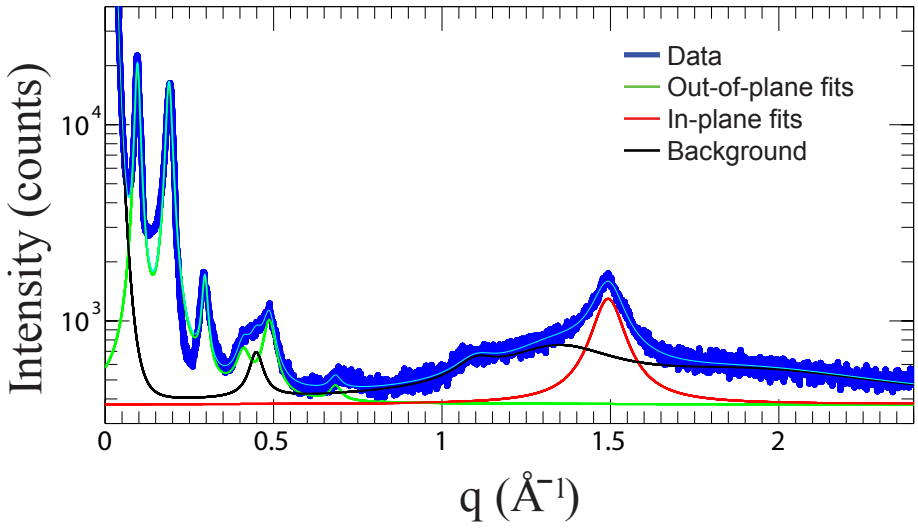

Figure 6.3: Typical x-ray scan of a DMPC sample
The scan shows both in-plane and out-of-plane peaks observed from a reflectivity scan of a pure DMPC sample at 20^{o}C. Due to the sample's isotropy this pattern would be observed regardless of the angular positioning of the glass slide.[61]

The DMPC samples for the neutron scattering case were prepared as a powder sample, similar to the x-ray scattering experiment discussed previously. Rather than being hydrated with H_2O, this powder sample was hydrated with D_2O. Also, when ethanol was added, the ethanol molecules used were deuterated ethanol - each hydrogen atom was replaced with a deuterium atom (A hydrogen atom with an extra neutron in the nucleus). This was done to take advantage of the vast differences between the size of scattering cross-sectional areas (σ) of hydrogen atoms and deuterium atoms, as shown in Table 6.1.

The data from Table 6.1 is displayed graphically in Figure 6.4. In the DMPC/water/ethanol samples, all non-lipid hydrogen atoms were carefully replaced with deuterium atoms. hydrogen's incoherent scattering cross-section is $\sim$40x larger than deuterium's, and

Atom	Coherent σ (b)	Incoherent σ (b)	Total σ (b)
^{1}H (hydrogen)	1.7583	80.27	82.03
^{2}H (deuterium)	5.592	2.05	7.64

Table 6.1: Neutron scattering cross-sectional areas (σ) of hydrogen and deuterium atoms. Units of b=barns, with 1 barn=10^{-24} cm^2. Data from [62].

the resulting intensity of neutrons scattering from hydrogen is larger by a similar factor. Thus water and ethanol are "invisible" to the neutrons, and our scans will focus solely on the lipids, making it possible to directly compare samples at different temperature and ethanol percentages.

6.2 High Flux Neutron Backscattering Spectrometer

This experiment was done using High Flux Neutron Backscattering Spectrometer (HFBS) at the NIST Center for Neutron Research (NCNR) in Gaithersburg, Maryland, USA. [63]. This unique instrument (as seen in Figure 6.5) allows for both elastic scans and quasi-elastic neutron scattering (QENS).

The elastic scans were performed at temperatures from 280K (7^{o}C) to 330K (56^{o}C), with a resolution of 0.2 K, spanning two phase transitions of DMPC, the transition from gel (L_β) to ripple ($P_{\beta'}$) to fluid phase (L_α). The 16 detectors in the HFBS instrument detected a q$\overrightarrow{q}$ range from 0.25 Å^{-1} (25 Å) to 1.75 Å^{-1} (3.6 Å). This range allows the observation of water dynamics at 3.6 Å, lipid tail dynamics at 4.2 Å and incoherent dynamics (lipid diffusion) from 5.7 to 8 Å. As temperature was increased components of the sample gained thermal energy and the intensity of neutrons scattered into each detector decreased, the result of a spreading of these peaks. Phase transitions can clearly be seen, and for the two lipid cases, the addition of ethanol makes these transitions more abrupt.

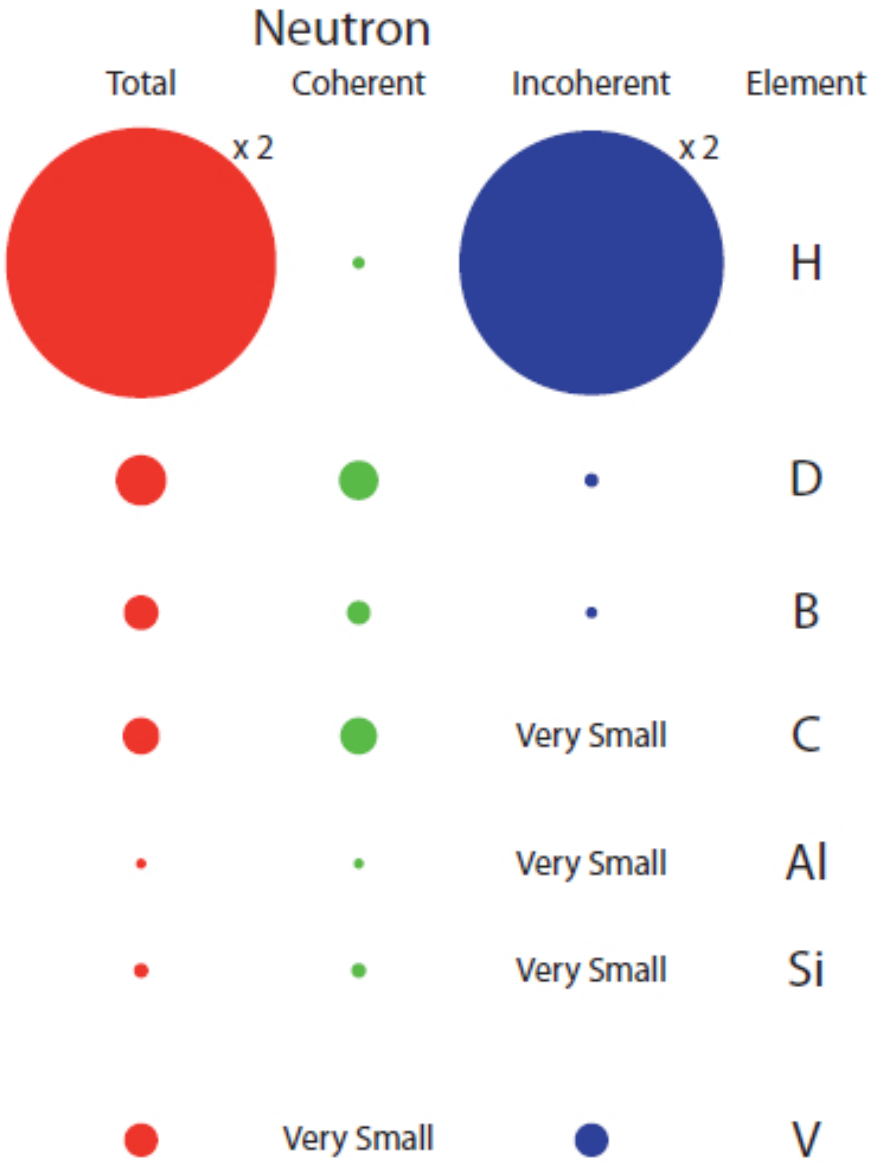

Figure 6.4: Neutron scattering cross-sections for common atoms
A comparison of scattering cross-sections of certain atoms. Take note of hydrogen's large incoherent scattering cross-section, compared to deuterium's. Adapted from [6].

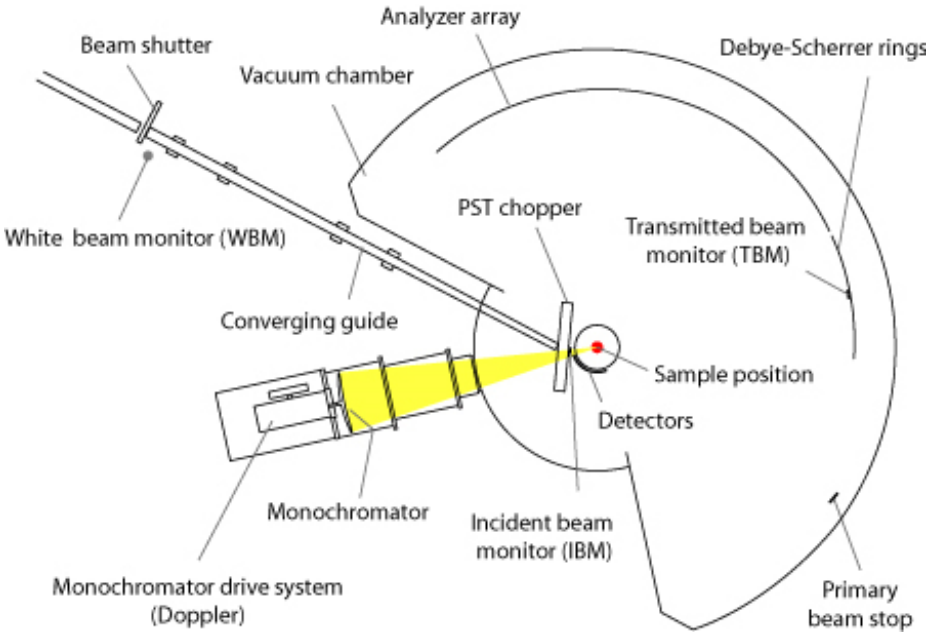

Figure 6.5: High Flux Neutron Backscattering Spectrometer at NCNR Overhead view of the HFBS at NCNR Neutrons enter from the top left and converge on the sample. A neutron energy of 2.08 meV is selected by the PST chopper, with higher and lower energies being Doppler shifted down or up, respectively. A dynamic range of maxiumum -15$\mu eV < \hbar\omega < 15\mu eV$ is selected by fast (up to 25 Hz) oscillation of the monochromator. The neutrons diffract through the sample, are reflected by the analyzing crystals and focused back to the detectors, resulting in high flux measurements.[63]

6.3 Quasi-elastic Neutron Scattering

Quasi-elastic neutron scattering was another technique used for the experiment in Paper VII. For a quasi-elastic scan, a single q-value was chosen, and a scan through neutron energy is obtained ($\hbar\omega$ is scanned through a range of -15$\mu eV < \hbar\omega < 15\mu eV$). This scan results in peaks from scattering sites which are not elastic and also do not have a well defined frequency (scatterers with a well defined frequency would appear as inelastic peaks, far from the $\hbar\omega$=0 point). We see the quasi-elastic scattering as an incoherent broad peak around $\hbar\omega$=0, relating to single particle dynamics and local relaxation processes. The theoretical structure factor which includes elastic, quasi-elastic and inelastic scattering peaks is displayed in Figure 6.6.

In the DMPC powder experiment, the quasi-elastic peak which was observed, is an

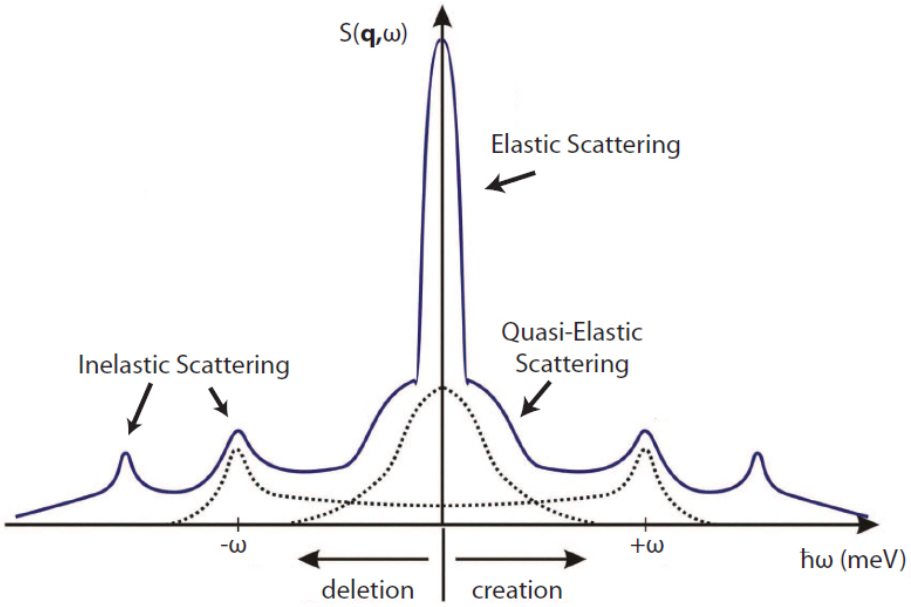

Figure 6.6: Quasi-elastic neutron scattering structure factor
The dynamical structure factor as a function of $\hbar\omega$ for different scattering techniques at a fixed q value.[25]

indicator of lipid diffusion. By taking these quasi-elastic scans at a range of q values (from 0.3 to 1.25 Å^{-1}) and plotting the width of the peak against the q-value one obtains a plot with a slope relating to the diffusion constant. More specifically, when a plot of quasi-elastic FWHM vs $\overrightarrow{q}^2$ will provide a linear solution to the equation $\text{FWHM}_{lipid}=2\hbar\ \text{D}\overrightarrow{q}^2$ [64]. A smaller diffusion constant results in lipids which move more slowly than a large diffusion constant.

Preface to Paper VII

The experiments for Paper VII were done in two parts. X-ray scans of a DMPC powder sample were carried out at McMaster University with the use of BLADE. These experiments were performed at 20^{o}C and 30^{o}C with a powder solution mixed with pure water, and with 2mol% ethanol. The neutron scans were done at NIST in Gaithersburg, Maryland, with a DMPC sample hydrated with either pure D_2O or D_2O and deuterated ethanol at 2mol%. Through these two experiments the position of ethanol in the gel and fluid phases of DMPC, the effect of ethanol on the lipid dynamics in gel, ripple and fluid phases and the diffusion of lipids in the gel and fluid phases was observed. Ethanol resides in the head-group region of the DMPC bilayer for both gel and fluid bilayers, and increases the permeability, allowing water molecules deeper into the bilayer. Ethanol molecules did not change the dynamics of the fluid phase, but appeared to have higher ordering in the gel and ripple phases. Finally ethanol causes slower diffusion in gel phase, but no appreciable change in the fluid phase.

My role in this paper was focused on the analysis of the x-ray scattering aspect of this experiment. The powder scans were analyzed by Laura Toppozini and I using the x-ray analysis macro discussed in 4.3. This paper has been submitted for publication as of June 30, 2012.

ARTICLE TYPE www. rsc.org/xxxxxx | XXXXXXXX

Interaction and Partitioning of Ethanol with Lipid Membranes as Seen by X-ray and Neutron Scattering

Laura Toppozini,*[a] Clare L. Armstrong,[a] Matthew A. Barrett,[a] Songbo Zheng,[a] Lindy Luo,[a] Hirsh Nanda,[b] Victoria Garcia Sakai,[c] Maikel C. Rheinstädter,[a,d]

Received Xth XXXXXXXXXX 20XX, Accepted Xth XXXXXXXXX 20XX
First published on the web Xth XXXXXXXXXX 200X
DOI: 10.1039/b000000x

(June 21, 2012) We present a combined neutron and x-ray scattering investigation to study the effect of ethanol on molecular structure and dynamics of lipid membranes. DMPC powder hydrated with a 5wt% ethanol solution (corresponding to 2mol% of ethanol) were used for this study. From high resolution x-ray experiments the position and participation of the ethanol molecules in the phospholipid bilayers was determined in their gel and fluid phase. We find that the ethanol molecules reside in the head group region of the bilayers, with 1.6 ethanol molecules per lipid molecule. We find evidence for enhanced permeability in both fluid and gel phases of the phospholipid bilayers in the presence of ethanol molecules. Elastic and quasi-elastic neutron scattering data, obtained using a neutron backscattering spectrometer, was used to study slow nanosecond molecular dynamics on length scales corresponding to lipid diffusion, acyl chain dynamics and solvent dynamics. While the presence of ethanol molecules had no observable effect on these types of dynamics in the fluid L_α phase, the membranes appeared to have a higher degree of order in gel (L_α) and ripple ($P_{\beta'}$) phase. In particular, lipid diffusion was found to be slower by a factor of two in the more rigid gel phase when ethanol was present.

1 Introduction

Our knowledge about interactions between ethanol and lipid membranes on the molecular scale mainly stems from two techniques: nuclear magnetic resonance (NMR) experiments[1–3] and molecular dynamics (MD) simulations[4–9]. In particular experiments using neutron and x-ray scattering to probe molecular dynamics and structure are scarce[10,11], most likely due to experimental challenges.

When partitioning into the bilayer, ethanol has been found to reside predominately at the membrane/water interface. Ethanol's relatively hydrophilic nature causes it to exhibit a lower degree of partitioning into the hydrophobic core of the bilayer, differing from longer chain alcohols that insert into the hydrophobic core with their hydrophobic chains aligned parallel to the lipid hydrocarbon chains[7,12]. The ethanol molecules can form hydrogen bonds with the lipid head groups with bond lifetimes of about 1 nanosecond[7,13]. It has been reported that ethanol has numerous effects on the lipid bilayer: it decreases

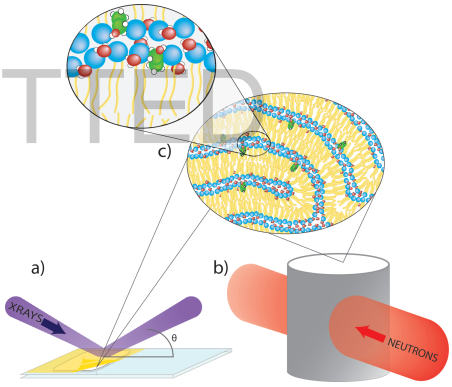

Fig. 1 Schematic diagram of the x-ray and neutron scattering experiments performed on a hydrated lipid powder. a) The powder was applied to a ∼1 mm depression in a glass slide for x-ray experiments. A 13μm Kapton sheet was placed over the depression to avoid evaporation. b) In the neutron scattering experiment, hydrated powder was applied to the sides of a annular aluminium sample holder. c) Cartoon of the membrane structure in the hydrated powder, notice the non-uniform bilayer orientation. DMPC: blue; H_2O: red; ethanol: green.

[a] *Department of Physics and Astronomy, McMaster University, Hamilton, ON, Canada. E-mail: toppozl@mcmaster.ca, rheinstadter@mcmaster.ca; Fax: +(905)546-1252; Tel: +(905)525-9140 ext.23134;*
[b] *NIST Center for Neutron Research, National Institute of Standards and Technology, Gaithersburg, MD, United States.*
[c] *ISIS Pulsed Neutron and Muon Source, Rutherford Appleton Laboratory, Didcot, United Kingdom.*
[d] *Canadian Neutron Beam Centre, National Research Council Canada, Chalk River, ON, Canada.*

the gel-to-fluid transition temperature [1,4], it has a weak effect on the area per lipid, and it increases membrane fluidity and disorder. [7] Finally, and perhaps most importantly, ethanol has been found to increase membrane permeability [7,14,15].

The aim of this study was to determine molecular structure and dynamics of phospholipid membranes immersed in a 5wt% ethanol solution. This concentration is much larger than concentrations typically found in human blood of ∼0.1wt% of ethanol. However, 5wt% can be considered a moderate alcohol concentration skin and mucous membranes in mouth and digestive system can be exposed to. We combined elastic and quasi-elastic neutron scattering and x-ray diffraction to study the properties of multi-lamellar lipid bilayers containing ethanol. Using elastic and inelastic neutron scattering, we determined the impact of ethanol on slow, nanosecond membrane dynamics at different length scales, such as lipid diffusion, nanoscale tail dynamics and hydration water dynamics. While ethanol did not alter dynamics in the fluid phase, the ripple and gel phases exhibited a higher degree of molecular order with slower dynamics. The lipid diffusion constant showed a significant 50% decrease in the gel phase of the membrane. From the x-ray scattering experiments, we were able to determine the position of the ethanol molecules in the membrane and determine their partition, i.e., the number of ethanol molecules per lipid molecule in the bilayer. In addition to this, we also have found experimental evidence suggesting an increase in the permeability of the membranes in the presence of ethanol.

2 Materials and Methods

2.1 Sample Preparation

To ensure a well defined ethanol concentration in the membranes, it is necessary that the bilayers are in direct contact with a water/ethanol solution. Hydrated lipid powders were used in this study. Highly concentrated suspensions of 1,2-dimyristoyl-sn-glycero-3-phoshatidylcholine (DMPC) were prepared by hydrating the lipid powder. Four types of samples were prepared, two for each scattering technique. In the dynamical neutron scattering experiments, lipids were hydrated with D_2O and D_2O/d-ethanol (deuterated ethanol) 5 wt%. In the x-ray scattering experiments, lipids were hydrated with ultra pure H_2O and an H_2O/5 wt% ethanol solution. The typical sample mass was ∼300 mg for the neutron and ∼15 mg for the x-ray experiment. A 3:1 mass ratio of water or water/ethanol solution to lipid powder was mixed to ensure full hydration of the bilayers. We envision the structure of the hydrated powder as depicted in the cartoon in Figure 1 as a randomly oriented multi-lamellar structure. We expect that in this type of sample preparation the number of water and ethanol molecules that attach to and incorporate into the bilayers change the concentration of the solution. About 7-8 water molecules per lipid molecule are found in the head group region of the bilayers [2,16]; we find about 1.6 ethanol molecules per lipid molecule (as will be shown below). Using these numbers the concentration of the water/ethanol solution changes from 2mol% to ∼1mol%. The number of ethanol molecules available to interact with the membranes is, therefore, not limited by the total number of ethanol molecules present.

An annular sample cell made of aluminium was used for the neutron experiments. The suspension was applied as a film to the inner wall of the hollow cylinder after which, an inner cylinder was inserted to form a seal. The sample was mounted inside of a cryostat. A temperature range between 280 K<T<335 K was used, which covers the temperatures of gel (L_β), ripple ($P_{\beta'}$) and fluid phase (L_α) of the bilayers. Temperature was controlled to better than 0.1 K.

In the x-ray experiments, the lipid mixture was spread on a ∼25 mm × 25 mm × 1 mm square well ground into a glass slide. This hydrated powder was sealed with a 13μm thick Kapton polyimide foil acting as an x-ray window using vacuum grease for adhesion. The sample was mounted in a temperature controlled humidity chamber during the x-ray experiments. Temperature was controlled using a bath controller with a temperature stability of better than 0.1 K. The structure of the lipid/ethanol system was studied at two temperatures: 293 K, allowing observation of the gel (ripple, $P_{\beta'}$) phase of the membranes, and 303 K, to observe their fluid L_α phase. Figure 1 shows schematics of the neutron and x-ray scattering sample and the experimental geometries.

2.2 Neutron Scattering Experiment

The neutron experiments were carried out at the High Flux Neutron Backscattering Spectrometer (HFBS) [20] at the NIST Center for Neutron Research (NCNR), Gaithersburg, in its standard set-up with Si(111) monochromator and analyzer crystals corresponding to an incident and analyzed neutron energy of 2.08 meV (λ = 6.27 Å). Two types of experiments were conducted: so-called elastic (fixed energy window, FEW) scans and quasi-elastic neutron scattering (QENS).

Elastic incoherent neutron scattering is an established tool for the detection of molecular freezing and melting [17,18,21–24]. Sample scattering is recorded as a function of temperature. At the energy resolution of ∼0.9 μeV, only molecular motions with characteristic times slower than ∼1 ns are monitored. The experiment covered lateral length scales of 3.5-12 Å to study dynamics down to nearest-neighbour distances of both lipid acyl tails and hydration water molecules. Performing elastic scans as a function of temperature, reveals dynamical changes on different length scales. Freezing and melting of molecular degrees of freedom can easily be identified because they lead to jumps or kinks in the recorded intensity.

Table 1 Neutron detector (D1-D16), corresponding centre Q-value, length scales and type of scattering and motion detected. The lipid acyl chain correlation peak is centred $Q \sim 1.5$ Å^{-1}. The hydration water correlation peak was reported at Q=1.85 Å^{-1} [17–19].

Detector	Q (Å^{-1})	Distance (Å)	Dominant Scattering	Associated Motion
D1	0.25	25		
D2	0.36	17		
D3	0.47	13		
D4	0.56	11		
D5	0.62	10		
D6	**0.75**	**8**		
D7	**0.87**	**7**	**incoherent**	**lipid diffusion**
D8	**0.99**	**6.3**		
D9	**1.11**	**5.7**		
D10	1.22	5.2		
D11	1.32	4.8		
D12	1.42	4.4		
D13	**1.51**	**4.2**	**lipid tail correlation peak**	**lipid tail dynamics**
D14	1.60	3.9		
D15	1.68	3.7		
D16	**1.75**	**3.6**	**hydration water correlation peak**	**hydration water dynamics**

The 16 HFBS detectors (D1−D16) cover a total Q range of 0.14 Å^{-1} to 1.81 Å^{-1}. Table 1 lists the centre Q-values and the corresponding length scales. Each detector covers an angular range of approximately 8°. Different types of motion fall into the length scales covered by the HFBS spectrometer.

Slow nanosecond dynamics of lipid and water molecules were studied previously using backscattering spectrometers by analyzing elastic scattering at the positions of the lipid acyl chain and hydration water correlation peaks.[17–19,24,25] Based on these results, different types of dynamics can be distinguished based on their length scale dependence:

- Incoherent scattering is dominant at intermediate Q values, between about 0.3 and 1.5 Å^{-1}, where no correlation peak occurs. This range of length scales between ∼4 and 21 Å is often used in neutron scattering studies (see, e.g.[21,23]) to study diffusion and molecular mean square displacements of lipid molecules. We assigned the Q-range from 0.7 Å^{-1} to 1.17 Å^{-1} (detectors D6-D9), to incoherent dynamics due to diffusion of lipid molecules, covering length scales from 6.3 Å- 10 Å.
- Detector D13, covers the Q range of the lipid acyl chain correlation peak (∼1.5 Å^{-1}) and was assigned to lipid tail fluctuations.
- The nearest-neighbour distance of the hydration water molecules leads to a correlation peak centred at 1.85 Å^{-1}, corresponding to a nearest-neighbour distance of 3.4 Å between hydration water molecules, slightly larger than bulk water. Detector D16 was, therefore, assigned to dynamics of hydration water molecules.

The multi-lamellar Bragg reflections due to stacking of the membranes are veritable Bragg peaks related to an order on basically infinite time scales. The in-plane correlations related to lipid tails and water molecules, which lead to the in-plane correlation peaks at high Q values above ∼0.7 Å^{-1} in Figure 2, however, are dynamic in nature. It has been shown using energy resolved neutron diffraction[17] that these correlations exist on time scales only up to nanoseconds. The absence of "true" elastic scattering is the fingerprint of a fluid structure; it is well known that lipid membranes show properties of a 2D fluid in their fluid phases. The corresponding reflections are usually observed in neutron and x-ray diffraction experiments as relatively weak and broad peaks as compared to the out-of-plane Bragg peaks. The scattering, which occurs at the peak positions of lipid acyl chain and hydration water molecules in our experiment is, therefore, not static but can be used to characterize the time scale of the underlying molecular degrees of freedom, as suggested in Table 1 and in[17,18,24].

Lipid diffusion, and lipid tail and hydration water dynamics were studied simultaneously by analyzing different detectors. Table 1 lists the dominant scattering contribution for different length scales and corresponding motion observed in the various detectors. Because the HFBS analyzers cover an angular range of approximately 8° each the experiment was not sensitive to shifts of the lipid and water correlation peak with temperature within this coarse Q resolution due to potential structural changes of the bilayers with temperature. The measured intensity at the Q position for diffusion, lipid tail and hydration water dynamics is shown in Figure 4. The scans cover a temperature range of 280 K$< T <$335 K. Data were taken in heating and cooling scans at a rate of 0.5 K/min. Because the counting time was set to 1 min, the temperature resolution of the experiment is determined to be 0.5 K.

Quasi-elastic neutron scattering is a powerful tool to gain access to slow nanosecond molecular dynamics in soft-matter and biophysics, see e.g.[26] for a recent review. Neutron spectra are recorded in quasi-elastic neutron scattering experiments. A mechanical Doppler drive was employed to produce an oscillatory motion of the monochromator in order to vary the incident energy of the neutrons. A dynamic range of -15 μeV$< \hbar\omega <$15 μeV is accessible using this set-up. By analyzing the shape of the inelastic scattering, detailed information about nanosecond molecular dynamics in the membranes can be obtained. We used quasi-elastic scattering to determine lipid diffusion coefficients at selected temperatures, as will be shown below. Phase transitions were determined first using

the elastic scans. Diffusion was then measured in the gel and fluid phases using QENS.

2.3 X-ray Scattering Experiment

X-ray scattering data was obtained using the Biological Large Angle Diffraction Experiment (BLADE) in the Laboratory for Membrane and Protein Dynamics at McMaster University. BLADE uses a 9 kW (45 kV, 200 mA) CuKα rotating anode at a wavelength of 1.5418 Å. Both source and detector are mounted on movable arms ensuring the sample stay horizontal during the measurements. Multi-layer focussing optics provide a high intensity beam with monochromatic x-ray intensities up to 10^{10} photons/(mm$^2\times$s). Data were obtained in reflection geometry using a collimated x-ray beam. A schematic of the scattering geometry is shown in Figure 1 a).

The scans cover a Q range from 0 to 2.5 Å^{-1}, which extends over length scales from intermolecular distances to the lamellar spacing between neighbouring membranes. As the multi-lamellar membranes are not oriented, Bragg peaks, due to the lamellar stacking perpendicular to the membranes and in-plane correlation peaks due to molecular alignment in the plane of the membranes, are observed simultaneously. The lamellar Bragg peaks are observed in the Q range between $\sim$0.1 and $\sim$0.7 Å^{-1}, corresponding to lamellar spacings of $\sim$60 Å. The lipid acyl chain correlation peak in DMPC occurs at a Q value of $\sim$1.5 Å^{-1} in the gel phase [17,27], below the main phase transition at T = 294 K.

The multi-lamellar Bragg peaks allow for the determination of the structure perpendicular to the plane of the membranes (see, e.g. [28,29] for recent reviews). Because of the membrane stacking, i.e. the convolution with the lamellar structure factor, the Fourier transform is not continuous but discrete. The different Fourier components are observed in the experiment as the integrated intensities of the out-of-plane Bragg peaks. The electron density, $\rho(z)$, is approximated by a 1D Fourier analysis [30]:

$$\begin{aligned}\rho(z) &= \rho_W + \frac{F(0)}{d_z} + \frac{2}{d_z}\sum_{n=1}^{N} F(q_n)\nu_n \cos(q_n z) \\ &= \rho_W + \frac{F(0)}{d_z} + \frac{2}{d_z}\sum_{n=1}^{N} \sqrt{I_n q_n}\nu_n \cos\left(\frac{2\pi n z}{d_z}\right) \quad (1)\end{aligned}$$

N is the highest order of the Bragg peaks observed in the experiment and ρ_W the electron density of water or solution. The integrated peak intensities, I_n, are multiplied by q_n and square rooted to obtain the form factors, $F(q_n)$ [31,32]. The bilayer form factor $F(q_z)$, which is in general a complex quantity, is real-valued in the case of centro-symmetry. The phase problem of crystallography, therefore, simplifies to the sign problem $F(q_z) = \pm|F(q_z)|$. The phases, ν_n, can only take the values ± 1. When the membrane form factor $F(q_z)$ is measured at several q_z values, a continuous function, $T(q_z)$, which is proportional to $F(q_z)$, can be fit to the data [10,31–33]:

$$T(q_z) = \sum_n \sqrt{I_n q_n} sinc(\pi d_z q_z - \pi n). \quad (2)$$

Once an analytical expression for $T(q_z)$ has been determined from fitting the experimental peak intensities, the phases ν_n can be determined from $T(q_z)$.

X-ray scans were measured for the pure DMPC bilayers and the DMPC/ethanol sample at two temperatures: T = 293 K, the gel phase for DMPC bilayers, and T = 303 K, their fluid phase. Data are shown in Figure 2. A background scan of the glass substrate with Kapton polyimide foil was subtracted from the data shown in parts a)-d). The pronounced Bragg peaks at Q values up to $\sim$0.7 Å^{-1} were assigned to a multi-lamellar membrane structure in the powder. We find lamellar d_z spacings of d_z^{DMPC} = 64.27 Å, $d_z^{DMPC/ethanol}$ = 64.89 Å in the gel phase at T = 293 K and d_z^{DMPC} = 61.10 Å and $d_z^{DMPC/ethanol}$ = 62.02 Å in fluid membranes. The measured d_z spacing for DMPC is in excellent agreement to lamellar spacings reported for fully hydrated bilayers [34].

The Bragg peaks were fit using Lorentzian peak profiles. Up to eight peaks could be fit and were used to reconstruct the electron density. Figure 3 displays relative electron densities as determined using Equations (1) and (2). $T(q_z)$ was fit to the experimentally determined peak intensities using Equation (2), where an array of ν_n values was determined out of the corresponding 2^8 combinations, assuming a phase of +1 or -1. The inset in Figure 2 a) shows the best fit of $T(q)$ for DMPC in its gel phase as example. All samples were well fitted using the following combination of phases:$\bar{1}\ \bar{1}\ 1\ 1\ \bar{1}\ \bar{1}\ 1\ 1$. The resulting electron densities are plotted in Figure 3.

The lipid acyl chain positional correlation peak is the result of closely packed acyl chains making up the hydrophobic core of the membrane. The corresponding correlation peaks were observed at 1.49 Å^{-1} in both the DMPC and DMPC/ethanol systems at T = 293 K, corresponding to a distance between neighbouring acyl chains of $\sim$4.21 Å in the gel phase. In the fluid phase, the lipid tail positional correlation peaks occur at 1.39 Å^{-1} in the DMPC and DMPC/ethanol samples at T = 303 K, corresponding to an increased distance between neighbouring acyl chains of $\sim$4.53 Å. The acyl chain packing is not significantly affected by the presence of ethanol as the corresponding peak does not change with ethanol.

3 Results

3.1 Molecular Freezing and Melting Studied by Elastic Neutron Scattering

Elastic scattering data, during heating and cooling, are shown in Figure 4. The heating curves in Figure 4 have been shifted

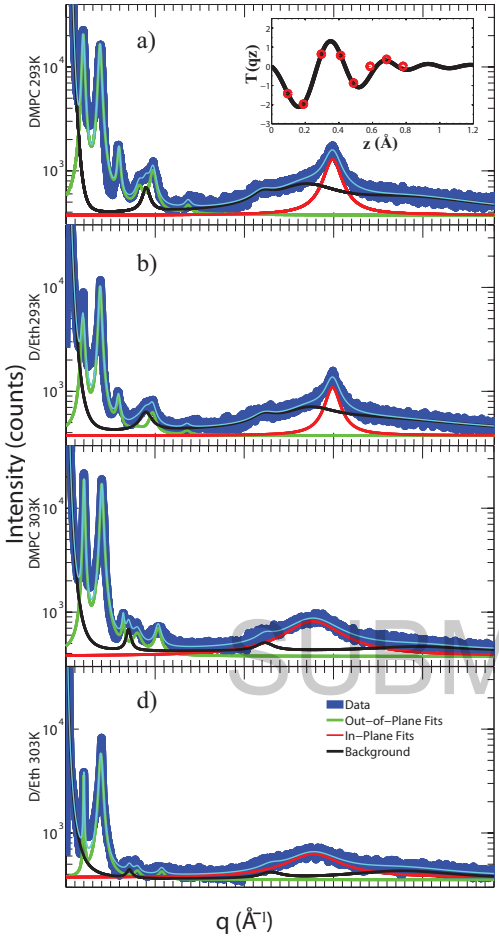

Fig. 2 Overview of the x-ray data. a) DMPC at T = 293 K (gel phase). The inset shows $T(q_z)$, as defined in Equation (2). b) DMPC/ethanol at T = 293 K (gel phase), c) DMPC at T = 303 K (fluid phase), d) DMPC/ethanol at T = 303 K (fluid phase). Background of the sample holder was subtracted from the data in a)-d). The total fit is shown in light blue. The low-Q scans were assigned to a multi-lamellar membrane structure and shown in green. The inter-acyl chain correlation peak at Q values of $\sim$1.5 Å^{-1} is shown in red.

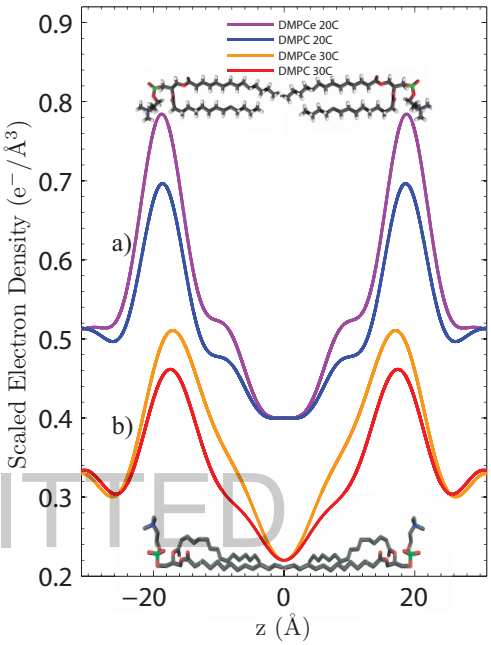

Fig. 3 Electron densities $\rho(z)$ for all sample variations, as determined from the data in Figure 2, using Equations (1) and (2). $\rho(z)$ was scaled to the electron density of a CH_3 group in the centre (i.e. where the end of the lipid tails meet) and water or ethanol/water electron density at the ends (i.e. between the hydrophilic headgroups of adjacent bilayers). The 293 K samples in a) are shifted by +0.18 e$^-$/Å^3 on the y-axis for clarity. $\rho(z)$ is increased in the presence of ethanol in the head-group region and at z-values around $\sim$9 Å.

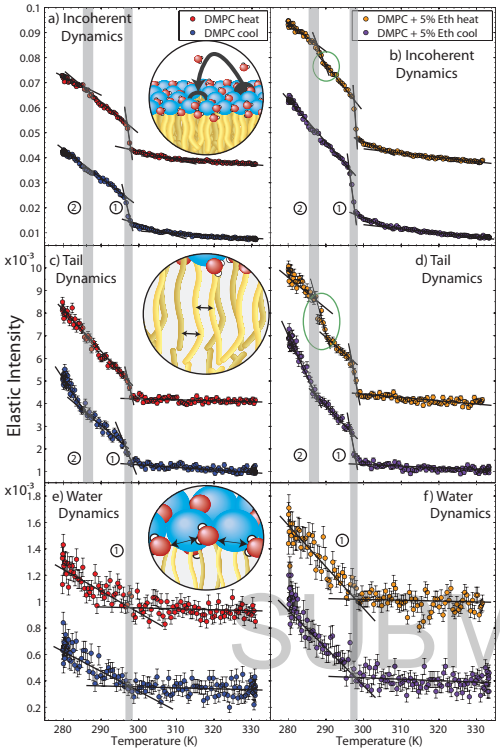

Fig. 4 The elastic neutron scattering experiment was sensitive to lipid diffusion, lipid acyl chain and hydration water dynamics. As listed in Table 1, data from detectors D5 through D8 were summed to create the lipid diffusion plots, detector D13 data for lipid acyl chain dynamics, and detector D16 data for hydration water dynamics. Heating and cooling scans are shown. All heating curves are shifted upward in intensity for clarity; the original data show closed loops. Error bars represent one standard deviation. The experimental temperature resolution was 0.5 K. The error in the determination of the transition temperatures is related to the determination of the intersection of the different slopes. For lipid dynamics we estimate the maximum error to be ∼2 K as determined by min. max. slopes. The hydration water data in c) has slightly larger statistical errors and the maximum error in the determination of the transition temperature was estimated to be ∼ 4 K.

upward on the intensity axis to distinguish the transition locations. The original data shows closed loops for all plots and the system always returned to its initial high temperature intensity also indicating that the number of particles in the beam was constant during the experiments.

Elastic scattering related to lipid diffusion is shown in Figure 4 a) for pure DMPC and b) for DMPC/ethanol. A pronounced step is observed at a temperature of T = 296 K. This temperature coincides well with the temperature of the main transition in fully hydrated bilayers made of DMPC, which was reported at T = 296.6 K in multi-lamellar DMPC systems[18,21]. The transition temperatures in a) and b) coincide, showing that within the temperature resolution of this experiment, ethanol does not change the temperature of the transition at this length scale. Comparing the pure DMPC and DMPC/ethanol, it is seen that the introduction of ethanol does not change the elastic intensity in the fluid phase. In the gel phases, however, the elastic intensity changes drastically when ethanol is introduced, we see this as an increase in the slopes of the transitions at these lower temperatures. This points to an enhanced order in the gel phase due to ethanol. The diffusion constants in the gel and fluid phase are determined below from the QENS experiments. An additional kink is observed at a temperature of T = 288 K, which can be assigned to the pre-transition in DMPC, i.e., the transition between the gel (L_β) and ripple ($P_{\beta'}$) phase of the bilayers. This pre-transition is much more pronounced in the presence of ethanol molecules. No hysteresis was observed between the cooling and heating curve within the experimental resolution.

Nanoscale lipid tail dynamics are observed in Figures 4 c) and d). A pronounced step in the elastic intensity is observed at T = 296 K, related to the main transition. The transition temperatures in DMPC and DMPC/ethanol coincide; within the instrumental resolution, ethanol does not change the temperature of freezing or melting of the lipid acyl chains on nearest-neighbour distances of acyl chains. The step in the elastic scattering is, however, slightly larger in the presence of ethanol indicating a better ordered state in the $P_{\beta'}$ phase. A second pronounced step is observed in the ethanol sample at T = 288 K, associated with the transition into the L_β phase. The transition is also more pronounced in the heating curve.

Dynamics of the hydration water are observed in Figures 4 e) and f). This detector is located at a Q position of ∼1.85 Å^{-1}. This length scale is mainly sensitive to hydration water, which has a slightly lower density as compared to bulk water. Freezing and melting of bulk water would be observed at a Q-value of 2 Å^{-1} and at a temperature of 273 K, both conditions outside of our measurement range. A pronounced kink in the elastic intensity is observed at T = 296 K, also observed in the lipids. The water dynamics follow that of the lipid molecules and ethanol does not seem to change their dynamical behaviour. No hysteresis is observed; the ethanol does

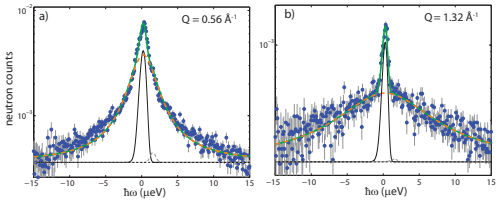

Fig. 5 QENS spectra of the DMPC/ethanol sample at T = 308 K recorded at low (a) and high (b) Q-values. The instrumental resolution is fit with two functions: an asymmetric Gaussian (solid black curve) and a second Gaussian function (dashed grey curves). The quasi-elastic broadening is fit with a Lorentzian (dashed orange curve) and a constant background (dashed black line), and the total fit is shown as a solid green curve.

Table 2 Properties of water, ethanol and the water/ethanol solution. The ethanol concentration is given as wt%, vol% and mol%. The calculated electron density is used to normalize the electron densities of the bilayers in Figures 3 and 7.

	Water (H_2O)	Ethanol (C_2H_6O)	Water/Ethanol
% by weight (wt%)			5
% by volume (vol%)			6.25
% by moles (mol%)			2.02
Molecular Weight (g/mol)	18.0153	46.06844	18.58104
Molecules/Å^3	$3.34{\cdot}10^{-2}$	$1.03{\cdot}10^{-2}$	$3.20{\cdot}10^{-2}$
Number of Electrons	10	26	10.3
Electrons density (e^-/Å^3)	0.334	0.268	0.330

not seem to change the freezing and melting of the hydration water within the temperature resolution of this experiment.

3.2 Nanosecond membrane dynamics and Diffusion studied quasi-elastic neutron scattering

QENS allows for the determination of lipid diffusion in the membrane. Exemplary QENS spectra for the DMPC/ethanol system at T = 308 K, in the fluid phase of the bilayers, are shown in Figure 5 for two selected Q values. The instrumental resolution was determined from a Vanadium sample and it was found that rather than exhibiting a simple Gaussian peak shape, the resolution had a slight gradual asymmetry at negative $\hbar\omega$ values (fit with an asymmetric Gaussian) and a small shoulder at positive $\hbar\omega$ values (fit with an additional small Gaussian). The asymmetric Gaussian used to accommodate the gradual asymmetry in the resolution function was composed of a Gaussian with an exponential function on one side of the peak[35],

$$y = y_o + H(\hbar\omega_o - \hbar\omega)Ae^{-\left(\frac{(\hbar\omega-\hbar\omega_o)^2}{2\sigma^2+\tau|\hbar\omega-\hbar\omega_o|}\right)} + H(\hbar\omega - \hbar\omega_o)Ae^{-\left(\frac{(\hbar\omega-\hbar\omega_o)^2}{2\sigma^2}\right)}, \quad (3)$$

where A is the amplitude, ω_o the elastic energy peak position, σ the Gaussian standard deviation, H is the Heaviside function, and τ the asymmetry parameter. For τ = 0, a symmetric Gaussian function is obtained. Values of τ used to fit this gradual asymmetry ranged from $\sim$ 0.030-0.217. A Q range of 0.55 Å^{-1} < Q <1.35 Å^{-1} was used for the determination of the diffusion constant.

The scattering obtained from the DMPC/ethanol sample is described by a narrow central component, corresponding to the instrumental resolution ($\sim$0.9 μeV), a constant background, and a quasi-elastic broadening due to relaxational dynamics of the lipid molecules. This broadening is fit with a Lorentzian function, convolved with the Gaussian instrumental resolution. It should be noted that the FWHM of the Lorentzian functions quoted in the paper are the deconvoluted values.

Figure 6 displays the FWHM for all measured Q-values as function of Q^2. In this plot the FWHM scale linearly with Q^2, a behaviour indicative of continuous diffusion ($FWHM_L = 2\hbar DQ^2$), as explained in great detail in, e.g., [36]. This behaviour was observed for the quasi-elastic broadening in the gel ($P_{\beta'}$) and fluid phase of the DMPC and DMPC/ethanol bilayers, as shown in Figure 6. The data fit is depicted by a blue line for the pure DMPC and red line for the DMPC/ethanol. From this linear fit the diffusion coefficients could be extracted and are displayed in Figure 6. These values are in agreement with diffusion coefficients quoted in the literature for similar systems [37–41]. We note that the linear fit in Figure 6 does not pass through the origin, as one would expect, and the offset is larger than the instrumental resolution. This effect is often observed in the literature, however no consistent explanation has been offered. We also note that the accessible Q range of the HFBS spectrometer is not sensitive to the ballistic diffusion regime [36] or a potential flow-like diffusion, as reported recently [39].

No difference in the diffusion constants in the fluid phase with or without ethanol was observed within the resolution of this experiment. Diffusion constants in the gel phase are significantly slower than in the fluid phase for both samples, with and without ethanol. However, diffusion in the gel phase in the presence of ethanol is slowed down by a factor of $\sim$2 as compared to pure DMPC, as shown in Figure 6 b).

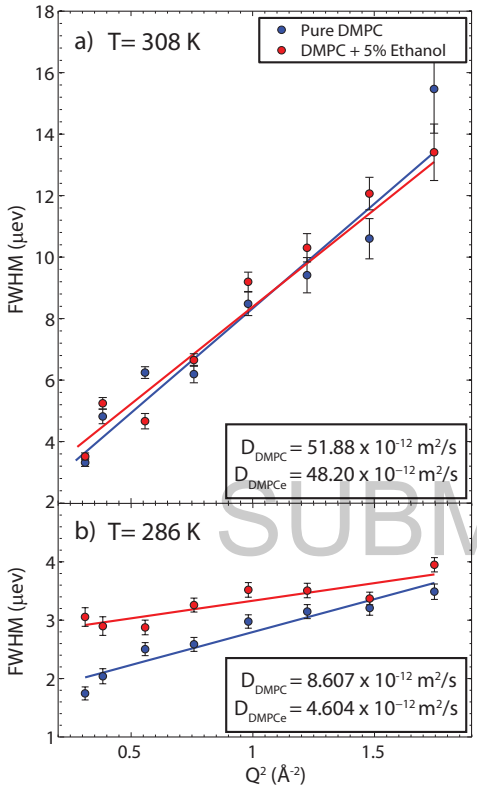

Fig. 6 FWHM of the quasi-elastic broadening as determined from the data in Figure 5. Data are plotted as function of Q^2 such that the slope of the line is directly proportional to the diffusion coefficients.

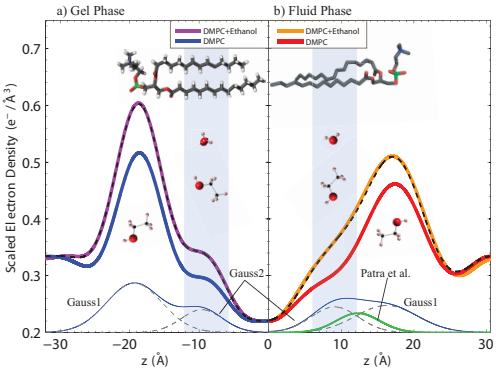

Fig. 7 Bilayer electron densities in gel and fluid phases. Each density is scaled to the electron density of CH_3 at the centre of the bilayer and the electron density of the respective solutes. One leaflet of a bilayer is shown. a): In the gel phase, the electron density is increased in the presence of ethanol. The increase can be described by the addition of two Gaussian functions to the DMPC density (dashed black line). b): In the fluid phase, an increase is seen in the presence of ethanol, which can also be described by two Gaussian distributions. The weight of the two Gaussians is, however, shifted as compared the gel phase. The two Gaussians can be assigned to the presence of ethanol and possibly water molecules in the bilayers. The green Gaussian function is extrapolated from a mass density plot determined by a molecular dynamics simulation of DPPC and ethanol from Patra *et al.*[7]

3.3 Electron Densities And Location of the Ethanol Molecules from X-Ray Scattering

The integrated intensities of out-of-plane Bragg peaks in Figure 2 were used to calculate the electron density profile perpendicular to the bilayers following Equation (1). Position and partitioning of the ethanol molecules in the bilayers can then be determined from the different $\rho(z)$, shown in Figure 3. In order to put $\rho(z)$ on an absolute scale, the electron densities were scaled to fulfil the condition $\rho(0)$=0.22 e/Å^3 (the electron density of a CH_3 group at the end of a lipid tail) in the centre of the bilayer, and the electron density of the solution outside the bilayers. The electron densities for water and water/5wt% ethanol solution are calculated in Table 2. We find $\rho(d_z/2)$=0.330 e/Å^3 for water/5wt% ethanol, and the well known $\rho(d_z/2)$=0.334 e/Å^3 for pure water.

The normalized electron density profiles for DMPC in its gel phase are depicted in Figure 3 a). The profile corresponds to a DMPC molecule in the well ordered gel state with both chains in all-trans configuration, as has been reported previously[30]. The electron rich phosphorous group in the head group region can be identified by the peak in the electron density at ∼22 Å. $\rho(z)$ monotonically decreases towards the bilayer centre at $z = 0$; only CH_3 group at the end of the lipid tails are found in the centre. The electron density profiles in the fluid phase in Figure 3 b) agree well with profiles reported in the literature[30,42,43]. The sharp dip at the centre is the telltale sign of a fluid membrane, i.e., the increasing number of kink-defects lower the density of the lipid tails in the bilayer centre.

The presence of ethanol leads to an increase in electron density in the head group region of the bilayers. $\rho(z)$ is also increased around z values of ∼9 Å, representing the presence of molecules that have permeated the membrane. The dip in the electron densities at z values of ∼27 Å is most likely related to a reduced density of the hydration water and solvent at the lipid/solvent interface, as will be discussed in detail below.

For a quantitative comparison, Figure 7 shows the electron density profile of a single leaflet for each temperature in more detail. The increase in electron density is the result of the presence of additional molecules in the bilayers. The addition of two Gaussian peak profiles $\left(\rho(z) = \rho_0 \exp[-\left((z-z_0)^2/2\sigma\right)^2]\right)$ to the electron density profiles of pure DMPC in Figure 7 a) and b) results in the dashed black lines, which show excellent agreement to the DMPC/ethanol data. In the gel phase, Gauss 1 is centred at 19.35 Å and Gauss 2 is centred at 9.6 Å, whereas for the fluid phase we obtain the Gauss 1 centred at 16.25 Å and Gauss 2 centred at 9.1 Å. While Gauss 1 is dominant in the gel phase, Gauss 1 becomes comparable to Gauss 2 in the fluid phase in Figure 7. Position, width and area of the Gaussian distributions in the different samples are summarized in Table 3.

The electron density of the lipid bilayer is defined by $\rho = e^-/V_L = e^-/(A_L \cdot dz)$, where V_L is the volume of a lipid molecule, A_L is the lipid area and dz the lamellar spacing, i.e., the size of the unit cell. One unit contains two lipid molecules and their hydration water, as depicted in Figure 3. The integral $e^- = A_L \int_0^{d/2} \rho(z)dz$ gives the number of electrons in one leaflet. For pure DMPC this number is calculated to be e^-_{gel}=514 and e^-_{gel}=622 in gel respective fluid phase. Using the number of electrons per lipid (374, $C_{36}H_{72}NO_8P$) and water molecule (10, H_2O), these numbers refer to 1 lipid molecule hydrated by 14 water molecules in the gel, and 1 lipid molecule hydrated by 25 water molecules in the fluid phase, in excellent agreement to literature values[16]. This agreement proves that our technique is capable to quantitatively determine electron densities, which is an important point when we will discuss partitioning of molecules below.

We note that the determination of lipid areas is an important field in membrane research. As discussed in detail in the literature[44,45], it is not straightforward to determine the area per lipid molecule directly from the inter-acyl chain correlation peak from the data in Figure 2. Lipid areas can be determined with high accuracy by a combined approach using x-ray and neutron scattering and computer simulations, see[28] for a recent review. We, therefore, used lipid areas published for DMPC in gel and fluid phase by the Nagle group[30,42] (listed in Table 3). We also note that lipid areas can be determined from the chain correlation peaks in de-hydrated gel phases, in the absence of lipid fluctuations[46].

The number of electrons related to the electron density in the Gaussian peaks can be calculated to $e^- = A_L \int_{Gauss} \rho(z)dz$. By dividing this number by the number of electrons of an ethanol or water molecule, the number of ethanol or equivalent water molecules per lipid molecule can be determined. As the x-ray experiment is averaging over a large number of those unit cells, a non-integer occupancy means that ethanol (or water) molecules can be shared between lipids. Partitioning of ethanol and water molecules in the lipid bilayers can be determined from these parameters and are calculated in Table 3 to be discussed in detail further below.

A dip in the electron densities in Figure 7 a) and b) was observed at z values of ∼28 Å, in the hydration water layer. The decrease in $\rho(z)$ is indicative of a reduced density of the first layer of hydration water, as will be discussed below.

4 Discussion

By combining x-ray diffraction and elastic incoherent and quasi-elastic neutron scattering, molecular structure and dynamics of lipid membranes containing ethanol was determined. To the best of our knowledge this is the first extensive scattering study of the interaction of ethanol with lipid

Table 3 Parameters of the Gaussian peaks, $\rho(z) = \rho_0 \exp[-\left((z-z_0)^2/2\sigma\right)^2]$, as determined from the fits in Figure 7. Gaussian 1 is assigned to the presence of ethanol molecules in the head group region of the bilayers. Gaussian 2 can be assigned to additional ethanol (scenario ①) or water molecules (scenario ②) in the hydrophobic membrane core. Numbers are provided for both scenarios. Literature values have been used for the lipid areas in gel and fluid phase.

	z_0 (Å)	ρ_0	σ (Å)	$\rho_0\sigma\sqrt{2\pi}$ (Å^2)	d_z (Å)	A_L (Å^2)	#electrons	#molecules
Gauss1 (gel)	19.35	0.087	4	0.872	64.89	47.2[42]	0.654	1.58 ethanol/lipid
Gauss2 (gel)	9.6	0.04	3	0.301	64.89	47.2[42]	0.226	① 0.55 ethanol/lipid ② 1.42 water/lipid
Gauss1 (fluid)	16.25	0.0475	4.25	0.506	62.02	60.6[30]	0.506	1.18 ethanol/lipid
Gauss2 (fluid)	9.1	0.045	3.25	0.367	62.02	60.6[30]	0.367	① 0.85 ethanol/lipid ② 2.22 water/lipid

membranes. The bilayers were in contact with a 5wt% water/ethanol solution, corresponding to 2mol% of ethanol. This concentration is significantly larger than typical, very low alcohol concentrations found in human blood of ∼0.092wt% (∼0.036mol%)[2]. We have chosen a moderate alcohol concentration of 5wt% of ethanol for this study, which we consider relevant as skin and mucous membranes in mouth and digestive system can be exposed to such alcohol concentrations.

Electron density profiles in Figures 3 and 7 allowed for the determination of the position of the ethanol molecules and their partition in lipid membranes. The presence of the ethanol molecules leads to an increase of the electron densities in gel and fluid phase. The difference between $\rho(z)$ with and without ethanol is well described by the addition of two Gaussian distributions to the electron densities of pure DMPC bilayers. Gaussian 1 is centred at ∼19 Å and ∼16 Å in gel and fluid phase, in the head group region of the membrane. Gaussian 2 is centred at ∼9 Å in gel and fluid phase, in the hydrophobic membrane core.

The two Gaussians contributions can be compared to results from NMR[1–3] and molecular dynamics simulations[7,8]: Barry and Gawrisch located the ethanol molecules from NMR experiments close to the lipid/water interface for bilayers in the fluid phase in the region of the headgroup, glycerol backbone and the uppermost chain methylene groups. The position of ethanol molecules as determined from molecular dynamics (MD) simulations by Patra *et al.* (interpolated from Figure 6 in[7] and scaled by electron density divided by mass density of ethanol) is marked by the solid green distribution in Figure 7. The MD simulations localize the ethanol molecules slightly closer to the membrane core, while NMR and x-ray diffraction experiments show good agreement and find it closer to the head group region, in the membrane water interface. We, therefore, assign Gaussian 1 to ethanol molecules in the head group region of the bilayers in agreement with NMR studies.

The number of ethanol molecules in the head group region can be determined by further analysis of the areas of the Gaussian peaks. As listed in Table 3, the increase in electron density corresponds to ∼1.6 ethanol molecules lipid molecule in the gel phase at T = 293 K. Immersion of DMPC in a 2mol% ethanol solution was found to result in a 1.6 molar concentration of ethanol in the head group region of the membranes. The number of ethanol molecules assigned to Gaussian 1 in the fluid phase is slightly less. We determine ∼1.2 ethanol molecules per lipid molecules.

Measuring membrane/ethanol and membrane/water partition coefficients in the presence of ethanol has proven to be difficult because of experimental challenges, mainly related to the small numbers and the volatility of the ethanol molecule. Partition coefficients must be measured in-situ, directly on lipid bilayers. Partition of ethanol in bilayers was measured using different techniques[2]: radioisotopes[47,48], calorimetry[9,49,50] and vapour pressure measurements[2,51]. The molar coefficient of ethanol partitioning into lipid bilayers, K_p, is defined as $K_p = X^{Et}_{lipid}/X^{Et}_{water}$, where X^{Et}_{lipid} and X^{Et}_{water} are the mole fractions of ethanol in lipid respective water phase. K_p can also be expressed using molar ratios $K_p = \frac{677.933}{18.015} \times molar\ ratio^{Et}_{lipid}/molar\ ratio^{Et}_{water}$, with M_{lipid}=677.933 g/mol and M_{water}=18.015 g/mol the molar masses of DMPC and water.

A K_p value of K_p=19 was reported recently for POPC bilayers[2] at a water/ethanol concentration of 0.036mol%. K_ps of $K_p \sim 8$[48], $K_p \sim 15$[9] and $K_p \sim 28$[50] were reported in DMPC. These coefficients correspond to molar concentrations in the order of ∼1mol%, i.e., concentrations of 1 ethanol molecule per about 100 lipid molecules in the bilayers. However, we find 1.6 respective 1.2 ethanol molecules per lipid molecule in gel and fluid phase. The fact that the coefficients reported in the literature[9,48] have been determined in solutions with much smaller ethanol concentrations may point to a nonlinear partitioning of ethanol in lipid bilayers, in particular at higher alcohol concentrations. Our result is in agreement with computer simulations by Terama *et al.*[9], who observed almost complete partitioning of the ethanol molecules.

We now address the origin of the second Gaussian, inside the membrane core. The solubility of ethanol in the hydrophobic membrane core was found to be small in NMR experiments[1,2] and computer simulations[6]. However, Gaussian 2 partially overlaps with the z position of ethanol molecules reported from MD simulations[7], as shown in Figure 7. In a more recent MD study using DPPC membranes in contact with a 1.9mol% ethanol solution (see Figure 4 in[8]) an additional peak was observed in the mass density of the bilayers near the bilayer centre, in agreement with the data in Figure 7. The second Gaussian contribution might, therefore, be related tot he presence of ethanol molecules in the hydrophobic membrane core. On the other hand, ethanol is also known to increase the permeability of lipid membranes for water molecules[53–56]. Alternatively, the increase in electron density may, therefore, be due to an increase of the number of water molecules in the membrane in a 1.9mol% water/ethanol solution.

Because we can not unambiguously assign Gaussian 2 to the presence of either ethanol or water molecules, we would like to discuss two scenarios to explain the second Gaussian contribution centred at ∼9 Å:

1. Gaussian 2 can be assigned to additional ethanol molecules in the hydrophobic membrane core.

2. Gaussian 2 can tentatively be attributed to water molecules in the bilayer, which have traveled into the hydrophobic core due to ethanol's effect of increased membrane permeability.

If Gaussian 2 is related to the presence of additional ethanol molecules in the membrane core, the increase in electron density corresponds to 0.55 ethanol molecules per lipid molecule in the gel phase and 0.85 ethanol molecules per lipid molecule in the fluid phase. It is believed that general anaesthetics, such as ethanol, dissolve in membranes thereby changing their physical properties and altering membrane function[57]. Changes in lateral pressure is speculated to be relevant for protein function and binding sites, and in particular functioning of ion channels[58]. The potential presence of ethanol molecules in the hydrophobic core, as listed in Table 3, is likely to be important to distinguish between different theories[58–61]. The presence and solubility of ethanol molecules in the hydrophobic membrane might also be relevant to model ethanol crossing event, as discussed in[7–9].

When we assign Gaussian 2 to the presence of water molecules in the hydrophobic membrane core, the increase in electron density corresponds to 1.42 water molecules per lipid molecule in the gel state of the phospholipid membranes. In the fluid phase at T = 303 K (Figure 7 b)), 2.22 water molecules per lipid molecule is dissolved in the hydrophobic membrane core

The results from elastic and quasi-elastic neutron scattering give access to molecular membrane dynamics in the presence of alcohol. Lipid diffusion in the fluid phase is not altered by the presence of ethanol molecules in the bilayers, as shown in Figure 6. The diffusion constant of $D \sim 52{\cdot}10^{-12}$ m^2/s agrees well with diffusion constants reported in the literature for similar systems[37–41]. This result is in excellent agreement to MD simulations, where no change of the lateral diffusion coefficient was observed in the fluid phase of a DPPC membrane in contact with a 1.9mol% ethanol solution[8]. A similar behaviour was reported from MD simulations in DPPC, however, at very low ethanol concentrations[9]. Diffusion is, however, significantly slower in the gel phase when ethanol is present, consistent with the elastic data in Figure 4. The inclusion of additional molecules to the head group region of the bilayers obviously reduces the mobility of the lipid molecules in the more rigid gel phase, leading to a smaller diffusion constant.

Molecular freezing and melting is observed in the elastic neutron scattering experiments. The temperatures of pre-transition (L_β to $P_{\beta'}$) and main transition ($P_{\beta'}$ to L_α) is not changed due to the presence of ethanol molecules within the temperature resolution of 0.5 K of this experiment. The data in Figure 4 show the effect of ethanol molecules on slow, nanosecond dynamics of the membranes on different length scales, corresponding to lipid diffusion, lipid tail and hydration water dynamics. Ethanol does not seem to change membrane properties in the fluid L_α phase as the elastic data coincide for DMPC and DMPC/ethanol for temperatures above 296 K. However, the absolute values of the elastic intensity are higher on all length scales in ripple and gel phase when ethanol is present, indicative of a better ordered lipid structure. While the pre-transition is not pronounced in pure DMPC in Figure 4 a) and c), a pronounced step in the elastic intensity occurs in the presence of ethanol molecules.

These results lead us to the conclusion that ethanol has little effect on the nanosecond dynamics in the fluid phase of lipid membranes. This type of dynamics includes diffusion, however also motions related to the elastic properties (e.g. undulation of the membranes), and molecular reorientations, which show relaxational dynamics. In a recent inelastic neutron scattering study ethanol was found to significantly increase the collective nanoscale dynamics of the lipid tails in the fluid phase of the membranes[11]. These dynamics are significantly faster than the dynamics probed here and happen on picosecond time scales and between neighbouring hydrocarbon tails. A new, low-energy phonon branch was observed in the presence of ethanol and speculated to be related to the mobility of kink defects perpendicular to the membranes, responsible for the increased permeability for small molecules.

Dynamics of the hydration water are observed in Figures 4 e) and f). A freezing and melting transition is observed at the temperature of the main transition at T=296 K as kink in the elastic intensity. Hydration water dynamics seem to be

coupled to freezing and melting of membrane dynamics at the temperature of the main transition. Bulk water freezing would be observed at T = 271 K (0°C). The occurrence of a freezing and melting transition in the water detector indicates that a large fraction of the water molecules in hydrated powder samples can be considered as membrane-bound water. While the water-water correlation peak in bulk water is observed at $\sim$2 Å^{-1} (3.14 Å), the nearest-neighbour distance in hydration water is found to be increased by $\sim$8% to 1.85 Å^{-1} (3.4 Å). This is consistent with the dip in the electron densities in Figures 3 and 7 at the lipid/solution interface at $z \sim$23 Å, which points to a reduced density of the hydration water density close to the lipid head groups. The value of the electron density is decreased by about 10% at the lipid/water interface, in agreement with the decrease in density of the hydration solvent due to the increased nearest-neighbour distance.

5 Conclusion

In summary we studied structure and dynamics of phospholipid membranes hydrated with a 5wt%, corresponding to 2mol%, water/ethanol solution. From x-ray scattering experiments we determine the position of the ethanol molecules and their partitioning in the bilayers in gel and fluid phase. We find that the ethanol molecules are located in the head group region of the membranes, at a concentration of 1.6 ethanol molecules per lipid molecule in the gel, and 1.2 ethanol molecules per lipid molecule in the fluid phase. The electron densities give experimental evidence for an increased permeability in the presence of ethanol, related to ethanol molecules in the hydrophobic membrane core or an enhanced permeability for water molecules.

Elastic and quasi-elastic neutron scattering was used to study the effects of ethanol on slow, nanosecond diffusion, lipid acyl chain and hydration water dynamics. We find that the dynamics of membrane and hydration water are unchanged by the presence of ethanol in the fluid phase of the membranes at this alcohol concentration. However, ethanol was found to lead to a stiffer, better ordered structure in ripple and gel phase. Lipid diffusion is found to be decreased in the gel phase of the bilayers by 50%.

Acknowledgements: This research was funded by the Natural Sciences and Engineering Research Council of Canada (NSERC), the National Research Council Canada (NRC), the Canada Foundation for Innovation (CFI) and the Ontario Ministry of Economic Development and Innovation. We thank the NIST Centre for Neutron Research for the allocation of beam time. This work utilized facilities supported in part by the National Science Foundation under Agreement No. DMR-0944772.

References

1 J. A. Barry and K. Gawrisch, *Biochemistry*, 1994, **33**, 8082–8088.
2 D. T. Nizza and K. Gawrisch, *Gen. Physiol. Biophys.*, 2009, **28**, 140145.
3 L. L. Holte and K. Gawrisch, *Biochemistry*, 1997, **36**, 4669–4674.
4 S. E. Feller, C. A. Brown, D. T. Nizza and K. Gawrisch, *Biophys. J.*, 2002, **82**, 1396–1404.
5 J. Chanda and S. Bandyopadhyay, *Chem. Phys. Lett.*, 2004, **392**, 249.
6 A. N. Dickey and R. Faller, *Journal of Polymer Science Part B: Polymer Physics*, 2005, **43**, 1025–1032.
7 M. Patra, E. Salonen, E. Terama, I. Vattulainen, R. Faller, B. W. Lee, J. Holopainen and M. Karttunen, *Biophys. J.*, 2006, **90**, 1121–1135.
8 A. N. Dickey and R. Faller, *Biophysical Journal*, 2007, **92**, 23662376.
9 E. Terama, O. H. S. Ollila, E. Salonen, A. C. Rowat, C. Trandum, P. Westh, M. Patra, M. Karttunen and I. Vattulainen, *J. Phys. Chem. B*, 2008, **112**, 4131–4139.
10 T. Adachi, *Chemistry and Physics of Lipids*, 2000, **107**, 93–97.
11 M. D. Kaye, K. Schmalzl, V. C. Nibali, M. Tarek and M. C. Rheinstädter, *Phys. Rev. E*, 2011, **83**, 050907.
12 P. Westerman, J. Pope, N. Phonphok, J. Doane and D. Dubro, *Biochimica et Biophysica Acta (BBA) - Biomembranes*, 1988, **939**, 64 – 78.
13 B. W. Koenig and K. Gawrisch, *J. Phys. Chem. B*, 2005, **109**, 75407547.
14 H. Komatsu and S. Okada, *Chem. Phys. Lipids*, 1997, **85**, 67–74.
15 H. V. Ly and M. L. Longo, *Biophys. J.*, 2004, **87**, 1013–1033.
16 E. Nováková, K. Giewekemeyer and T. Salditt, *Phys. Rev. E*, 2006, **74**, 051911.
17 M. C. Rheinstädter, T. Seydel and T. Salditt, *Phys. Rev. E*, 2007, **75**, 011907.
18 M. C. Rheinstädter, T. Seydel, F. Demmel and T. Salditt, *Phys. Rev. E*, 2005, **71**, 061908.
19 A. M. Gaspar, S. Busch, M.-S. Appavou, W. Haeussler, R. Georgii, Y. Su and W. Doster, *Biochimica et Biophysica Acta*, 2010, **1804**, 7682.
20 A. Meyer, R. M. Dimeo, P. M. Gehring and D. A. Neumann, *Rev. Sci. Instrum.*, 2003, **74**, 2759–2777.
21 M. Weik, U. Lehnert and G. Zaccai, *Biophys. J.*, 2005, **89**, 3639–3646.
22 D. M., G. S. V. , O. S., M. J.K. and de Pablo J.J., *Biophys. J.*, 2007, **92**, 147–161.
23 K. Wood, M. Plazanet, F. Gabel, B. Kessler, D. Oesterhelt, D. J. Tobias, G. Zaccai and M. Weik, *Proc. Natl. Acad. Sci. U.S.A.*, 2007, **104**, 1804918054.
24 L. Toppozini, C. L. Armstrong, M. D. Kaye, M. Tyagi, T. Jenkins and M. Rheinstädter, *ISRN Biophysics*, 2012, **in press**, 0.
25 M. C. Rheinstädter, J. Das, E. J. Flenner, B. Brüning, T. Seydel and I. Kosztin, *Phys. Rev. Lett.*, 2008, **101**, 248106 (4 pages).
26 V. G. Sakai and A. Arbe, *Current Opinion in Colloid & Interface Science*, 2009, **14**, 381–390.
27 M. C. Rheinstädter, C. Ollinger, G. Fragneto, F. Demmel and T. Salditt, *Phys. Rev. Lett.*, 2004, **93**, 108107.
28 G. Pabst, N. Kučerka, M.-P. Nieh, M. Rheinstädter and J. Katsaras, *Chemistry and Physics of Lipids*, 2010, **163**, 460 – 479.
29 G. Fragneto and M. Rheinstädter, *Comptes Rendus Physique*, 2007, **8**, 865–883.
30 S. Tristram-Nagle, Y. Liu, J. Legleiter and J. F. Nagle, *Biophysical Journal*, 2002, **83**, 3324–3335.
31 J. F. Nagle and M. C. Wiener, *Biophys. J.*, 1989, **55**, 309–313.
32 J. Nagle, R. Zhang, S. Tristram-Nagle, W. Sun, H. Petrache and R. Suter, *Biophys. J.*, 1996, **70**, 1419–1431.
33 G. I. King and C. R. Worthington, *Physics Letters*, 1971, **35A**, 259–260.
34 N. Chu, N. Kučerka, Y. Liu, S. Tristram-Nagle and J. F. Nagle, *Phys. Rev. E*, 2005, **71**, 041904.
35 K. Lan and J. Jorgenson, *J. Chromatogr. A*, 2001, **915**, 1–13.
36 C. L. Armstrong, M. Trapp, J. Peters, T. Seydel and M. C. Rheinstädter,

Soft Matter, 2011, **7**, 8358–8362.
37 C. L. Armstrong, M. D. Kaye, M. Zamponi, E. Mamontov, M. Tyagi, T. Jenkins and M. C. Rheinstädter, *Soft Matter*, 2010, **6**, 5864–5867.
38 W. Pfeiffer, T. Henkel, E. Sackmann and W. Knorr, *Europhys. Lett.*, 1989, **8**, 201–206.
39 S. Busch, C. Smuda, L. Pardo and T. Unruh, *J. Am. Chem. Soc.*, 2010, **132**, 3232–3233.
40 A. Buchsteiner, T. Hauß, S. Dante and N. Dencher, *Biochim. Biophy. Acta*, 2010, **1798**, 1969–1976.
41 S. König, W. Pfeiffer, T. Bayerl, D. Richter and E. Sackmann, *J. Phys. II France*, 1992, **2**, 1589–1615.
42 N. Kučerka, Y. Liu, N. Chu, H. I. Petrache, S. Tristram-Nagle and J. F. Nagle, *Biophys. J.*, 2005, **88**, 2626–2637.
43 N. Kucerka, S. Tristram-Nagle and J. F. Nagle, *Biophysical Journal: Biophysical Letters*, 2006, **90**, L83–85.
44 A. Spaar and T. Salditt, *Biophys. J.*, 2003, **85**, 1576–1584.
45 T. T. Mills, G. E. S. Toombes, S. Tristram-Nagle, D.-M. Smilgies, G. W. Feigenson and J. F. Nagle, *Biophysical Journal*, 2008, **95**, 669681.
46 M. A. Barrett, S. Zheng, G. Roshankar, R. J. Alsop, R. K. R. Belanger, C. Huynh, N. Ku?erka and M. C. Rheinstdter, *PLoS ONE*, 2012, **7**, e34357.
47 K. Y. and D. J. M., *J. Membr. Biol.*, 1974, **17**, 69–86.
48 Y. Katz and J. M. Diamond, *Journal of Membrane Biology*, 1974, **17**, 101–120.
49 R. E. S., *Mol. Pharmacol.*, 1982, **22**, 133–139.
50 C. Trandum, P. Westh, K. Jörgensen and O. G. Mouritsen, *Biochimica et Biophysica Acta*, 1999, **1420**, 179–188.
51 P. Westh and C. Trandum, *Biochim. Biophys. Acta*, 1999, **1421**, 261–272.
52 B. J. A. and G. K., *Biochemistry*, 1995, **34**, 88528860.
53 D. Huster, J. Jin, Albert, K. Arnold and K. Gawrisch, *Biophys. J.*, 1997, **73**, 855–864.
54 B. Deamer and J. Bramhall, *Chem. Phys. Lipids*, 1986, **40**, 167–188.
55 S. Paula, A. Volkov, A. Van Hoek, T. Haines and D. Deamer, *Biophys. J.*, 1996, **70**, 339–348.
56 G. Lahajnar, P. Macek, P. Smid and I. Zupancic, *Biochim Biophys Acta.*, 1995, **1235**, 437–442.
57 P. Seeman, *Pharmacol. Rev.*, 1972, **24**, 583–655.
58 H. Jerabek, G. Pabst, M. Rappolt and T. Stockner, *J. AM. CHEM. SOC.*, 2010, **132**, 79907997.
59 K. Pang, *Mol. Pharmacol.*, 1980, **18**, 84.
60 J. Trudell, *Anesthesiol*, 1977, **46**, 5.
61 D. Mountcastle, *PNAS*, 1978, **75**, 4906.

Chapter 7

Aβ peptide in brain-like membranes

An investigation of brain-like membranes containing Amyloid beta proteins will be discussed in this chapter. Amyloid beta is a 36-43 amino acid length protein, and although is present and accomplishes other tasks in the brain (protection against metal-induced oxidizers and modification of cholesterol transport)[65], the aggregates of this protein are commonly associated with Alzheimer's disease.[66, 67]

Samples containing saturated, unsaturated and charged phospholipids (in ratios appropriate to that of a mammal brain as determined by centrifugation[68] - 59% saturated, 38% unsaturated and 3% charged) were prepared using the sample preparation approach as was discussed in Section 4.2. Cholesterol was added to these samples, creating a set of samples with 0 to 40mol% cholesterol. The position of the in-plane peak was plotted against cholesterol percentage, and a non-linear region was observed between 30mol% and 40mol% cholesterol.

Two additional samples were made, with a 1mol% Aβ peptide (amino acids 25-35), and a low (32.5mol%) and high (37.5mol%) cholesterol concentration. From the in-plane scattering we observe peaks which resemble aggregated and dispersed protein peaks.

7.1 Amyloid beta aggregates in Alzheimer's patients

The protein Amyloid beta is present in healthy brain cells. A healthy patient's brain will keep these proteins dispersed. It is not well understood how the plaques effect brain activity, but patients who experience neurodegenerative symptoms are likely to have possess these plaques. A cartoon depiction of plaques in the brain is shown in Figure 7.1. The plaques have been found (through dissections post-mortem) to reside in the membrane of cells occupying the area between neurons.

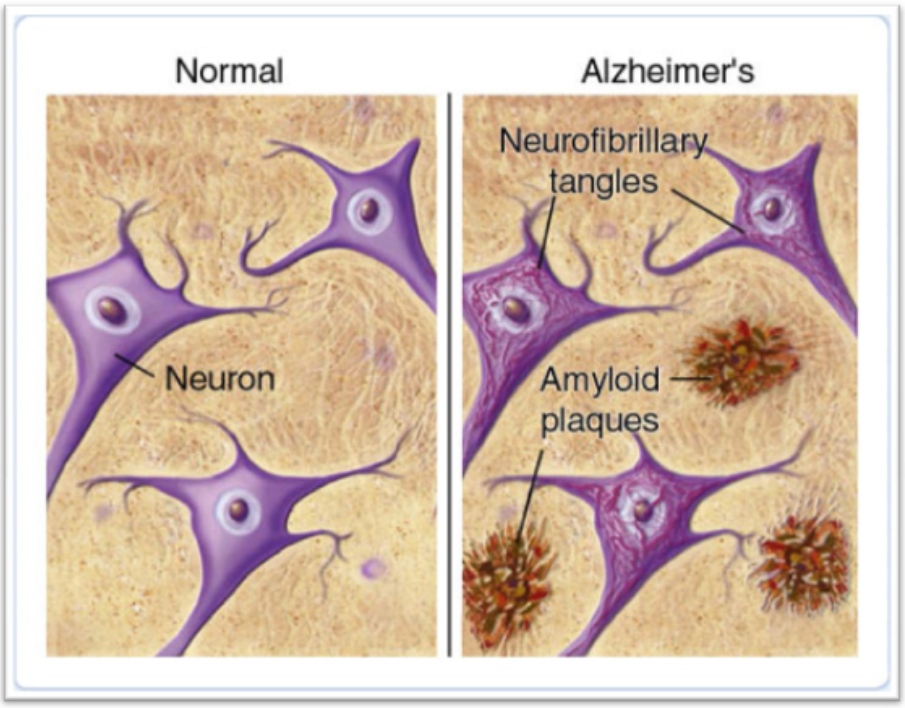

Figure 7.1: Cartoon of healthy brain and brain with Alzheimer's disease
A comparison of brain cells with and without amyloid-beta aggregation. Amyloid-β proteins aggregate and form plaques between the neurons of the brain, these plaques are linked to Alzheimer's disease.[69]

Amyloid beta at full length has from 39 to 42 amino acids. This full length protein, and also shorter fragments are membrane active. The fragment consisting of amino acids 25-35 is the membrane spanning section of the protein and represents

the dominant region for the neurotoxic effect which is observed. In the following experiments the membrane spanning fragment Aβ(25-35) was used.

7.2 Brain-like membranes with cholesterol

We created model membranes with a mix of various lipids and cholesterol. To try and best replicate real brain cell membranes, our models were composed of saturated, unsaturated and charged lipids in the ratio 59:38:3, respectively. This composition has been determined for mice brains (the assumption is made that mice and humans have similar brain lipid components) through centrifugation.[68] Similarly to Paper III, where a series of samples were made with DMPC and various concentrations of cholesterol up to 60% were constructed, samples were prepared with 0 to 40% choleterol in the brain-like lipid membranes. We attempted to construct samples with higher cholesterol percentages, but it seems that for this particular mix of lipids, 40% is cholesterol's solubility limit. These samples were prepared using the steps outlined in Section 4.2.

High-resolution reciprocal space map (RSM) scans were obtained using BLADE. From these RSM scans the position of Bragg rods representing lipid tail-tail spacing (see Figure 7.2) was determined for each cholesterol percentage.

The position of each of these tail-tail peaks can be related to the spacing between lipids, and if we assume a hexagonal distribution the area per lipid can also be calculated. A plot relating the measured position of the tail-tail peak to the cholesterol percentage was created and is seen in Figure 7.3.

7.3 Membrane curvature may encourage aggregation

The fact that the 25-35 amino acid fragment of the Amyloid-β peptide is membrane active, and spans the membrane motivates the need to discuss membrane curvature and it's role in aggregation/dispersion. Aranda-Espinoza *et al.* describe the free energy of a lipid bilayer (equation 7.1) and how the spontaneous curvature will affect this free energy.[70]

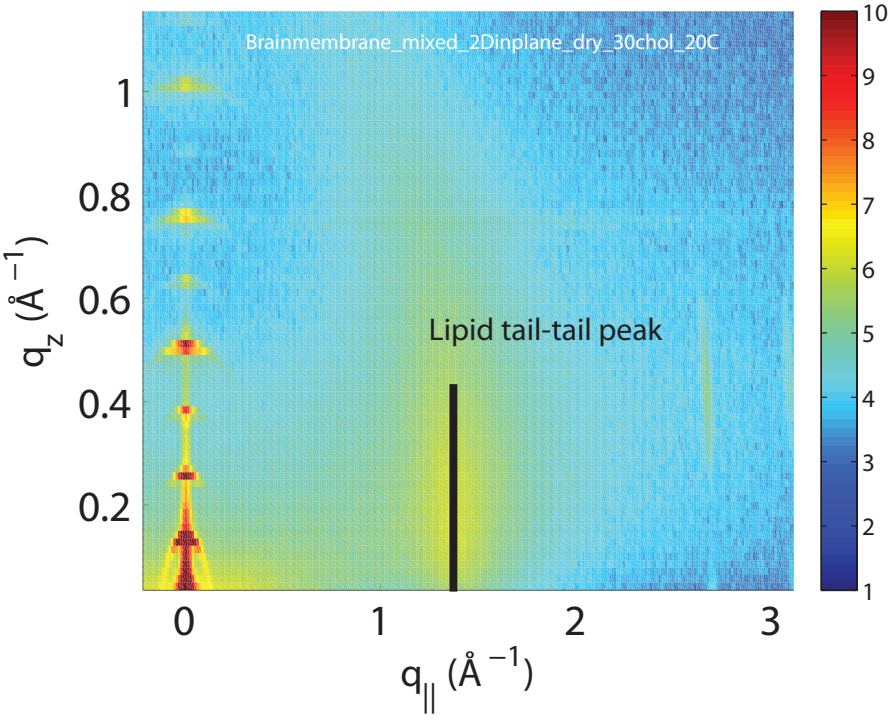

Figure 7.2: RSM of 30% Cholesterol in brain-like mixed lipid membrane 30% Cholesterol in brain like lipid membrane (59% saturated:38% unsaturated:3% charged). The position of the lipid tail-tail peak is shown with the vertical black line at $\overrightarrow{q}_{\parallel}$=1.5 Å^{-1}.

$$F(u,a) = \gamma a + G(u) + K(a)(\nabla^2 u - \kappa(a))^2 \tag{7.1}$$

In this equation, u=monolayer thickness, a=area/lipid, γ=surface tension, G(u)= compression/expansion of the lipids, K(a)=bending stiffness of the bilayer and κ(a)=spontaneous curvature of the bilayer. For a more detailed look at spontaneous curvature please refer to Figure 7.4.

The spontaneous curvature of a bilayer is based on a few factors, including the aspect ratio between the headgroup and tailgroup of a lipid molecule, the presence of any additional molecules (cholesterol, for example, sits in the tail region of the bilayer, causing a more negative curvature) and the number of unsaturated bonds present in the lipid tail structure. To attain the minimum free energy state, hydrophobic matching of the lipid and protein inclusion occurs. This process involves having the

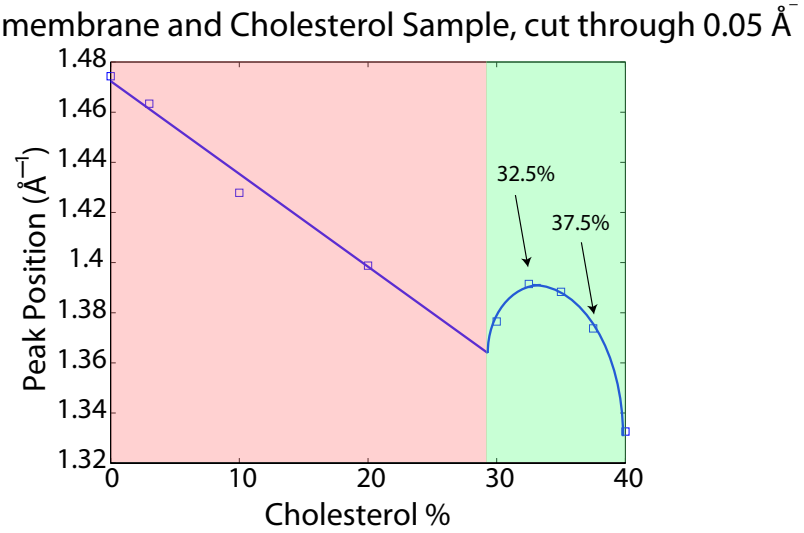

Figure 7.3: Tail-tail peak position and cholesterol %
The lipid tail-tail Bragg peak position is plotted as a function of cholesterol. Notice the linear regime (in pink) and the non-linear regime (in green). A low and high cholesterol value (32.5% and 37.5%) in the non-linear regime were chosen for further exploration.

hydrophobic region of the protein physically adjacent to the hydrophobic tail region of the bilayer. Depending on the curvature of the membrane, and the size of the protein inclusion this could result in a dispersed or aggregated protein arrangement.

We tested the hypothesis that the addition of cholesterol would change the spontaneous curvature of our brain-like membrane and at different cholesterol values we could drive the system from an aggregated to dispersed state.

7.4 Aggregate and dispersed samples

The non-linear region of Figure 7.3 encouraged the notion that this is an unstable regime. Two cholesterol concentrations in this region (a 'low' cholesterol percentage - 32.5%, and a 'high' cholesterol percentage - 37.5%) were remade with the addition

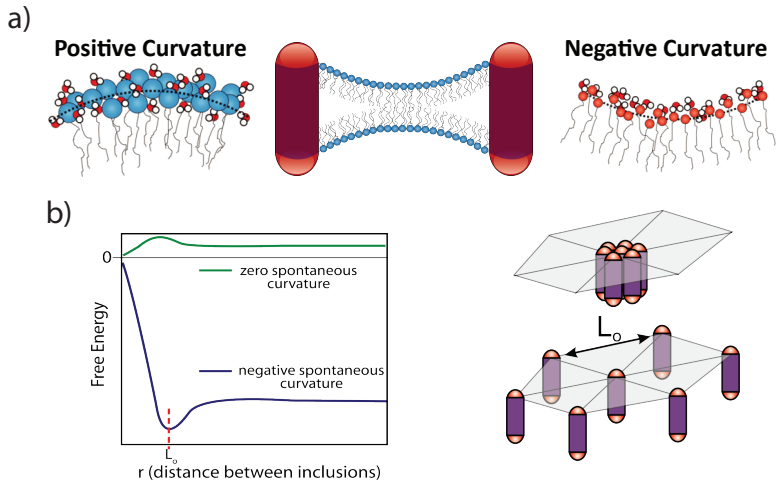

Figure 7.4: Spontaneous curvature and its effect on inclusion (protein) spacing a) Negative and positive spontaneous curvatures are shown. The lowest free energy state is shown in the centre, protein size creates a hydrophobic match for a negative spontaneous curvature. b) The free energy plotted for a zero spontaneous curvature example and a negative spontaneous curvature example. In this example, due to the size of the bilayer inclusion a negative spontaneous curvature results in a L_o spacing between inclusions.[70]

of 1% Aβ (25-35) peptide to the sample.

The sample was prepared using almost the same procedure as was discussed previously in section 4.2. The one diversion from this is before adding the powdered Amyloid peptide to the lipid and cholesterol mixture it was pre-treated in TFA (Trifluoroacetic acid) to disaggregate the peptide. This procedure is discussed in detail in [71].

Large reciprocal space and small (higher resolution) reciprocal space scans are shown in Figure 7.5. Figure 7.5a) and c) show a 32.5% cholesterol sample, a high x-ray intensity region at 0.15 $Å^{-1}$ (seen in c)). When converted to real-space distance this corresponds to L_o 40Å. On the other hand, this high intensity peak is not present in b) or d), rather a Bragg rod at 1.40 $Å^{-1}$ is observed in b). This is real-space corresponds to a distance of L_o 4.5Å.

For the low cholesterol sample we see a protein spacing indicating a dispersed distribution and for the high cholesterol sample the spacing is much smaller, on the

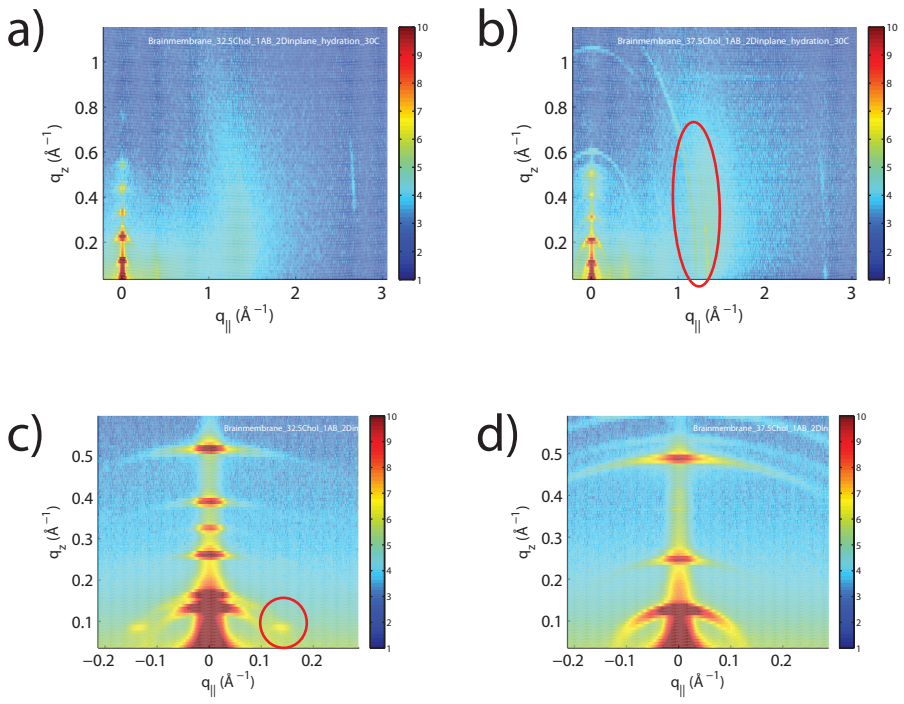

Figure 7.5: Disperse and aggregate Amyloid-β protein in brain-like membranes All scans shown are 1% Amyloid-β (25-35 fragment) in brain-like lipid bilayer. a) 32.5% cholesterol large reciprocal space scan b) 37.5% cholesterol large reciprocal space scan c) 32.5% high resolution small reciprocal space scan d)37.5% high resolution small reciprocal space scan

same order as the diameter of the protein. By increasing the cholesterol percentage of our sample we have changed from a dispersed to aggregated protein distribution.

7.5 Next steps

More samples must be created to obtain a phase diagram for our system. (See Figure 7.6).

Understanding exactly what makes our model brain-like system turn from a healthy (dispersed) to Alzheimer's (aggregated) state would provide insight to both model membranes with proteins and to Alzheimer's research.

An array of samples would help us to discover if changing the concentration of

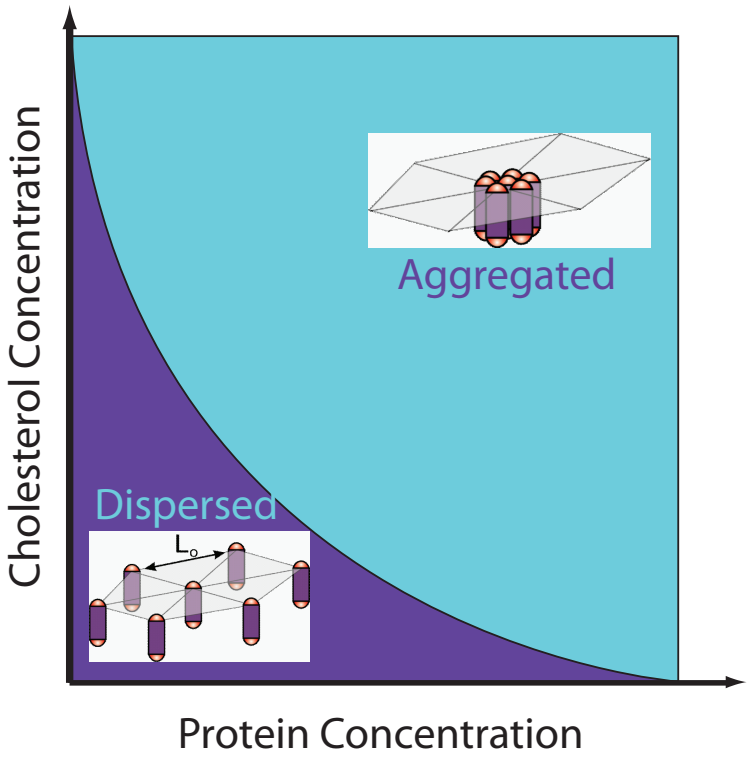

Figure 7.6: Prospective phase diagram for our Amyloid-β brain-like samples
A phase diagram showing dispersed and aggregated protein configurations.

lipids, cholesterol or amyloid beta protein has a large effect on the protein configuration.

Chapter 8

Conclusions

In the preceding document structural and dynamical information of microscopic systems was obtained using neutron and x-ray scattering techniques. These experiments were performed at world-class laboratories including Institut Laue-Langevin (Grenoble, France), Laboratory for Membrane and Protein Dynamics (McMaster University, Canada), Canadian Neutron Beam Centre (Chalk River, Canada) and NIST (Gaithersberg, USA).

The experiments contained in this thesis provide insight into understanding new nano-materials (cobalt magnetic fluid), determining the action of Asprin medicine in membranes, how it acts to counter high cholesterol (ASA and Cholesterol), elucidating the processes which occur within the human body's millions of membranes (cholesterol and lipid dynamics), finding a solution to drug delivery with ethanol (ethanol DMPC hydrated membranes) and to understanding the processes involved in Alzheimer's disease (Amyloid-β in brain-like membranes).

Bibliography

[1] J. Embs, H. W. Müller, C. E. Krill III, F. Meyer, H. Natter, B. Müller, S. Wiegand, M. Lücke, K. Knorr, and R. Hempelmann. Characterization of the grain size in ferromagnetic colloids: Comparing torsional-pendulum measurements with standard complementary methods. *Z. Phys. Chem.*, 220:153–171, 2006.

[2] Des McMorrow Jens Als-Nielsen, editor. *Elements of Modern X-Ray Physics*. John Wiley and Sons, Ltd, New York, NY, 2005.

[3] G. Pabst, N. Kučerka, M.-P. Nieh, M.C. Rheinstädter, and J. Katsaras. Applications of neutron and x-ray scattering to the study of biologically relevant model membranes. *Chemistry and Physics of Lipids*, 163(6):460 – 479, 2010.

[4] J. Katsaras T.A. Harroun, G.D. Wignall. *Neutron Scattering For Biology*, pages 1–18. Neutron Scattering in Biology, Techniques and Applications. Springer, Heidelberg, 2006.

[5] G.L. Squires. *Introduction to the theory of thermal neutron scattering*. Dover Publications, Inc., Mineola, New York, 1978.

[6] A.-J. Dianoux and G. Lander, editors. *Neutron Data Booklet*. Old City Publishing Group, Philadelphia, 2nd edition, 2003.

[7] Gsta Ekspong, editor. *From Nobel Lectures, Physics 1922-1941*. Elsevier Publishing Company, Amsterdam, 1965.

[8] Wilhelm Conrad Roentgen. Ueber eine neue art von strahlen (vorlaeufige mittheilung). *Wrzburger Physik.-medic. Gesellschaft*, 1895.

[9] Rigaku. Automated multipurpose x-ray diffractometer. SmartLab X-ray Diffractometer manual, 2010.

[10] S.J. Singer and G.L. Nicolson. The fluid mosaic model of the structure of cell membranes. *Science*, 175:720731, 1972.

[11] Tony Pawson and Piers Nash. Assembly of cell regulatory systems through protein interaction domains. *Science*, 300:445–452, 2003.

[12] Superti-Furga G. Gavin AC. Protein complexes and proteome organization from yeast to man. *Curr Opin Chem Biol.*, 7:21–27, 2003.

[13] Dietrich C. Jacobson K. Looking at lipid rafts. *Trends Cell Biol.*, 9:87–91, 2003.

[14] Russell RB. Betts MJ. The hard cell: from proteomics to a whole cell model. *FEBS Lett.*, 581:2870–6, 2007.

[15] Yuichi Oba Mitsuhiro Nakamura Yoko Hotta Ryota Iino1 Rinshi S. Kasai Kazuhiko Yamaguchi Takahiro Fujiwara Chieko Nakada, Kenneth Ritchie and Akihiro Kusumi. Accumulation of anchored proteins forms membrane diffusion barriers during neuronal polarization. *Nature*, 5:626–634, 2003.

[16] A. Abbott. Cell biology: Hopping fences. *Nature*, 433:680–683, 2005.

[17] Dennis R. Voelker Gerrit van Meer and Gerald W. Feigenson. Membrane lipids: where they are and how they behave. *Nat Rev Mol Cell Biol.*, 9:112124, 2008.

[18] Subramaniam S. Brown H. A. Glass C. K. Merrill A. H. Murphy R. C. et al. Fahy, E. A comprehensive classification system for lipids 1. *Journal Of Lipid Research*, 46:839–861, 2005.

[19] Subramaniam S. Murphy R. C. Nishijima M. Raetz C. R. H. Shimizu T. et al. Fahy, E. Update of the lipid maps comprehensive classification system for lipids 1. *Journal Of Lipid Research*, S:9–14, 2009.

[20] Douglas P. Lee Rosalind A. Coleman. Enzymes of triacylglycerol synthesis and their regulation. *Progress in Lipid Research*, 43:134176, 2004.

[21] B. Ramstedt and J. P. Slotte. Membrane properties of sphingomyelins. *FEBS Letters*, 531:33–37, 2002.

[22] R. Lipowsky and E. Sackmann, editors. *Structure and Dynamics of Membranes*, volume 1 of *Handbook of Biological Physics*. Elsevier, Amsterdam, 1995.

[23] T. N. Gobley. Sur la lcithine et la crbrine. *Journal de Pharmacie et de Chimie*, 20:98–103, 161–166, 1874.

[24] Sergey Pogodin and Vladimir A. Baulin. Coarse-grained models of phospholipid membranes within the single chain mean field theory. *FEBS Letters*, 6:2216–2226, 2010.

[25] Martin D. Kaye. Studies of lipid bilayer structure and dynamics. M.sc. thesis, McMaster University, 1280 Main Street West, Hamilton, 2011.

[26] D. Marsh, editor. *CRC Handbook of Lipid Bilayers*. CRC Press, 1990.

[27] V.A. Raghunathan Bibhu Ranjan Sarangi, Sanat Karmakar. X-ray and neutron scattering studies of lipidsterol model membranes. *Advances in Planar Lipid Bilayers and Liposomes*, 11:159186, 2010.

[28] David J. Griffiths, editor. *Introduction to Quantum Mechanics*. Pearson Prentice Hall, Upper Saddle River, NJ, 2nd edition, 2005.

[29] R.E. Rosensweig, editor. *Ferrohydrodynamics*. Cambridge University Press, Cambridge, 1985.

[30] F. Boue, V. Cabuil, J.C. Bacri, and R. Perzynski. Small-angle neutron scattering of ionic ferrofluids. *J. Magn. Magn Mater.*, 122:78–82, 1993.

[31] L.M. Pop and S. Odenbach. Investigation of the microscopic reason for the magnetoviscous effect in ferrofluids studied by small angle neutron scattering. *J. Phys.: Condens. Matter*, 18:S2785–S2802, 2006.

[32] Stefan Odenbach, editor. *Colloidal Magnetic Fluids: Basics, Development and Application of Ferrofluids*. Springer, Heidelberg, 2009.

[33] M. Shliomis. *Sov. Phys.-Usp.*, 17:153, 1974.

[34] Ashcroft and *Solid State Physics*. Thomson Learning, 1976.

[35] J.P. Huang, Z.W. Wang, and C. Holm. Computer simulations of the structure of colloidal ferrofluids. *Phys. Rev. E*, 71:061203 1–11, 2005.

[36] Boualem Hammouda. Probing nanoscale structures - the sans toolbox. National Institute of Standards and Technology Center for Neutron Research.

[37] Oxford-Instruments. Split pair magnets for neutron scattering. www.oxford-instruments.com/, 2012.

[38] Kenneth Barbalace. Periodic table of elements - sorted by cross section. EnvironmentalChemistry.com, 2012.

[39] J. Faraudo M. Benelmekki C. Rebollo J. Andreu, J. Camacho and Ll. Martnez. Simple analytical model for the magnetophoretic separation of superparamagnetic dispersions in a uniform magnetic gradient. *Phys. Rev. E*, 84, 2011.

[40] Juan Camacho Jordi Andreu, Carles Calero and Jordi Faraudo. On-the-fly coarse-graining methodology for the simulation of chain formation of superparamagnetic colloids in strong magnetic fields. *Phys. Rev. E*, 85, 2012.

[41] P.J. Quinn. A lipid matrix model of membrane raft structure. *Prog Lipid Res.*, 49:390–406, 2010.

[42] Sigma Aldrich. Acetylsalicylic acid. www.sigmaaldrich.com, 2011.

[43] E. Sackmann. Supported membranes: Scientific and practical applications. *Science*, 271:43–48, 1996.

[44] E. T. Castellana and P. S. Cremer. Solid supported lipid bilayers: From biophysical studies to sensor design. *Surface Science Reports*, 61:429–444, 2006.

[45] B. Liedberg K. Uvdal R. Erlandsson H. Elwing I. Lundstroem E. Vandenberg, L. Bertilsson. Structure of 3-aminopropyl triethoxy silane on silicon oxide preparation of aptes surfaces. *Interface*, 147:103–118, 1991.

[46] Jin Gang Wang, Zhan-Hui. Silicon surface modification with a mixed silanes layer to immobilize proteins for biosensor with imaging ellipsometry. *Colloids and Surfaces*, 34:173–117, 2004.

[47] Jiyu Fang Charles Dulcey Paul A. Heiney, Kirsten Grüneberg and Ranganathan Shashidhar. Structure and growth of chromophore-functionalized (3-aminopropyl)triethoxysilane self-assembled on silicon. *Langmuir*, 16:2651–2657, 2000.

[48] D. Constantin C. Li and T. Salditt. Biomimetic membranes of lipid-peptide model systems prepared on solid support. *J. Phys.: Condens. Matter*, 16:2439–2453, 2010.

[49] Hasegawa Saburo Wexler, Arnold. Relative humidity-temperature relationships of some saturated salt solutions in the temperature. *Colloids and Surfaces*, 53:19–26, 1954.

[50] P.P. Ewald. Introduction to the dynamical theory of x-ray diffraction. *Acta Crystallographica*, 25:103, 1969.

[51] Omega. Equilibrium relative humidity: Saturated salt solutions. www.omega.com, 2012.

[52] W. Kraus and G. Nolze. Powdercell for windows. Federal Institute for Materials Research and Testing.

[53] Stephanie Tristram-Nagle, Yufeng Liu, Justin Legleiter, and John F. Nagle. Structure of gel phase dmpc determined by x-ray diffraction. *Biophysical Journal*, 83:3324–3335, 2002.

[54] Tomohiro Adachi. A new method for determining the phase in the x-ray diffraction structure analysis of phosphatidylcholine:alcohol. *Chemistry and Physics of Lipids*, 107:9397, 2000.

[55] P. Huffman D. Jacobson, M. Arif and R. Satija. A new neutron imaging facility at bt-6 for thenon-destructive analysis of working fuel cells. NCNR-NIST Annual Report, 2004.

[56] Barrett M. Hiess A. Shi A. C. Armstrong, C. L. and M. C. Rheinstädter. Effect of cholesterol on the lateral nano-scale dynamics of fluid membranes. *European Biophysics Journal*, In press, 2012.

[57] Gsta Ekspong, editor. *Nobel Lectures, Physics*. World Scientific Publishing Co., Singapore, 1997.

[58] Institut Laue-Langevin. Thermal neutron three-axis spectrometer in8. www.ill.eu, 2010.

[59] P. Martel. Flux measurements at various beamports. Atomic Energy of Canada Memorandum, 1987.

[60] National Research Council Canada. Neutron spectrometers. www.nrc-cnrc.gc.ca, 2011.

[61] Armstrong C. L. Barrett M. Zheng S. Luo L. Nanda H. Sakai V. G. Toppozini, L. and M. C. Rheinstädter. The interaction of ethanol with lipid membranes seen by x-ray and neutron scattering. *In Preparation*, 2012.

[62] V.F. Sears. Neutron scattering lengths and cross sections of the elements and their isotopes. *Neutron News*, 3:29–37, 1992.

[63] P. M. Gehring A. Meyer, R. M. Dimeo and D. A. Neumann. The high-flux backscattering spectrometer at the nist center for neutron research. *Rev. Sci. Instrum.*, 74:2759, 2003.

[64] J. Peters T. Seydel C.L. Armstrong, M. Trapp and M.C. Rheinstädter. Short range ballistic motion in fluid lipid bilayers studied by quasielastic neutron scattering. *Soft Matter*, 7:8358–8362, 2011.

[65] Debomoy K. Lahiri and Bryan Maloney. Beyond the signaling effect role of amyloidbeta-42 on the processing of abeta pp, and its clinical implications. *Exp Neurol.*, 225:51–54, 2010.

[66] Dennis J. Selkoe. Alzheimer's disease–genotypes, phenotype, and treatments. *Science*, 275:630–631, 1997.

[67] John Hardy. Toward alzheimer therapies based on genetic knowledge. *Annual Review of Medicine*, 55:15–25, 2004.

[68] Blank M. Moehl A. Cotman, C. W. and F. Snyder. Lipid composition of synaptic plasma membranes isolated from rat brain by zonal centrifugation. *Biochemistry*, 8:46064612, 1969.

[69] American Health Assistance Foundation. Alzheimer's disease research: Plaques and tangles. www.ahaf.org, 2012.

[70] N. Dan P. Pincus S. Safran H. Aranda-Espinoza, A. Berman. Interaction between inclusions embedded in membranes. *Biophysical Journal*, 71:648–656, 1996.

[71] J. Talafous R. Orlando S.C. Jao, K. Ma and M. G. Zagorski. Trifluoroacetic acid pretreatment reproducibly disaggregates the amyloid beta-peptide. *Amyloid-International Journal of Experimental and Clinical Investigation*, 4:240–252, 1997.